



The
University
Of
Sheffield.

Aerodynamic optimisation of sports stadiums towards wind comfort

By:

Polytimi Sofotasiou

A thesis submitted in partial fulfilment of the requirements for the degree of
Doctor of Philosophy

The University of Sheffield
Faculty of Engineering
Department of Mechanical Engineering

January 2017

Dedication

Στο Γιάννη, τη Βούλα & τη Μαρία Σοφοτάσιου

To Gianni, Voula & Maria Sofotasiou

Acknowledgement

I would like to express my gratitude firstly to Dr. Ben Richard Hughes who trusted to me this PhD role and believed in me. He is a real inspiration of a hardworking person, supervisor and father.

Secondly, I would like to thank Dr. John Calautit, who supported me during the first stages of my PhD, by guiding me, teaching me and correcting me.

Starting my PhD thesis in the University of Leeds, I met great people who introduced me to Computational Fluid Dynamics. I would like to thank Prof. Nigel Wright, who was my supervisor during the first year, and also Dr. Nikolaos Nikitas for his support and advices during my research studies.

During the experimental part of my research in the University of Nottingham, Dr. John Owen, Dinh Nguyen and Mr. Jim's team were those who helped me to successfully complete my experimentation study in the wind tunnel facility of the Civil Engineering Department.

PhD is a lonely path, but there are friends who were there when I was losing my strength and motivation. I would like to thank my best friends Dani, Natassa, Mariathi, Katerina, John, Dimitris and Baris, as well as my colleagues Kate, Diana and Dominic, whose support was always advantageous.

Last, but always first in my heart and mind, I would like to thank my father Ioannis Sofotasios and my sister Maria Sofotasiou for their psychological support all these years. "Father, thank you for sacrificing your life to our family and for all the things that you gave us so generously".

List of Publications

Journal Papers

1. **Sofotasiou, P.**, Hughes, B. and Calautit, J. (2015). Qatar 2022: Facing the FIFA World Cup climatic and legacy challenges. *Sustainable Cities and Society*, 14, pp.16-30.
2. **Sofotasiou, P.**, Calautit, J., Hughes, B. and O'Connor, D. (2016). Towards an integrated computational method to determine internal spaces for optimum environmental conditions. *Computers & Fluids*, 127, pp.146-160.
3. **Sofotasiou, P.**, Nguyen, D., Owen, J., Hughes, B., Ghani, S.. CFD modelling of an open-circuit low-speed Atmospheric Boundary Layer wind tunnel. *Wind Engineering and Industrial Aerodynamics*. (Under review).
4. **Sofotasiou, P.**, Hughes, B., Ghani, S.. CFD-based optimisation of a generic oculus stadium roof structure to improve wind comfort for players and spectators. *Energy and Buildings*. (Under review).

Conference Papers

5. **Sofotasiou, P.**, Calautit, J. and Hughes, B. (2015). 'Thermal Performance Evaluation of Semi-Outdoor Sport Stadia- A Case Study of the Upcoming 2022 FIFA World Cup in Qatar'. In: 3rd International Conference "ENERGY in BUILDINGS 2014", 15 November, Athens, Greece. ASHRAE Hellenic Chapter. Available at: http://ashrae.gr/EinB2014/EinB2014_Proceedings.pdf.
6. **Sofotasiou, P.**, Calautit, J., Hughes, B., O'Connor, D. (2016). 'Towards an integrated computational method to optimise design strategies for the built environment'. In: Rodrigues, L. ed., Sustainable Energy for a Resilient Future: Proceedings of the 14th International Conference on Sustainable Energy Technologies, 25-27 August 2015, Nottingham, UK. University of Nottingham: Architecture, Energy & Environment Research Group. Volume 3, pp 48-57. Available from: eprints.nottingham.ac.uk.

Contents

Dedication	ii
Acknowledgement	iii
List of Publications	iv
List of Figures	x
List of Tables	xviii
Abbreviations	xx
Nomenclature	xxii
Abstract	xxvi
Chapter 1 Introduction	27
1.1 Aims and objectives	30
1.2 Research methodology	30
1.3 Thesis layout	32
Chapter 2 Literature Review	34
2.1 Introduction	34
2.2 Wind engineering	34
2.2.1 Wind climate	35
2.2.2 Influence of terrain	36
2.2.2.1 Atmospheric boundary layer thickness (δ).....	36
2.2.2.2 Zero-plane displacement (d)	37
2.2.2.3 Surface shear velocity (u^*)	37
2.2.2.4 ABL velocity profile	38
2.2.3 Aerodynamics effects.....	38
2.2.3.1 Wind load	38
2.2.4 Wind flow distribution	45
2.3 Wind comfort	51
2.3.1 Porosity in stadiums	55

2.4	Environmental comfort conditions in stadiums	58
2.4.1	Thermal performance	59
2.4.2	Natural ventilation.....	60
2.4.3	Pollution dispersion.....	62
2.4.4	Wind-driven rain	63
2.4.5	Thermal and energy performance	66
2.5	Stadium design considerations	68
2.6	Design optimisation	70
2.7	Research gap	73
2.8	Summary	73
 Chapter 3 Wind Tunnel Experimentation.....		76
3.1	Introduction	76
3.2	Wind tunnel classification.....	76
3.3	Wind tunnel similarity criteria	77
3.4	ABL wind tunnels	78
3.4.1	Roughness elements for ABL simulation	81
3.5	The ABL wind tunnel facility of the University of Nottingham.....	81
3.5.1	Description of the facility.....	81
3.5.1.1	Simulation of the suburban boundary layer	82
3.5.2	Description of the equipment	83
3.5.2.1	Hot wire probe calibration:	85
3.5.2.2	Data acquisition system:	87
3.6	Experimental set-up on empty domain	88
3.6.1	Experimental results.....	90
3.7	Stadium design selection.....	93
3.7.1	Design cases	95
3.8	Experimental stadium model.....	95
3.8.1	Pressure measurements	97
3.8.2	Experimental results.....	100
3.8.2.1	Non-elevated roof at 0° wind angle (Ref. case)	100
3.8.2.2	Roof wind pressure results	103
3.8.2.3	Terraces wind pressure results	106
3.8.2.4	Pitch wind pressure results.....	109
3.9	Errors and uncertainties.....	111

3.10	Summary	113
Chapter 4 Computational Fluid Dynamics.....		115
4.1	Introduction	115
4.2	Governing equations	115
4.3	Space discretisation	116
4.3.1	Cell Types	117
4.3.1.1	Structured Mesh	117
4.3.1.2	Unstructured Mesh	118
4.3.1.3	Hybrid Mesh.....	120
4.3.2	Mesh Quality	121
4.3.3	Mesh Comparison	122
4.3.4	Mesh Recording	124
4.4	Equation discretisation	125
4.4.1	The structure of the turbulent Boundary Layer (BL).....	125
4.4.2	Modelling turbulence	128
4.4.3	The Standard $k-\varepsilon$ model (SKE)	129
4.4.4	The Realizable $k-\varepsilon$ turbulence model (RKE)	130
4.4.5	The Spalart-Allmaras model (SA)	131
4.5	Verification and Validation.....	132
4.6	ABL flow simulation	135
4.6.1	Computational requirements	137
4.6.2	Computational recommendations.....	139
4.7	CFD stadium parameterisation.....	141
4.7.1	Computational domain and discretisation	141
4.7.2	Simulation set-up	145
4.8	Grid verification	146
4.9	Summary	152
Chapter 5 Results and Discussion.....		153
5.1	Introduction	153
5.2	CFD results	153
5.2.1	Non-elevated roof configuration	153
5.2.1.1	Pressure distribution.....	154
5.2.1.2	Airflow distribution.....	156

5.2.2	Elevated roof opening	159
5.2.2.1	Pressure distribution.....	159
5.2.2.2	Airflow distribution.....	162
5.3	Further interpretation of the results.....	165
5.3.1	Wind environmental impact.....	165
5.3.2	Wind flow distribution	169
5.3.2.1	Auxiliary area.....	169
5.3.2.2	Spectator tiers.....	172
5.4	Turbulence model validation	176
5.5	Limitations	184
5.6	Summary	184
Chapter 6 Design Optimisation.....		186
6.1	Introduction.....	186
6.2	Theoretical background.....	186
6.3	Optimisation concept and methodology	187
6.3.1	Design of Experiments (DoE) set-up	189
6.3.1.1	Selection of input parameters.....	190
6.3.1.2	Selection of output parameters.....	190
6.3.1.3	Generation of design points	191
6.4	Response Surface Methodology (RSM)	195
6.4.1	RSM meta-models.....	195
6.4.2	Goodness of fit	197
6.4.2.1	Response surfaces	198
6.5	Goal driven optimisation (GDO)	200
6.5.1	Optimisation results	201
6.5.2	GDO verification.....	203
6.6	GDO sensitivities	204
6.7	Interpretation of results	205
6.8	Limitations	209
6.9	Summary	210
Chapter 7 Conclusions.....		211
7.1	Future work	216

Chapter 8 References	218
Appendix A	231
A.1. Hot Wire Probe Calibration	231
A.2. Description of the ABL wind tunnel facility.....	234
A.3. CFD Modelling of the ABL Wind Tunnel Facility.....	239
Appendix B	242
B.1. Description of the scaled stadium model	242
B.2. Wind Tunnel Results.....	246
Appendix C	253
C.1. Element Shapes	253
C.2. 2D Conformal Hexahedral Mesh	254
Appendix D	255
Appendix E	260

List of Figures

Figure 1-1 Research methodology steps.	32
Figure 2-1 The wind-load chain as described by Davenport (Announcement of the Alan G. Davenport Wind Loading Chain, 2011).	34
Figure 2-2 Graphical representation of the atmospheric boundary layer (Garratt, 1994).	35
Figure 2-3 Profiles of mean wind velocity over different terrain roughness (Houghton and Carruthers, 1976).	37
Figure 2-4 External pressure coefficients for duopitch roofs under 0° wind angle (European Standard, 2005).	40
Figure 2-5 Cp distribution charts for curved roofs with rectangular (left) and circular base (right) (European Standard, 2005).	41
Figure 2-6 Illustration of the Hong Kong stadium structure (left) and 1:300 wind tunnel scaled model (right) (Thompson et al., 1998).	42
Figure 2-7 ABL wind tunnel experimentation of a football stadium under two roof perimeter configurations (Marighetti et al., 2000).	42
Figure 2-8 Distribution on the mean pressure coefficient values on the Manfredonia's grandstand roof (Biagini et al., 2007).	43
Figure 2-9 Distribution of pressure coefficients generated on the roof of the Delle Aphi stadium with (left) and without (right) radial tensile structure (left) (Biagini et al., 2007).	44
Figure 2-10 Wind tunnel test model (left) and generated mean pressure coefficients at the roof surface (right) (Chen et al., 2016).	45
Figure 2-11 Flow distribution and turbulence features around a building without openings (Blocken and Carmeliet, 2004).	45
Figure 2-12 Far field and close field CFD velocity vectors for $U_{ref} = 10$ m/s and dimensionless velocities along a vertical line below the windward roof edge for the stadium cases with ascending (a), flat (b) and descending (c) roof configuration (Persoon et al., 2008).	47
Figure 2-13 Velocity vectors generated in a vertical central plane for the four stadium configurations with flat roof; two opposite grandstands (a), four grandstands with open corners (b), four grandstands with open corners and windshields on the grandstand edges (c), enclosed stadium (d) (van Hoof et al., 2011).	48

Figure 2-14 Schematic representation of the wind flow patterns for the four different stand configurations and dimensionless velocity contours on a horizontal plane 1 m above ground; $U_{ref} = 10$ m/s (van Hoof et al., 2011).	49
Figure 2-15 Wind tunnel model of the Ibrox Park stadium (left) and illustration of the wind speed distribution over the pitch area (right) (Reid and Travers, 1991).	50
Figure 2-16 Dimensionless velocity contours on the pitch area under southeast wind direction (Goliger, 2010).....	50
Figure 2-17 Dimensionless wind values on the pitch corner areas for the case of open (left) and close entrance doors (Goliger, 2010).	51
Figure 2-18 Structural design interventions to be considered for the wind comfort improvement of the Ross-Ade Stadium (Mei and Qu, 2016).	51
Figure 2-19 Criteria for comfort zone of flexible outlines for semi-open stadia (Szucs et al., 2007).....	53
Figure 2-20 Evolution of the average Ψ values in function of the façade porosity for different wind incidences (Szucs et al., 2007).	54
Figure 2-21 Stadium model with 43 % porosity (left) and iso- Ψ lines for the resultant airflow distribution (right); dark and light coloured areas represent the intensively ventilated and the calm zones respectively (Szucs et al., 2009a).....	56
Figure 2-22 Iso- Ψ values for an enclosed stadium with flat roof configuration (Szucs et al., 2009b).....	57
Figure 2-23 Mean iso-velocity maps (as percentage of $U_{ref} = 3.64$ m/s) generated for the old (left) and the new (right) roof (Biagini et al., 2007).	58
Figure 2-24 Prediction of local climatic conditions for a hot, sunny day of the Stadium Australia integrated with semi-transparent roof (Fiala and Lomas, 1999). .	59
Figure 2-25 Thermal performance assessment of the stadium of France (A) and the Ataturk stadium (B) at 17 h (Bouyer et al., 2007).	60
Figure 2-26 Dimensionless wind velocities for the experimental (bold) and the numerical study (italics) (Blocken and Persoon, 2009).	61
Figure 2-27 Generation of the ratio of ACH to U_{10} for different wind direction for the Amsterdam Arena stadium (van Hoof and Blocken 2010a).	62
Figure 2-28 Percentage of wetted stand length for seven roof configurations under variable raindrop diameter, reference velocity (U_{ref}) and power law coefficient (a_p) (Pearsoon et al., 2008).....	64

Figure 2-29 Percentage of wetted stand for the twelve stadium configurations and the four raindrop diameters; $U_{ref} = 10\text{m/s}$ (van Hoof et al., 2011).....	65
Figure 2-30 Computational example of the rain drop trajectories (Soligo et al., 2000).	65
Figure 2-31 Wind (left) and temperature (right) distributions generated on a vertical plane in the middle of the model (Stamou et al., 2008).	67
Figure 2-32 CFD predictions for air temperature (a) and air speed (b) (Ucuncu et al., 2010).	67
Figure 2-33 Air flow distribution patterns (c) generated after conduction of smoke tests on the lower (a) and upper (b) spectator tiers for the Malmö Arena (Lestinen et al., 2016).	68
Figure 2-34 The dimensional characteristics of the auxiliary area (FIFA, 2011).....	69
Figure 2-35 Dimensional recommendations for spectator tiers (FIFA, 2011).....	70
Figure 2-36 Increased trend of number of optimisation studies in building science (Nguyen et al., 2014).....	70
Figure 3-1 Illustration of the total ABL wind tunnel facility.....	82
Figure 3-2 The boundary layer simulation arrangement for the wind tunnel facility.	83
Figure 3-3 Standard Pitot-static tube used for the wind tunnel experiment.....	84
Figure 3-4 Single wire probe with BNC connector used for the wind tunnel experiment (Dantecdynamics.com, 2017).....	85
Figure 3-5 Air velocity calibrator and micromanometer (a) and hot wire calibration setup (b).....	86
Figure 3-6 The calibration system employed for the wind tunnel study.	87
Figure 3-7 Data acquisition system at the wind tunnel facility of University of Nottingham.....	88
Figure 3-8 Illustration of the measurement locations for monitoring the velocity profile and the air temperature (a); roughness-line (a), (b); turntable-line (c).....	89
Figure 3-9 Illustration of location points for the velocity measurements in the roughness-line (left), along with the hot wire stands used per height case (right). ...	90
Figure 3-10 Vertical profiles for velocity and turbulent intensity at full height (top) and at the lower height levels (bottom), generated at the roughness-line.	91
Figure 3-11 Vertical profiles of velocity (blue) and turbulence intensity (red) for the six wind case studies on the turntable-line.....	92

Figure 3-12 Fit comparison of average velocity data with the logarithmic law, up to 0.2δ ($= 0.2 \text{ m}$).	92
Figure 3-13 Description of the stadium areas (A-F); perspective (a), side (b) and cross-sectional view (c).	94
Figure 3-14 Illustration of the four stadium design cases; for non-elevated and elevated roof configuration and for 0 and 90 degrees impinging wind angle.	95
Figure 3-15 Side and top view of the stadium model constructed for the wind tunnel experiments.	96
Figure 3-16 Stadium position at the turntable for the case study of 0° wind angle with elevated roof configuration.	97
Figure 3-17 Location of pressure taps on the stadium roof.	98
Figure 3-18 Location of pressure taps at the quadrant of the stadium terraces.	98
Figure 3-19 Location of pressure taps at the auxiliary area.	99
Figure 3-20 Schematic representation of the static pressure acquisition data.	100
Figure 3-21 C_p results on the roof surface for the reference stadium case of 0° wind angle and non-elevated (Cl) roof configuration; $U_{\text{ref}} = 4.65 \text{ m/s}$.	101
Figure 3-22 C_p results on the surface of the spectator terraces for the reference stadium case of 0° wind angle and non-elevated (Cl) roof configuration; $U_{\text{ref}} = 4.65 \text{ m/s}$.	102
Figure 3-23 C_p results on the surface of the auxiliary area for the reference stadium case of 0° wind angle and non-elevated (Cl) roof configuration; $U_{\text{ref}} = 4.65 \text{ m/s}$.	103
Figure 3-24 C_p results on the roof surface for the cases of 0° wind direction for the elevated (Op) and the non-elevated (Cl) roof configuration at $U_{\text{ref}} = 4.65 \text{ m/s}$.	104
Figure 3-25 C_p results on the roof surface for the cases of 90° wind direction for the elevated (Op) and the non-elevated (Cl) roof configuration at $U_{\text{ref}} = 4.65 \text{ m/s}$.	105
Figure 3-26 C_p results on the terraces' surfaces for the case of 0° wind angle for the back (top) and front (bottom) areas for the elevated (Op) and the non-elevated (Cl) roof opening configuration at $U_{\text{ref}} = 4.65 \text{ m/s}$.	107
Figure 3-27 C_p results on the terraces' surfaces for the case of 90° wind angle for the back (top) and front (bottom) areas for the elevated (Op) and the non-elevated (Cl) roof opening configuration at $U_{\text{ref}} = 4.65 \text{ m/s}$.	108
Figure 3-28 C_p results on the surface of the auxiliary area for the case of 0° wind direction for the elevated (Op) and non-elevated (Cl) roof configuration at $U_{\text{ref}} = 4.65 \text{ m/s}$.	110

Figure 3-29 Cp results on the surface of the auxiliary area for the case of 90° wind direction for the elevated and non-elevated roof configuration at $U_{ref} = 4.65$ m/s. .	110
Figure 4-1 A cubic body meshed with orthogonal structured grid method.	117
Figure 4-2 A cubic body meshed with orthogonal structured grid method.	118
Figure 4-3 Mesh generation based on cutcell method; split geometry (left) and generated mesh (right).....	118
Figure 4-4 Unstructured mesh generation with tetrahedral (left) and polyhedral (right) elements.	119
Figure 4-5 Construction of polygonal duals based on primal triangular mesh (Balafas, 2014).	120
Figure 4-6 Block structure meshed with hybrid mesh type, containing hexahedral, prism and tetrahedral cells.	121
Figure 4-7 Mesh generation using hexahedral, tetrahedral and polyhedral discretisation scheme (from left to right).	122
Figure 4-8 Residuals convergence history for the hexahedral, tetrahedral and polyhedral mesh (from left to right).....	123
Figure 4-9 Mesh generation using automatic method (top) and recording sequence meshing method (bottom).	124
Figure 4-10 The structure of the turbulent boundary layer.	126
Figure 4-11 Dimensionless velocity profile for a turbulent boundary layer (Wilcox, 1993).	127
Figure 4-12 Representation of the log-law ABL velocity profile on the first cell and mean velocity at the centre point of the cell (Blocken et al., 2007).....	138
Figure 4-13 Structure of the computational grid for the simulation of a bluff body at the centre of the longitudinal axis (Blocken et al., 2007).	139
Figure 4-14 Dimensions of the computational domain around the studied area (Franke et al., 2004).	140
Figure 4-15 Schematic representation of an empty ABL wind tunnel (a) and the empty computational domain (b) and the position at the turntable where the incident flow profiles require similarity (Blocken et al., 2008).....	141
Figure 4-16 Description of the computational domain used for the simulation of the stadium model.	142
Figure 4-17 Illustration of the discretised computational domain (a) and the symmetric domain for simulation (b).....	143

Figure 4-18 Side and top view of the generated grid for the computational domain.	144
Figure 4-19 Computational mesh on the symmetry plane of the domain (a, b) and on the stadium walls (c).	145
Figure 4-20 Grid structure on the roof surface for the generated meshes; 25,096,036 (a), 35,904,441 (b), 36,875,810 (c) and 41,870,905 (d).....	147
Figure 4-21 Comparison of the dimensionless velocity profiles along a horizontal line crossing the stadium 0.105 m above ground level; $U_{ref} = 5.23$ m/s and $L_{stadium} = 0.96$ m.	148
Figure 4-22 Y^+ values on the stadium interior and exterior walls for the generated meshes; 25,096,036 (a), 35,904,441 (b), 36,875,810 (c) and 41,870,905 (d).....	149
Figure 4-23 Residuals history for the generated meshes; 25,096,036 (a), 35,904,441 (b), 36,875,810 (c) and 41,870,905 (d).	150
Figure 5-1 C_p contours on the external stadium walls for the non-elevated roof case and the wind angle of 0 (a) and 90 (b) degrees.	154
Figure 5-2 C_p contours on the roof wall generated for the closed roof for the wind angle of 0 (a) and 90 (b) degrees.....	155
Figure 5-3 C_p contours on the pitch and terraces walls for the non-elevated roof case and the wind angle of 0 (a) and 90 (b) degrees.	156
Figure 5-4 Side view of the dimensionless streamlines of velocity for the elevated roof stadium model at 0 degrees (a) and 90 (b) degrees wind angle; $U_{ref} = 5.23$ m/s.	157
Figure 5-5 Top view of the dimensionless streamlines of velocity for the non- elevated roof stadium model at 0 degrees (a) and 90 (b) degrees wind angle; $U_{ref} = 5.23$ m/s.....	158
Figure 5-6 C_p contours and normalised velocity vectors on a horizontal plane 0.01 m above the entrances' level, for the non-elevated roof model; 0 (a) and 90 (b) degrees wind angle.	159
Figure 5-7 C_p contours on the front and back stadium walls for the open roof cases and the wind direction of 0 (a) and 90 (b) degrees.	160
Figure 5-8 C_p contours on the roof wall generated for the open roof for the 0 (a) and 90 (b) degrees wind angle.	161
Figure 5-9 C_p contours on the pitch and terraces walls for the open roof case and the wind direction of 0 (a) and 90 (b) degrees.	162

Figure 5-10 Side view of the dimensionless streamlines of velocity for the open roof stadium model at 0 degrees (a) and 90 (b) degrees wind direction; $U_{ref} = 5.23$ m/s.	163
Figure 5-11 Top view of the dimensionless streamlines of velocity for the open roof stadium model at 0 (a) and 90 (b) degrees wind direction; $U_{ref} = 5.23$ m/s.....	164
Figure 5-12 C_p contours and normalised velocity vectors on a horizontal plane 0.01 m above the entrances' level, for the elevated roof model; 0 (a) and 90 (b) degrees wind angle.....	165
Figure 5-13 C_p contours on the ground level for the configurations: non-elevated roof 0 (a) and 90 (b) degrees and elevated roof 0 (c) and 90 (b) degrees.	166
Figure 5-14 Normalised velocity vectors and dimensionless velocity streamlines of the flow around the non-elevated roof stadium model for the 0 (a) and 90 (b) wind angle; S_f and S_b the front and rear stagnation points, $U_{ref} = 5.23$ m/s.....	168
Figure 5-15 Dimensionless velocity streamlines on the front stadium wall for non-elevated (a) and elevated (b) roof configurations and plot of the U/U_{ref} on a vertical line in front of the stadium model; $U_{ref} = 5.23$ m/s.....	169
Figure 5-16 Illustration of the dimensionless contours and normalised vector of velocity generated on a horizontal plane 0.003 m above the auxiliary area for the stadium models with non-elevated roof 0° (a) and 90° (b) and the elevated roof 0° (c) and 90° (d) wind angle; $U_{ref} = 5.23$ m/s.	170
Figure 5-17 Chart of the dimensionless velocity values generated on a vertical line at the centre of the auxiliary area for the four stadium configurations; $U_{ref} = 5.23$ m/s.	172
Figure 5-18 Illustration of the dimensionless contours and normalised vectors of velocity generated on a plane 0.003 m above the spectator terraces for the stadium models with non-elevated roof 0°(a) and 90° (b) wind angle; $U_{ref} = 5.23$ m/s.....	173
Figure 5-19 Illustration of the dimensionless contours and normalised vectors of velocity generated on a plane 0.003 m above the spectator terraces for the stadium models with elevated roof 0° (a) and 90° (b) wind angle; $U_{ref} = 5.23$ m/s.....	174
Figure 5-20 Chart of the dimensionless velocity values generated on a vertical line at the front of the windward spectator tiers for the four stadium configurations; $U_{ref} = 5.23$ m/s.....	175

Figure 5-21 Chart of the dimensionless velocity values generated on a vertical line at the front of the leeward spectator tiers for the four stadium configurations; $U_{ref} = 5.23$ m/s.....	176
Figure 5-22 Contours of dimensionless velocity generated on the symmetric plane for the Spalart-Allmaras (a), the standard k- ϵ (b) and the realisable k- ϵ (c) models; $U_{ref} = 5.23$ m/s.....	178
Figure 5-23 Streamlines of the dimensionless velocity for the Spalart-Allmaras, the standard k- ϵ and the realisable k- ϵ models; $U_{ref} = 5.23$ m/s.	179
Figure 5-24 Turbulence models results of scaled residuals history for the first 250 iterations (a, b, c) and the last 5,000 iterations of the simulation runs (d, e, f); monitor convergence history of the dimensionless velocity (g, h, i); $U_{ref} = 5.23$ m/s.	180
Figure 5-25 Comparative results of the C_p values generated on the roof surface for the stadium model with non-elevated roof, among the three turbulence models and the wind tunnel experiments.	181
Figure 5-26 Comparative results of the C_p values generated on the auxiliary area of the stadium model with non-elevated roof, among the three turbulence models and the wind tunnel experiments.	182
Figure 5-27 Comparative results of the C_p values generated on the back and front spectator terraces of the stadium model with non-elevated roof, among the three turbulence models and the wind tunnel experiments.	183
Figure 6-1 Schematic representation of the generated design points.....	193
Figure 6-2 Coefficients of spatial variation of velocity at the areas of the upper and bottom terraces and the pitch.	194
Figure 6-3 Dimensionless maximum velocity values generated at the upper and bottom spectator tiers and the pitch area; $U_{ref} = 5$ m/s taken at the stadium roof height.....	195
Figure 6-4 Methodology followed by SVM hyperplanes to separate data in classes and minimise the distance of points falling out of the margins (Schölkopf et al., 1999).	196
Figure 6-5 Goodness of fit based on non-parametric regression meta-model.	197
Figure 6-6 Response surfaces for selective sets of input-output parameters within the design space; (left) P7 vs P1 and P3, (right) P4 vs P1 and P2.	199
Figure 6-7 Local sensitivities for the initial design case, DP 0.....	200

Figure 6-8 RSM vs CFD results for verification for the CP 1 and the CP 2.....	204
Figure 6-9 Global sensitivity chart of input-output parameters.	205
Figure 6-10 Side view of the streamlines of the dimensional velocity developed at the stadium bowl, for the CP 1 (a) and the initial design case (b); $U_{ref} = 5.23$ m/s .	206
Figure 6-11 User defined pressure coefficient contours and normalised velocity vectors generated at the central plane of the stadium model for the CP 1 (a) and the initial design case (b); $U_{ref} = 5.23$ m/s.	206
Figure 6-12 Top view of the streamlines of the dimensional velocity developed at the stadium bowl, for the initial design case (a) and the CP 1 (b); $U_{ref} = 5.23$ m/s.	207
Figure 6-13 User defined C_p contours and normalised vectors of velocity for the initial (a) and the CP 1(b) design, generated at the horizontal plane 0.01 m above the entrance level.	208
Figure 6-14 Contours of the dimensionless velocity at the spectator tiers and the pitch area, for the initial design case (a) and the CP 1 (b); $U_{ref} = 5.23$ m/s.	209

List of Tables

Table 2-1 Revised Davenport roughness classification (Wieringa, 1992).....	36
Table 2-2 Criteria for wind comfort and danger (Willemsen and Wisse, 2007).....	52
Table 2-3 Results on the wind speed and flow homogeneity for different roof inclination values, generated in Szucs et al., (2007).	55
Table 2-4 Wind speed behind barriers of vertical height h , expressed as a percentage of the upstream wind speed flow, shown in multiples of the fence height (h) downwind of the barrier ((Thompson et al., 1998).	56
Table 3-1 Design characteristics of the screens and the honeycomb used in the ABL wind tunnel of Nottingham.	82
Table 3-2 Comparative results for the C_p values generated on the roof surface for the four stadium cases.	105
Table 3-3 Comparative results for the C_p values generated on the surfaces of the spectator terraces for the four stadium cases.....	109
Table 3-4 Comparative results for the C_p values generated on the auxiliary area surface for the four stadium cases.	111
Table 4-1 Comparison of mesh characteristics for each different cell type.....	123

Table 4-2 Quality measures for the generated mesh.....	145
Table 4-3 Solver settings for the simulation study of the stadium model.....	146
Table 4-4 Grid independency study based on the four meshes and the RE and GCI techniques.....	152
Table 6-1 Four step methodology of the RSM optimisation study (Sofotasiou et al., 2016).	189
Table 6-2 Separation of the fluid domain into four controllable zonal areas.....	190
Table 6-3 Description of the input parameters and the defined constrains for spatial variance.	192
Table 6-4 Description of the input parameters for the generated design points based on OSF scheme.	193
Table 6-5 Optimisation objectives and constraints set for the output parameters. ..	201
Table 6-6 Input and output parameters generated for the CP1 and deviation from initial design case.	202
Table 6-7 Input and output parameters generated for the CP2 and deviation from initial design case.	203
Table 8-1 Analytical description of the wind tunnel equipment used for the study.	232

Abbreviations

ABL	Atmospheric boundary layer
ADV	Acoustic Doppler velocimetry
ASHRAE	American Society of Heating Refrigerating and Air-Conditioning Engineers
BIM	Building Information Modelling
BL	Boundary layer
CAD	Computer Aided Design
CCRD	Central composite rotatable design
CFD	Computational Fluid Dynamics
DoE	Design of Experiments
DP	Design point
DTM	Dynamic Thermal Modelling
HPC	High Performance Computing
GA	Genetic algorithms
GCI	Grid convergence index
HVAC	Heating ventilation and air conditioning
LDV	Laser Doppler velocimetry
MOGA	Multi-Objective Genetic Algorithm
N-S	Navier-Stokes
OSF	Optimal space-filling
PET	Physiological equivalent temperature
PIV	Particle image velocimetry
PMV	Predicted mean vote
RANS	Reynolds-averaged Navier-Stokes
RE	Richardson extrapolation
RKE	Realizable k - ε turbulence model

RNG	Renormalization Group k - ε turbulence model
RSM	Response Surface Methodology
SA	Spalart Allmaras model
SFD	Space-filling design
SIMPLE	Semi-Implicit Method for Pressure Linked Equations
SKE	Standard k - ε turbulence model
SVM	Support Vector Machine

Nomenclature

A	area	m^2
a, b, c	constant parameters for the King's Law fitting curve	
$C_{1\varepsilon}, C_{2\varepsilon}, C_{3\varepsilon}$	constants for the RANS turbulence models	
C_p	pressure coefficient	
C_s	roughness constant	
C_{sv}	coefficient of spatial variation	
C_v	average velocity coefficient	
C_μ	constant of turbulence viscosity	
d	zero-plane displacement or boundary layer displacement	m
E	the voltage at the anemometer output	V
E_1, E_2	Richardson error estimators	%
E_c	universal constant	9.8
ϵ	estimator for numerical solution difference	
F_s	safety factor in GCI	
$f(x)$	response of interest (RSM)	
f_1, f_2, f_3	grid numerical solution	
g	fluid acceleration of gravity	m/s^2
G_b	buoyancy generation term	Pa/s
G_k, G_ε	buoyancy generation term due to k and ε	Pa/s
H, h	height	m
I	turbulence intensity	%
i, j, k	Cartesian coordinates of vectors	
l	characteristic length	m
k	turbulence kinetic energy	m^2/s^2
k_s	roughness height	m

L	length	m
M	Mach number	
P, P_s, P_{static}	static pressure	Pa
P_{total}	Total pressure	Pa
P_{ref}	static reference pressure	Pa
P_{∞}	free-stream static pressure	Pa
p	order of convergence	
q_e	angle for equiangular face or cell	degrees
q_{min}	the smallest angle in face or cell	degrees
q_{max}	the largest angle in face or cell	degrees
R	coefficient of determination for fitted regression line	
R	discretisation convergence value (GCI)	
R	radius (RSM)	m
r	refinement ratio	
r_{eff}	effective refinement ratio	
Re	Reynolds number	
$Re_{critical}$	critical Reynolds number	
S_{φ}	source/ sink term	
\bar{S}_{ij}	mean strain-rate tensor	
t	time	s
T	temperature	°C
U, u	velocity	m/s
v, v, w	instantaneous fluid velocity components	m/s
U_{inlet}	velocity at the inlet boundary of the computational domain	m/s
\overline{U}_{ref}	average wind velocity at the reference point	m/s

U_δ	velocity at the atmospheric boundary layer thickness height	m/s
U_∞	free-stream velocity	m/s
u^*	surface shear velocity	m/s
u_{ABL}^*	ABL friction velocity	m/s
u^+	dimensionless velocity values	
\bar{u}_i, \bar{u}_j	mean components of velocity	m/s
ν	kinematic viscosity	m ² /s
W	width	m
w	weight factor (RSM)	
x_r, x_s	support vectors (RSM)	
x_1, x_2, x_k	design variables (RSM)	
y	design response (RSM), height	[-], m
y^+, y^*	dimensionless distance from the wall for a wall-bounded flow	
y_p	height of the cell centre	m
y_0	aerodynamic roughness length	m
Z, z	height	m
z_0	aerodynamic roughness length	m

Greek Symbols

α	power law exponent, speed of sound	[-], m/s
α_i^*, α_i	Lagrange variables	
$\beta_0, \beta_1, \beta_k$	unknown regression coefficients (RSM)	
Γ_φ	Diffusion coefficient	
δ	atmospheric boundary layer thickness	m

ε	statistical error (RSM)	
ε	turbulence kinetic dissipation rate	m^2/s^3
η	design response (RSM)	
κ	von Karman's constant	
μ_t	turbulence viscosity	$\text{kg}/(\text{ms})$
μ_{tf}	effective turbulence viscosity	$\text{kg}/(\text{ms})$
ρ	density of fluid	kg/m^3
σ	standard deviation	
$\sigma_k, \sigma_\varepsilon$	turbulence Prandtl numbers for k and ε	
σ_{ref}	standard deviation of velocities at the reference point	
τ	surface shear stress	Pa
φ	changing property	
Ψ	flow homogeneity index	
$\Psi_{90\%}$	10 % extreme maximum values of flow homogeneity	
$\Psi_{10\%}$	10 % extreme minimum values of flow homogeneity	

Abstract

The aim of this work was to investigate the aerodynamic performance of sports stadiums located in the built environment and conduct a design optimisation study to improve the wind comfort conditions for both players and spectators. A 1:300 scale semi-open stadium model was assessed with combined Atmospheric Boundary Layer (ABL) wind tunnel experimentation and Computational Fluid Dynamics (CFD) techniques against pressure and velocity distribution patterns in both interior and exterior areas of the stadium bowl. The validation of the numeric analysis was performed with the experimental results of pressure coefficients.

The aerodynamic performance analysis compared two impinging wind angles (0° and 90°) and two building envelope porosities, defined by the existence of an elevated and non-elevated roof configuration. The results indicated that the wind direction caused small differentiations on the developed wind distribution patterns, with the wind angle of 90° generating smaller negative pressures in both interior and exterior stadium surfaces. Further analysis of the air velocity distribution results indicated that the provision of a horizontal ventilation opening between the roof and the upper spectator tiers substantially improves the airflow distribution for the benefit of spectators, but induces up to 25 % higher velocities at the centre of the pitch level.

Parametric studies were performed to evaluate the impact of the roof geometry changes on the developed wind comfort conditions for the players and the spectators. By employing coupled CFD-Response Surface Methodology (RSM) techniques, it was found that the wind speeds and the flow homogeneity at the stadium bowl are more susceptible to firstly the roof height and secondly the roof radius. Finally, the generated response surfaces formed the basis for the conduction of a multi-objective optimisation study, which revealed that a drastic reduction of the roof height and the roof radius by 96.9 % and 50 % respectively may reduce the wind speeds and the flow heterogeneity up to 37 % and 49.6 % in the occupied areas.

1 Introduction

The built environment, from the smallest to the largest of its scale is a patchwork of multivariable spatial and temporal characteristics that need to be considered for evaluation during the early design phase. Depending on the functional purpose of the building, different standards need to be used and different design procedures need to be followed, which even if they change through time, the main scope of providing a safe and comfort environment for the users remains the same.

In the case of major structures that count for high impact and contribution to the society, the challenges are even bigger, since they have to confront to established regulations, satisfy their functional purpose and cope with unexpected and unknown factors. Structures need to focus on the improvement of users' comfort within the built environment, while aiming at the harmonious coexistence of an environmentally susceptible and climate rational design, resulting in a complete and consistent structure (Parr and Zaretsky, 2011).

Major structures that are widely acknowledged for their holistic appraisal of all the aforementioned parameters are stadium structures. International sports stadia of the 21st century, through total design considerations, turn into iconic building structures with lasting legacy. Known for their large capacity (Rungrado 1st of May Stadium), their architectural façade design (Beijing National Stadium), their strategies towards sustainability (London Olympic Stadium, Wembley Stadium) and their large stakeholders' investments (MetLife Stadium), stadium structures are deemed to be studied analytically and critically to offer the best of their services to the society and the users.

With ever-increasing emphasis on stadium constructions hosting sport mega-event organisations, such as the FIFA World Cup, the sports industry requires international standards of high quality, due to the worldwide attention that they attract (Preuss, 2013). Mega sport venues pursue the attraction of a large number of attendees, operating for the benefit of international development, strengthening of the urban infrastructure and services and sustaining prosperity. For this reason, regardless of the event, stakeholders and design teams should give responses to a series of self-posed questions related to stadium's occupants. "*Who* are the spectators, *what* are they looking for in the facility, and *how* can their number be maximised, *which* is the

1 Introduction

best playing environment and *how* athletes' performance can be promoted /or increased?" (John and Sheard, 2000).

Bearing these questions in mind, newly developed or even renovated stadia aim to achieve not only full compliance with the predefined construction and sustainability guidelines, but also deliver sport events that will satisfy users' needs and microenvironmental comfort expectations. The realisation of these objectives towards microenvironmental comfort is inextricably linked with the location of the construction, the spatial and temporal margins, the budget constraints and the availability of the required technological resources and tools.

In international sports stadia, a high quality environment is deemed crucial and inextricably linked to successfully delivered sport-events with winning titles, set of new records and satisfied users. More specifically, the human response to the developed aerothermal conditions in the stadium bowl is considered the 'litmus test' for the implemented structural design and the adopted environmental control strategies, since the anthropocentric character of the sport is meant to be highlighted. Aiming at the provision of ultimate wind and thermal comfort conditions, environmental neutralising techniques are commonly employed that promote the performance of the players and satisfy the expectations of the spectators (Levinson and Christensen, 1996).

Environmental neutrality in sports stadia is mainly attributed to the architectural characteristics of the structure and thus it is a fundamental consideration for evaluation during the early design phase. In stadiums with closed (domed) or retractable roof, the environmental neutrality can be easily achieved and the aerothermal comfort standards can be effortlessly fulfilled with the use of mechanical and/ or non-mechanical techniques, since closed roof configurations create a well-controlled microenvironment. These techniques may be implemented by promoting natural ventilation or by integrating Heating Ventilation and Air-Conditioning (HVAC) devices in the sport facilities (Culley and Pascoe, 2005). On the other hand, open or semi-open stadiums make the maintenance of aerothermal comfort standards difficult to attain due to the direct interactions with the external environment that may lead to very energy-intensive intervention strategies, especially in locations (and/ or seasons), where extreme weather conditions prevail (John and Sheard, 2000).

1 Introduction

However, the maximum performance of the stadium microenvironment may be achieved only if the holistic approach, including the processes and their in-between interactions, behind the stadium itself, are fully understood. Despite the fact that the exact mechanisms are well-known individually, the effect produced by their synergy is difficult to evaluate, due to the plethora of the physical phenomena occurring in stadia. Turbulent flow, heat and mass transfer, buoyancy, radiation and species transport are only some of the processes that need to be assessed when studies on stadium environments are performed to improve users' aerothermal comfort conditions.

Towards solving questions of such complexity, when there is a multi-million pound budget and a large number of stakeholders to be satisfied, the adoption of computerising assistance is deemed necessary and inevitable, in order to achieve an integral conceptual design, which will be structurally feasible and sustainable for the environment and the users (Fazio et al., 1989). Thereby, the continuous development of engineering makes the study of several design parameters for the achievement of comfort conditions possible, economic and less computational expensive. Computer Aided Design (CAD), Building Information Modelling (BIM), Computational Fluid Dynamics (CFD) and wind tunnel experimentation are only a few of the available tools used to design, predict, assess, optimise and validate structural designs during the decision-making process.

Towards the assessment of the developed stadium microenvironment, the use of sustainable building design tools, reduced scale experiments (Reid and Traverse, 1991) and CFD (Culley and Pascoe, 2005) have proven to be vital techniques for simulation and validation of the occurring flow phenomena. Thus, it is possible to produce an overall view of the aerodynamic behaviour of the structure within the urban environment, predict the developed microclimate at the stadium bowl, validate the flow distribution predictions in any area of interest, as well as investigate the wind comfort responses of the users. By employing coupled techniques and software tools, optimum design solutions for stadia can be developed. This approach may consequently promote users' aerothermal comfort by integrating low-energy technologies with improved performance, promoting the energy efficiency of the stadium.

1 Introduction

1.1 Aims and objectives

The overall aim was to evaluate the aerodynamic performance of semi-open stadium structures, targeting the improvement of the wind environment at the stadium bowl and the provision of enhanced wind comfort conditions for both players and spectators, by employing design optimisation techniques.

The research objectives of the thesis are listed below:

- O.1. To assess the aerodynamic performance of a semi-open stadium by simulating the pressure distributions on the stadium surfaces, on the basis of experimental tests in a validated ABL wind tunnel facility.
- O.2. To simulate numerically the pressure distributions and the air flow patterns within the stadium bowl, under selected wind directions and critical envelope porosities.
- O.3. To investigate the effect of different orthogonal wind directions and envelope porosities on the users' wind microenvironment.
- O.4. To study the flow phenomena and the interactions between the built and the stadium wind environment with qualitative research approach.
- O.5. To evaluate the most decisive design parameters of the roof geometry and their responses on the developed wind microenvironment at the stadium bowl.
- O.6. To investigate the optimum roof configuration that improves the stadium wind comfort conditions for the users.

1.2 Research methodology

The study focused on the development and validation of a new methodology that could enable the decision-making process for stadiums to achieve wind comfort for users. The identification of the parameters affecting the comfort sensation and the interactions between the urban and the built environment are of paramount importance for a holistic wind comfort optimisation study. The simultaneous appraisal of the prevailing design factors and simulation criteria provide a complete approach to the problem, formulating a methodological tool for the accurate approximation of wind behaviour in semi-open stadia located in the built environment.

The literature review provided information on the fundamental wind engineering aspects that need to be considered on the study of the flow interactions between the

1 Introduction

urban and the stadium scale. The previous work that has been conducted in stadia, was presented, regarding wind and thermal comfort, design recommendations, assessment methodologies and established wind comfort criteria. It was an overview of what has been done up to date, clarifying the gaps and the limitations that set the framework for this research.

The aerodynamic performance of the stadium in a suburban environment was assessed using CFD tools and FVM for steady state simulations. In order to produce acceptable results tangible to validation, the dimensional and geometrical characteristics of the computational model were in line with the corresponding characteristics of the wind tunnel facility and the scaled stadium model.

The validation of the computational model was performed in the ABL wind tunnel facility of the University of Nottingham. For the simulation of the suburban environment, the wind tunnel test section was integrated with turbulence generators and ground surface roughness blocks. Multiple simulation/ validation studies were performed to ensure that both the inlet profile at the test section and the developed ABL profile at the model position were within acceptable error limits.

For the identification of optimum design solutions that promote wind comfort conditions at the stadium bowl, a coupled CFD-based optimisation method was followed using Response Surface Methodology techniques. This involved a very time-consuming process, since a substantial number of simulations needed to be performed to accurately predict the designs that fit within the predefined design constraints and optimisation objectives. It was an iterative process that supplied the CFD solutions with information relevant to the design scope.

The results gave valuable information on the wind distribution in and around the stadium environment, the alterations depending on the impinging wind angle and also the impact on the aerodynamic performance with and without the existence of a horizontal ventilation opening between the roof and the upper spectator terraces. Additional results on the methodology steps that needed to be considered when performing ABL studies in wind tunnel facilities were also presented in detail. Figure 1-1 summarises the principle steps followed.

1 Introduction

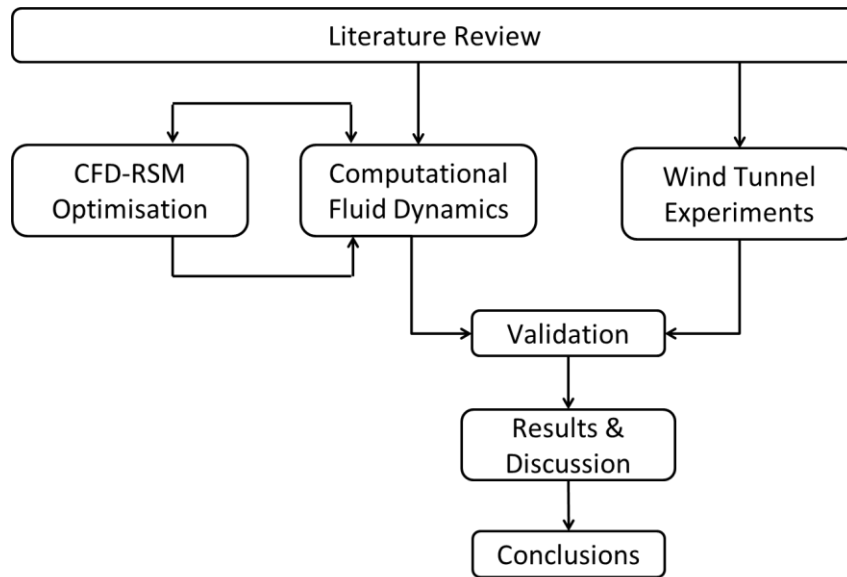


Figure 1-1 Research methodology steps.

1.3 Thesis layout

The thesis is organised in 7 chapters, thereafter, as follows:

Chapter 2 presents the theoretical background of wind engineering, including the definition and the flow characteristics of the Atmospheric Boundary Layer. The chapter covers important aspects of the stadium aerodynamics as part of the large category of buildings, along with the established wind comfort criteria for users. The chapter also reviews the existing literature on which the methodology of the thesis will rely. Previously conducted studies that assessed the aerodynamic performance and the environmental comfort in sports stadia are presented, along with the published studies that employed optimisation techniques to assess physical phenomena in building structures.

Chapter 3 presents the theoretical and technical background to be considered on the conduction of ABL wind tunnel experimentation studies. The chapter comprises the description of the wind tunnel facility and the mechanical equipment used for the current experimental study, together with the set-up and the presentation of the acquired results.

Chapter 4 covers the turbulence modelling theory and the important considerations during the conduction of CFD studies of structures in the built environment. The chapter describes the CFD parametrisation for the simulation of the stadium model, including the grid verification study.

1 Introduction

Chapter 5 presents the CFD results of the stadium design cases, together with the assessment of the turbulence model performance, as part of the validation of the computational model.

Chapter 6 presents the design optimisation study. The chapter describes the use of multi-objective optimisation algorithms for the investigation of optimum roof configurations that may improve the wind microclimate for users. The CFD-based optimisation theory is explained together with the parametrisation of the stadium model and the generated results are analysed.

Chapter 7 summarises the conclusions and presents the future work based on some prospective points that could enhance the knowledge in stadium studies.

2 Literature Review

2.1 Introduction

The study of the aerodynamic performance of a stadium structure and the effect on the users' wind comfort conditions requires a good-understanding of the flow phenomena and the wind interactions between the urban and the stadium scale. In this chapter, the key aspects of wind engineering are initially presented, as they are detrimental for the exploration of the stadium flow phenomena during computational and experimental analysis. The aerodynamic performance of stadium structures is theoretically approached, as part of the wide category of building structures. The literature also presents the studies that have been conducted in stadia, regarding the assessment of the environmental comfort criteria, including wind, temperature and rain, the performance of HVAC mechanisms and the prediction of the pollution dispersion. Furthermore, the main structural design characteristics of sports stadia hosting international events are described. Finally, design optimisation techniques that have been used in literature to improve important building comfort criteria are reviewed and the research gaps to formulate this research are identified.

2.2 Wind engineering

Wind is one of the most important climatic characteristics that determine the environmental conditions in global, urban, building and human scale. It could be described as a sequential chain reaction, the links of which have to be included in the building engineering without any exception (Dyrbye and Hansen, 1997). As demonstrated in Figure 2-1, the links to the successful selection of the design criteria are inextricably connected and interrelated. However, the parameters involved can only be represented by statistical methods, due to the high uncertainty and randomness of their prediction.

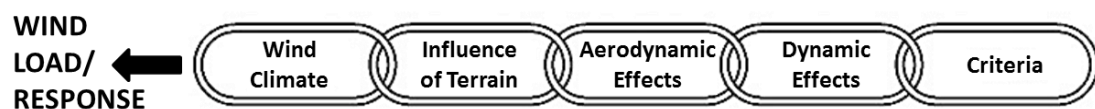


Figure 2-1 The wind-load chain as described by Davenport (Announcement of the Alan G. Davenport Wind Loading Chain, 2011).

2 Literature Review

2.2.1 Wind climate

From an aerodynamic point of view, the wind environment is formed by the high turbulent atmospheric motion scales that occur above a rough terrain composing the atmospheric boundary layer (ABL) (Cermak et al., 1995). The ABL consists of stratified layers of air that are interrelated and interact with one another. A neutral ABL is categorised in two main layers and additional sublayers, depending on the gradient height and the respective dominant forces, as shown in Figure 2-2.

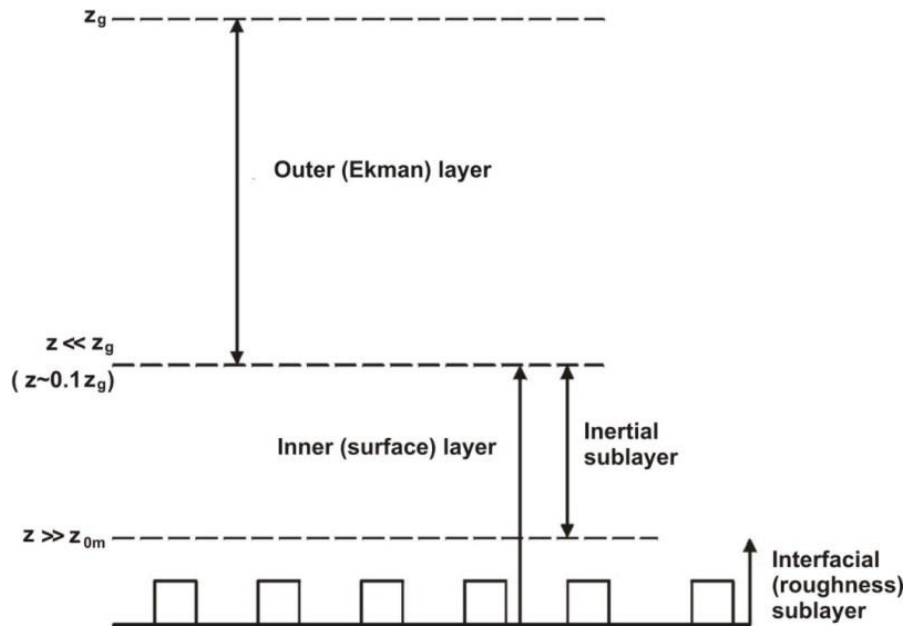


Figure 2-2 Graphical representation of the atmospheric boundary layer (Garratt, 1994).

The upper region, known as outer or Ekman layer, is mainly dependent on the Coriolis effect, caused by Earth's rotation, and there is only a minor influence from the nature of the ground surface. The bottom region, known as inner layer is separated in two sublayers. The interfacial or roughness sublayer ranges between $z = 0$ m up to a height where there is no discrete influence of the roughness elements and the flow becomes inhomogeneous and turbulent (Rotach, 1991). The roughness sublayer is the lowest boundary layer level, on which the air flow is directly related to the ground friction and topography, known also as ground roughness. The ABL can vary from a few hundred meters to up to 1 km, with thickness that is inseparably linked to the ground topography. Above ABL the free atmosphere extends up to 11 km.

2 Literature Review

2.2.2 Influence of terrain

The aerodynamic roughness length, z_0 , is a ground characterisation parameter used to describe the ground terrain type. In theory, the roughness length represents the height where the wind speed becomes zero (see Equation 2.3 of the logarithmic wind profile). The updated classification of the ground surfaces is presented in Table 2.1 below and shows the values of the roughness length for a wide range of different terrain types.

Table 2.1 Revised Davenport roughness classification (Wieringa, 1992).

Roughness Length, z_0 (m)	Description
0.00002 “Sea”	Open sea or lake, snow-covered flat plan, featureless desert, tarmac and concrete, with free fetch of several kilometres.
0.005 “Smooth”	Featureless land surface without any noticeable obstacles and with negligible vegetation.
0.03 “Open”	Level country with low vegetation (i.e. grass) and isolated obstacles with separations of at least 50 obstacle height.
0.10 “Roughly Open”	Cultivated area with regular cover of low crops or moderately open country with occasional obstacles at relative horizontal distances of at least 20 obstacle heights.
0.25 “Rough”	Recently-developed “young” landscapes with high crops or crops of varying height and scattered obstacles at relative distances of about 15 obstacle heights.
0.5 “Very rough”	“Old” cultivated landscape with many rather large obstacle groups separated by open spaces of about 10 obstacle heights. Also low vegetation with small spaces and “young” densely-planted forest.
1.0 “Closed”	Landscape totally quite regularly covered with similar-size large obstacles, with open spaces comparable to the obstacle heights (i.e. homogeneous cities, villages or mature regular forests).
≥ 2.0 “Chaotic”	Centres of large towns with mixture of low-rise and high-rise buildings. Also irregular large forests with many clearings.

2.2.2.1 Atmospheric boundary layer thickness (δ)

The thickness of the ABL describes the height at which the velocity approaches the value of the free-stream velocity (U_∞), or $U_\delta = 0.99 * U_\infty$ (Garratt, 1994). It is primarily contingent upon the roughness characteristics and the atmospheric stability. Depending on the terrain type, the alterations to the boundary layer height are quite significant. As shown in Figure 2-3, the transition from a marine and open flat area with small roughness to an urban environment causes increase of the boundary layer height.

2 Literature Review

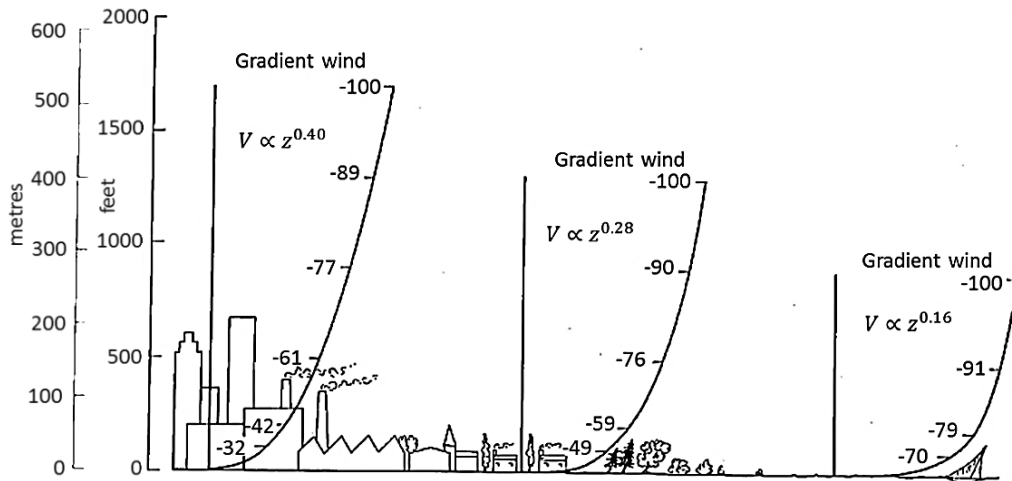


Figure 2-3 Profiles of mean wind velocity over different terrain roughness (Houghton and Carruthers, 1976).

2.2.2.2 Zero-plane displacement (d)

On the definition of the ABL, the boundary layer displacement, d , is another important parameter solely determined by the roughness length (z_0). In other words, depending on the ground roughness, a shift of the boundary layer upwards is expected on approximately the two-thirds of the roughness elements' height. This displacement is known as zero-plane displacement and it is indicative of the density of the environment along with the roughness characteristics (Passe and Battaglia, 2015). It represents a datum height above which the normal turbulent exchange occurs (Hansen, 1993) and it is considered an important parameter when studying high-vegetation or built-up areas (Wieringa, 1992).

2.2.2.3 Surface shear velocity (u^*)

In case of neutral atmospheric conditions and constant aerodynamic roughness length, the vertical wind profile can be described by a log-linear distribution. In reality, the wind velocity close to ground surface is susceptible to changes due to thermal effects that need to be considered on the determination of the velocity profile at different vertical positions (Blumberg and Greeley, 1993). The surface shear velocity is used to describe the influence of wind particles on the ground wall boundary, given by the Equation 2.1, where τ is the surface shear stress and ρ the density of the fluid (air):

2 Literature Review

$$u^* = \sqrt{\tau/\rho} \quad (2.1)$$

2.2.2.4 ABL velocity profile

The laws that describe the boundary layer velocity profiles are 1) the power law (Equation 2.2) and 2) the logarithmic profile (Equation 2.3).

$$u = u_{ref} \left(\frac{z}{z_{ref}} \right)^{1/a} \quad (2.2)$$

$$u = \frac{u_{ABL}^*}{\kappa} \ln \left(\frac{z-d}{z_0} \right) \quad (2.3)$$

where u is the velocity at height z , u_{ref} is the velocity at reference height z_{ref} , u_{ABL}^* is the ABL friction velocity, d the zero-plane displacement, z_0 the roughness length and κ the von Karman's constant ($\approx 0.4 - 0.42$).

Both equations are used for the estimation of the velocity values in the vertical direction. According to Cook (1985), the logarithmic profile provides a good prediction for the wind speed profiles at heights lower than 100 m, in comparison to the power law that may be used up to 1 km, the upper layer of the planetary boundary layer.

2.2.3 Aerodynamics effects

The interactions between the urban and the building scale are continuous, unpredictable and spatial and temporal dependent. It is a subject under continuous research, because it is directly related to the human factor. However, the research on stadium structures is limited as opposed to other buildings, owing to their geometrical complexities, the big structural size and the multiscale characteristics involved; aspects that constitute a deterrent to further in-depth studies.

2.2.3.1 Wind load

In the urban environment, building structures may be considered as obstacles to the approaching wind flow. More specifically, the distortion of the approaching undisturbed airflow patterns results to significant wind speed changes and pressure fluctuations on the building surfaces (Dyrbye and Hansen, 1996). In the case of stadium structures, the pressure distributions on both stadium interior and exterior

2 Literature Review

surfaces are primarily dependent on the geometrical characteristics of the construction. The existence, the size and the geometry of the roof, the sharp or round wall edges, the number of openings on the wall surfaces and the existence of other objects/ structures on the direct proximity are only some of the parameters that may influence the pressure and wind distribution around and inside the stadium bowl.

A powerful tool that enables the presentation and comparison of wind load distributions on structures of varying design and complexity is the dimensional analysis, which involves the generation of pressure coefficients as the dimensionless parameter of pressure (Cook, 1985). The pressure coefficient, C_p , is calculated based on Equation 2.4 as the ratio of the actual pressure on the model structure to the dynamic pressure.

$$C_p = \frac{P - P_{ref}}{\frac{1}{2} \rho U_H^2} \quad (2.4)$$

where P is the static pressure measured at the model surface, P_{ref} , is the static reference pressure (or the free-stream pressure), U_H the mean velocity measured at reference height H and ρ the air density taken equal to 1.225 kg/m^3 , as measured at 15°C ambient temperature.

Figure 2-4 illustrates the external pressure distribution on a generic building structure with rectangular core and duopitch roofs with positive and negative pitch angles. The C_p values are related to the building height (h), the building width (b) the roof inclination (α), the wind angle. The Eurocodes determine the critical pressure coefficient values based on the wind loaded area (A), which is equal to $C_{pe,1}$ for local coefficients ($A = 1 \text{ m}^2$) and equal to $C_{pe,10}$ for overall coefficients ($A = 10 \text{ m}^2$) and the parameter e ($e = \min [b, 2h]$).

2 Literature Review

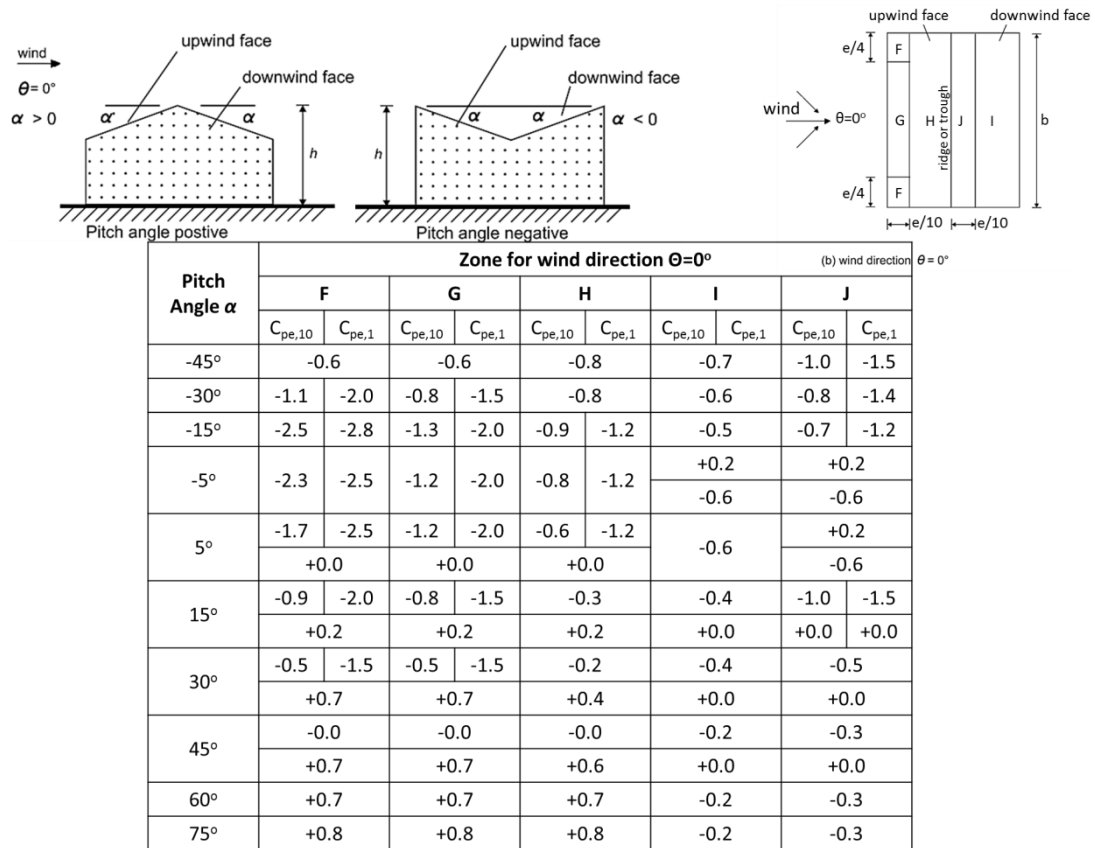


Figure 2-4 External pressure coefficients for duopitch roofs under 0° wind angle (European Standard, 2005).

However, stadium structures do not have pitch roofs but curved that may be either vaulted or with an oculus configuration. Additional to this, the main building core is neither rectangular nor circular, which makes their standardisation particular difficult. According to Eurocodes, the pressure distributions on a curved roof are dependent on the dimensional characteristics of both the building core and the roof; the building height (h), the roof height (f) and the building width and arc diameter (d). Figure 2-5 illustrates the pressure distributions for curved roof structures with rectangular and circular bases. It can be observed that the areas with positive pressure are limited to the lower roof levels of the windward side. Similar observations are reported in Cook (1985).

2 Literature Review

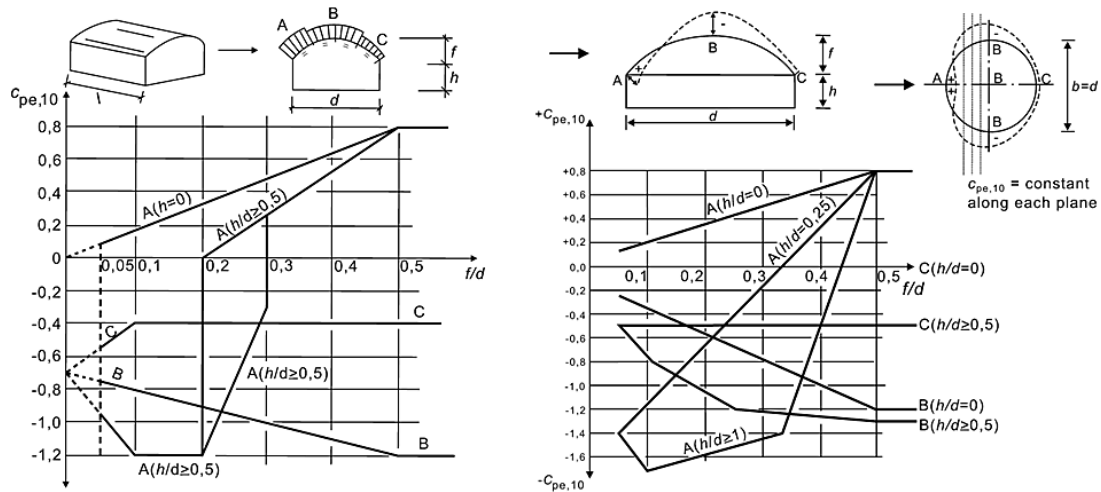


Figure 2-5 C_p distribution charts for curved roofs with rectangular (left) and circular base (right) (European Standard, 2005).

Overall, even if the wind performance of the stadium is not far from the performance of an ordinary building structure subject to wind loads, the uniqueness of their shape makes their standardisation difficult to achieve. Biagini et al., (2007), considering that the roof component is the most important on the evaluation of wind loads, had aptly mentioned that stadium roofs are particular malleable structural components that cannot be classified to Codes.

Thus, the successful construction of any stadium structure presupposes the assessment of the wind load during the early design phase, commonly performed with reduced scale experimentation. The need to employ wind tunnel techniques to assess the wind performance of stadiums is crucial, in order to generate reliable information on the structural safety and the pressure and air flow distribution on and around the stadium surfaces (Reid and Travers, 1991).

Thompson et al. (1998) stated the wind tunnel experimentation study of the Hong Kong stadium, which investigated the wind load on the roof configuration and the impact of the structure's location in the urban environment. The detailed wind tunnel experimentation was conducted in an ABL wind tunnel facility in the scale of 1:300, as shown in Figure 2-4. Important information were generated on the wind performance and structural safety of the stadium under variable wind directions, highlighting the developed negative pressures on the roof canopies in case of south winds, which are related with upwards wind loads.

2 Literature Review



Figure 2-6 Illustration of the Hong Kong stadium structure (left) and 1:300 wind tunnel scaled model (right) (Thompson et al., 1998).

Marighetti et al. (2000) investigated the pressure distributions on the roof periphery of a football stadium using ABL wind tunnel experimentation. The stadium, illustrated in Figure 2-7, was assessed against a closed and an open roof perimeter. Using area-averaged measurement techniques, pressure coefficients values were generated, indicating similar patterns for both case studies. More specifically, the roof inclination of 5° led to positive C_p values at the windward roof surfaces and negative C_p on the leeward. Despite the trend similarity, the roof with open perimeter showed better performance, with slightly higher pressure coefficient values, which is an indicator of less suction zones.

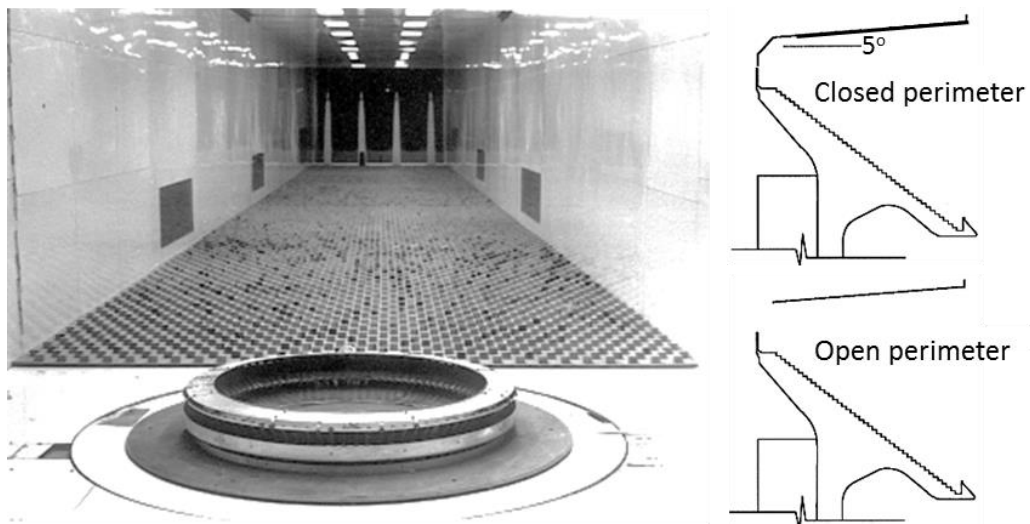


Figure 2-7 ABL wind tunnel experimentation of a football stadium under two roof perimeter configurations (Marighetti et al., 2000).

Biagini et al. (2007) performed a series of ABL wind tunnel experiments in three different stadium models. The study aimed at the identification of the pressure coefficient distribution patterns on different roof structures, by providing a detailed methodology of the experimentation procedure. The authors highlighted the need to acquire pressure data on both inner and outer surfaces of the roof components, in

2 Literature Review

order to identify the critical areas of the structure. The results on the curved grandstand roof component of the Manfredonia stadium are presented in Figure 2-8, indicating that the highest pressure coefficient values are observed at the windward areas of the roof.

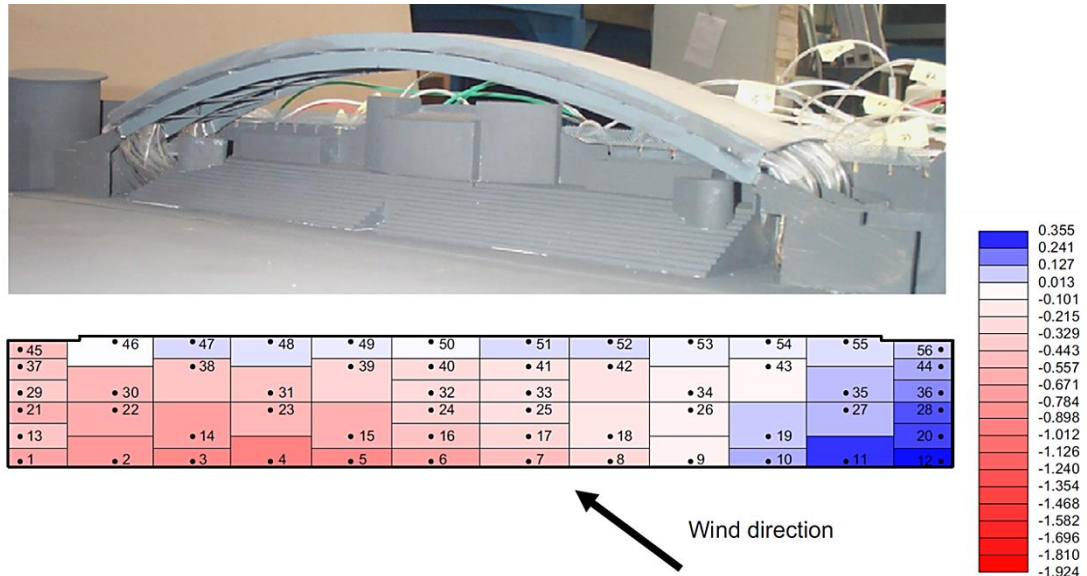


Figure 2-8 Distribution on the mean pressure coefficient values on the Manfredonia's grandstand roof (Biagini et al., 2007).

The same study generated valuable information on the importance of the roof design on the pressure distribution patterns. More specifically, Figure 2-9 illustrates a potential retrofitting scenario for the flat roof of the Delle Alphi stadium. According to the results, the radial tensile structure covering the roof produced solely positive pressure coefficient values on the roof top surface, as opposed to the negative values obtained without the presence of the tensile structure, which diminished the wind performance of the stadium. Again, higher pressure coefficient values were observed at the windward areas of the roof.

2 Literature Review

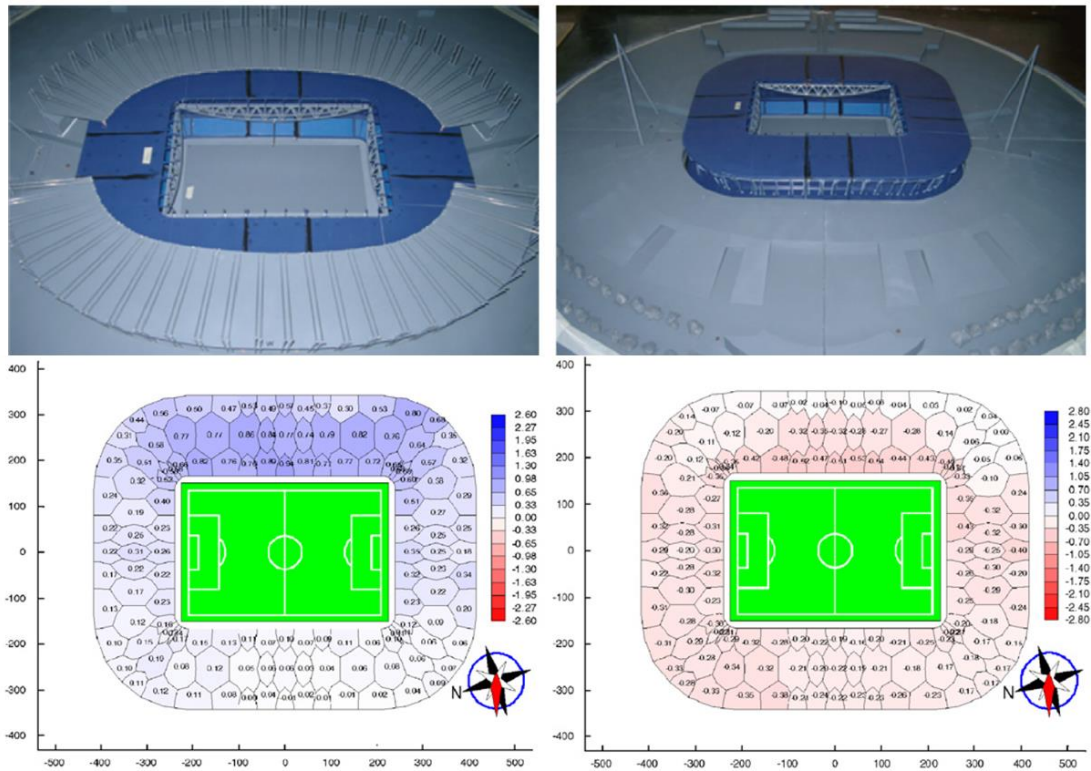


Figure 2-9 Distribution of pressure coefficients generated on the roof of the Delle Aphi stadium with (left) and without (right) radial tensile structure (left) (Biagini et al., 2007).

A recent work of Chen et al. (2016) studied the wind responses of the Bao'an stadium. The stadium had an oculus roof configuration and a peripheral horizontal opening between the roof and the upper spectator tiers. The performance of the structure was assessed in an ABL wind tunnel facility. The upper and bottom roof surfaces were integrated with 698 pressure taps and the generated values of the total mean wind pressure coefficients are illustrated in Figure 2-10. According to the results, positive pressures were developed on the windward roof side, which were decreased in value when approaching the oculus configuration. Negative pressures were obtained around the oculus, with the highest negative values to be observed at the rear side of it. Finally, negative values were also generated at the leeward roof surface.

2 Literature Review

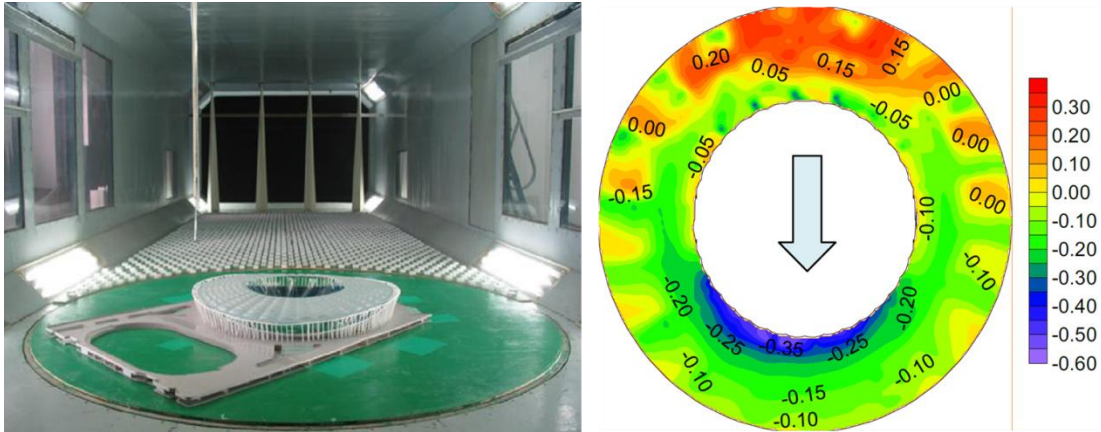


Figure 2-10 Wind tunnel test model (left) and generated mean pressure coefficients at the roof surface (right) (Chen et al., 2016).

2.2.4 Wind flow distribution

The investigation of the wind flow distribution is an equally important consideration during the assessment of the aerodynamic performance of buildings. The flow movement defines the developed wind microenvironment around and inside the structures and determines the wind comfort levels that for the case of sports stadiums are detrimental for the successful conduction of sports events. Figure 2-11 presents the main characteristics of the wind flow distribution around a tall and wide building without openings.

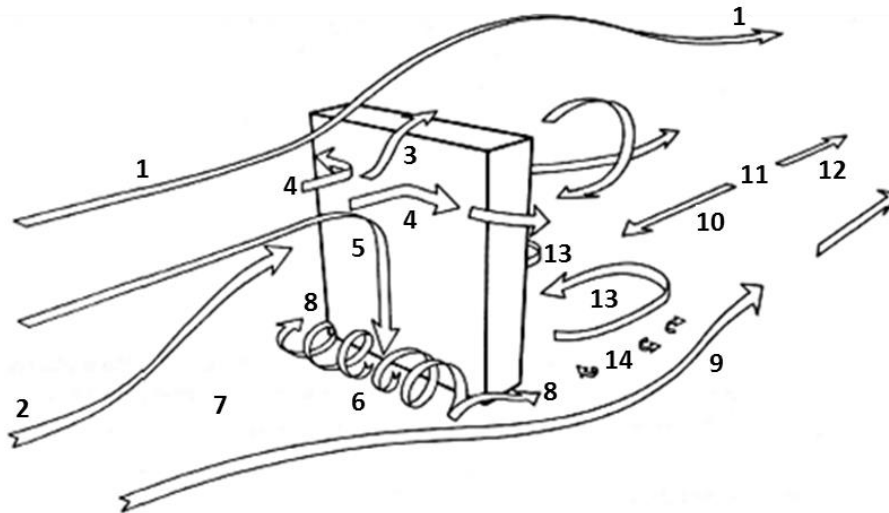


Figure 2-11 Flow distribution and turbulence features around a building without openings (Blocken and Carmeliet, 2004).

The airflow is separated in different regional categories: (1) the flow that passes above the building, avoiding the large building obstacle, (2) the impinging flow at the building surface, which leads to the creation of a stagnation point, where $U = 0$ m/s and $P_{static} = \text{maximum}$, (3) high accelerating flows detached from the

2 Literature Review

building surface, causing flow separation, (4) high accelerating flows on the vertical edges of the building, (5) descending flow towards the ground level, (6) recirculation zone on the ground level, on the windward building side, known as standing vortex or horseshoe vortex, (7) the location where the impinging flow meets the standing vortex with opposite flow direction, (8) high accelerated flow on the bottom corners of the building, causing flow separation, (9) horseshoe vortex system and mean separation lines reattached to main flow, (10) backflow on the leeward side of the building due to developed underpressure areas, (11) the mean cavity reattachment line, (12) the turbulent wake, (13) the recirculation zones on the leeward side of the building, (14) vortices behind the building with vertical axis (Blocken and Carmeliet, 2004).

However, the wind distribution at the stadium bowl is inseparable from the roof geometrical configuration, the existence of ventilation and ground entrance openings and the presence of buildings in the close proximity. These factors when applied individually or combined may lessen or enhance the wind performance of the stadium structure. Despite the importance of understanding the flow phenomena in the stadium environment for the benefit of the users, limited studies have been conducted that address the airflow distribution patterns. These studies were conducted either with wind tunnel experimentation or CFD simulation techniques.

An initial attempt of understanding the flow distribution in the stadium bowl using CFD techniques was performed by Persoon et al. (2008), as part of a two-dimensional assessment study of the wind-driven rain in a stadium structure consisted of two roof-covered grandstands. The computer simulations gave important information on the wind flow patterns at the stadium bowl that even if they were conservative, due to the two-dimensionality, they were good indicators of the flow phenomena occurring in the stadium environment. The results involved the study of different roof configurations. As illustrated in Figure 2-10, the velocity patterns were quite similar between the different cases. More specifically, the main characteristics of the flow involved the development of a primary vortex occupying the central area of the bowl and two secondary vortices limited on the spectator terraces. The change of the roof contributed to small spatial changes of the primary vortex but to important relocations of the secondary vortices that sequentially could improve or diminish the environmental comfort of spectators. The study concluded

2 Literature Review

that a roof configuration descending towards the pitch of about 13 degrees could produce advantageous comfort conditions for the spectators.

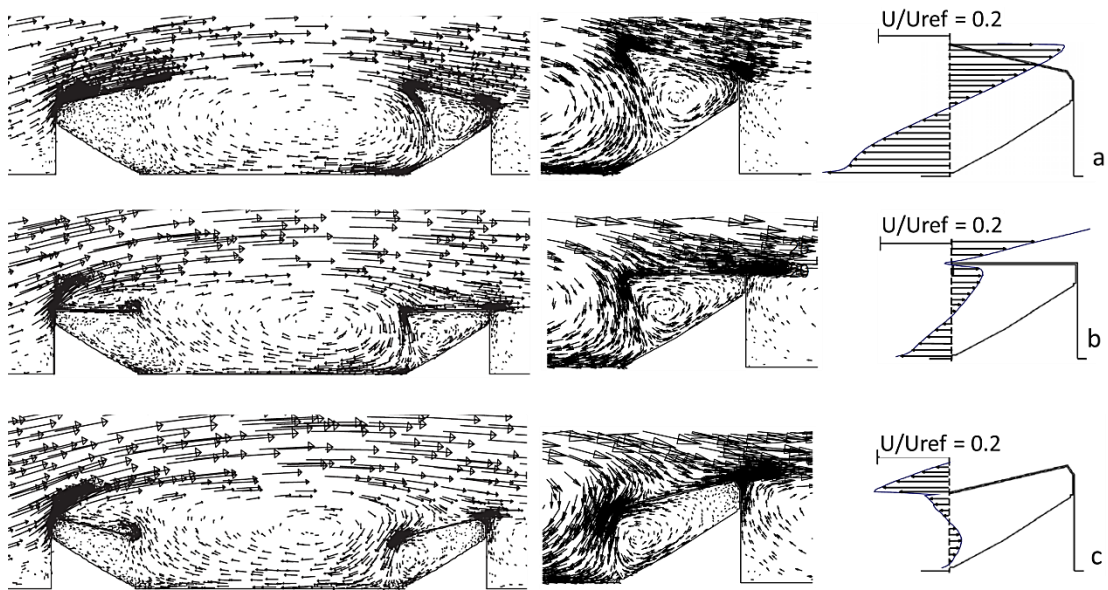


Figure 2-12 Far field and close field CFD velocity vectors for $U_{ref} = 10$ m/s and dimensionless velocities along a vertical line below the windward roof edge for the stadium cases with ascending (a), flat (b) and descending (c) roof configuration (Persoon et al., 2008).

van Hoof et al. (2011) conducted a study on three-dimensional stadium geometries under four different stand arrangements. Using CFD techniques and the realisable $k-\epsilon$ turbulence model a comprehensive illustration of the wind flow patterns was generated. Figure 2-13 illustrates the obtained velocity vectors on a vertical central plane. The first two stadium models developed similar wind flow patterns, which involved two large vertical vortices, one located close to the ground level and one between the roof edges. For the third stadium configuration no vortices were observed on the vertical plane, due to the intense flow streams entering the stadium bowl through the open corners. Finally, the enclosed stadium structure resulted to the creation of a large vertical vortex, which partially complied with the two-dimensional case study, with main difference the absence of the secondary vortices below the windward and leeward spectator tiers.

2 Literature Review

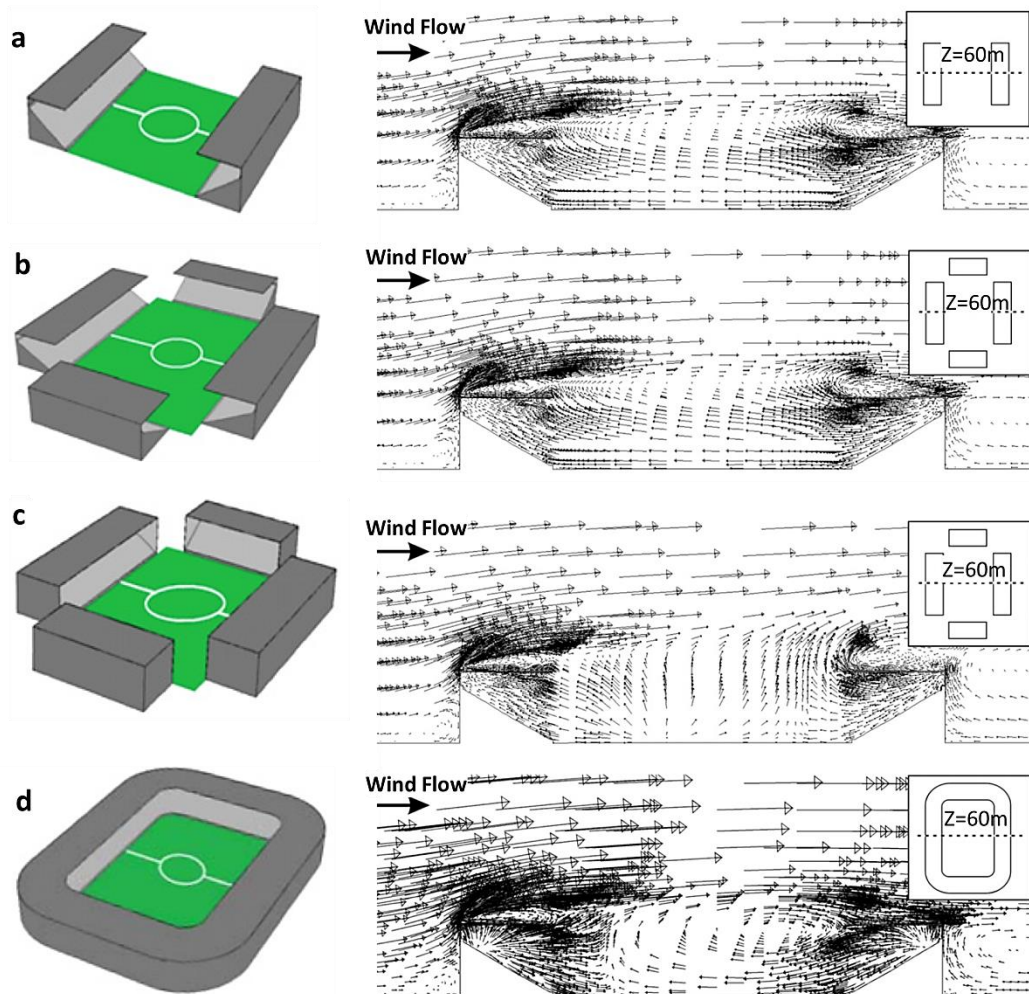


Figure 2-13 Velocity vectors generated in a vertical central plane for the four stadium configurations with flat roof; two opposite grandstands (a), four grandstands with open corners (b), four grandstands with open corners and windshields on the grandstand edges (c), enclosed stadium (d) (van Hoof et al., 2011).

Additional results generated from the same study are illustrated in Figure 2-14. The schematic representation of the wind behaviour around the stadium models matches greatly the one presented in Figure 2-11. Recirculation zones were observed at the windward and leeward stadium walls, as well as at the interior of the stadium bowl. The velocity contours gave more details on the wind speed intensity, according to which the existence of corner openings may contribute greatly to the wind flow conditions around and in the stadium model. With main exception the third stadium design case, two symmetrical horizontal vortices of opposite direction were developed at the playing field area. The grandstand windshields of the third case resulted to high intensity ventilation zones in the form of wind jets discharged at the playing field that might be proved disadvantageous for the players' performance.

2 Literature Review

Finally, high wind speeds were observed in all windward corners of the stadium models.

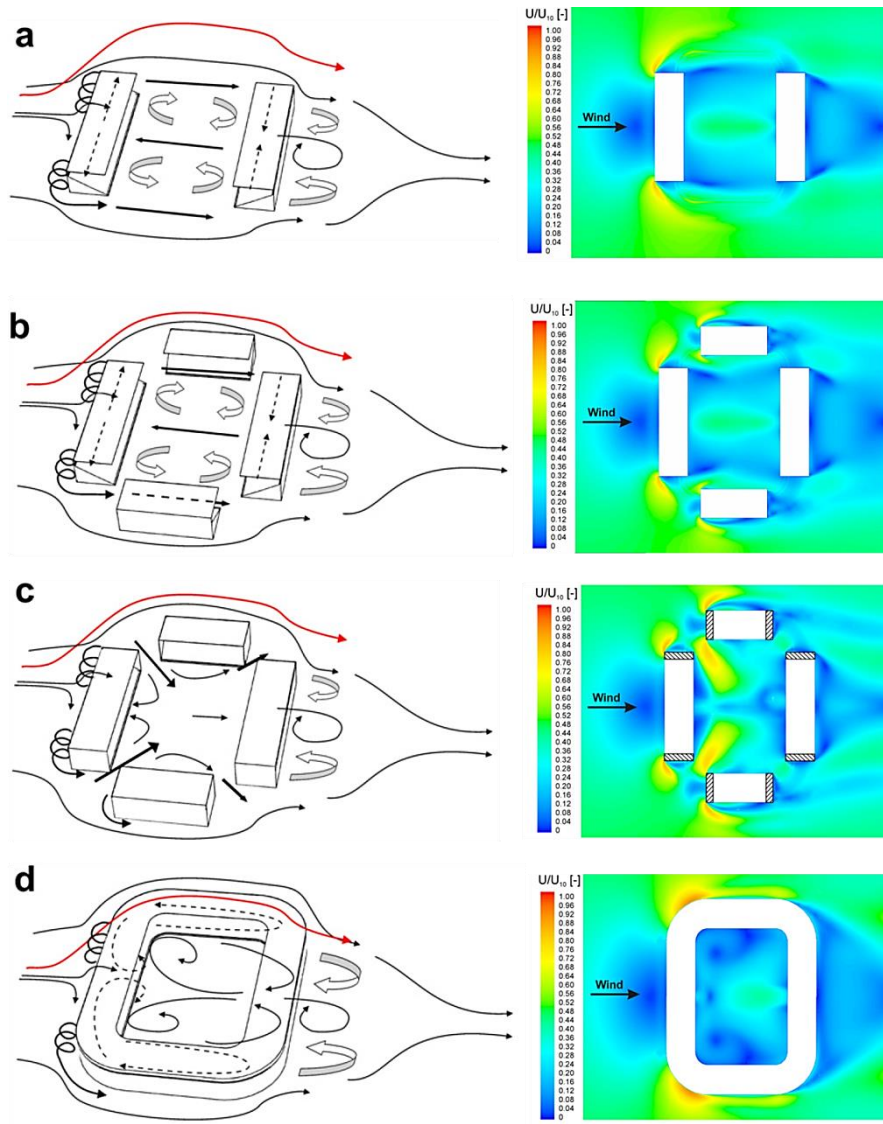


Figure 2-14 Schematic representation of the wind flow patterns for the four different stand configurations and dimensionless velocity contours on a horizontal plane 1 m above ground; $U_{ref} = 10$ m/s (van Hoof et al., 2011).

The wind distribution at pitch level has also been investigated, since it may contribute to adverse wind conditions for the players. Reid and Travers (1991) quoted the wind tunnel experimentation results obtained for the Ibrox Park stadium. As illustrated in Figure 2-15, the existence of side openings between the grandstands may result to an increase of the wind speed up to 25 % at the areas close to the side openings and to a decrease of 25 % on the areas at the centre of the pitch, when compared with the reference velocity.

2 Literature Review

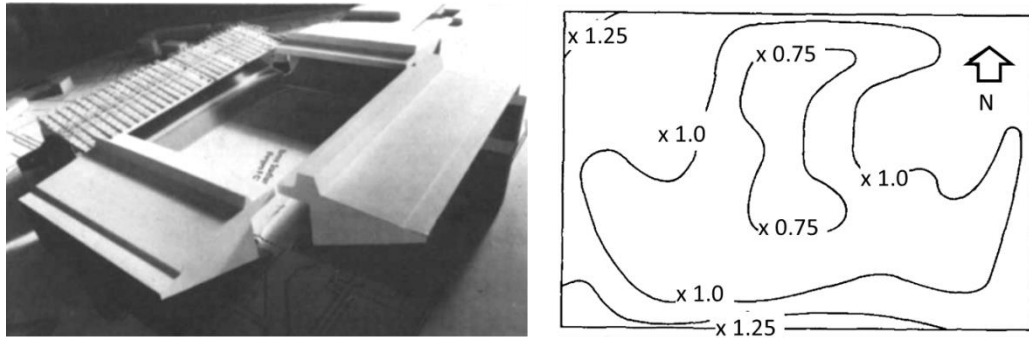


Figure 2-15 Wind tunnel model of the Ibrox Park stadium (left) and illustration of the wind speed distribution over the pitch area (right) (Reid and Travers, 1991).

Goliger (2010) performed a series of wind tunnel experiments to assess the impact of several design characteristics on the wind microenvironment over the pitch area. Reduced scale experiments were performed for an open stadium structure with two opposite grandstands and with 5 m earth berms, acting as wind protectors. The generated velocity contour lines are illustrated in Figure 2-16, indicating the development of high intensity winds under the most critical wind direction that confirmed players' complaints.

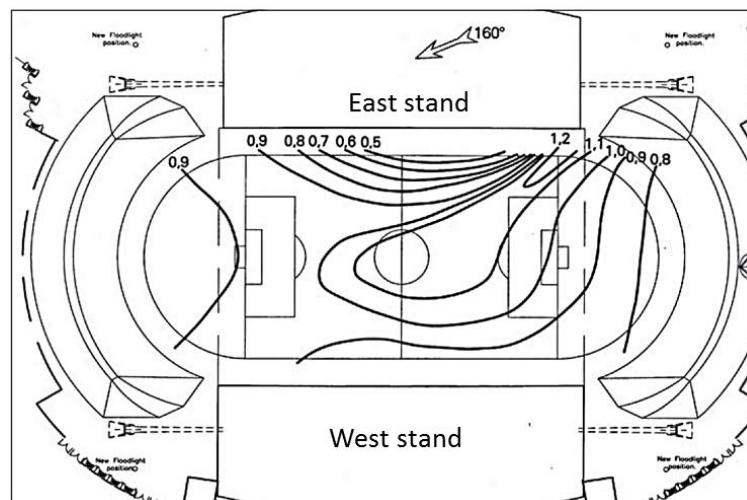


Figure 2-16 Dimensionless velocity contours on the pitch area under southeast wind direction (Goliger, 2010).

The same study assessed the developed wind microenvironment at the stadium bowl, regarding open and closed side entrances. The obtained results indicated the development of recirculation zones and high velocities on the pitch corners, which may affect the performance of the players (Figure 2-17).

2 Literature Review

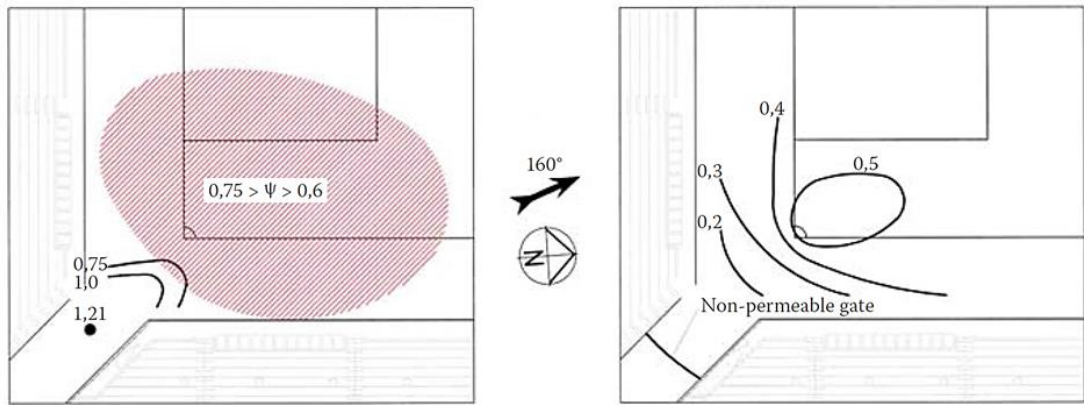


Figure 2-17 Dimensionless wind values on the pitch corner areas for the case of open (left) and close entrance doors (Goliger, 2010).

Structural interventions on the Ross-Ade Stadium in Indonesia were assessed in the study of Mei and Qu (2016) with the use of CFD tools. The work focused on the evaluation of the flow distribution on a football stadium with regard to the surrounding built environment (see Figure 2-18). Several wind directions and wind speeds were assessed for the initial and the proposed stadium model modifications. The results were poorly presented, without any details on the CFD methodology and parameterisation. Nevertheless, the generated velocity data highlighted the importance of the impinging wind direction, upon which the proposed design solution was based. The structural extension allowed the improvement of the wind comfort for players and reduced spatially the developed vortices at the stadium model.

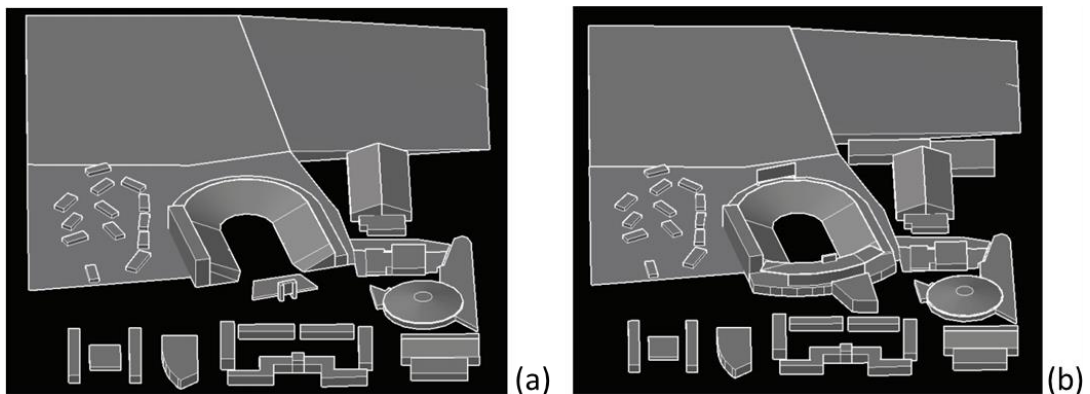


Figure 2-18 Structural design interventions to be considered for the wind comfort improvement of the Ross-Ade Stadium (Mei and Qu, 2016).

2.3 Wind comfort

In sports stadia, wind comfort is one of the most important parameters to be studied during the design conceptual phase. Wind comfort and wind safety studies that have been conducted for open urban environments may not be representative of the wind

2 Literature Review

conditions occurring in a semi-open stadium bowl, but they set important wind thresholds for consideration and highlighted the need for similar studies within the built environment.

According to Arens et al. (1986) and the developed bioclimatic chart, a minimum wind speed of 0.26 m/s is used to express the minimum air movement induced by the body motion. A maximum wind speed of 6 m/s in environments of low turbulence is considered acceptable. However, as the turbulence increases, the comfort wind speed limit is decreased. The proposed bioclimatic chart includes velocities up to 4 m/s, since higher values of wind speed do not add to further improvement of the thermal comfort level.

Wind comfort and danger criteria for urban open spaces were produced by Willemsen and Wisse (2007) for the country of Netherlands and used thereafter in wind comfort studies in urban environments. According to Table 2.2, the wind comfort and safety are dependent on the activity level and the exposure time to the relevant wind conditions. For example, wind speeds of 5.0 m/s – 10 m/s may be considered good for people who traverse, moderate for people who stroll and poor for those who are sitting.

Table 2.2 Criteria for wind comfort and danger (Willemsen and Wisse, 2007).

P ($V_{IS} > 5$ m/s) (in % hours per year)	Grade	Activity Area		
		Traversing	Strolling	Sitting
< 2.5	A	Good	Good	Good
2.5 – 5.0	B	Good	Good	Moderate
5.0 – 10	C	Good	Moderate	Poor
10 – 20	D	Moderate	Poor	Poor
> 20	E	Poor	Poor	Poor
Wind danger				
P ($V_{IS} > 15$ m/s) (in % hours per year)	Limited risk	0.05 – 0.3 % hours per year		
	Dangerous	> 0.3 % hours per year		

In sport facilities, the wind comfort criteria are relevant to the activity level of the users. The ideal wind environment should offer comfortable conditions for the spectators and wind speeds that will not compromise the performance of the players. Figure 2-19 illustrates the developed chart for thermal and wind threshold criteria for semi-open stadia that was produced after a series of wind tunnel experiments and the consideration of the Arens et al. (1986) revised bioclimatic chart.

2 Literature Review

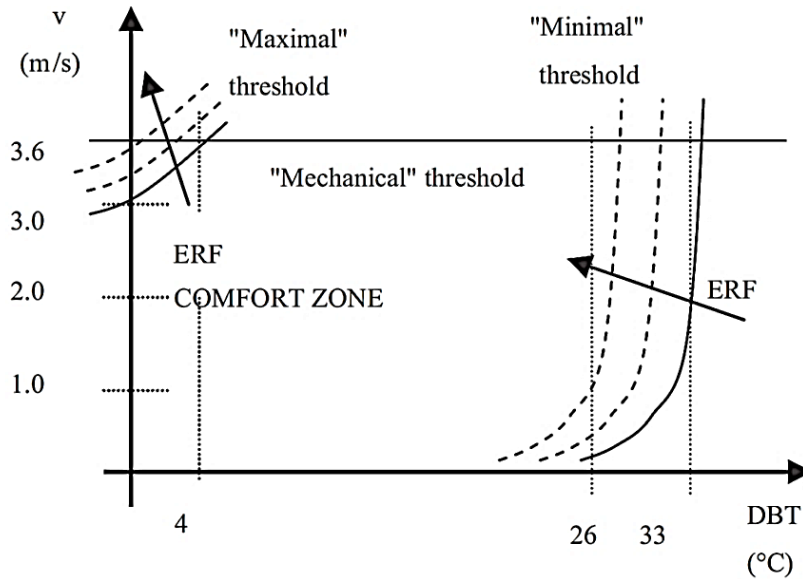


Figure 2-19 Criteria for comfort zone of flexible outlines for semi-open stadia (Szucs et al., 2007).

According to the chart, the comfort zone, which lies between 4°C and 26°C for temperatures and up to 3.0 m/s for wind speeds, may be extended to certain limits. More specifically, the mechanical threshold counts for wind speeds up to 3.6 m/s, which includes an average speed of 3.0 m/s and 20 % standard deviation according to Beaufort scale (Szucs, 2004). At these wind speeds, a light breeze begins to occur that may lead to some discomfort incidents, including hair disturbance and difficulties in reading (Baniotopoulos et al., 2011). The maximal threshold represents the maximum allowed air speed at temperatures lower than 10°C. Finally, the minimal threshold determines the maximum required wind speeds in high temperatures, to achieve cooling through evaporation, improving the thermal comfort levels in hot weather conditions.

The chart is representative of the comfort thresholds set for spectators in semi-open stadia and it incorporates two out of the four dominant environmental factors (Szucs, 2004); the air temperature, humidity, air speed and solar radiation. Szucs (2004) classified the first two parameters as uncontrolled and the latter two as moderated. In other words, the microclimate in a stadium bowl and the aero-thermal comfort conditions can partly be moderated with conceptual design interventions that may alter the levels of air velocity and solar radiation penetration in the stadium bowl.

Another way to classify wind comfort in stadiums relies on the flow homogeneity, which implies similar airflow conditions in the occupied areas. The estimation of the flow homogeneity is based on Equation 2.5, which involves the calculation of the

2 Literature Review

average velocities at several measurement locations divided by the average reference velocity.

$$\Psi = \frac{\bar{U}_i + \sigma_i}{\bar{U}_{ref} + \sigma_{ref}} \quad (2.5)$$

where \bar{U}_i is the average wind velocity at a point i , σ_i the standard deviation of velocities at a point i , \bar{U}_{ref} the average wind velocity at the reference point and σ_{ref} the standard deviation of velocities at the reference point (Szucs, 2004).

The generated results may be presented in a histogram that enables the identification of the extreme 10 % maximum and minimum Ψ -values, $\Psi_{90\%}$ and $\Psi_{10\%}$ respectively. The ratio of the extreme values over the mean Ψ values is representative of the flow homogeneity. The closer the ratio value to 1 the higher the homogeneity on the studied areas, since the extreme values tend to approach the mean velocity value. However, flow homogeneity should be used purely as a supplementary criterion on the quantification of the wind comfort, because it might produce misleading conclusions in cases of a stadium with large façade porosity¹. As illustrated in Figure 2-20, building envelopes with large openings may result to the development of high wind speeds at the stadium bowl that approach the average velocity. In these cases, ratios of the extreme Ψ values to the mean Ψ values will be very close to 1, without complying with the wind speed thresholds of Figure 2-19.

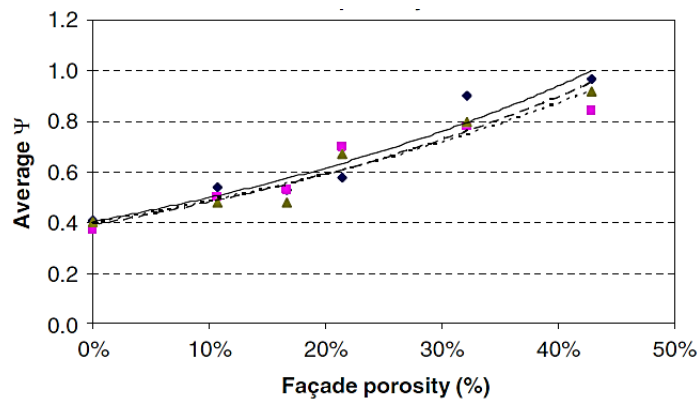


Figure 2-20 Evolution of the average Ψ values in function of the façade porosity for different wind incidences (Szucs et al., 2007).

Szucs et al., (2007) conducted wind tunnel experiments to assess the flow homogeneity in a semi-open stadium model. According to the results, in all wind directions, calm zones were generated on the lower terraces of the leeward side and

¹ Stadium porosity is defined as the ratio of either vertical or horizontal façade openings to the overall façade area of the stadium.

2 Literature Review

more intense ventilated at the upper terraces of the windward side. A parametric study of the roof inclination change revealed that a flat roof may offer homogeneity for all wind directions, with intensive ventilation at the upper tiers around the whole perimeter of the stadium. A 15° inclined roof may offer slightly less disturbance on the windward upper terraces, but in overall the heterogeneity is increased. In the case of a declined roof over 15° the average values of homogeneity are decreased by 25-30 %, but the fact that the average velocities have increased at all points resulted to a higher homogeneity on the intensively ventilated zones. A summary of the outcomes are presented in Table 2.3.

Table 2.3 Results on the wind speed and flow homogeneity for different roof inclination values, generated in Szucs et al., (2007).

Inclination		0°	+15°	-15°	Overhang	Oculus
Air Velocity (Ψ index)	Upper Tiers	2	2	1 ^{+30%}	1 ^{++30%}	1 _(corners)
	Bottom Tiers	3	3 ⁺	2	2	3 ⁺
Homogeneity		√	x	√	x	x

1 = intense, 2 = less intense, 3 = calm

2.3.1 Porosity in stadiums

Another important characteristic of stadium structures that can greatly affect the wind comfort at the stadium interior is the porosity of the building envelope. The change of the porosity in stadiums has been studied as part of the integration of windbreaks on the structure's façade to improve the interior wind microenvironment. The reasoning behind introducing porosity in stadiums is due to the developed pressure differences. More specifically, a porosity of 0 %, which implies the absence of any type of openings on the stadium windbreak walls, causes large pressure differences between the exterior and the interior stadium environment. The high negative pressures that are developed at the stadium bowl create a vacuum effect, introducing turbulence, which is transferred at the playing field area (Thompson et al., 1998). On the other hand, when applying porosity into the windbreak walls, a more equilibrated wind environment is created, with reduced areas of low pressure and thus suction. Table 2.4 summarises the effect of different windbreak wall porosities on the wind speed flow. According to several conducted studies, a porosity of 40-50 % may contribute to favourable wind flow conditions at the occupied areas of the stadium interior (Thompson et al., 1998).

2 Literature Review

Table 2.4 Wind speed behind barriers of vertical height h , expressed as a percentage of the upstream wind speed flow, shown in multiples of the fence height (h) downwind of the barrier ((Thompson et al., 1998).

Distance from wind break fence	0h	2h	5h	10h	15h	20h	25h	30h	40h
Type of barrier (porosity %)									
Open (70 %)	90	80	70	75	85	90	95	100	100
Medium (50 %)	40	25	20	25	50	60	75	90	100
Dense (0 %)	0	20	40	65	80	85	95	100	100

The wall porosity on stadium structures has been a subject for further experimental studies. Szucs (2004), after the conduction of a series of boundary layer wind tunnel experiments, observed that the porosity of the stadium envelope, together with the roof inclination were the primary determinants on the development of the stadium microclimate under different wind directions. Important outcomes of the research were the development of a methodology to measure the homogeneity and the generation of a graphical representation of the comfort zones for spectators, based on the revised bioclimatic chart by Arens et al. (1986), as discussed earlier in Section 2.3.

Szucs et al. (2009a) published a supplementary study with important features and design recommendations for stadia located in hot climates. In order to promote the air movement at the stadium interior, the construction of vertical and horizontal openings should be considered, since the lateral porosity was deduced to be detrimental for the aerothermal comfort of both spectators and players. Wind tunnel experimentation results indicated that stadiums in warm climates with high values of surface porosity appear to have increased air intensity in favour of stadiums' microclimate (see Figure 2-21).

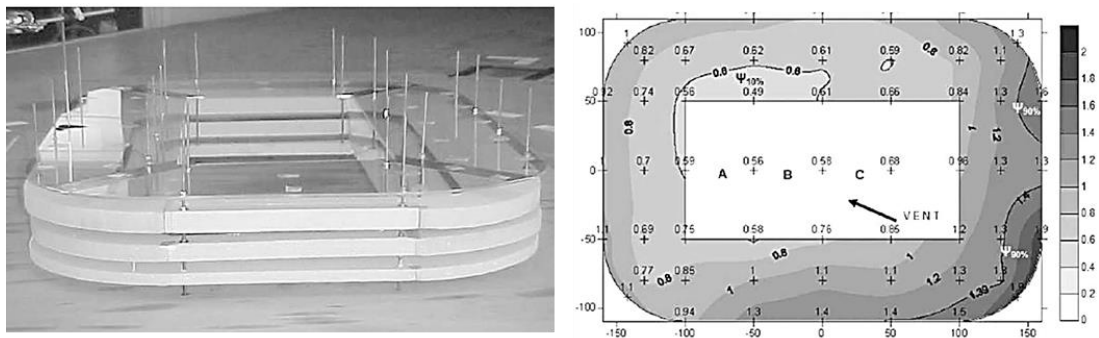


Figure 2-21 Stadium model with 43 % porosity (left) and iso- Ψ lines for the resultant airflow distribution (right); dark and light coloured areas represent the intensively ventilated and the calm zones respectively (Szucs et al., 2009a).

2 Literature Review

However, from spectators' perspective, intense airflows within the recommended thresholds are beneficial only if the air temperature is less than the skin temperature, enabling convective heat loss. From player's perspective, on the other hand, calm airflow zones are vital for their athletic performance enhancement.

Szucs et al. (2009b) studied sports stadia for operation in cold climates. For the investigation of the aerothermal comfort conditions, the wind chill index was employed that correlates the atmospheric cooling and its effect on human comfort. The study involved wind tunnel experiments and the results were similar to the ones generated by Szucs et al. (2007) and Szucs et al. (2009a). However, the results of a stadium with 0 % porosity that were not previously reported, showed increased ventilation zones on the upper four spectator corners, where the roof is connected with the main structural core, also shown in Figure 2-22.

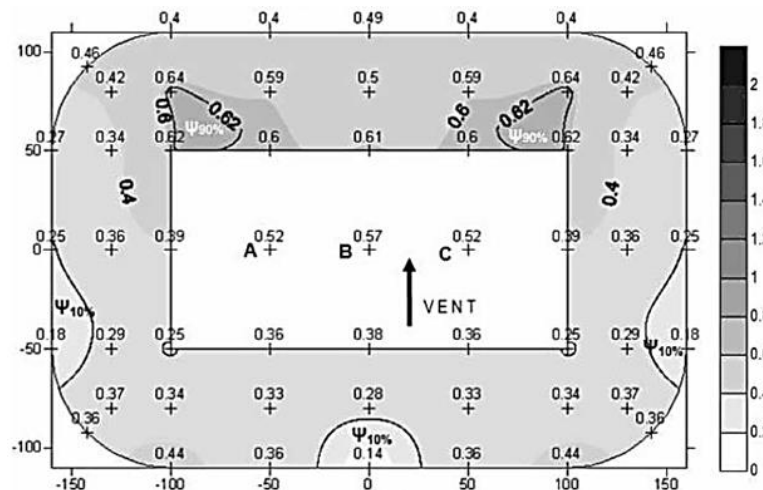


Figure 2-22 Iso- Ψ values for an enclosed stadium with flat roof configuration (Szucs et al., 2009b).

The lateral porosity on the stadium envelope in terms of the existence of a ventilation opening between the roof and the upper spectator tiers has also been assessed. Wind tunnel techniques were used by Biagini et al. (2007) to study the wind performance of lightweight roof components in three stadiums. By employing particle image velocimetry (PIV) techniques, the ventilation performance at the highest rows of the upper terraces of one discontinuous stadium structure was evaluated. The results indicated that the provision of a horizontal ventilation opening may conclude to substantial improvements of the wind comfort levels, enabling the air to escape, as shown in Figure 2-23.

2 Literature Review

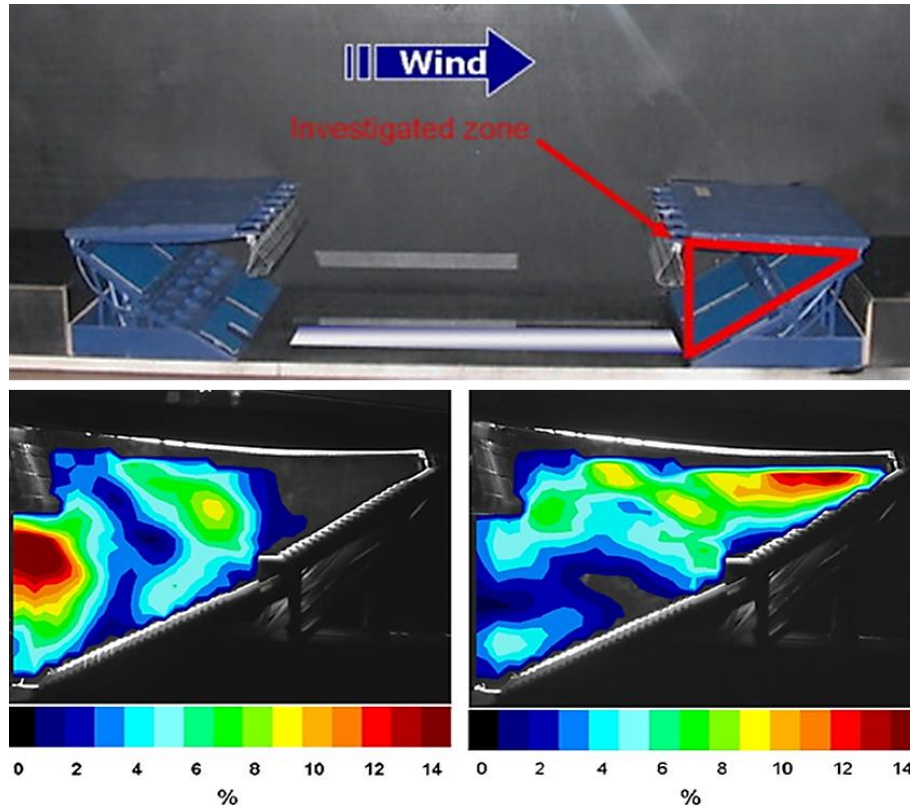


Figure 2-23 Mean iso-velocity maps (as percentage of $U_{ref} = 3.64$ m/s) generated for the old (left) and the new (right) roof (Biagini et al., 2007).

Similar observations were made by Goliger (2010), who conducted a technical study to optimise the use and wind safety in sports-stadiums, with a series of wind tunnel tests. The study concluded that the horizontal ventilation opening between the roof and the upper spectator tiers may successfully promote the wind comfort, but only for the last eight spectator rows. The author also highlighted that the wind discomfort is relevant to a large number of parameters, including the activity level, the wind exposure duration and mainly the stadium design configuration.

2.4 Environmental comfort conditions in stadiums

On the study of the environmental comfort in sports stadiums, the wind is considered one of the primary environmental criteria for evaluation. However, several studies have been performed in stadium structures to prevent uncomfortable environmental conditions, induced by the air temperature, the solar radiation and the rain infiltration, to assess the heating, ventilation and air-conditioning mechanisms and predict pollution dispersion. These studies are analytically presented thereafter, since they are considered important for the identification of the critical design characteristics of the stadium structure towards the improvement of the wind microenvironment.

2 Literature Review

2.4.1 Thermal performance

The first scientific study that considered the human factor as an important parameter on the stadium design was by Fiala and Lomas (1999), who produced a computational model to assess the thermal environment on the Stadium Australia. His findings on the performance of the semi-transparent roof under intense solar radiation showed that the roof temperature on the areas of limited air movement could rise up to 50°C, causing intensively discomfort conditions for the spectators seating on the upper terraces (Figure 2-24). On that study, the careful roof design and material selection, along with adequate air flow recirculation were highlighted as the most detrimental factors for consideration in stadium structures located in hot climates.

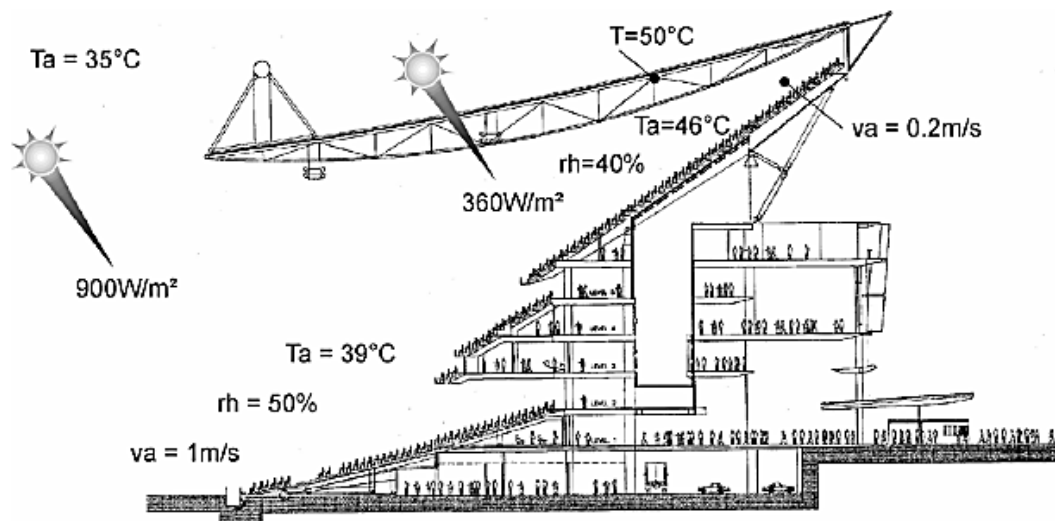


Figure 2-24 Prediction of local climatic conditions for a hot, sunny day of the Stadium Australia integrated with semi-transparent roof (Fiala and Lomas, 1999).

Bouyer et al. (2007), on their study on semi-open stadia, focused on the effect of the lateral porosity and the sky opening size on the stadiums' thermal comfort performance. By combining the Physiological Equivalent Temperature (PET) thermal comfort index that estimates the thermal sensation and the corresponding heat stress level, and a virtual reality platform they studied two stadia of different roof geometry and porosity. The results showed that for both sport facilities, the developed thermal comfort conditions are primarily dependent on the induced solar radiation, rather than the thermal performance of the structural materials, as reported in Szucs et al., (2009b). The areas of highest discomfort were the ones continuously exposed to direct sunlight, mainly located on the lower spectator tiers, as shown in Figure 2-25.

2 Literature Review

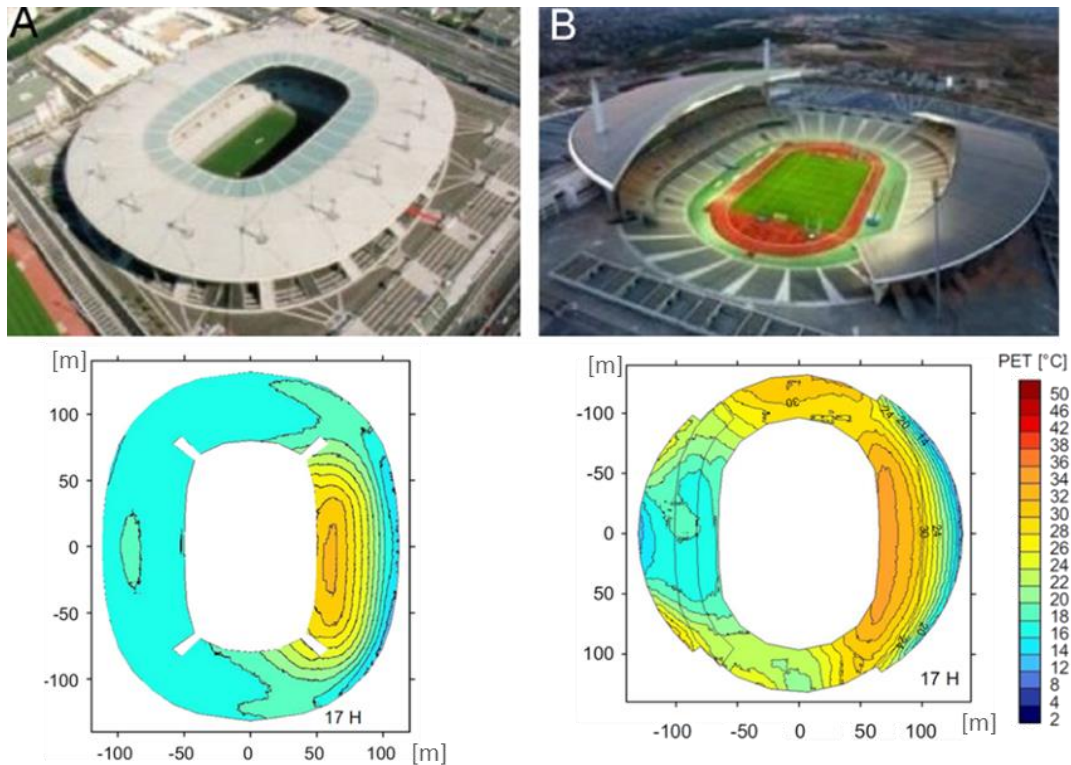


Figure 2-25 Thermal performance assessment of the stadium of France (A) and the Ataturk stadium (B) at 17 h (Bouyer et al., 2007).

2.4.2 Natural ventilation

The importance of obtaining a holistic approach on the flow phenomena occurring in both interior and exterior areas of the stadium structures was stated by Blocken and Persoon (2009). By performing CFD simulations and full scale experiments the pedestrian wind comfort and the natural ventilation performance of the semi-open stadium of Amsterdam Arena was assessed. The results indicated the high dependence of the airflow on the surrounding building structures and the wind direction. As shown in Figure 2-26, the wind direction is the dominant parameter on the flow rate through the side entrance openings, which may cause alteration on the flow rate values through the side entrance openings and different levels of wind discomfort. On the paper the methodology for studying buildings within the built environment is presented and considered important during the conceptual design phase and the decision-making process.

2 Literature Review

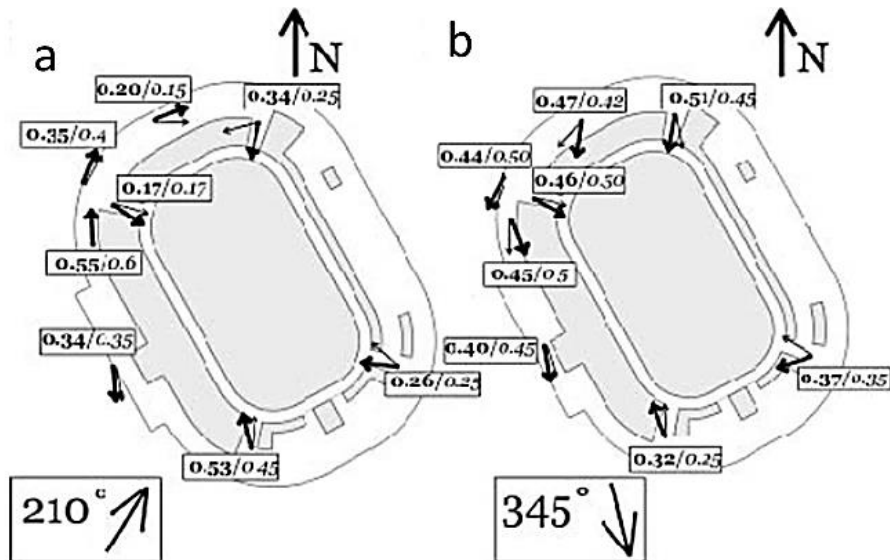


Figure 2-26 Dimensionless wind velocities for the experimental (bold) and the numerical study (italics) (Blocken and Persoon, 2009).

The natural ventilation performance of the Amsterdam Arena stadium was further investigated by van Hoof and Blocken (2010b; 2009). CFD simulations indicated that small opening alterations may contribute to up to 43 % change of the ventilation rate from 1.36 to 1.95 h^{-1} , under specific wind direction. However, the full scale validation study revealed large deviations between the results, of up to 50 % at the areas of the stadium wake, highlighting the difficulties of accurately simulating high turbulent flow phenomena that are highly dependent on the urban surroundings.

A more analytic study on the effect of the wind direction on the natural ventilation performance of the Amsterdam Arena stadium was performed by van Hoof and Blocken (2010a). In that study, CFD simulations were performed using the realisable $k-\varepsilon$ model and the Fluent commercial code to study the stadium and the surrounding built environment under eight different wind directions. The results of the air changes per hour (ACH) are shown in Figure 2-27, with the highest values to be obtained for the wind flow induced from the direction with the lowest urban density.

2 Literature Review

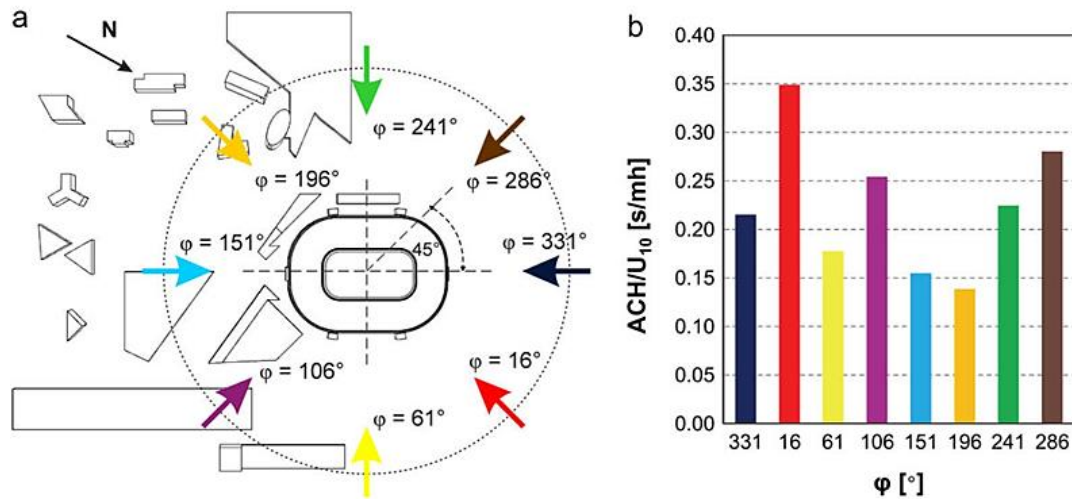


Figure 2-27 Generation of the ratio of ACH to U_{10} for different wind direction for the Amsterdam Arena stadium (van Hoof and Blocken 2010a).

2.4.3 Pollution dispersion

CO₂ concentration measurements, as part of the natural ventilation performance, were a case of study for the Amsterdam Arena stadium conducted by van Hoof and Blocken (2012). The study also focused on the computational and experimental limitations that arose during the conduction of the study. More specifically, computational models that involve multiscale characteristics pose several challenges on mesh resolution for accurate CFD studies. Wind tunnel experiments on the other hand cannot reproduce the buoyancy effects due to temperature differences, and finally, full scale measurements may acquire only a limited number of measurements for validation.

Another study on the assessment of the air quality in international sports stadiums was performed by Faber et al. (2013). The work included a field study in the Coface Arena to calculate the distribution of aerosol particles during a football game. The study used a multivariable factor analysis technique, known as positive matrix factorisation (PMF), to perform a chemometric evaluation and model environmental data sets. The results indicated that among all the anthropogenic sources of organic aerosols, the cigarette smoke was the dominant component with concentration that exceeded the PM_{2.5} (particulate matter) target established by the European Union. Nevertheless, the ventilation performance of the open roof stadium was considered satisfactory, since an hour after the end of the game all species' concentrations were back to their initial levels.

2 Literature Review

For the same stadium structure, measurements of gas-phase volatile organic compounds (VOCs) were performed (Veres et al., 2013). The in-situ measurements were conducted during an evening football match, in order to eliminate the impact of the surrounding external environment-induced VOCs. The measurements on the species concentrations were used to produce general conclusions on the importance of considering the direct impact on the micro and macro environment of large human gatherings in both building and urban scale.

2.4.4 Wind-driven rain

Also discussed earlier, studies of the wind-driven rain performance of semi-open stadiums have been conducted, because it is a significant premise during the conduction of sport events, mainly attributed to the induced level of discomfort for the spectators. The primary study of Persoon et al., (2008) involved the performance evaluation of two-dimensional simplified stadium structures with seven different roof configurations against the wind and the rain. The methodology employed Lagrangian particle tracking for the raindrop trajectories. The results revealed that a downward-sloping roof of 13° degrees can provide less wind disturbance on the spectator tiers and consequently less rain discomfort (Figure 2-28).

2 Literature Review

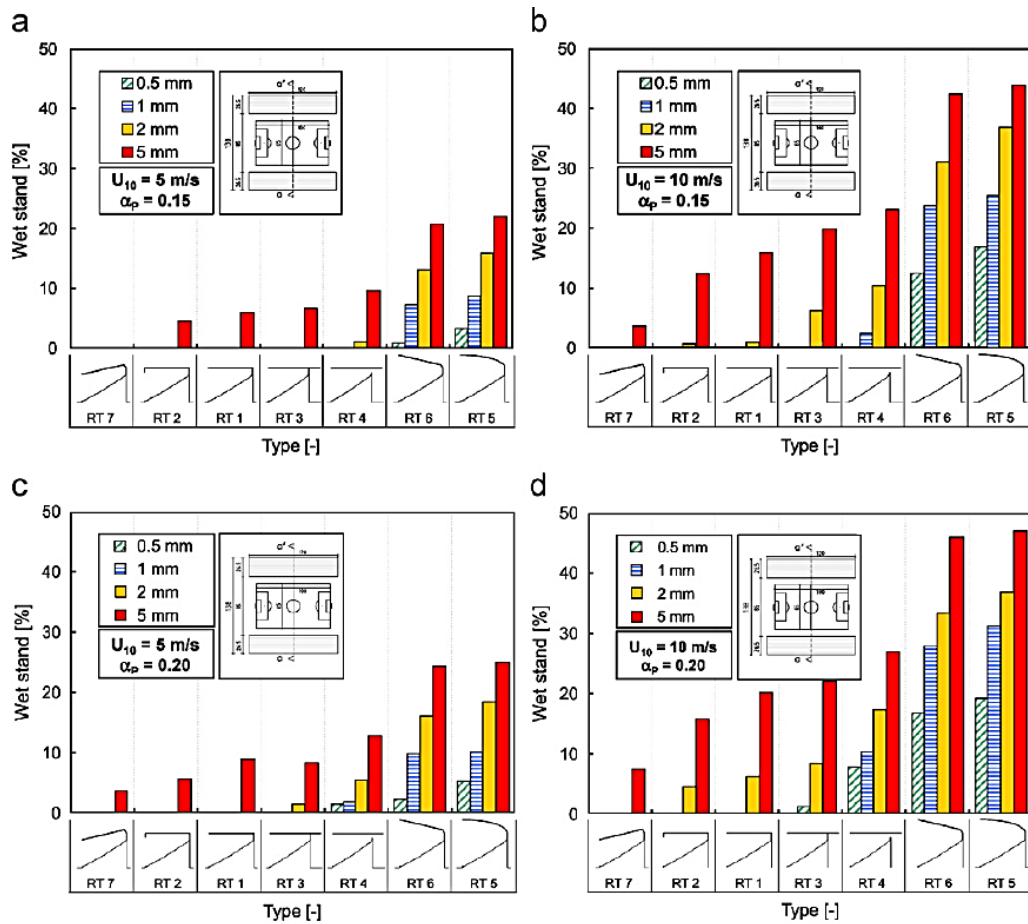


Figure 2-28 Percentage of wetted stand length for seven roof configurations under variable raindrop diameter, reference velocity (U_{ref}) and power law coefficient (α_p) (Pearsoon et al., 2008).

Three-dimensional studies of stadium structures were also conducted by van Hoof et al. (2011) to assess the wind-driven rain performance for four stand arrangements and three roof types. The CFD wind-driven rain simulations considered the evaluation of four raindrop diameters in total twelve stadium configurations. The results revealed the high dependence of the wind and rain paths on primarily the stadium geometry and secondarily the roof type. The plots of the percentage of wetted areas on the spectator tiers are illustrated in Figure 2-29. According to the results, the enclosed stadium with an inclined towards the pitch roof configuration provides the most comfortable environment against the rain. The results also highlighted the dependence of the rain patterns on the airflow distribution patterns and the fact that a comfortable environment from rain presupposes wind comfort.

2 Literature Review

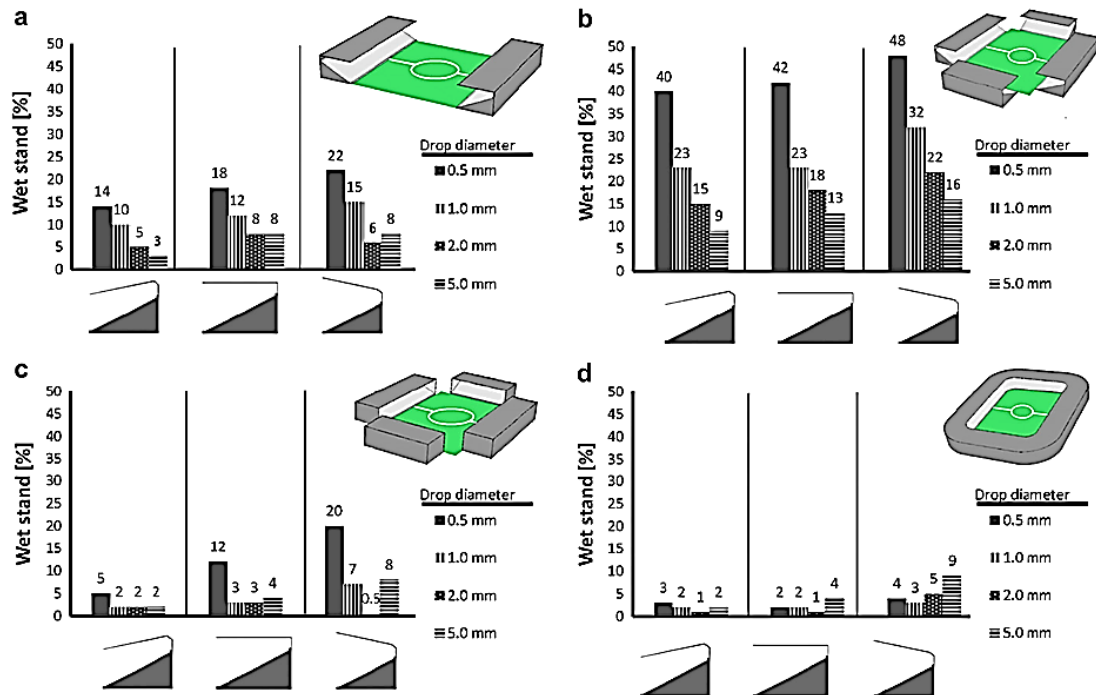


Figure 2-29 Percentage of wetted stand for the twelve stadium configurations and the four raindrop diameters; $U_{ref} = 10\text{m/s}$ (van Hoof et al., 2011).

Soligo et al. (2000) stated a study on the rain infiltration for the baseball stadium of Pacific Northwest Ballpark located in Seattle. The study included the conduction of CFD simulations with wind and rain data obtained from the local meteorological station. Results were generated for three rain droplet dimensions, with a computational example to be presented in Figure 2-27. The study concluded that the wind direction is the primary factor of the rainfall patterns and the rain penetration under the spectator tiers. Additional conclusions involved the consideration of wind deflectors and rainscreens to improve the stadium comfort levels.

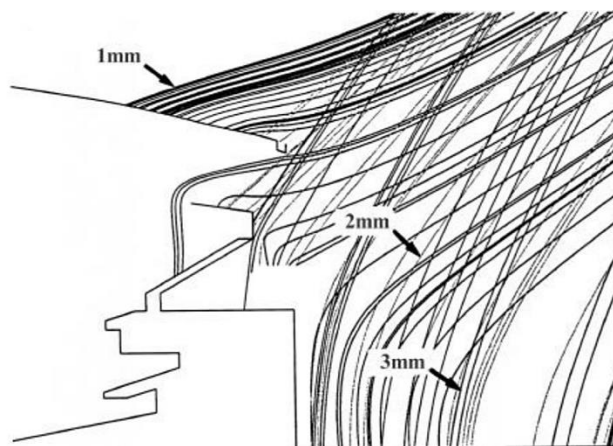


Figure 2-30 Computational example of the rain drop trajectories (Soligo et al., 2000).

2 Literature Review

2.4.5 Thermal and energy performance

Studies assessing the thermal and energy performance of stadia have also been conducted. Lomas et al., (1997) performed a study to provide thermal comfort conditions at the interior areas (halls) of the Stadium Australia. By employing CFD techniques and the ESP-r modelling software they assessed the performance of several cooling and natural ventilation scenarios during the conceptual design phase of the facility. The generated results highlighted the benefits of employing computer simulation and thermal analysis tools on the improvement of the cooling and heating loads of the facility and the study of design interventions, partly of which were adopted in the final design.

Closed stadiums offer the advantage of an easily controlled environment that may be adapted in any climatic fluctuations. Limited work has been conducted in domed stadia, and it is mainly focused on the assessment of the thermal and energy performance. Nishioka et al., (2000) measured the temperature distribution in a large indoor stadium integrated with seat air-conditioning units of 20°C diffuser temperature. The results showed a well-controlled and uniform temperature distribution up to 20 m, satisfying the users' comfort needs. The advantageous design of an air-remover at the top of the roof enabled the cumulative hot air to exit the stadium. The six month cooling and heating loads for the stadium bowl were also recorded equal to 5,1 GJ and 0.89 GJ respectively, which was considered small for the cooling season.

Stamou et al. (2008) performed a thermal comfort assessment study for the indoor Galati Arena in Athens. The stadium was integrated with 256 jet nozzles located on the roof, above the main side entrances, on the floor close to the playing area, on some peripheral walls and under the spectator seats. By employing CFD simulation techniques and the shear stress transport (SST) $k-\omega$ turbulence model results on the wind and temperature distribution at the stadium interior were generated, as shown in Figure 2-31. The calculated thermal comfort indices indicated satisfactory comfort conditions for both players and spectators with only 7 % dissatisfaction in specific areas of the terraces.

2 Literature Review

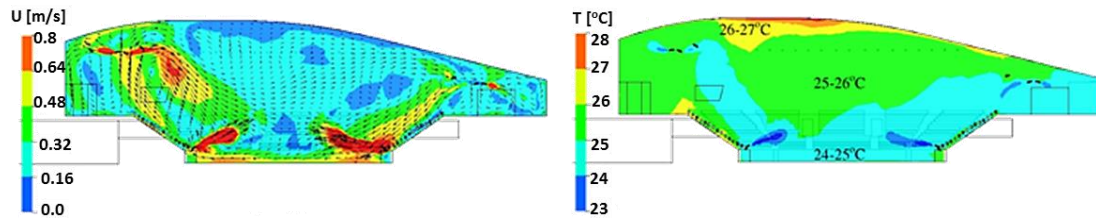


Figure 2-31 Wind (left) and temperature (right) distributions generated on a vertical plane in the middle of the model (Stamou et al., 2008).

Another study on thermal comfort of spectators in stadia located in hot climates was conducted by Ucuncu et al., (2010). Dynamic Thermal Modelling (DTM) and CFD techniques were used to determine the effect of the roof on the air and temperature distribution in a semi-open stadium. The DTM-generated results highlighted the importance of the roofing materials in the thermal performance of the stadium, since it can contribute to an increase of the mean radiant temperature at the stadium bowl, due to the convective heat exchange between the element surfaces and the surrounding air. The obtained results from the CFD study indicated the improved performance of a cooling system installed underneath spectators' seats (near-field), when compared to a system integrated on the roof structure (far-field) (Figure 2-32). Great limitations of the study were the simulation of a single human figure within a stadium section that consisted of 12 seats in a horizontal row.

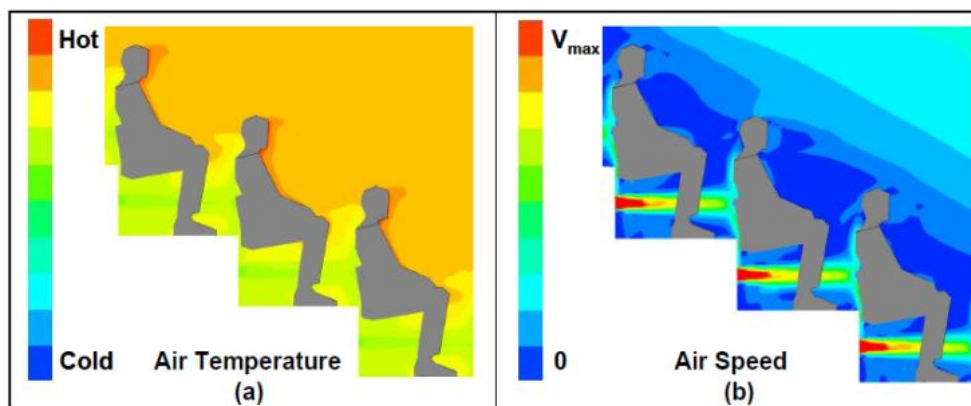


Figure 2-32 CFD predictions for air temperature (a) and air speed (b) (Ucuncu et al., 2010).

Sofotasiou et al., (2015) stated the imposed climatic and legacy challenges for the upcoming FIFA World Cup in Qatar. The potentiality of using low-energy cooling technologies to compensate the expected cooling load was stated and an assessment study using dynamic thermal modelling was conducted for a semi-open stadium structure. The results on the cooling load requirements indicated that a game taking place in July would require 115 MWh to provide thermal comfort conditions for both players and spectators at all occupied areas of the facility.

2 Literature Review

A more recent study of Lestinen et al., (2016) assessed the ventilation performance of the indoor multipurpose Malmö Arena, in Sweden. The stadium is integrated with displacement ventilation at the bottom spectator tiers and zoning ventilation systems at the upper spectator tiers. In situ experimentation was conducted acquiring data on temperature, wind speed, humidity, CO₂ concentrations and sound levels. Temperature and airflow distributions were investigated with CFD tools and the use of the SST $k-\omega$ turbulence model. The results indicated the high dependence of the developed microclimate on the supply air temperature, the airflow rates, the number of spectators and the retractable seats' arrangement. Nevertheless, the combined ventilation system proved to be effective on providing uniform temperature ranges per area of interest and low wind speeds. Finally, an under seat cooling systems was proposed as a potential solution to improve further the ventilation performance and thus the indoor stadium climate.

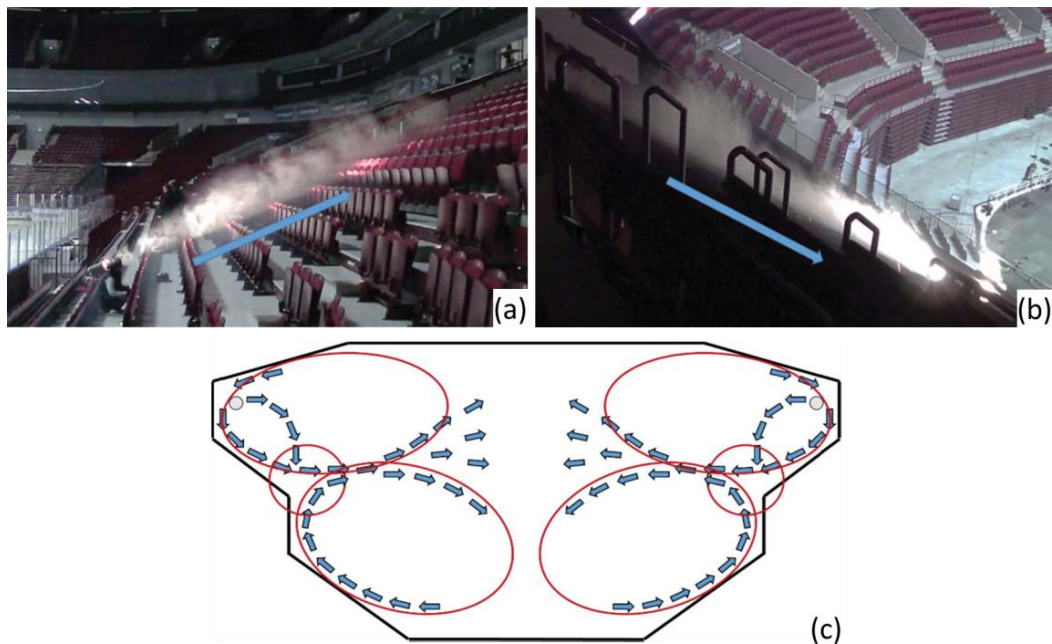


Figure 2-33 Air flow distribution patterns (c) generated after conduction of smoke tests on the lower (a) and upper (b) spectator tiers for the Malmö Arena (Lestinen et al., 2016).

2.5 Stadium design considerations

Regarding the aforementioned environmental comfort criteria and velocity and pressure distribution considerations, every stadium design can be considered as a new case study. For this project, a stadium structure for FIFA sport events was constructed, regarding the critical decisions that need to be taken in order to develop environmental friendly conditions for both players and spectators. FIFA has

2 Literature Review

established a series of technical requirements and recommendations that every new or renovated stadium needs to comply with (FIFA, 2011). These prerequisites are easily replicated during the stadium design phase and are briefly summarised below:

Stadium orientation: the north-south orientation is commonly selected for pitch orientation, $\pm 45^\circ$ regarding the average sun position at the half-time for an afternoon match.

Roof construction: the roof needs to allow natural sunlight penetration to promote the natural growth of the grass and at the same time protect the spectators from the direct sunlight and the wind-driven rain that may cause disturbance and uncomfortable.

Stadium capacity: the facility should be able to host at least 30,000 spectators, with possible consideration of structurally feasible assembling and disassembling to adapt to the relevant needs.

Auxiliary area: the dimensional characteristics of the auxiliary area are depicted in Figure 2-34. The area includes the field area ($105 \times 68 \text{ m}^2$), the grass area ($115 \times 78 \text{ m}^2$), and additional auxiliary space for the players, the media and the advertising.

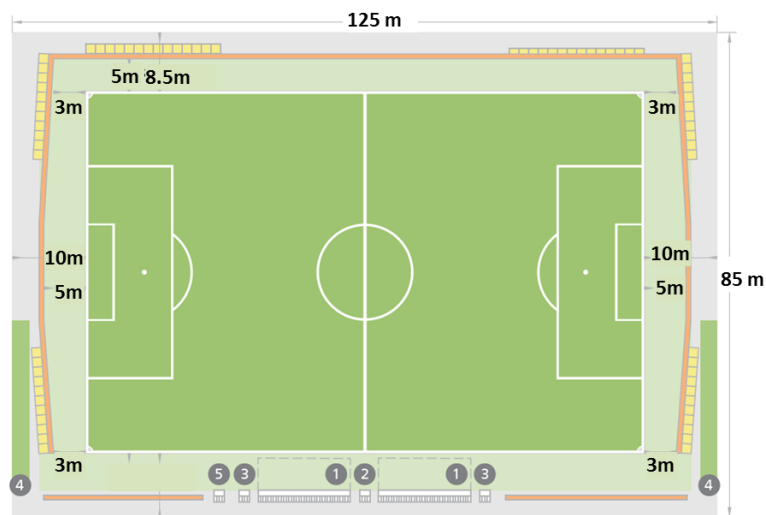


Figure 2-34 The dimensional characteristics of the auxiliary area (FIFA, 2011).

Seating: the position of the spectator tiers should provide visibility at all times to the playing field area, starting from the corner on the pitch level. As shown in Figure 2-35, a barrier of 0.8 m height should be placed in front of the first seat row for security reasons, the seating riser (a) should be at least 0.3 m, the seating thread (b)

2 Literature Review

at least 0.8 m, the rake angle (d) should not exceed the 34° and the vertical distance (c) for pitch vision no less than 0.06 m.

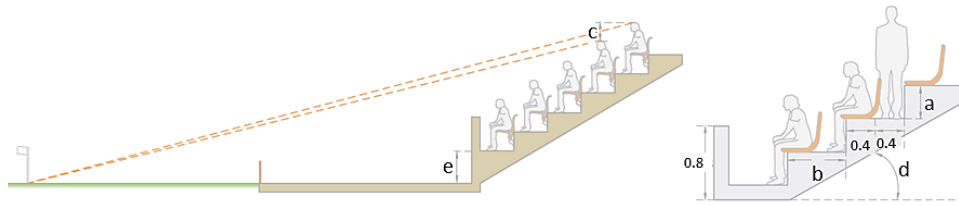


Figure 2-35 Dimensional recommendations for spectator tiers (FIFA, 2011).

2.6 Design optimisation

The need for optimum structural design solutions that satisfy users' needs and at the same time comply with the relevant requirements, has led engineers to develop techniques that enable the decision-making process during the early design stages (Figure 2-36). By combining computational models with mathematical and statistical tools, it is possible to conduct parametric studies towards design optimality with substantial reduction in computational cost and effort.

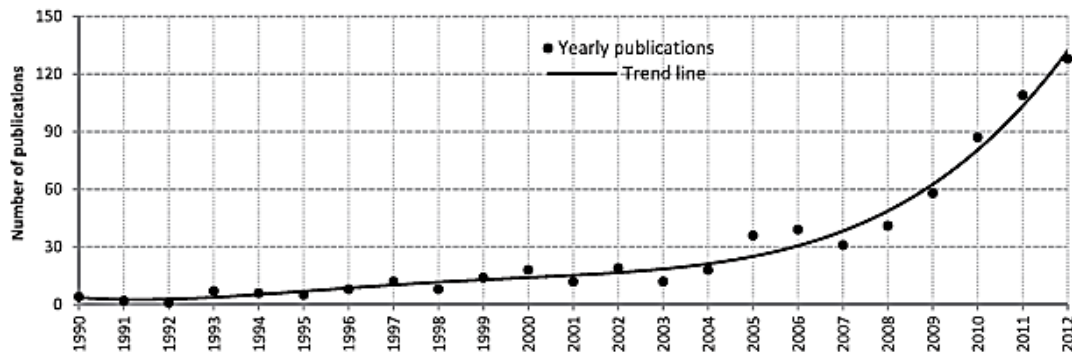


Figure 2-36 Increased trend of number of optimisation studies in building science (Nguyen et al., 2014).

The most commonly statistical methods and optimisation algorithms on the investigations of optimum design solutions in building structures are briefly described and presented below:

Response Surface Methodology (RSM) is a collection of mathematical and statistical methods that seek the optimisation of the performance of a system, which is described by a polynomial fit based on the behaviour of a data set.

Genetic Algorithm (GA) is a competitive algorithm for the investigation of a problem space to deliver solutions in optimisation and search problems. It belongs to Evolutionary Algorithms and works towards an optimum design solution for both

2 Literature Review

constraint and unconstrained problems by employing a process similar to biological evolution (Mitchell, 2002).

Artificial Neural Networks (ANN) algorithms are based on the biological brain's learning ability and can be used as predicted models by learning the patterns in both experimental and numerical non-linear data.

In literature, several studies have used the advantageous characteristics of CFD tools, Response Surface Methodology (RSM) techniques and optimisation algorithms to investigate optimum design solutions for buildings. Malkawi et al. (2005) employed CFD techniques and Genetic Algorithms (GA) to investigate several design variables in a simple room integrated with air terminals. The study including assessment of the room size, the positioning and size of wall openings and the supply duct parameters, towards thermal and ventilation optimality.

Ng et al. (2008) employed coupled CFD-RSM techniques to predict the air diffusion performance index in a displacement ventilated office. The study involved the assessment of three design parameters, including the location of the displacement diffuser, the supply temperature and the exhaust position, The RSM analysis was performed with the MINILAB statistical software and the Box-Behnken design method. The results revealed the adequacy of the method to successfully improve the comfort conditions, after selecting the most favourable combination of design parameters.

Zhou and Haghghat (2009a) published an optimisation scheme methodology to improve the ventilation performance of an office environment. The study was conducted with coupled CFD-GA optimisation with an integrated artificial neural network (ANN) for the response surface approximation. By careful selection of the input and output parameters, the thermal comfort and the overall indoor air quality was improved as opposed to the initial ventilation arrangement, without compromising system's energy efficiency (Zhou and Haghghat, 2009b).

Norton et al. (2010) employed coupled CFD-RSM techniques to promote the ventilation performance and the flow homogeneity of a livestock building. The study focused on the optimisation of geometrical building characteristics, with the assessment of 11 different design configurations generated based on Box-Behnken experimental design. The standard $k-\varepsilon$ model was used for the CFD simulations, as it showed the best performance after the turbulence model assessment study. The

2 Literature Review

results revealed the sensitivity of the flow microenvironment under the studied design parameters and highlighted the advantageous use of RSM techniques on the optimising buildings.

A series of studies have been performed by Stavrakakis et al. (2010; 2011; 2012) who developed a coupled CFD-ANN computational tool to evaluate the response of the different predicted mean vote (PMV) thermal comfort indices under variable window opening configuration and wind direction. The results indicated the optimum design solutions, but also highlighted the sensitivity of the results under specific inputs and the need for a large number of simulations for global optimum solutions. Their study was further developed considering PMV indices for non-air-conditioning areas and for different activity levels. Optimal window designs were generated and the possibility for doable use of the methodology in a wider scale of parameters and cases was suggested.

Shen et al. (2012) employed Design of Experiments (DoE) and RSM techniques to investigate the ventilation rate under variable wind speed and direction. The method evaluated different DoE methods, generated the design point responses with CFD simulation runs and fitted the results in quadratic response surfaces. It was concluded that the central composite rotatable design (CCRD) for the generation of the design points produced more accurate results. Similar conclusion was drawn in their former work (Shen et al., 2013), with the study of different DoE methods, which highlighted the good performance of both CCRD and Space-filling design (SFD), in case of computer-based experiments.

In 2013, Xue et al. proposed a methodology and developed a simulation platform that successfully couples GA and CFD tools optimising the inlet boundary conditions (inlet temperature, supply velocity and direction) towards comfort optimality for enclosed spaces. The study involved optimisation of the indoor airflow distribution patterns, by employing reverse optimisation techniques to achieve compliance with the PMV thermal comfort index requirements.

Based on CFD simulations and GA optimisation algorithms, Wang and Malkawi (2015) assessed the pressure distribution on the façade of a building structure to improve the natural ventilation performance. The study involved simulation of the ABL velocity profile and the investigation of the optimum building shape form of a tall structure located in the urban environment. The work highlighted the advantages

2 Literature Review

of the optimisation study to produce a structural form that promoted natural ventilation and the disadvantages of the computational intensive process.

Finally, Sofotasiou et al. (2016) validated a CFD-based RSM optimisation technique to optimise the indoor environment of a cross ventilated building block. For the simulation study the standard $k-\varepsilon$ turbulence model was used and the results were validated with wind tunnel experiments. The identification of the optimum window design solution achieved to improve both the flow rate and flow homogeneity at the building interior, adding to the environmental comfort conditions.

2.7 Research gap

Several studies have been conducted on the evaluation of the environmental performance of semi-open stadium structures by employing experimental and computer-aided simulation techniques. However, the restricted number of CFD studies on stadium structures reflects the imposed computational limitations, mainly related to geometrical complexities and simulation cost effectiveness. Adding to this, the already conducted studies have shown that every stadium structure should be considered as a new case study, since it is highly dependent on its unique design and the spatial and temporal characteristics.

The research gaps that have been identified in literature are summarised thereafter:

1. There is lack of understanding the nature of the flow phenomena occurring in the microenvironment of semi-open stadiums.
2. There are no analytical computational-based studies that assess the interactions occurring between the urban and the stadium flow environment.
3. There are no published CFD studies that describe analytically the airflow distribution patterns at the stadium bowl, regarding the relevant design configurations and the developed wind comfort responses of the users.
4. The use of coupled CFD-RSM optimisation tools have not been previously exploited in the design of stadium structures.

2.8 Summary

This chapter provided the theoretical background to be considered in the wind engineering studies and summarised the work that has been conducted on semi-open and enclosed stadia, with respect to the established wind comfort criteria and the

2 Literature Review

relevant design characteristics. The studies were mainly based on wind tunnel experimentation using small scale models, and on CFD simulations replicating the regional spatial and temporal characteristics of the relevant stadium geometry. The generated results gave an insight on the flow interactions occurring at both interior and exterior areas of the sports facilities, with main focus on the assessment of the wind and thermal performance. Important design parameters were highlighted that appear to affect the stadium microenvironment, including the porosity percentage of the building envelope, the presence of a roof oculus and/ or ventilation openings, the roof geometry, the building materials, the positioning of the cooling and heating systems and the building urban planning design on the close vicinity of the facility. Table 2.5 summarises the most influential studies on stadiums towards microenvironmental improvement for the users.

Table 2.5 Summary of the most influential research findings on stadium structures towards microenvironmental comfort of users.

Reference	Stadium design	Employed method	Results description
Marighetti et al. (2000)	Oculus Circular stadium	Wind tunnel	An open roof perimeter with 5° roof inclination produces less suction zones.
Pearsoon et al. (2008)	2D semi-open stadium designs	CFD & Lagrangian particles	A downward-sloping roof of 13° provides less wind disturbance and rain discomfort to spectators.
Van Hoof et al. (2011)	3D semi-open stadiums	CFD	An enclosed stadium with inclined roof minimises rain discomfort for spectators.
Goliger (2010)	3D open stadium with 2 opposite grandstands	Wind tunnel	Wind discomfort for players under prevailing wind direction and high wind intensity.
Szucs et al. (2007)	3D semi open stadiums	Wind tunnel	Development of wind comfort criteria for semi open stadiums. A 15° inclined roof reduces wind disturbance but increases heterogeneity. A 15° declined rood increases the overall wind speeds and the homogeneity.
Thompson et al. (1998)	Open stadium with windbreaks	Full scale experiments	40-50% porosity contributes to favourable wind environment at the stadium bowl.
Szucs et al. (2009a)	Semi open stadiums	Wind tunnel	Porosity on stadium is favourable for hot climates.
Szucs et al.	Semi open	Wind tunnel	0% porosity leads to increased ventilation

2 Literature Review

(2009b)	stadiums		zones on the upper spectator corners.
Biagini et al. (2007)	Manfredonia stadium/ grandstand roof components	Wind tunnel	A radial tensile structure on flat oculus configurations develops solely positive C_p values on the roof surface improving serviceability. A ventilation opening between roof and the upper spectator terraces provides local wind comfort for spectators.
Blocken and Persoon (2009)	Amsterdam Arena	CFD/ full scale experiments	Crucial parameters on ventilation: wind direction, urban surroundings, integrated ventilation openings. Validation error up to 50%.

The methods that have been used to develop optimum building design features that may promote the indoor conditions were also discussed. By combining statistical methods and CFD tools, favourable design solutions may be generated with substantial reductions in computational cost and effort. However, even if the optimisation algorithms are not well known and widely used in building studies, it is an important asset for the scientific community.

3 Wind Tunnel Experimentation

3.1 Introduction

Wind tunnels have attracted great interest due to their ability to study full or reduced scale phenomena, taking into account a wide number of parameters. In the current chapter a brief description of the wind tunnels is given, followed by the similarity criteria that must be met when performing wind tunnel experiments. The main characteristics of the ABL wind tunnel facilities used to simulate urban phenomena are presented according to literature. The ABL wind tunnel facility of the University of Nottingham, where the stadium validation study was conducted, is introduced, along with the experimental equipment used. Finally, the velocity profile results on the empty wind tunnel facility and the wind pressures on the stadium surfaces are interpreted, along with the considered limitations.

3.2 Wind tunnel classification

Wind tunnels are classified based on speed and geometry regimes. In accordance with the first regime and the maximum achievable speed, the wind tunnels are divided in subsonic and supersonic. The Mach number (M) is used as the classification measure, defined as the ratio of the air speed to the speed of sound. Subsonic wind tunnels develop velocity speeds less than the speed of sound, $M < 1$, and supersonic equal or greater, $M \geq 1$ (Libii, 2011). For studies of the built environment, where the developed speeds are substantially smaller than the speed of sound, subsonic low-speed wind tunnel facilities are used. Based on the geometry regime, wind tunnels are classified to open and closed return, shortly described below:

Open return: describes a wind tunnel facility without air recirculation. The fan used to provide the adequate velocity speeds, results to increased energy demands and important difficulties to maintain a constant flow mass rate at the test section inlet. On the other hand, it occupies less space, allowing the easy performance of flow visualisation studies.

Closed return: describes a wind tunnel that recirculates the air in the facility, moderating the energy consumption requirements and enabling the easy control of the flow conditions. However, several difficulties are posed, mainly relevant to the

3 Wind Tunnel Experimentation

provision of flow homogeneity in the test section, parallel to its axis and the minimisation of the roughness effects induced by the boundary walls.

More details on the advantages and disadvantages of each facility may be found in Barlow et al. (1999). Generally, the selection of the wind tunnel facility is primarily dependent on the purpose of the study, followed by the available fund and the provision of the adequate experimental equipment.

3.3 Wind tunnel similarity criteria

Wind tunnel studies that can accurately simulate real life flow phenomena, presuppose the achievement of geometrical, kinematic, dynamic, and thermal similarities (Chaudhry and Cermak, 1971; Avissar et al., 1990). The term geometric similarity implies that all the dimensional characteristics of the modelled and the real design should be of constant ratio. Kinematic similarity requires same length and time scales for the scaled model and the prototype and it necessitates geometric similarity. Dynamic similarity is the most difficult to achieve, as the forces applied to the experimental model and the prototype need to have a constant scale factor. Finally, thermal similarity implies that the buoyancy force should be equal or in a constant scale factor between the model and the prototype. The conduction of wind tunnel experiments presupposes additional consideration of the forces that characterise the flow phenomena; the inertia, the viscous, the gravity and the elasticity forces, as they are described below:

Inertia force: is the force created due to fluid movement, expressed in the left part of the Navier-Stokes equation (Equation 4.5). The air is strongly affected by the bodies/obstacles, resulting to fluid acceleration. Mathematically, it can be expressed by Equation 3.1:

$$\text{Inertia Force} = \frac{\rho l^3 U}{t} = \rho l^2 U^2 \quad (3.1)$$

where ρ is the fluid density, l is the characteristic length of the body, U the velocity of the body and t the time.

Viscous force: is the frictional shear force created by the interaction of the fluid and the moving boundaries, described by Equation 3.2:

3 Wind Tunnel Experimentation

$$\text{Viscous Force} = \mu l U \quad (3.2)$$

where μ is the fluid viscosity, further described in Equation 4.14.

Gravity force: is the force due to gravity of the fluid, expressed by Equation 3.3:

$$\text{Gravity Force} = \rho l^3 g \quad (3.3)$$

where g is the fluid acceleration of gravity.

Elasticity force: is the body force that enables the body to retain its original shape after stress exertion, described by Equation 3.4:

$$\text{Elasticity Force} = P l^2 = \rho \alpha^2 l^2 \quad (3.4)$$

where P is the pressure applied to the fluid body and α the speed of sound ($\sim \frac{P}{\rho}$).

The dimensionless parameters that arise from the ratio of these forces are detrimental for the flow phenomena and the achievement of dynamic and kinematic similarity. More specifically:

$$\text{Reynolds number} = \frac{\text{inertia force}}{\text{viscous force}} = \frac{\rho l U}{\mu} \quad (3.5)$$

$$\text{Mach number} = \frac{\text{inertia force}}{\text{elasticity force}} = \frac{U}{\alpha} \quad (3.6)$$

$$\text{Froude number} = \sqrt{\frac{\text{inertia force}}{\text{gravity force}}} = \sqrt{\frac{U^2}{gl}} \quad (3.7)$$

In wind tunnel studies these dimensionless numbers need to be equal or of a constant scale factor for the model and the prototype. In low-speed wind tunnels with static models, as is the case of this work, the Froude number can be neglected as it is important in cases with body motion. The Mach number is not critical in subsonic studies ($M \ll 1$), since the compressibility effects can be neglected and the density can be considered constant. The Reynolds number is the most important scaling parameter that needs to be considered in low speed wind tunnel studies of static models (Houghton and Carruthers, 1976).

3.4 ABL wind tunnels

ABL wind tunnels deem to represent full scale atmospheric flow phenomena. As mentioned in Section 2.2.1, the atmospheric boundary layer is separated in layers

3 Wind Tunnel Experimentation

and sublayers, which are interrelated and interact with one another. Thus, when performing ABL wind tunnel studies great attention should be given to the scaled quantities that determine the accuracy of the experiment, including the mean velocity profiles, the Reynolds stresses, the aerodynamic roughness length, the turbulence intensity distributions, the power spectral density behaviour and the integral length scale distribution (Hohman et al., 2015).

By definition, the wind tunnels are an approximation of the real occurring physical phenomena, because 1) flows above 100 m are highly affected by the Coriolis acceleration, which may not be simulated and 2) thermal effects that occur simultaneously with the vertical wind shear, can only be reproduced in specifically designed facilities, otherwise it is assumed that the generated turbulence is attributable to mechanical turbulence only (Garratt, 1994). Along these lines, since the lower levels (< 100 m) of the atmosphere are more interrelated to the surface characteristics, they can be more accurately simulated as compared to the upper surface layers (Avisar et al., 1990). According to McVehil et al. (1967), any atmospheric flow that is homogeneous, aerodynamically rough and does not have any pressure gradients may be modelled with high precision.

In practice, matching Reynolds number is quite challenging (if not impossible). In applications involving turbulence effects, the dynamic similarity achievement might require dramatic increase in the velocity values. Let us consider for instance a typical ABL turbulent flow with $Re = 10^6$ and reference wind speed of 7 m/s at reference height of 15 m. The simulation of the flow in an ABL wind tunnel facility of 1:300 scale, with constant Reynolds number, would require an increase of the velocity speed by 300 times, in order to achieve dynamic similarity. According to Equation 3.5, the velocity should be increased by 300 times and be equal to 2,800 m/s. Such high velocities are not possible to be developed in subsonic facilities, and thus, it is important to determine the dominant parameters for the specific case study.

In ABL wind tunnels, in order to attain dynamic similarity, it is advisable to artificially create turbulence effects and eddies. This is achieved by the integration of vortex generators, in the form of fences and spires, at the inlet of the wind tunnel test section and by the placement of ground surface roughness, in the form of element blocks, representing the relevant terrain type. It is also recommended to have models

3 Wind Tunnel Experimentation

with rough/ sharp edges, to allow for separation zones and creation of further turbulence, matching the prototype's aerodynamic performance (Sachs, 1978).

However, a minimum critical Reynolds number is required to minimise local viscous effects. The critical number is highly dependent on the geometry of the model, and thus, different formulas have been reported in the literature, regarding different flow parameters; the height of the relevant building model (H), the velocity speed (U), the friction velocity (u^*), the height of the roughness elements (h), the aerodynamic roughness (z_0) and the kinematic viscosity (ν):

Kozmar (2009)	$Re_{z_0} = \frac{u^* z_0}{\nu} > 5$	(3.8)
---------------	--------------------------------------	-------

Banta and Blumen (1990)	$Re > 10^4 - 10^6$	(3.9)
-------------------------	--------------------	-------

Meroney (1980)	$Re = \frac{U H}{\nu} > 10,000$	(3.10)
----------------	---------------------------------	--------

Snyder (1972)	$Re_{z_0} = \frac{u^* z_0}{\nu} \geq 2.5$	(3.11)
---------------	---	--------

Castro and Robbins (1977); Snyder (1972)	$Re_{building} = \frac{U H}{\nu} \geq 4,000$	(3.12)
---	--	--------

Wind tunnel studies in fully developed boundary layer flows have reported different critical building Reynolds numbers varying between 2,100 and 7,500 (Uehara et al., 2003). According to Mochida et al. (1994), the critical Reynolds number value is dependent on the purpose of the experimental study, concluding to a $Re_{critical}$ value at building height equal to 7,500 for accurate prediction of the dispersion on the model rooftop and 2,500 for the prediction of the recirculation zone on the rear side of the model. A Reynolds number value $Re > 12,000$ for ABL wind tunnel studies at every measuring point is considered acceptable (Niemann, 1993). For tall buildings (Blocken et al., 2008) and stadium design models (van Hooff and Blocken, 2012), studied in ABL wind tunnels, the building Reynolds number and the ventilation openings Reynolds number had been reported larger than the critical value of 11,000 set by Snyder (1981).

Another common observation in ABL wind tunnel is the continuous changes of the vertical profiles of mean velocity and turbulence intensity downstream the test section. This occurs due to the spatial limitation of the top boundary that prevents fully diffusion of turbulence energy to occur (McVehil et al., 1967).

3 Wind Tunnel Experimentation

3.4.1 Roughness elements for ABL simulation

The development of a homogeneous ABL flow presupposes the artificial replication of the actual occurring conditions, including the aerodynamic roughness characteristics, the turbulence effects and the mean velocity profiles. The importance of simulating ABL flows of high accuracy led researchers to study the optimum conditions, under which the wind tunnel shows best performance, satisfying all requirements (De Paepe et al., 2016; Blackman et al., 2015; Teclé et al., 2013; Kozmar, 2009; Wang et al., 1996).

For the generation of the turbulence effects at the wind tunnel inlet fences and spires are used. Further information for the design and positioning of the turbulence generators are given by Counihan (1969), Irwin (1981) and Hohman et al. (2015). For the simulation of the ground surface and the relevant aerodynamic roughness, block elements are used, with dimensional characteristics that correspond to the full scale ground surface characteristics.

3.5 The ABL wind tunnel facility of the University of Nottingham

Wind tunnel experimentation was conducted for the validation of the CFD study in the ABL wind tunnel facility of the University of Nottingham. In this section the wind tunnel facility is described along with the performed flow characterisation study. The equipment used for monitoring the velocity and the pressure distributions is also presented, along with the calibration and the data acquisition system. Finally, the experimental set up for the stadium case study is analysed together with the imposed limitations.

3.5.1 Description of the facility

The University of Nottingham is equipped with an open circuit low-speed wind tunnel, the holistic illustration of which is given in Figure 3-1. The wind tunnel has a 14.0 m long test section with a cross-sectional area of 2.4 m width and height which is 1.80 m after the contraction part and extends up to 1.90 m after the turntable. A slight increase in the height of the test section ensures zero pressure gradient in the longitudinal direction (see also 0, Sheet A-1 for the detailed dimensional design). The wind tunnel is incorporated with a turntable of 2.0 m diameter, located 12.5 m from the beginning of the test section that allows multidirectional wind studies.

3 Wind Tunnel Experimentation

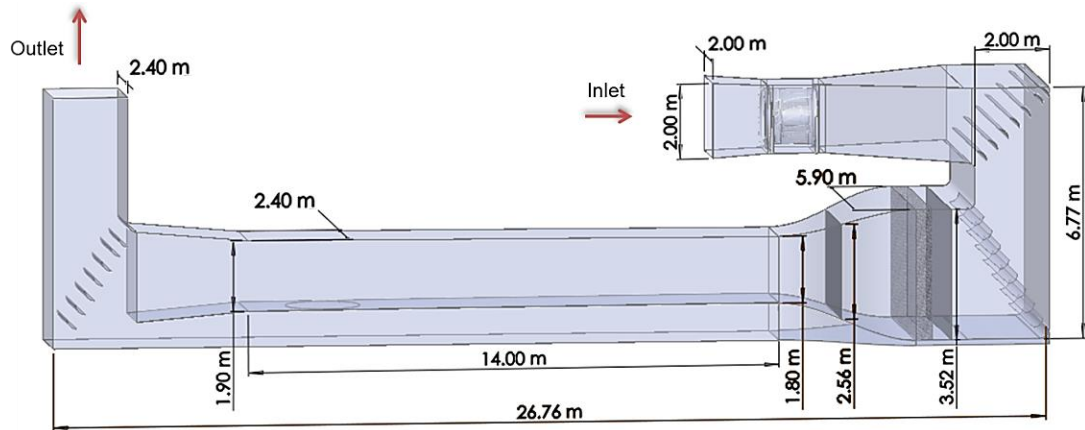


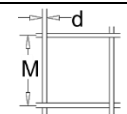
Figure 3-1 Illustration of the total ABL wind tunnel facility.

The wind tunnel is equipped with an axial fan that enables the generation of velocity speeds up to 11 m/s when empty. The flow homogeneity is achieved by the installation of a series of equidistant blades (0.45 m), at the upper and lower contraction corners and at the end corner of the diffuser. In addition to this, the wind tunnel is integrated with a 0.45 m thick honeycomb and a series of fibremesh screens that operate as flow straighteners and at the same time prevent the entrance of large particles in the test section. Their characteristics are presented in Table 3.1.

Table 3.1 Design characteristics of the screens and the honeycomb used in the ABL wind tunnel of Nottingham.

Description	Distance from test section inlet [m]	d^1 [mm]	M^2 [mm]	β^3	K_0^4	Re_d^5	f^6
Screen 1	1.605	1.5	2.8	0.675	1.655	165	0.55
Screen 2	4.554	1.5	2.8	0.675	1.655	165	0.55
Honey-comb	3.505	-	-	0.95	-	-	-

where ¹ is the wire diameter, ² the mesh width, ³ the porosity, ⁴ the local pressure coefficient, ⁵ the wire diameter Reynolds number and ⁶ is the function $f(Re_d)$ (Laws and Livesey, 1978)



3.5.1.1 Simulation of the suburban boundary layer

The Nottingham wind tunnel facility aimed at the generation of a suburban terrain, at a scale of 1:400, which results to a power law exponent (α) equal to 0.28 and a target boundary layer depth (δ) equal to 400 m in full scale or 1 m in wind tunnel scale (Simiu and Scanlan, 1996). The turbulence suburban terrain characteristics were developed by the integration of a series of vortex generators and surface roughness elements, in the form of a fence, spires and roughness blocks. Their design was performed according to the guidelines of Irwin (1981) and Simiu and Scanlan (1996)

3 Wind Tunnel Experimentation

for a suburban environment. Full dimensional designs are given in 0, Sheet A-2, A-3 and A-4, for the fence, the spires and the roughness blocks respectively.

The arrangement of the components on the wind tunnel test section is presented in Figure 3-2. The fence, which covers almost the whole width of the wind tunnel section, is placed first with a gap of 0.05 m from the side walls. The spires are in line with the fence and positioned 0.34 m from the inlet. They are placed equidistant from the walls (0.05 m) and between each other (0.20 m). The roughness blocks are placed 0.80 m after the row of spires. In total 8 baseboards are placed of total length 9.76 m, which is greater than the recommended value of $6h$ (where h is the spire height) that allows for the development of the desired mean wind profile (Simiu and Scanlan, 1996).

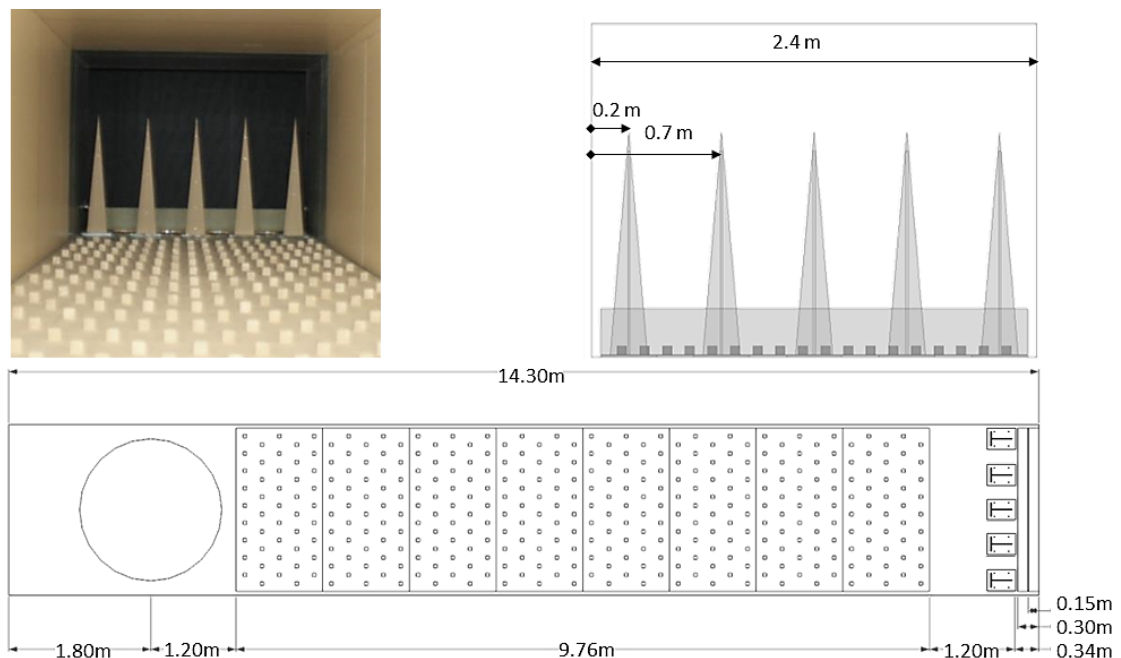


Figure 3-2 The boundary layer simulation arrangement for the wind tunnel facility.

3.5.2 Description of the equipment

Velocity and pressure measurements are the most important on experimental studies of fluid flow phenomena. The current methods used for wind speed measurements are classified in: 1) pressure-based methods, 2) anemometer methods and 3) flow visualisation methods (Ristić et al., 2004). In pressure-based methods, the velocity measurements are obtained by acquiring static pressure data with the use of pressure probes. The anemometer methods give the opportunity to acquire instantly velocity vector values with the use of hot wire anemometers, Laser Doppler velocimetry (LDV), particle image velocimetry (PIV) and acoustic Doppler velocimetry (ADV).

3 Wind Tunnel Experimentation

Finally, in the flow visualisation methods, free-stream smoke and surface oil flow equipment are employed to illustrate the velocity distribution. In the current experiments, pressure-based and anemometer methods were employed, with the equipment to be presented thereafter.

The Pitot-static tube is the most common device to measure static and total pressure in wind tunnels. The pressure difference between the total and static pressure, according to Bernoulli's equation (3.13), is equal to $\frac{1}{2}\rho V^2$ and it is known as dynamic pressure.

$$\Delta P = P_{total} - P_{static} = \frac{1}{2}\rho U^2 \quad (3.13)$$

The static pressure (P_{static}) is a constant value determined by the flow outside the boundary layer. The velocity of the flow varies from zero at the walls to a maximum free-stream value, undisturbed from the walls. The dynamic pressure is used for the calculation of the velocity values, regarding the local fluid density properties. For the current experiment a Standard Pitot-static tube was used and was positioned in alignment with the airflow, as illustrated in Figure 3-3. Alternatively, a series of pitot tubes could be used to determine the flow angularity at a given location on a wind tunnel model.

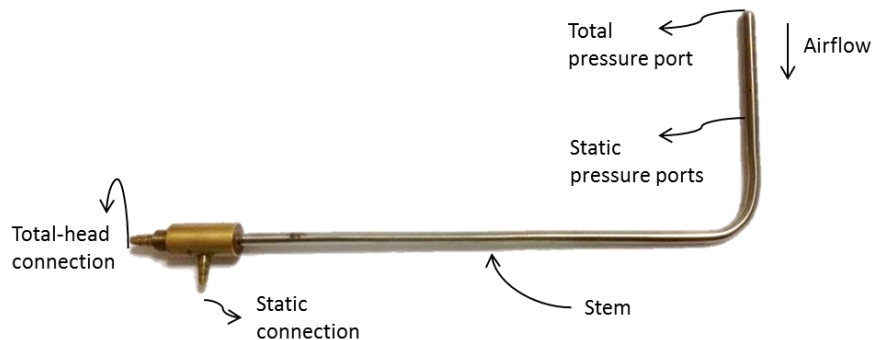


Figure 3-3 Standard Pitot-static tube used for the wind tunnel experiment.

The hot wire probe is a diagnostic instrument that includes a thin wire integrated in a prong. The prong is aligned with the flow direction. Electricity is used for the wire to generate heat, which is subsequently carried away by the air flow. The heat transfer is proportional to the velocity of the flow. Errors may arise from the fact that the probe alters slightly the impinging flow speed and direction. For the current experiment a Dantec single-wire probe was used, as shown in Figure 3-4.

3 Wind Tunnel Experimentation

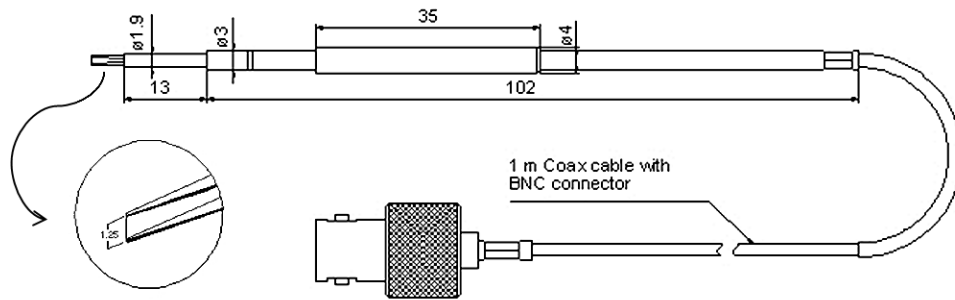


Figure 3-4 Single wire probe with BNC connector used for the wind tunnel experiment (Dantecdynamics.com, 2017).

The thermocouple probe is a sensor used for flow temperature measurements. It consists of two different metal wires, which are connected on the one end to a data generation device compatible with the sensor and on the other end they are joined together with a thermocouple thermometer. The operating principle of the thermocouple module is based on the voltage production due to change of the temperature on the junction of the two metal wires that can be translated into temperature.

For pressure measurements, pressure scanning modules are employed, which monitor the static pressure in different locations of the model's surface. The modules are commonly consisted of several pressure ports that enable the parallel measuring of pressure in multiple locations. The operating principle is on monitoring the mean difference between the absolute pressure at a point and the ambient atmospheric pressure obtained from the reference point. For the current experiment, a DSA 3217/16 Px scanner was used, which is equipped with 16 transducers, all manifold to a single reference port.

3.5.2.1 Hot wire probe calibration:

Prior the conduction of the experiment, the calibration of the Dantec single-wire probe was performed for a range of wind speeds up to 16 m/s. For the calibration, a system of a velocity calibrator with a low pressure microprocessor micromanometer (see Figure 3-5a) was used, with accuracy of \pm one digit below 10 %. The micromanometer was connected to the air velocity calibrator (see Figure 3-5b), where the hot wire was calibrated against different velocity values. In Figure 3-5b the hot wire is placed in line to the nozzle outlet (horizontal position) to match one direction of the flow measurements.

3 Wind Tunnel Experimentation

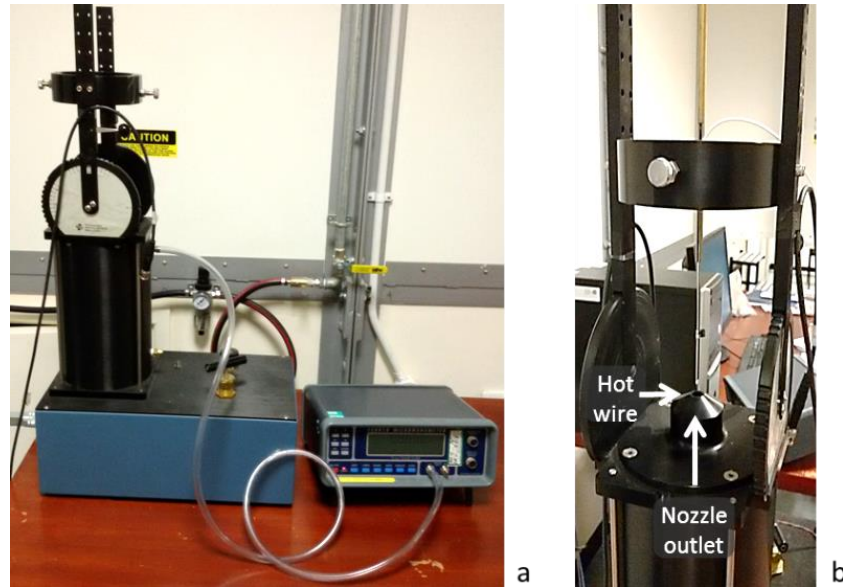


Figure 3-5 Air velocity calibrator and micromanometer (a) and hot wire calibration setup (b).

The calibration system was connected to the TSI IFA-300 system that allows monitoring the flow temperature via a T-thermocouple module. The obtained results were analysed using a MATLAB code, and the King's law (3.14) was applied for the best curve fitting.

$$E^2 = a + b * U^c \quad (3.14)$$

where E is the voltage registered at the anemometer output, U is the velocity and a , b and c are constants parameters determined by the fitting curve.

In total, the hot wire was calibrated against the perpendicular and the horizontal position to comply with the experimental locations of velocity measurements, close and far from the stadium model (see also Appendix 0). The calibration system is illustrated in Figure 3-6.

3 Wind Tunnel Experimentation

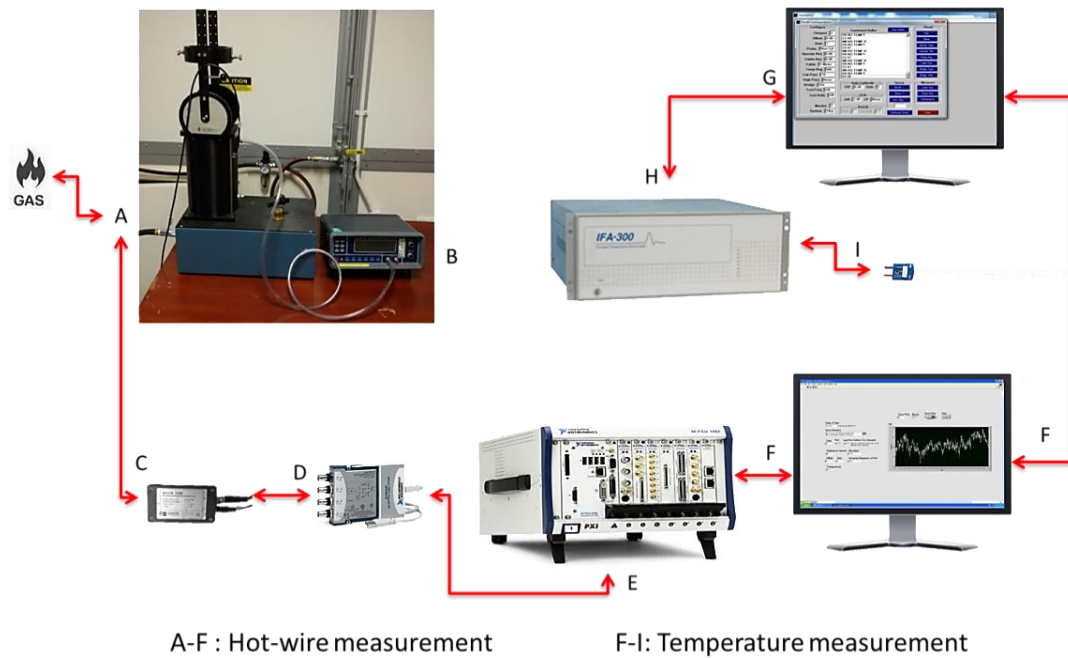


Figure 3-6 The calibration system employed for the wind tunnel study.

3.5.2.2 Data acquisition system:

The collection of data was performed with a similar to the calibration system, with main difference that both the single hot-wire probe and the T-thermocouple module were placed in the wind tunnel test section. The T-thermocouple was placed closed to wall, to prevent flow disturbance and parallel to the hot wire, to monitor the temperature fluctuations. The hot wire was adjusted to the desired position by the aid of a steel stand. The data were acquired with a TSI IFA-300 system and analysed with a MATLAB code, using the calibration constants obtained in the previous step. The total data acquisition system is illustrated in Figure 3-7. The full description of the technical characteristics of the experimental equipment used, in Table A-1.

3 Wind Tunnel Experimentation

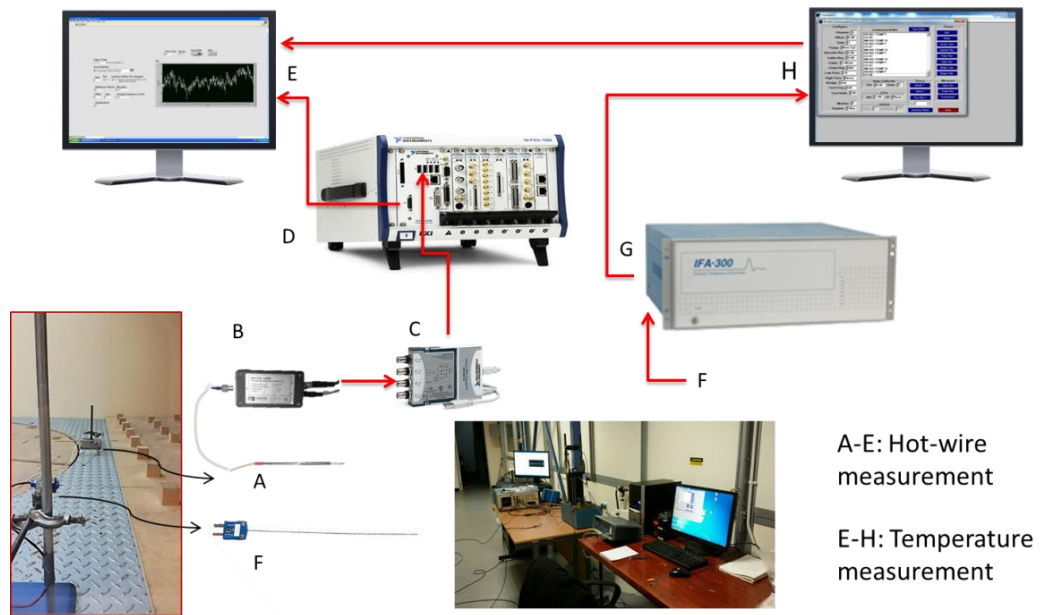


Figure 3-7 Data acquisition system at the wind tunnel facility of University of Nottingham.

3.6 Experimental set-up on empty domain

The wind tunnel facility was tested against its validity to represent the suburban ABL velocity profile. For the purpose of this, a series of hot wire anemometer measurements were carried out. A Dantec single-wire probe was used with 5 mm and 1.25 mm sensor active diameter and length respectively. The probe was calibrated in a TSI air velocity calibrator, integrated with a micro-manometer and a thermocouple probe, at velocities from 0.5 m/s to 16 m/s, as analysed in Section 3.5.2.1.

For the ABL flow characterisation, two measurement locations were selected. The first location (roughness-line) was set immediately after the end of the last row of roughness blocks, or 11.3 m from the inlet and 1.21 m from the side wall. The second location (turntable-line) was set in the centre of the turntable, or 12.55 m from the inlet, as shown in Figure 3-8. In addition, a thermocouple probe was installed as close as possible to the hot-wire probe to monitor the air temperature, which would be applied later to convert voltages to wind speeds using the King's Law.

3 Wind Tunnel Experimentation

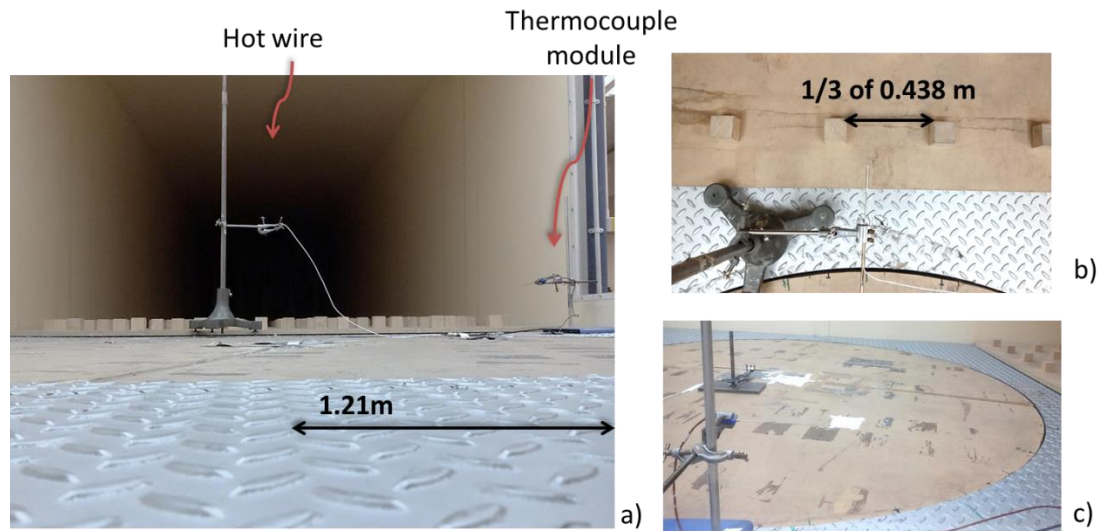


Figure 3-8 Illustration of the measurement locations for monitoring the velocity profile and the air temperature (a); roughness-line (a), (b); turntable-line (c).

In total, measurements were performed in 26 and 25 points for the roughness-line and the turntable-line respectively. Equidistant locations were selected with a gradually increased step with height, focusing on the near-wall boundary layer turbulence. The point locations are presented in Figure 3-9. At both measurement locations, 6 different fan frequencies were applied that resulted in wind speeds of 2 m/s (case 1), 4 m/s (case 2), 6 m/s (case 3), 8 m/s (case 4), 10 m/s (case 5) and 11 m/s (case 6), measured at the mid-height of the empty test section. The data acquisition included 5 iterations per wind speed, of 60 secs duration each, at a frequency of 2,000 Hz and 95 % confidence interval.

3 Wind Tunnel Experimentation



Figure 3-9 Illustration of location points for the velocity measurements in the roughness-line (left), along with the hot wire stands used per height case (right).

3.6.1 Experimental results

The data were acquired with a TSI IFA-300 system and analysed with a MATLAB code. Since a single hot-wire was used, results were generated for the mean velocity vectors only on the flow direction (U_u) and the relevant turbulence intensities, based on the following equations:

$$U_u = \frac{1}{n} \sum u \quad (3.15)$$

$$I = \frac{u'}{U_u} = \frac{\sqrt{\frac{1}{n} \sum (u - U_u)^2}}{U_u} \quad (3.16)$$

Figure 3-10 (top) shows the generated results of the velocity and turbulence intensity profiles measured at the roughness line at all wind speed cases. The results indicated lack of consistency on the lower levels of the profiles, caused by the developed recirculation zones on the rear side of the roughness blocks. The boundary layer height was estimated between 1.0 m and 1.2 m with a measuring variance of 1 %, for all wind cases.

Additional results were generated for the zero-plane displacement height. Figure 3-10 (bottom) presents a closer view of the lower heights of the velocity profiles for the roughness line. The zero-plane displacement occurs at a height of $d = 0.03$ m,

3 Wind Tunnel Experimentation

which complies with the literature that defines the displacement to occur at around the $2/3^{\text{rd}}$ of the roughness element height, equal to 0.033 m for the current experiment (Garratt, 1994).

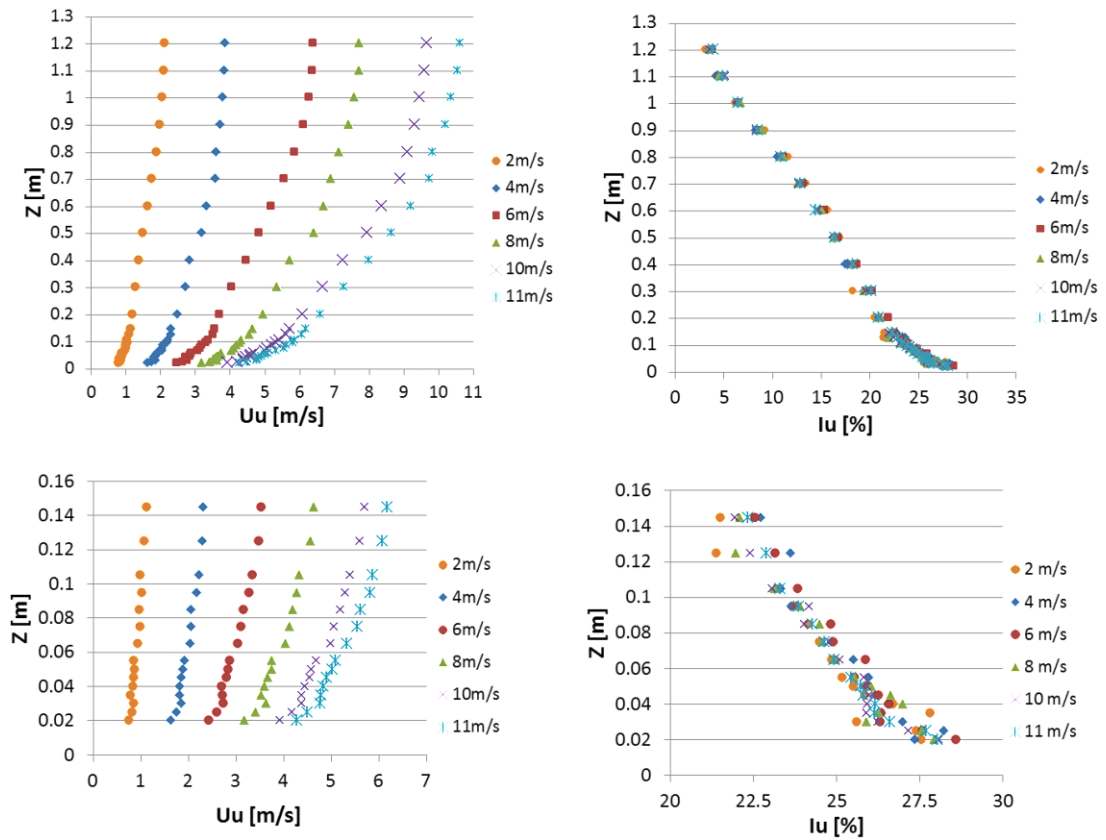


Figure 3-10 Vertical profiles for velocity and turbulent intensity at full height (top) and at the lower height levels (bottom), generated at the roughness-line.

The plots in Figure 3-11 show the velocity and turbulent intensity profiles measured at the turntable-line for the six wind speed cases. The exponential coefficient (α) was calculated using the data to fit a trend line for the power law regression. The results show good fit of the power law ($R^2 \cong 0.994$). The power exponential coefficient of 0.282 (± 0.003) corresponds to all the wind cases, which complies with the theoretical value, with an error of 0.7 %, achieving to simulate a suburban environment.

3 Wind Tunnel Experimentation

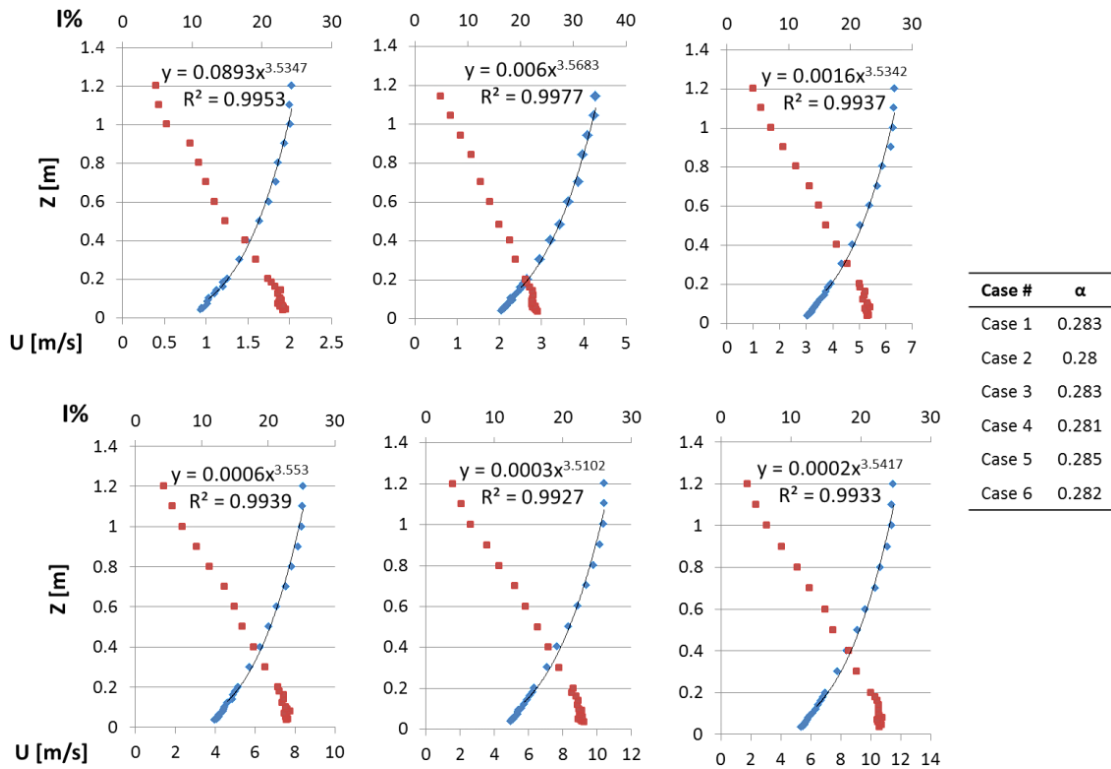


Figure 3-11 Vertical profiles of velocity (blue) and turbulence intensity (red) for the six wind case studies on the turntable-line.

Adding to the verification of the experiment, the generated data up to 0.2δ agree with the logarithmic law, as shown in Figure 3-12. Similar observations have been reported by Kozmar (2009) and Thuillier and Lappe (1964).

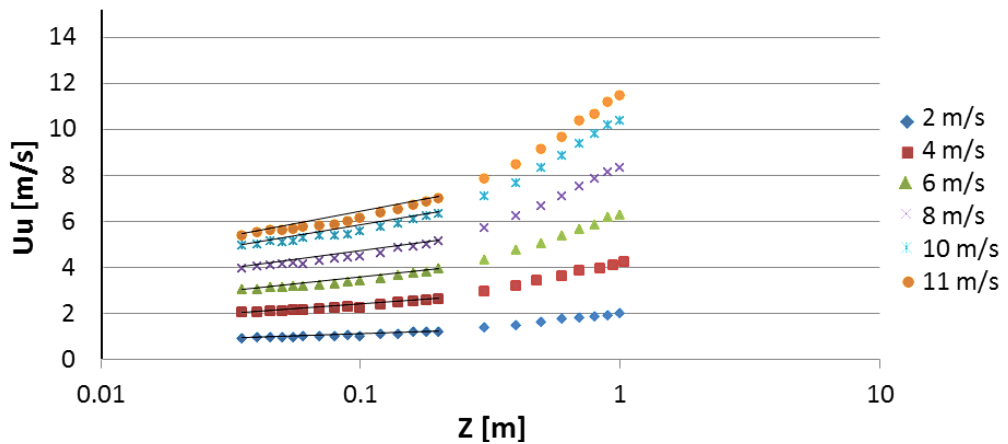


Figure 3-12 Fit comparison of average velocity data with the logarithmic law, up to $0.2 \delta (= 0.2 \text{ m})$.

3 Wind Tunnel Experimentation

3.7 Stadium design selection

The design of the construction was made upon the basic FIFA requirements discussed in Section 2.5. The sport facility aimed at a seating capacity of 80,000. The structure's external dimensions of Length x Width x Height are equal to 254 x 288 x 59 m³ respectively. As shown in Figure 3-13, the stadium can be separated in six operational layers (A-F):

- A. The roof, as the intermediate component connecting the urban and the stadium environment, was arbitrary but rationally designed. The oculus configuration, with an opening of 72 x 109 m² (L x W), allows the natural sunlight to penetrate, and at the same time provides full coverage to the tiers.
- B. The upper spectator terraces consist of 28 seating rows with 30° inclination able to accommodate 50,000 spectators. The entrances to the terraces are not included in the design.
- C. The intermediate level between the two terraces is a 3.5 m high space designed to accommodate the VIP rooms and some media rooms.
- D. The bottom spectator terraces consist of 26 seating rows with 24° inclination able to accommodate 30,000 spectators. Again, the entrances to the terraces are not included in the design.
- E. The ground level includes four entrances of 61 x 7 x 5.5 m³ (L x W x H), wide and high enough to accommodate large vehicles.
- F. The base was designed for constructional reasons, to match the scaled model for the wind tunnel experimentation. It is 4.5 m high and includes the auxiliary area of 88 x 125 m² (L x W), within the recommended values. The auxiliary area is also elevated by 2 m to provide full visibility of the four corners at all times from any terrace location.

Additional design characteristics include the integration of a 0.8 m safety barrier in front of the first seating rows for both upper and bottom spectator tiers and a 3 m extended barrier of 0.5 m thickness, located between the bottom tiers and the entrance doors, operating as a downwash deflector of the expected developed vortices.

3 Wind Tunnel Experimentation

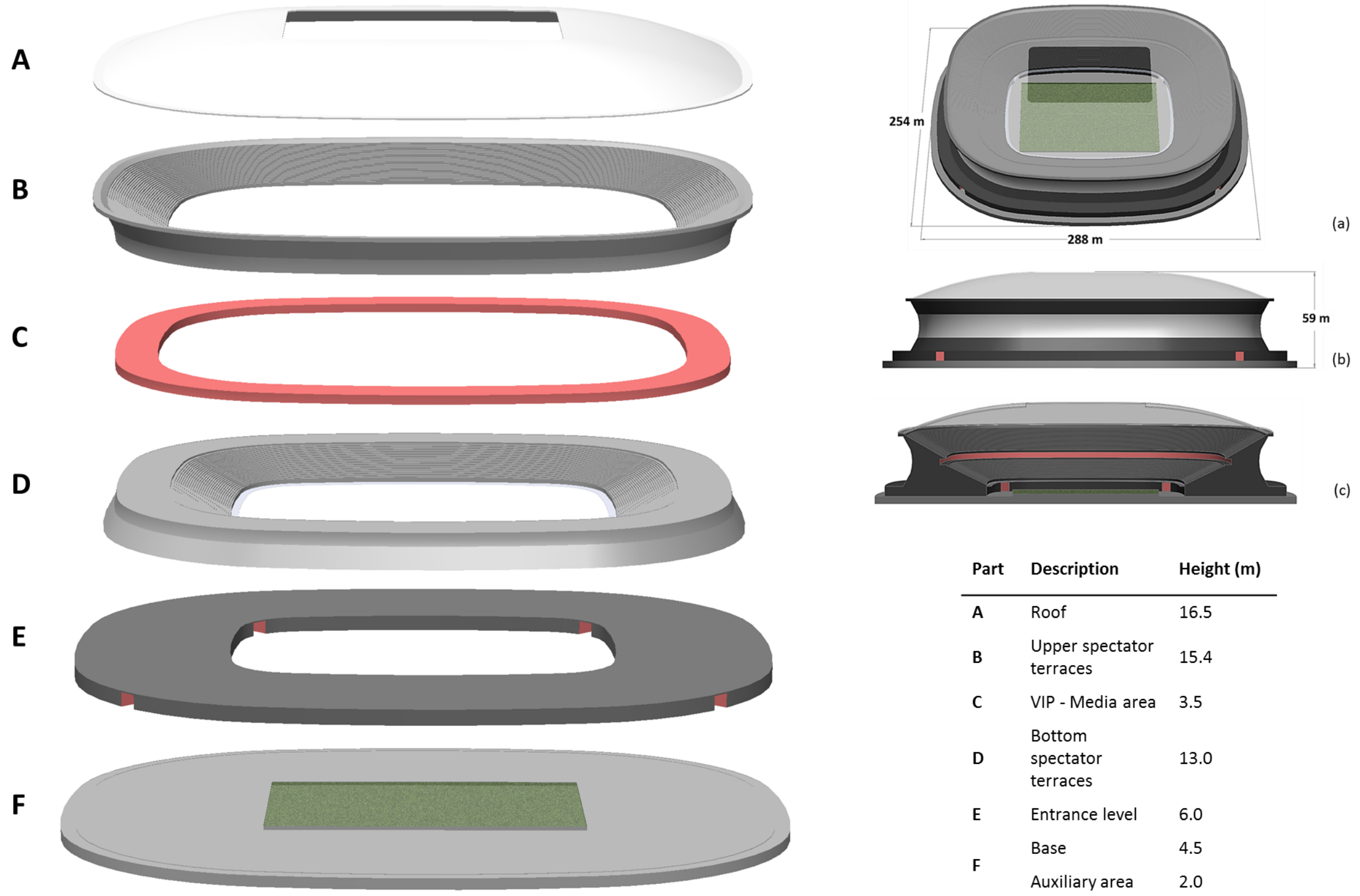


Figure 3-13 Description of the stadium areas (A-F); perspective (a), side (b) and cross-sectional view (c).

3 Wind Tunnel Experimentation

3.7.1 Design cases

According to the up-to-date research status on stadia, the simultaneous study of the plethora of parameters that affect the aerodynamic performance of the structure is difficult to perform. In the current study, two parameters were considered for evaluation; the first one takes into account the urban characteristics and the impinging wind direction and the second one the structural characteristics and the envelope porosity in the form of a horizontal ventilation opening of 3 m between the roof and the upper spectator tiers, extended along the whole perimeter of the stadium. Figure 3-14 illustrates the four stadium design cases, including the reference case with 0° wind angle and non-elevated roof configuration, the case of 90° wind angle and non-elevated roof configuration, the case of 0° wind angle and elevated roof configuration and the case of 90° wind angle and elevated roof configuration.

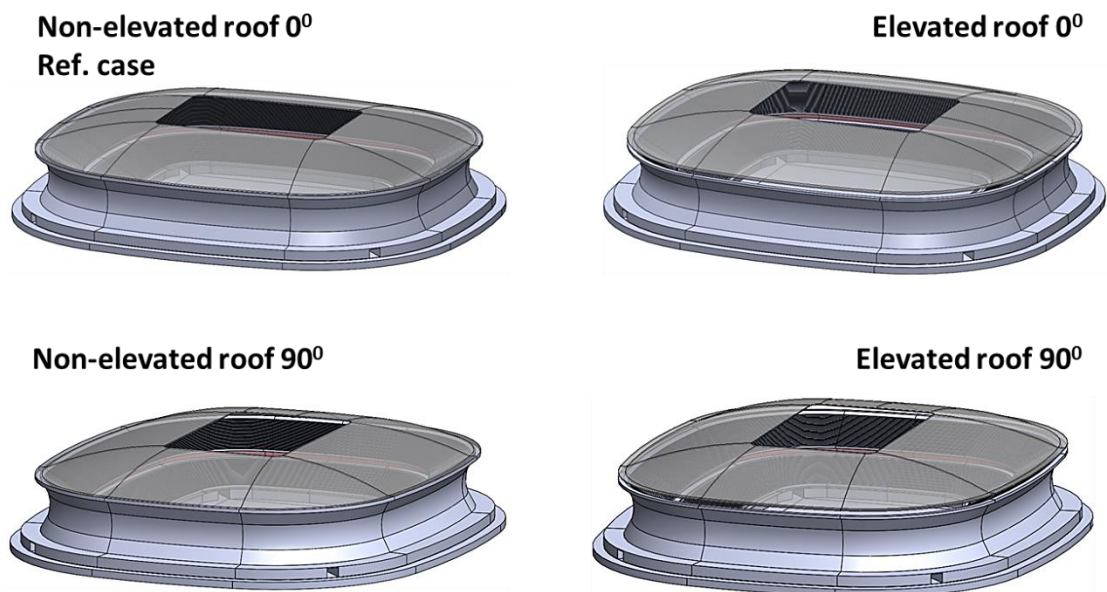


Figure 3-14 Illustration of the four stadium design cases; for non-elevated and elevated roof configuration and for 0 and 90 degrees impinging wind angle.

3.8 Experimental stadium model

For the wind tunnel experimental study, the stadium structure, as presented in Section 3.7, was constructed in 1:300 scale. The scale of the model was selected after considering two important factors: 1) a small blockage ratio, smaller than the recommended of 5 % (Kozmar, 2009; Holmes, 2001), to prevent the model flow

3 Wind Tunnel Experimentation

interactions with the test section walls and 2) the adequacy of the roof elevation height and the side openings to allow the air intrusion at the stadium bowl.

Figure 3-15 illustrates the scaled stadium model with geometrical dimensions equal to $0.85 \times 0.96 \times 0.20 \text{ m}^3$ (L x W x H) and the full dimensional details to be presented in Appendix 0. The stadium base was constructed by wood and the plastic roof was 3D printed in high accuracy. The spectator seats were replaced by a straight surface and the safety barriers in front of the first row of each terrace were excluded from the model, due to manufacturing restrictions.

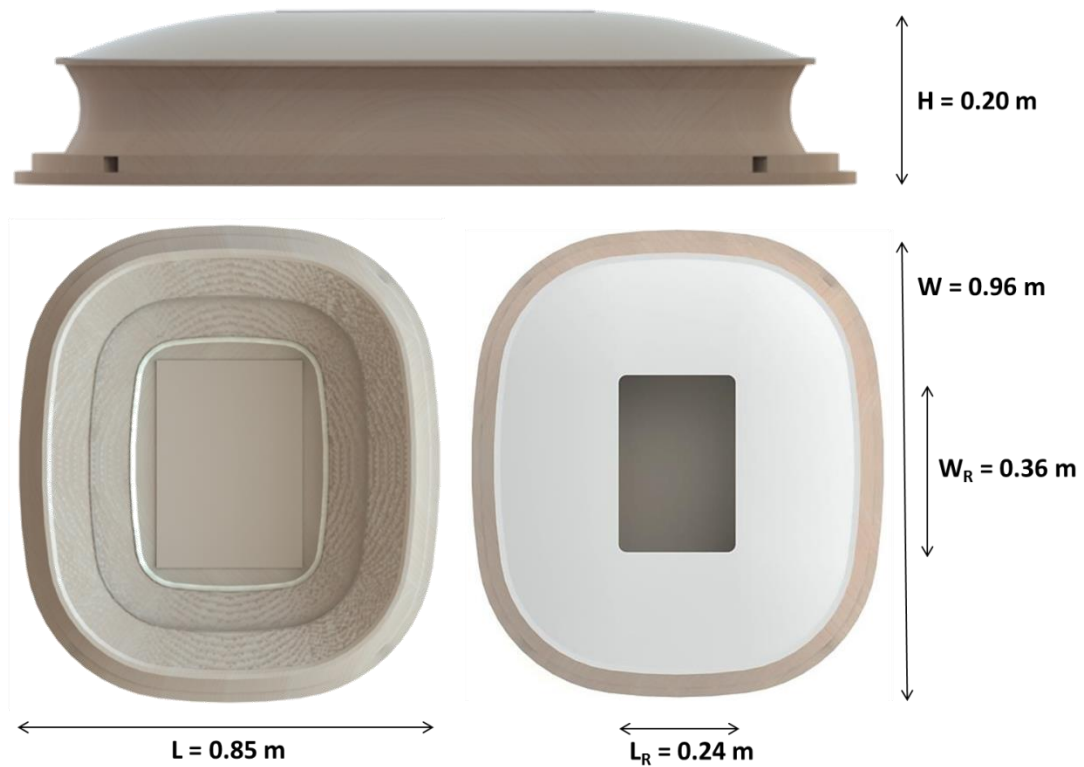


Figure 3-15 Side and top view of the stadium model constructed for the wind tunnel experiments.

The stadium model was positioned at the centre of the turntable, as shown in Figure 3-16, resulting to a blockage ratio of 3.4 % and 2.9 % for the case of 0° and 90° wind direction, complying with the recommended value of 5 %.

3 Wind Tunnel Experimentation

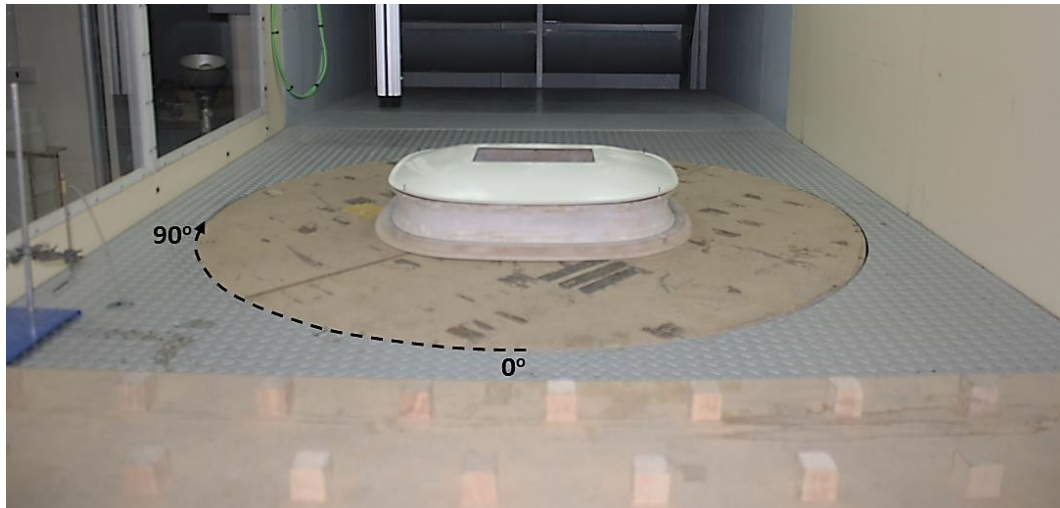


Figure 3-16 Stadium position at the turntable for the case study of 0° wind angle with elevated roof configuration.

3.8.1 Pressure measurements

All four cases described in Section 3.7.1 were studied against the pressure distributions, using the pressure transducer device presented in Section 3.5.2. The measurement point positions were decided after considering: 1) the important design parameters that define the aerodynamic performance of the stadium structure, 2) the occupied areas at the stadium bowl for the wind comfort assessment study, 3) the capacity of the pressure transducer to take simultaneous measurements, 4) the structural limitations of the test section and 5) the time limitations to carry out the experiment.

The first set of experiments was performed for the study of the pressure distributions on the stadium roof. The roof is considered by the author the most important structural component, since it is the intermediate geometry between the urban and the stadium interior environment. In total 16 points were selected that allow simultaneous acquisition of data via all the available ports of the transducer. The measurement locations were separated in two rows of 8 on the periphery of the oculus, with centre distances from the roof opening edges equal to 0.01 m and 0.0715 m for each row respectively. A schematic representation of the pressure taps' locations is given in Figure 3-17 (see also Appendix 0, Sheet B-3).

3 Wind Tunnel Experimentation

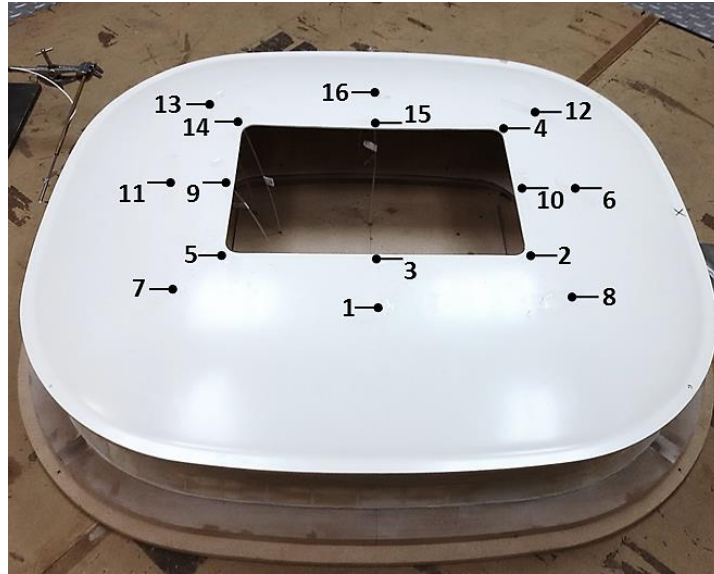


Figure 3-17 Location of pressure taps on the stadium roof.

The second set of experiments included the study of the pressure distributions on the spectator terraces. Due to the small number of pressure ports, it was decided to study the pressure values on one quadrant of the stadium. Assuming flow symmetry, only two measurement sets were performed for each case study (8 in total), generating data for the front and back spectator tiers, after rotating the model through an angle of 180° . The location of the pressure taps was made bearing in mind the important stadium areas in wind comfort studies, but also the structural restrictions that will prevent bending or damage of the pressure taps. As shown in Figure 3-18, 7 ports (1-7) were created at the upper tiers, with main focus on the higher rows of the terraces (1, 3, 5 and 7) and 9 ports (9-16) on the bottom terraces (see also Appendix 0, Sheet B-2).

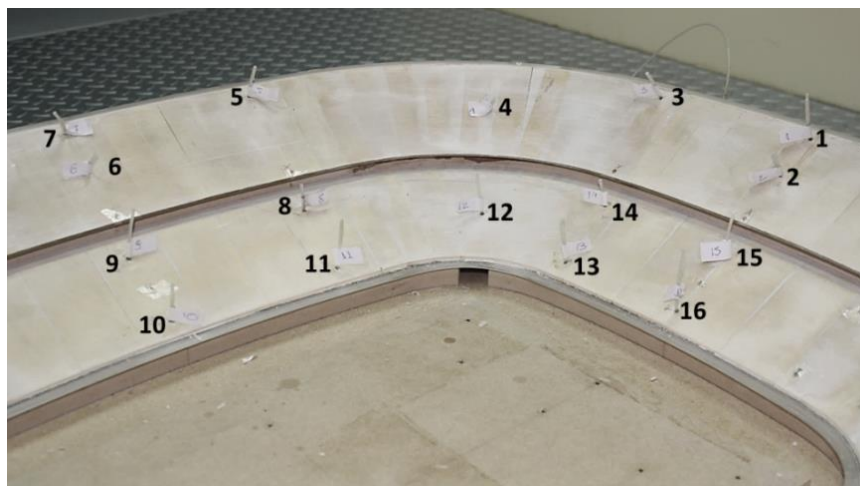


Figure 3-18 Location of pressure taps at the quadrant of the stadium terraces.

3 Wind Tunnel Experimentation

Finally, the third set of experiments deemed to generate pressure data at the auxiliary area, to assess the developed wind microenvironment around the players. As illustrated in Figure 3-19, 14 pressure sensors were used, symmetrically distributed on the surface of the auxiliary area (see also Appendix 0, Sheet B-2). Particular focus was given on the corners of the auxiliary area that are subject to intense airflow streams from the side entrances (Goliger, 2010).

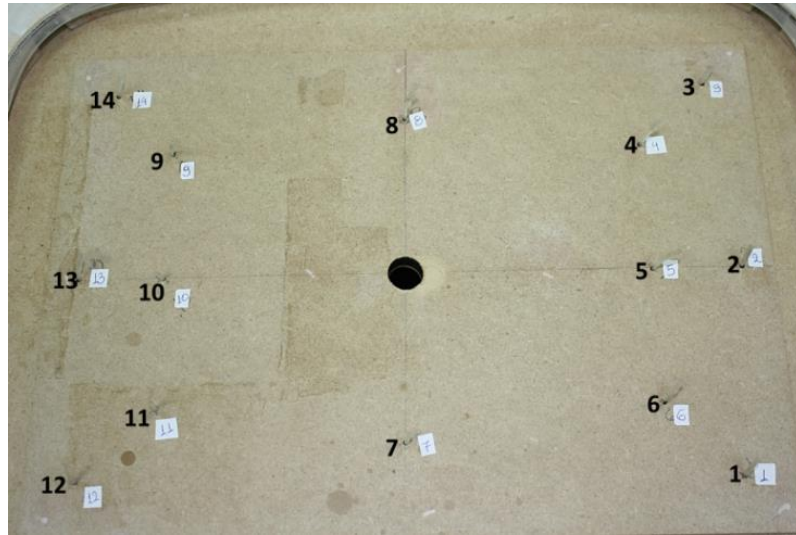


Figure 3-19 Location of pressure taps at the auxiliary area.

Results of local static pressure, P_S^i , were generated for each measurement point i at the stadium model. The pressure values obtained from the pressure transducer, P_S^{Tran} , included automatic subtraction of the static Pitot tube pressure, P_S^{Ref} , from the static pressure P_S^i , as illustrated in Figure 3-20. For each experimental set, 60 measurements were performed per point, in 4.8 seconds interval with a sampling period of 5,000 microseconds and a scan rate of 500 Hz. The final average wind pressure value at each point was determined arithmetically by averaging the pressure data obtained from the transducer. In total four inlet wind speeds were assessed, 6 m/s, 8 m/s, 10 m/s, and 11 m/s, since they produce more realistic velocity speed results at the stadium roof height that could be compared with full scale results.

3 Wind Tunnel Experimentation

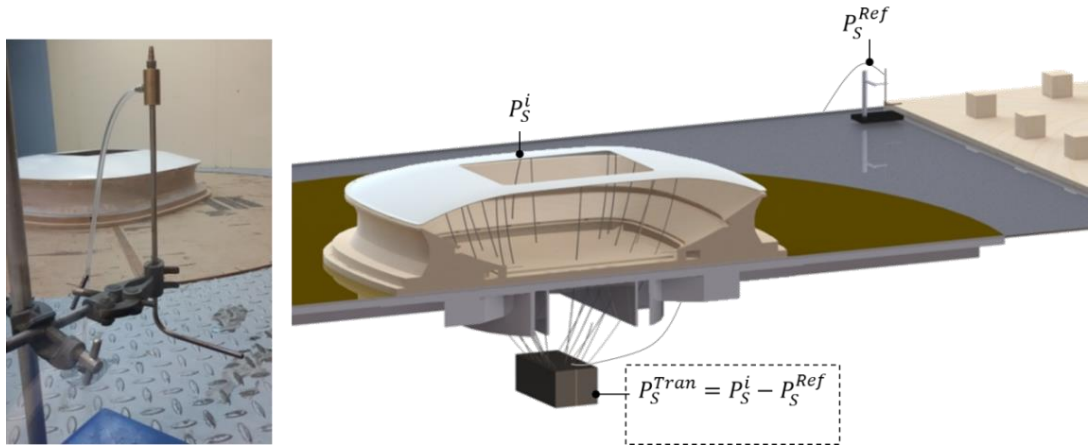


Figure 3-20 Schematic representation of the static pressure acquisition data.

3.8.2 Experimental results

Due to the large amount of generated data, only the wind pressure results for the case of 8 m/s inlet velocity will be presented for the four stadium configurations. The rest of the results are given in Appendix 0. To enable the interpretation process, the results were divided into wind direction and were compared with the reference case of 0° wind angle and non-elevated roof configuration. The calculation of the pressure coefficients was based on Equation 2.4. As mean reference velocity was used the one measured at the stadium roof height. For the case of $U_{inlet} = 8$ m/s, the reference velocity, $U_{ref} = 4.65$ m/s was used, which was the experimental value acquired at $H = 0.145$ m, the closest to the roof height (0.148 m).

3.8.2.1 Non-elevated roof at 0° wind angle (Ref. case)

Figure 3-21 illustrates the results generated for the reference stadium case study and the pressure coefficients generated on the roof surface. According to the results negative pressure values were obtained for all measurement points. The values were within the interval $[-1.20, -0.75]$, with an average value of 0.92 and a standard deviation of 0.13. The highest negative value was observed at the Point 15 (-1.20), located at the centre of the rear side of the oculus configuration. With only exception the Point 1, located at the front side of the roof structure, the measurement points at the rear side of the oculus (Points 4, 12, 13, 14, 15 and 16) generated higher negative pressure coefficient values, indicators of higher suction.

3 Wind Tunnel Experimentation

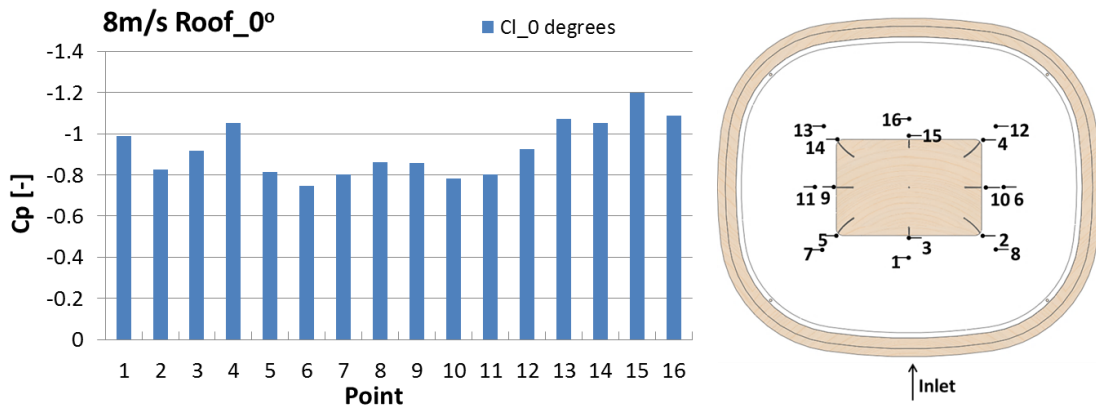


Figure 3-21 C_p results on the roof surface for the reference stadium case of 0° wind angle and non-elevated (Cl) roof configuration; $U_{ref} = 4.65$ m/s.

The results of pressure coefficients on the windward (back) and leeward (front) surfaces of the spectator terraces are presented in Figure 3-22. Similarly, solely negative pressure coefficients were developed at the stadium interior in the range $[-0.91, -0.62]$, with an average value of -0.80 and standard deviation of 0.07 . More specifically, the C_p at the windward (back) spectator tiers were within the interval $[-0.91, -0.62]$ and the highest negative values were observed at the Points 11 (-0.91), 12 (-0.90), 15 (-0.88) and 1 (-0.87), followed by Points 16 (-0.86), 10 (-0.84) and (-0.84), indicating intense flow movements at the bottom and the lateral upper spectator tiers. At the leeward (front) spectator tiers the C_p values were within the interval $[-0.87, -0.69]$ and the highest negative values were monitored at the Points 11, 12, 15, 16 and 1 with variance between -0.87 (for Point 11) and -0.84 (for Point 1). Again, the highest pressure coefficients were observed at the bottom and the upper lateral spectator tiers.

3 Wind Tunnel Experimentation

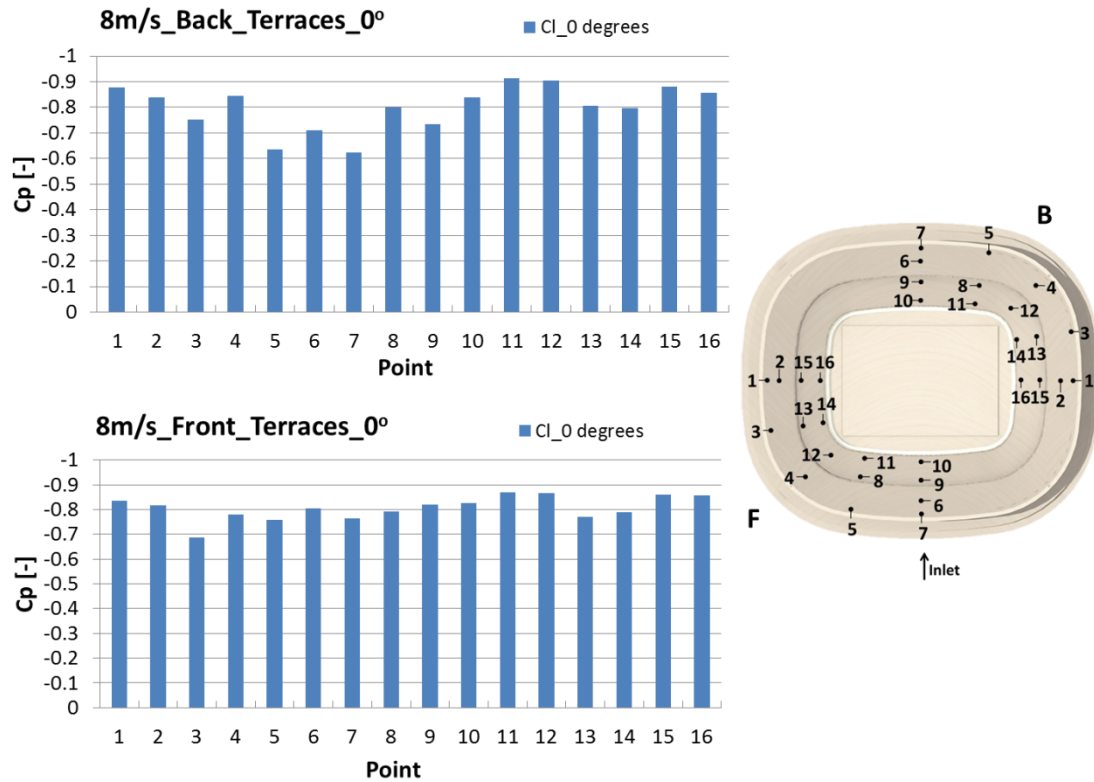


Figure 3-22 C_p results on the surface of the spectator terraces for the reference stadium case of 0° wind angle and non-elevated (Cl) roof configuration; $U_{ref} = 4.65$ m/s.

The pressure coefficients on the auxiliary area were in the range of $[-0.92, -0.68]$, with an average C_p of -0.84 and a standard deviation of 0.06 . As shown in Figure 3-23, the majority of the relevant measurement points follow symmetric pressure distribution, apart from the set of pressure taps 3-14, which indicates the failure of the pressure tap at Point 3 to capture the accurate wind pressure measurements, possibly due to tube bending that does not allow for sufficient development of the differential pressure.

The highest negative pressure coefficient values were observed at the symmetric Points 1 and 12 with a value of -0.91 , followed by their diagonal Points 6 and 11 with a pressure value equal to -0.89 . On the comparison of the developed pressures at the four corners, it can be concluded that higher suction zones are developed at the corners of the windward auxiliary area, since higher negative pressures were monitored, which is a result of the incoming flow through the rear side openings and the recirculation flow at the stadium bowl.

3 Wind Tunnel Experimentation

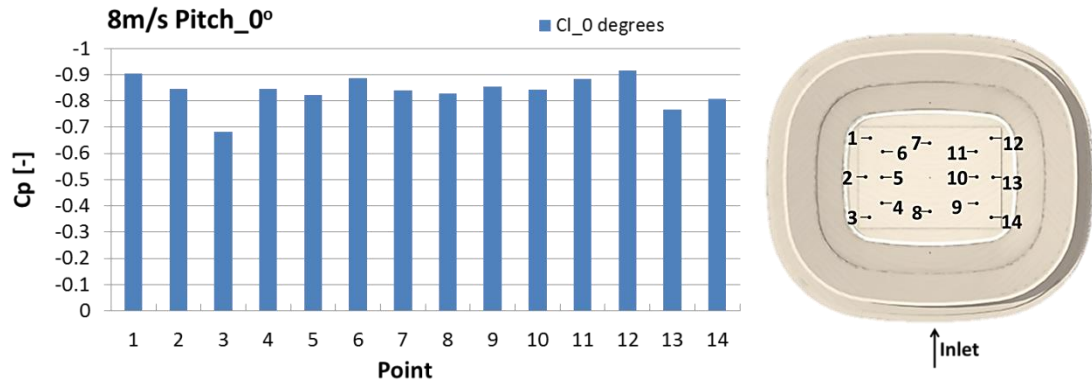


Figure 3-23 C_p results on the surface of the auxiliary area for the reference stadium case of 0° wind angle and non-elevated (Cl) roof configuration; $U_{ref} = 4.65$ m/s.

3.8.2.2 Roof wind pressure results

According to Figure 3-24, both roof configurations contribute to similar static pressure trends on the roof surface, with specific differences that will be discussed thereafter. For the 0° wind angle and elevated roof configuration the pressure coefficient varies between -1.44 and -0.72, with an average C_p value of -0.94, which is 1.3 % smaller than the average value of the reference case and a standard deviation of 0.21. The non-elevated roof appears to develop slightly higher negative pressures at the front and lateral sides of the oculus and smaller on the rear side of the oculus configuration, when compared with the values of the stadium with elevated roof. A preliminary explanation could rely on the fact that the elevated roof configuration creates several passages for the air to either enter or exit the stadium bowl, as opposed to the non-elevated roof, for which the roof opening is considered the primary airflow inlet and outlet of the stadium bowl. The highest negative C_p peak is observed at the Point 15, similar to the reference case, with a value of -1.44, which is 20.4 % smaller than the value at the reference case, indicating the development of stronger suction.

3 Wind Tunnel Experimentation

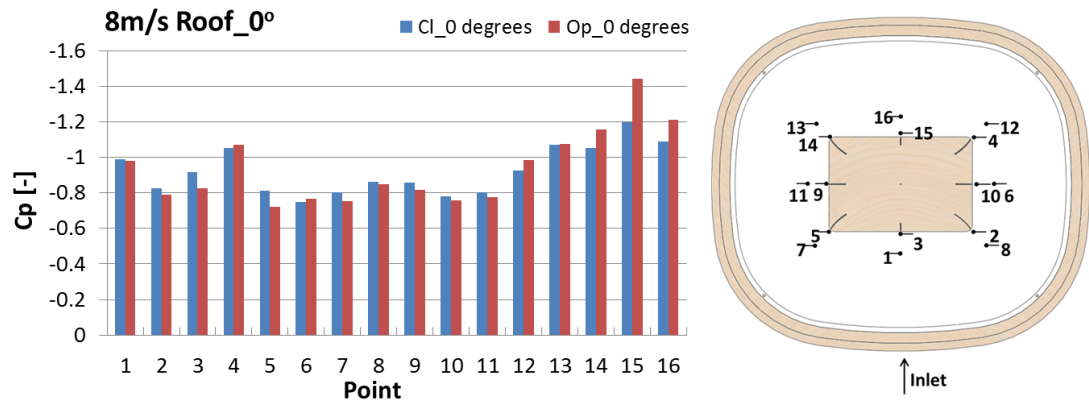


Figure 3-24 C_p results on the roof surface for the cases of 0° wind direction for the elevated (Op) and the non-elevated (Cl) roof configuration at $U_{ref} = 4.65$ m/s.

Figure 3-25 shows the results generated for the case study of 90° wind angle that indicated smaller negative values at all comparable points when compared with the previous wind direction. More specifically, the static pressure coefficients for the non-elevated are within the interval $[-1.13, -0.27]$, with an average C_p equal to -0.77 , which is 16.4 % higher than the average value of the reference case, and a standard deviation of 0.22. For the elevated roof configuration the C_p values were within the interval $[-1.2, -0.52]$, with an average value of -0.81 , which is 12.6 % higher than the average value of the reference case, and a standard deviation of 0.23. Similar pressure coefficient trends for the two roof configurations were observed. The maximum negative C_p values were monitored at the rear side of the oculus and the Points 2, 4, 6, 8, 10 and 12. However, for the current wind direction, higher negative pressure coefficient values were observed for the elevated roof, at almost all measurement points. Again the peak negative pressure coefficient was monitored at the Point 10 (similar to Point 15 for the 0° wind angle), with C_p values equal to -1.12 and -1.24 for the non-elevated and the elevated roof, which is 6.1 % higher and 3.5 % smaller than the reference case study, respectively. Finally, the abnormal pressure reading at the Point 16, for the non-elevated roof configuration, is possibly attributable to pressure tap bending during the rotation of the turntable and thus is excluded from the data interpretation.

3 Wind Tunnel Experimentation

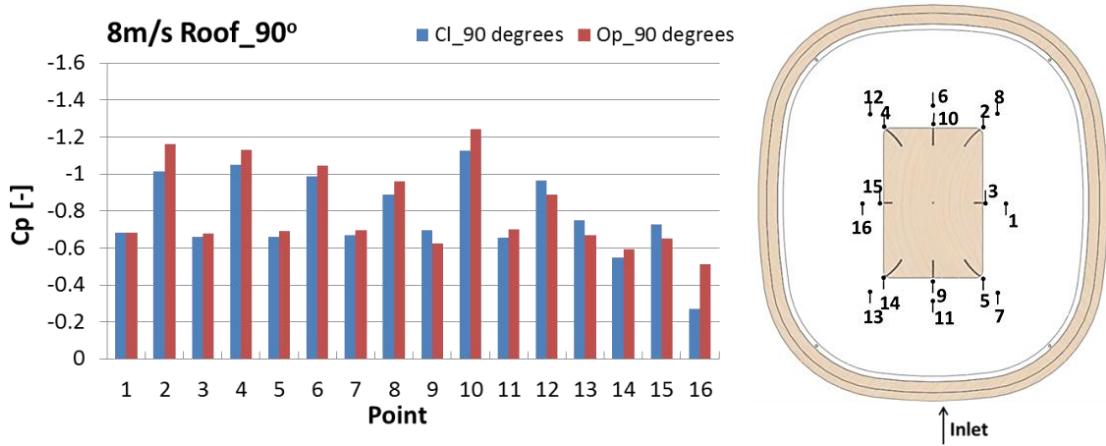
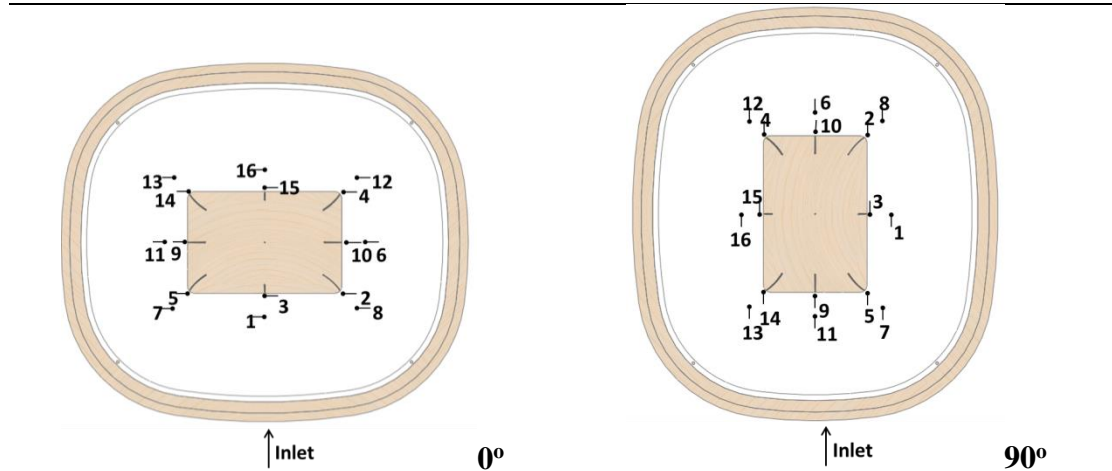


Figure 3-25 C_p results on the roof surface for the cases of 90° wind direction for the elevated (Op) and the non-elevated (Cl) roof configuration at $U_{ref} = 4.65$ m/s.

Table 3.2 summarises the pressure coefficient results generated on the roof surface for the four stadium cases, providing comparative values for the average C_p and minimum C_p values obtained at the Point 15 for the 0° wind angle and Point 10 for the 90° wind angle.

Table 3.2 Comparative results for the C_p values generated on the roof surface for the four stadium cases.

Stadium Case	0° , non-elevated roof (Ref. case)	0° , elevated roof	90° , non-elevated roof	90° , elevated roof
C_p range	[-1.20,-0.75]	[-1.44,-0.72]	[-1.12,-0.55]	[-1.24,-0.52]
Average C_p	-0.92	-0.94	-0.77	-0.81
Deviation from Ref.	-	1.3%	-16.5%	-12.6%
Min C_p Point	Point 15	Point 15	Point 10	Point 10
Deviation from Ref.	-	20.4%	-6.1%	3.5%



3 Wind Tunnel Experimentation

3.8.2.3 Terraces wind pressure results

Figure 3-26 shows the pressure coefficient results for the case of 0° wind angle. With main exception the C_p value at the Point 6 of the windward (back) spectator tiers, lower negative values were monitored at all points for the elevated roof configuration. The pressure coefficient values were within the interval $[-0.82, -0.59]$, with an average value of -0.73 , which is 8.9% higher than the average C_p value of the reference case study, and a standard deviation of 0.06 .

Specifically, on the windward spectator tiers, the highest values occur at the Points 15 (-0.82), 12 (-0.80), 1 (-0.79) and 11 (-0.79), indicating intense flow movement. The lowest negative values were recorded at the Points 3 (-0.59) and 5 (-0.59), located at the highest rows of the upper spectator tiers. On the leeward side, the highest pressure coefficient values are obtained at the Points 11 (-0.80) and 12 (-0.79), located at the bottom terraces and the minimum at the Point 3 (-0.69) located at the highest rows of the upper side spectator tiers.

On the comparison of the two roof configurations, it is worth mentioning the differences in C_p values for the Point 4 and Point 3 located at the windward spectator tiers. The substantial difference of -0.20 or 31.6% , for the Point 4, and -0.16 or 26.4% , for the Point 3, indicate that the non-elevated roof configuration results to more intense ventilation zones at the highest rows of the side windward upper tiers. Local high ventilation zones on the upper windward terraces were also observed by Szucs et al. (2009b) in the case of an enclosed flat roof configuration.

3 Wind Tunnel Experimentation

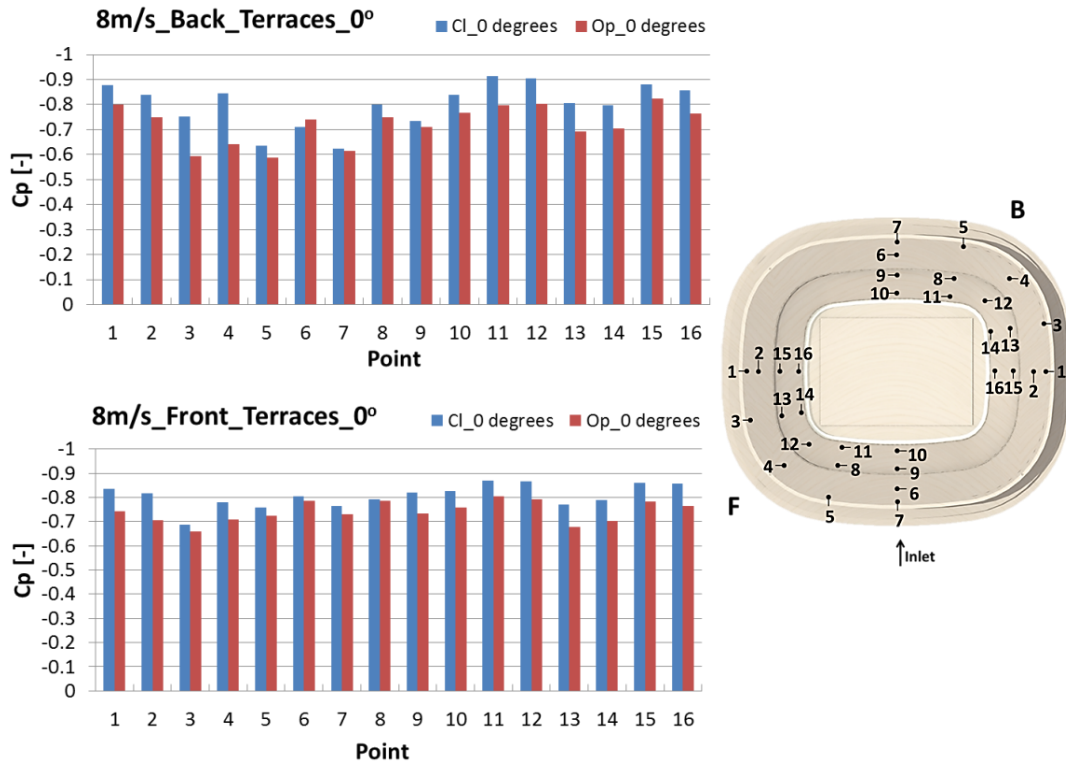


Figure 3-26 C_p results on the terraces' surfaces for the case of 0° wind angle for the back (top) and front (bottom) areas for the elevated (Op) and the non-elevated (Cl) roof opening configuration at $U_{ref} = 4.65$ m/s.

The C_p results for the 90° wind angle are presented in Figure 3-27. All values have negative sign, fluctuating between -0.43 and -0.78. Symmetry is also present between the relevant points (6, 7, 9 and 10). At first glance, the Points 1, 2 and 3, located in both leeward (front) and windward (back) terraces show higher negative values for the elevated roof configuration, as opposed to the non-elevated one. This indicates more intense airflow movement and the existence of potential airflow inlets, from both the front and rear side of the roof peripheral opening.

More specifically, for the non-elevated roof configuration, the C_p values are within the interval [-0.78,-0.43], with an average value of -0.67, 17 % higher than the one generated for the reference case study, and a standard deviation of 0.09. The highest negative pressure coefficient values at the windward (back) spectator tiers are observed at the Points 6 (-0.782), 8 (-0.772), 11 (-0.766) and 12 (-0.733), comprising the areas at the bottom corner and side spectator tiers and the centre of the upper lateral terraces. At the leeward (front) spectator tiers the highest negative pressure coefficients are monitored at the Point 6 (-0.775), which is symmetric to the aforementioned Point 6 (windward tiers) with a very small deviation of 0.8 % and the Points 11 (-0.759) and 8 (-0.747), on the bottom lateral terraces.

3 Wind Tunnel Experimentation

In case of the elevated-roof configuration, the pressure coefficient values are within the interval $[-0.76, -0.45]$, with an average value of -0.63 , 22.0 % higher than the one generated for the reference case study, and a standard deviation of 0.08. The highest negative C_p values at the windward tiers are observed at the Points 6 (-0.74), 8 (-0.69), 16 (-0.68) and 15 (-0.67). The pressure coefficient values overall are substantially higher, with suction to occur at the centre of the bottom windward tiers (Points 15 and 16) and the lateral tiers (Points 6 and 8) similarly to the non-elevated case. On the leeward spectator tiers the pressure distribution differs greatly. High negative C_p values are observed at the upper spectator tiers, and particularly at the Point 1 (-0.76), which is an indicator of the airflow entering the stadium bowl. The Points 6 (-0.76) and 8 (-0.75) have the following highest negative values, located at the centre of the lateral upper spectator tiers and the highest rows of the bottom side spectator tiers respectively.

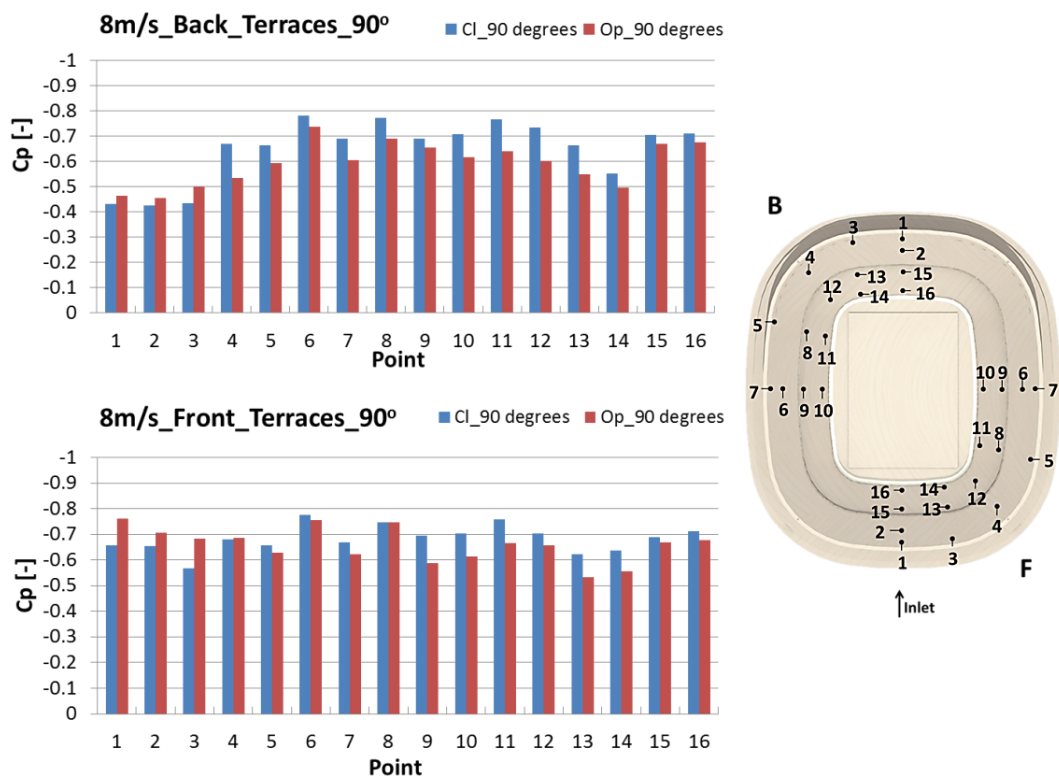


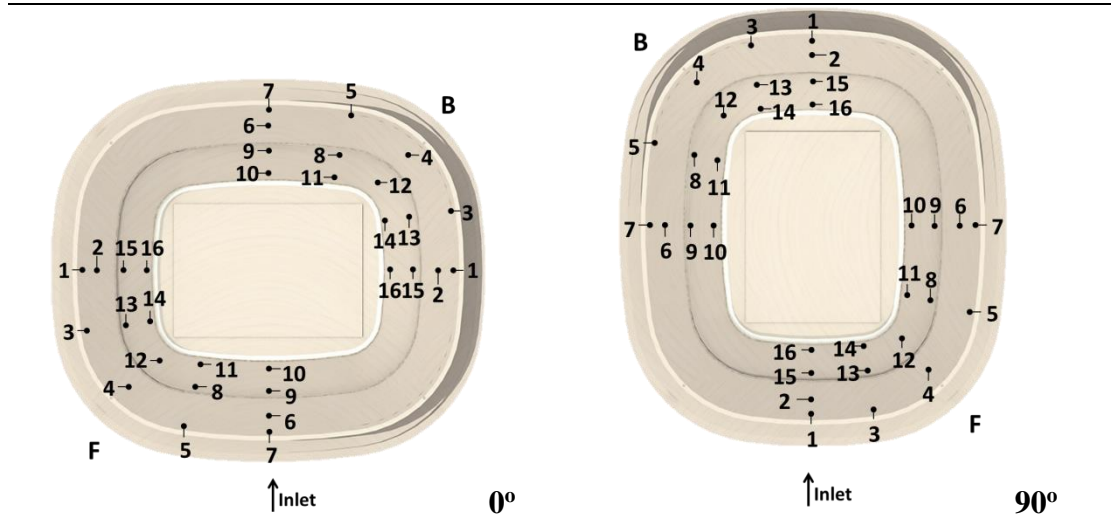
Figure 3-27 C_p results on the terraces' surfaces for the case of 90° wind angle for the back (top) and front (bottom) areas for the elevated (Op) and the non-elevated (Cl) roof opening configuration at $U_{ref} = 4.65$ m/s.

Table 3.3 summarises the pressure coefficient results generated on the surfaces of the spectator terraces for the four stadium cases, providing comparative values for the average C_p and minimum C_p values.

3 Wind Tunnel Experimentation

Table 3.3 Comparative results for the C_p values generated on the surfaces of the spectator terraces for the four stadium cases.

Stadium Case	0°, non-elevated roof (Ref.)	0°, elevated roof	90°, non-elevated roof	90°, elevated roof
C_p range	[-0.91,-0.62]	[-0.82,-0.59]	[-0.78,-0.43]	[-0.76,-0.45]
Average C_p	-0.80	-0.73	-0.67	-0.63
Deviation from Ref.	-	-9.0%	-17.0%	-22.0%
Min C_p Point	Point 11 (B)	Point 15 (B)	Point 6 (B)	Point 1 (F)
Deviation from Ref.	-	-9.9%	-14.4%	-16.8%



3.8.2.4 Pitch wind pressure results

Figure 3-28 shows the acquired results of the wind pressure coefficient for the auxiliary area and the wind angle of 0°. In all cases, the elevated roof configuration appears to have the smaller negative C_p values at all points, following similar trends with the results of the non-elevated roof configuration. Symmetry was observed for the majority of the points, with the highest deviation error of 19 % to occur at the measurement set of the Points 2 and 13. The C_p values were within the interval [-0.86,-0.67], with an average value of -0.76, which is 9.2 % higher than the one obtained from the reference case, and a standard deviation of 0.05. The minimum pressure coefficient value was measured at the Point 6 with a value of -0.86, 5.8 % higher than the one of the reference case study.

3 Wind Tunnel Experimentation

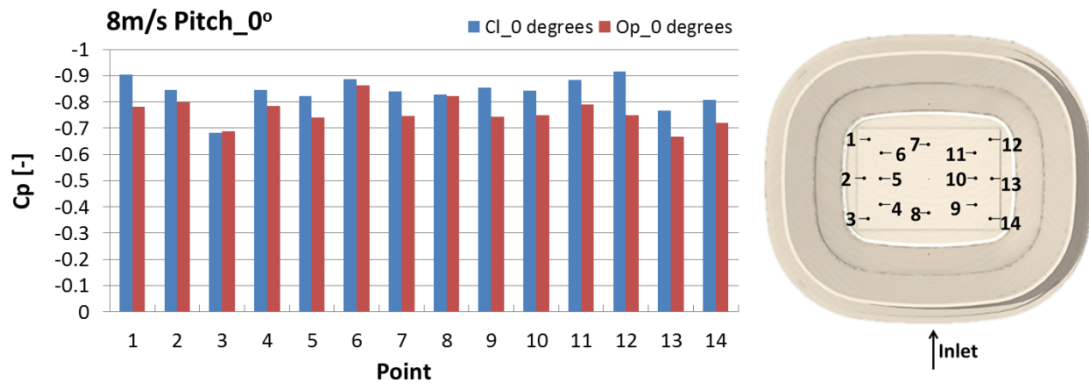


Figure 3-28 C_p results on the surface of the auxiliary area for the case of 0° wind direction for the elevated (Op) and non-elevated (Cl) roof configuration at $U_{ref} = 4.65$ m/s.

Figure 3-29 presents the C_p results for the case of 90° wind angle. All measurement points generated smaller negative pressure coefficients when compared to the 0° wind angle. For the case of non-elevated roof configuration, the C_p values were within the interval $[-0.77, -0.64]$, with an average value of -0.70 , which is 16.6 % higher than the average C_p value of the reference case study, and a standard deviation of 0.05. The minimum pressure coefficient value was measured at the Point 12, which is 16 % higher than the minimum C_p value of the reference case study, located at the front corner of the auxiliary area.

For the case of the elevated roof configuration, the pressure coefficient values were within the interval $[-0.75, -0.59]$, with an average C_p value equal to -0.67 , which is 20.1 % higher than the average value of the reference case study, and a standard deviation of 0.05. The minimum C_p was observed at the Point 6, with a value 17.7 % higher than the minimum value of the reference case study.

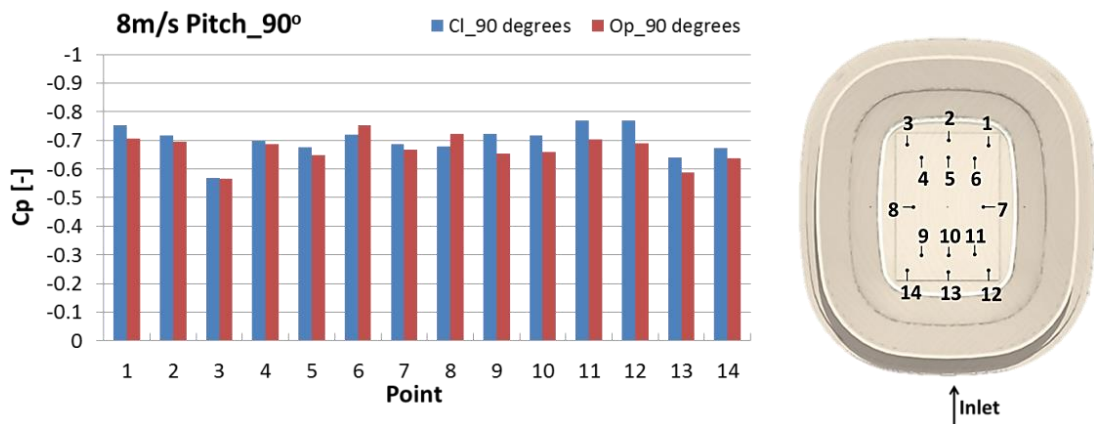


Figure 3-29 C_p results on the surface of the auxiliary area for the case of 90° wind direction for the elevated and non-elevated roof configuration at $U_{ref} = 4.65$ m/s.

The measurement points failed to satisfy symmetry, which may be attributed to incorrect positioning of the model under the exact wind angle of 90° .

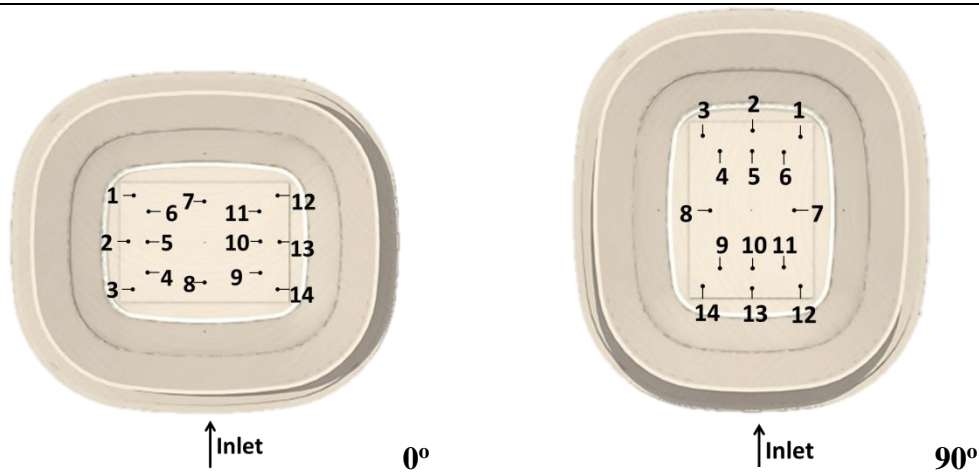
3 Wind Tunnel Experimentation

Nevertheless, with main exception the measuring set of the Points 12 and 14, which produced a deviation error of 14 % for the case of the non-elevated roof, the rest of the symmetrical points generated a small deviation error with an average value of 4 %. Again, the Point 3 was excluded from the data interpretation, due to malfunction of the pressure tap. The smallest negative value for both roof configurations was observed at the Point 13, located at the centre of the leeward side of the auxiliary area, indicating decreased local velocities, as opposed to the rest of the studied points.

Table 3.4 summarises the pressure coefficient results generated on the surface of the auxiliary area for the four stadium cases, providing comparative values for the average C_p and minimum C_p values.

Table 3.4 Comparative results for the C_p values generated on the auxiliary area surface for the four stadium cases.

Stadium Case	0°, non-elevated roof (Ref.)	0°, elevated roof	90°, non-elevated roof	90°, elevated roof
C_p range	[-0.92,-0.68]	[-0.86,-0.67]	[-0.77,-0.64]	[-0.75,-0.59]
Average C_p	-0.84	-0.76	-0.70	-0.67
Deviation from Ref.	-	-9.2%	-16.6%	-20.1%
Min C_p Point	Point 12	Point 6	Point 12	Point 6
Deviation from Ref.	-	-5.8%	-16.0%	-17.7%



3.9 Errors and uncertainties

During the conduct of every wind tunnel experiment there were several sources of error that can be depicted on the generated results. The errors are classified in two main categories, described below.

3 Wind Tunnel Experimentation

Systematic errors or bias: include the errors generated from the instrumentation. The systematic error may be eliminated by regular calibration and maintenance of the equipment. In case of continuous repeatability of the error, then it is accepted and the difference between the measured and the real value is incorporated in the final result (Tropea et al., 2007).

Random or precision errors: describe a wide variety of error sources identified in the wind tunnel, originated from uncontrollable parameters, including temperature changes, induced airflow turbulence, geometrical characteristics, generated vibration, voltage fluctuations and the roughness of the theoretically smooth surrounding surfaces (Biswas and Eswaran, 2002). The random error can be identified by performing a series of measurements for a specific physical value, under similar conditions (i.e. wind direction, location and measuring port). The acquired data will enable the identification of the measurement differences, cancelling the random uncertainties. In case of scatter results, then statistical methods are recommended to be employed to calculate the standard deviation of the actual solution.

For the current experimental study, several uncertainties on the generated results were considered, mainly caused due to procedure limitations and human errors. For the velocity distribution measurements at the empty wind tunnel the following limitations are considered:

1. The stands employed for the velocity measurements are additional obstacles that interact with the flow stream. This is a recognised systematic error caused by the surrounding components.
2. The stand used for the velocity measurements above 0.2 m (see Figure 3-9) was subject to intense vibration for wind speeds higher than 6 m/s. In order to compensate that movement and improve the accuracy of the hot wire measurements, pieces of attached string on the test section walls were used to stabilise the stand.
3. The reference velocity speeds used to describe the fan frequencies, do not represent the velocities at the inlet of the test section. The identification of the velocity inlet profiles would require the simulation of the whole wind tunnel facility, which is not the purpose of this work.

3 Wind Tunnel Experimentation

For the pressure measurements at the stadium model, the following limitations should be taken into consideration:

4. The difference on the diameter between the holes on the stadium model (0.003 m) and the pressure taps (0.0015 m) was adjusted manually, by using tape to increase the thickness of the pressure taps and then adhesive substances to attach them parallel to the relevant surface.
5. During the rotation of the model to study different wind directions, the pressure tap 16 and 3 were subject to bending and thus, in some cases the measurements may have a large deviation.
6. For wind speeds above 6 m/s (inlet reference speed), the excitation of the roof due to vortex shedding was apparent. The result of the high turbulent flow involved the development of vortex-induced vibration on the roof structure. In order to minimise the vibration effect six supports (0.01 m polystyrene foam) were provided on the structural extension between the roof and the upper spectator tiers. The vibration may have added to the asymmetry of the measurement results.
7. For the roof pressure measurements, the wind disturbance caused by the existence of the pressure taps at the stadium interior should be considered, especially at the points located at the back of the roof, which are affected by the flow recirculation in the stadium bowl.
8. The model direction against the impinging wind plays a significant role on the development of symmetric pressure distributions. The incorrect placement of the model under exact 0° or 90° wind angle would result to unsymmetrical solutions at the relevant measurement points. Such asymmetries were present on the study of the pressure distributions on the auxiliary area.

3.10 Summary

In this chapter the wind tunnel facilities and their use in studying urban flow phenomena were discussed with main focus on the studies of the atmospheric boundary layer. One of the most important similarity criteria to be satisfied is the dynamic similarity that involves the generation of turbulence effects by employing artificial aerodynamic roughness elements.

The ABL wind tunnel facility of the University of Nottingham was also described, along with the mechanical equipment that was used during the conduct of the

3 Wind Tunnel Experimentation

experiment. The velocity profile of a suburban environment was developed and validated against the theoretical values.

The reduced scale stadium model was introduced along with the experimental set-up and the stadium design cases for evaluation. The experiment focused on the generation of wind pressure coefficients, as the most important dimensionless quantity to assess the aerodynamic performance of the model. Measurement data were acquired for the pressures on the roof component, the terraces and the auxiliary area to support the wind comfort assessment study. However, a complete interpretation of the results requires a CFD simulation study and validation of the pressure measurements, which will be presented in 5.

4 Computational Fluid Dynamics

4.1 Introduction

The evaluation of stadium aerodynamics and wind comfort state at the interior of the structure requires the simulation of the physical phenomena occurring in the urban/built environment; phenomena which are characterised with continuous turbulent behaviour, inherently generated and randomly varied with time and space (Wilcox, 1993). State-of-the-art technique, in which many research studies have been based for accurate prediction results of the atmospheric flow characteristics, is Computational Fluid Dynamics (CFD). CFD techniques use numerical models and algorithms to predict the multiscalar fluid flows, to understand, evaluate and assess complex turbulent phenomena and accelerate development, within affordable computational performance and time (Souza, 2003).

In this chapter, the turbulence modelling theory is presented along with the CFD parameterisation steps to be followed. Main focus is given to the attributes upon which ABL and building aerodynamic studies are more dependent. The CFD parameterisation for the aerodynamic study of the stadium model is also presented, along with the grid verification study.

4.2 Governing equations

CFD codes employ the three governing equations of the fluid motion to evaluate the fundamental flow parameters; the continuity equation, or conservation of mass, the momentum conservation in the form of Navier-Stokes equations, and the energy equation, which is not further required in this work. The general form of these three partial differential equations can be written as follows:

$$\frac{\partial(\rho\varphi)}{\partial t} + \text{div}(\rho\vec{u}\varphi - \Gamma_{\varphi}\text{grad}\varphi) = S_{\varphi} \quad (4.1)$$

where ρ is the fluid density, t is the time, \vec{u} is the vector of velocity, Γ_{φ} the diffusion coefficient, S_{φ} is the source/ sink term and φ is a changing property, which is equal to 1 for the continuity equation, equal to v , v , w , for the instantaneous fluid velocity components (m/s) of the Navier-Stokes equations and equal to temperature (T) or enthalpy (h) for the energy equation (Anderson, 1995).

4 Computational Fluid Dynamics

These partial differential equations form a highly non-linear system, which admits of no analytical solution. By employing CFD techniques, the system is discretised and a numerical solution may be approached in two steps. The first step is the space discretisation, which involves the replacement of the continuous problem by a series of grid points or cells, where the numerical values of the flow variables are to be determined (Bhaskaran and Collins, 2002). The second step is the equation discretisation, on which the governing equations are converted into discrete algebraic equations.

The three most commonly used numerical discretisation methods are: 1) the Finite Difference Method (FDM), where the fluid domain is discretised into grid points, 2) the Finite Element Method (FEM), where the domain is discretised into small elements and 3) the Finite Volume Method (FVM), in which the domain is discretised into volumes. For CFD studies of turbulent flow the FVM is commonly used, as it is applicable in complex geometries and in high turbulent flows.

4.3 Space discretisation

Mesh/ grid is defined a computational domain that is discretised into a number of partitions/ cells. The partial differential equations are calculated at cell centres, if cell-centre discretisation scheme is selected, or at cell vertices, if cell-vertex discretisation scheme is selected. 2D domains may be consisted by triangular or/ and quadrilateral cells. 3D domains may contain one or a combination of tetrahedral, prism, pyramid, hexahedral and polyhedral cell types. A graphical illustration of the different cell types is given in Appendix 0.

Geometrically, the cells map the surface of the modelled physical area, the resolution of which designates the mesh adaptation (Eiseman, 1985). The number of cells defines the mesh density. Higher mesh density is necessary in the areas of the domain where rapid changes of the flow characteristics may appear, such as sudden geometrical changes (like turns, gaps, peaks, etc.), or steep flow gradients. Lower mesh density is usually employed in areas where fewer changes are expected due to uniformity, flow homogeneity, or lack of geometrical obstacles. The selection of the mesh density is highly correlated on the model geometry, the availability of computational time and memory, the attainment of a grid-independent solution, the numerical accuracy and the simulation errors.

4 Computational Fluid Dynamics

4.3.1 Cell Types

A careful approach on grid construction process is important for high fidelity simulation results and the generation of accurate and converged solutions. Depending on the complexity of the geometry either structured, unstructured, or hybrid grid types are used to map the computational domain and match the boundaries of the bodies.

4.3.1.1 Structured Mesh

The structured mesh is composed of hexahedra (for 3D) or quadrilaterals (for 2D) cells, forming a regular pattern with orthogonal coordinates (see Figure 4-1). This type of mesh is recommended for high quality discretised domain. The primacy of the structured mesh over the unstructured is second to none. The main advantages are focused on the mesh generation time, which is substantially reduced, as well as the computer memory usage. The hexahedral cells (or quadrilateral) have 6 surfaces (or 4 edges), that permit local connection with the neighbour cells, allowing at the same time the parallel positioning of the cells to the boundaries (Kowalski et al., 2014). Additionally, the simulation solution achieves faster convergence. The algorithm calculation is performed sequentially, by transferring the solution information to the next cells (left to right, top to bottom).

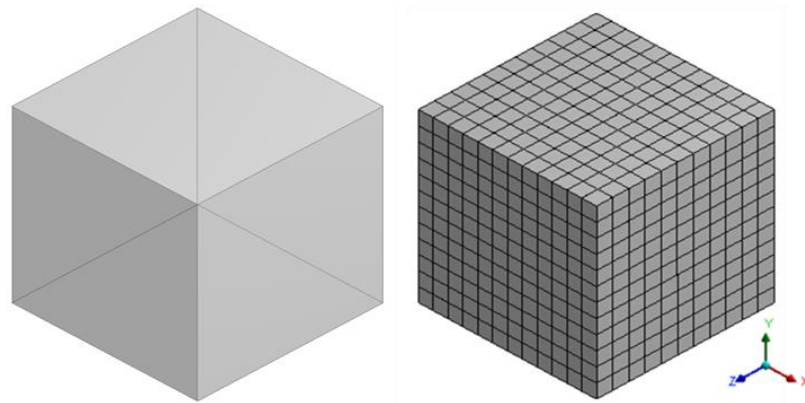


Figure 4-1 A cubic body meshed with orthogonal structured grid method.

In case of complex geometries, where boundary orthogonal hexahedron (or quadrilateral) cells are not practicable, different techniques are performed. These techniques involve algorithm methods to generate body-fitted non-orthogonal structured grid cells, as shown in Figure 4-2.

4 Computational Fluid Dynamics

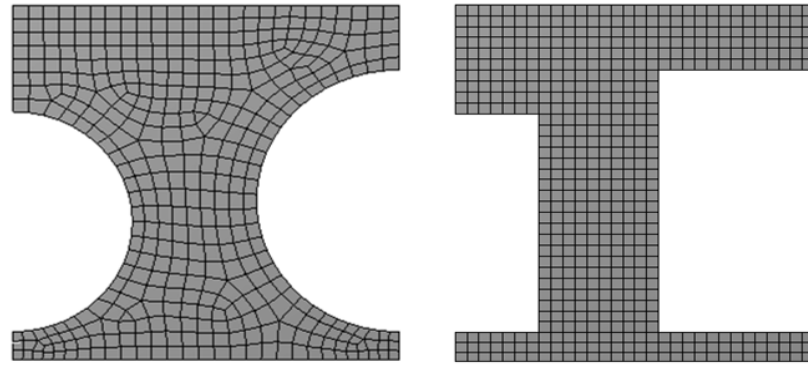


Figure 4-2 A cubic body meshed with orthogonal structured grid method.

Another method is based on the separation of the computational area in segments/blocks that permits conformal mesh generation. This technique is known as multiblock, which is more time consuming as each body needs to be sized separately. However, higher grid refinement can be achieved at the areas of interest, such as bodies, edges and flow separation areas. In case of multidimensional models, with large scale differences, the simulations may lead to inaccurate results, as the flow transition fails in cells with high aspect ratio (Katz and Sankaran, 2012) (see also Appendix 0). Figure 4-3 shows a grid domain generated using the cutcell method of the multiblock mesh family. The transition from the one body to the other is made by refining the cell size by a ratio of 2. This leads to the generation of orthogonal hex-dominant cells with hanging nodes, giving the opportunity to provide higher resolution mesh to the most complex zones of the domain.

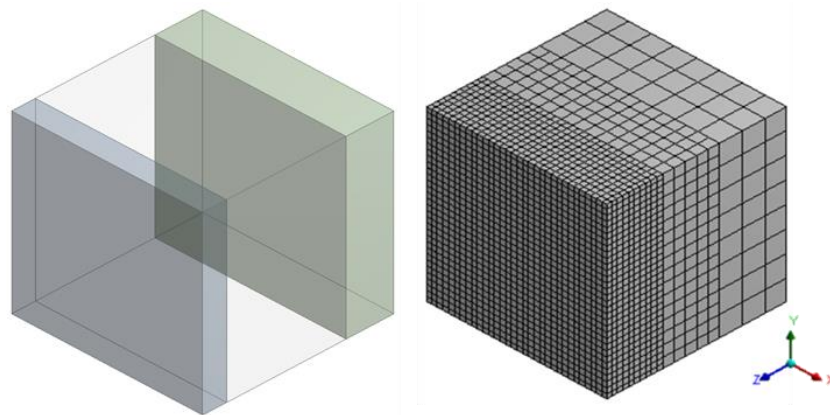


Figure 4-3 Mesh generation based on cutcell method; split geometry (left) and generated mesh (right).

4.3.1.2 Unstructured Mesh

The unstructured mesh is composed by tetrahedral; (for 3D) or triangular (for 2D) elements, forming no regular pattern (Figure 4-4 left). Due to the arbitrary position

4 Computational Fluid Dynamics

of the cells there are difficulties in vectorising the process; the algorithm computation at each point presupposes the calculation of the solution at the precedent point (Anderson, 1992). The main advantage is the level of adaptability in geometries of high complexity, allowing high cell concentration in the areas of interest. Moreover, the computational time consumed for the mesh construction (not for mesh generation) is relatively reduced, since there is no need for further body decomposition, as it is required in certain cases of structured grid. Polyhedral grid is a recently highlighted method for unstructured mesh generation (Figure 4-4 right). The polyhedral mesh is constructed upon the tetrahedral pattern.

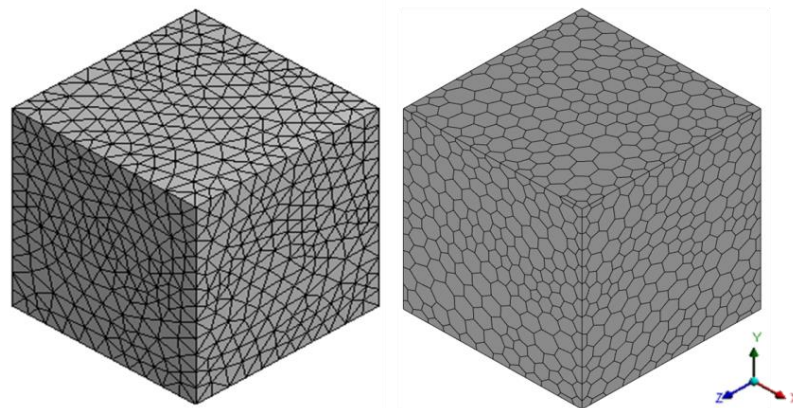


Figure 4-4 Unstructured mesh generation with tetrahedral (left) and polyhedral (right) elements.

More specifically, as shown in Figure 4-5, polygons are formed by constructing vertices that pass from the primal edge and face centroids of the tetrahedrons (ANSYS Inc., 2011). This conversion leads to coarser mesh structures, but with faster and higher convergence performance. Polyhedrons have a larger number of neighbour cell faces, as opposed to four for the tetrahedrons, making information distribution and gradient calculations more accurate² (Kim and Chung, 2014).

² In tetrahedrons, the neighbour cells may all be positioned in a single plane, making the calculation/prediction of the gradients in the direction normal to the plane impossible.

4 Computational Fluid Dynamics

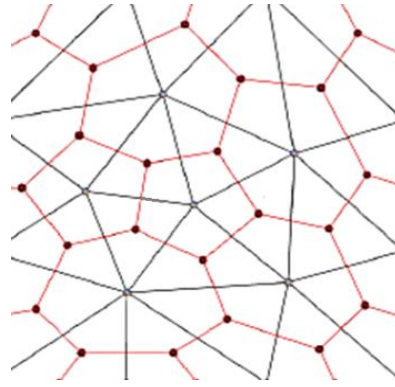


Figure 4-5 Construction of polygonal duals based on primal triangular mesh (Balafas, 2014).

Perić (2004) on his studies on polyhedral meshes highlighted their superior performance over the tetrahedral ones. According to the results converged solutions were obtained in less computational time and with less memory usage. Results obtained with the SIMPLE-algorithm and second order spatial discretisation scheme were almost similar to those obtained from structured meshes. Additional LES and DNS studies showed that the turbulence kinetic energy, k , is conserved at almost the same level as in hexahedral grids (Moulinec et al., 2005; Perić, 2004). Several works have been published using polyhedral grids, also highlighting their good performance when compared with tetrahedral grids (Spiegel et al., 2011; Tritthart and Gutknecht, 2007; Muzaferija and Gosman, 1997).

4.3.1.3 Hybrid Mesh

The hybrid mesh is another type of grid that combines one or more cell types (Figure 4-6). The selection of this mesh is advantageous for models that contain complex obstacles that cannot be treated with multiblock structured grid. The hybrid mesh requires great attention during implementation, due to the discontinuity issues that may arise leading to non-conformal interfaces between the bodies.

4 Computational Fluid Dynamics

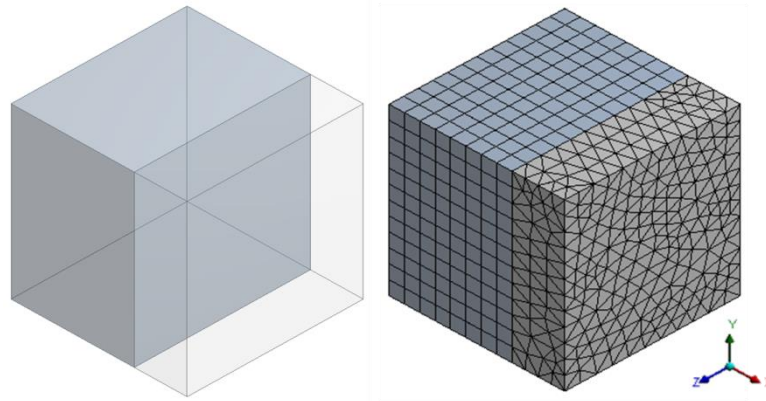


Figure 4-6 Block structure meshed with hybrid mesh type, containing hexahedral, prism and tetrahedral cells.

4.3.2 Mesh Quality

The generated mesh, regardless the element type selected, requires to be checked against its quality, to ensure that the results are not mesh-dependent, but model-dependent. The mesh is checked against the cell quality, including aspect ratio, orthogonality, skewness and squish index, and against grid smoothness, briefly explained below (ANSYS Inc., 2011):

Aspect ratio is the ratio value of the maximum over the minimum edge length value, expressing the stretchiness of the cell. An aspect ratio equal to 1 is considered ideal.

Orthogonality is calculated using the vector from the cell centroid to each of cell faces, the corresponding face area vector, and the vector from the cell centroid to the centroids of each of the adjacent cells. The best cells have orthogonality equal to 1 and worst equal to 0.

Skewness shows the extent to which a cell is deformed from an equilateral cell of equivalent volume and the same basic shape (triangle, square, cube, etc.). The skewness can be determined by the following two methods:

Equivolume skew, which applies to triangle and tetrahedral cells according to the Equation 4.2:

$$\text{equilateral skewness} = \frac{\text{optimal cell size} - \text{cell size}}{\text{optimal cell size}} \quad (4.2)$$

Equiangle skew, which applies to every cell type and is calculated based on the Equation 4.3:

4 Computational Fluid Dynamics

$$\text{equiangular skewness} = \max \left[\frac{q_{max} - q_e}{180 - q_e}, \frac{q_e - q_{min}}{q_e} \right] \quad (4.3)$$

where q_{max} is the largest angle in face or cell, q_{min} is the smallest angle in face or cell and q_e is the angle for equiangular face or cell (60 for triangle and 90 for square). The best value for skewness, regardless the method is the 0 and the worst 1.

Cell Squish Index, which measures how far a cell deviates from orthogonality with respect to its faces. It is calculated from the dot products of each vector pointing from the centroid of a cell towards the centre of each of its faces. This criterion applies to all element types and the best value is equal to 0.

Face Squish Index, which measures the quality of polyhedral meshes and it is calculated from the dot products of each face area vector and the vector that connects the centroids of the two adjacent cells. The best quality cells have a face squish index value equal to 0.

4.3.3 Mesh Comparison

The evaluation of the mesh characteristics and the assessment of the simulation performance were conducted by a simple experiment in ANSYS Fluent 15.0. A cube of $1 \times 1 \times 1 \text{ m}^3$ (L x W x H) was assessed against 1) mesh type, 2) mesh size and 3) solution convergence criteria. The block was discretised in hexahedral, tetrahedral and polyhedral elements, with cell size equal to 0.1m, as shown in Figure 4-7.

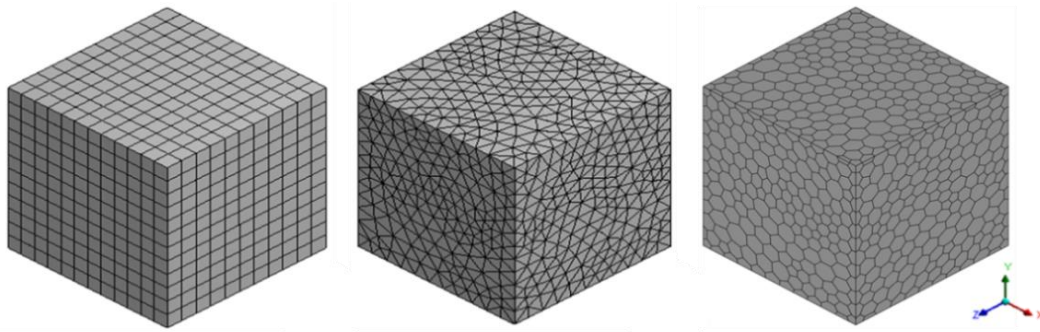


Figure 4-7 Mesh generation using hexahedral, tetrahedral and polyhedral discretisation scheme (from left to right).

Table 4.1 summarises the mesh characteristics of each block. The hexahedral mesh had the minimum number of cells, faces and nodes, since it can perfectly fill the domain with fully structured orthogonal elements. The tetrahedral mesh had more than 7 and 4.6 times more cells and faces respectively. The polyhedral mesh,

4 Computational Fluid Dynamics

tetrahedral-derived, had 4.7 and 1.5 times less cells and faces as opposed to its “parent mesh”.

Table 4.1 Comparison of mesh characteristics for each different cell type.

Mesh type	Mesh size (cells)	Mesh faces	Mesh nodes
Hexahedral	1,584	5,160	2,028
Tetrahedral	11,508	23,941	2,412
Polyhedral	2,412	15,965	13,556

A further insight into the numerical performance of the different meshes was gained after simulating the block fluid volume considering inviscid air conditions, a laminar flow with inlet velocity equal to 1 m/s and no slip conditions for the wall boundaries. The residuals’ history is shown in Figure 4-8. It is remarkable the behaviour similarity of the hexahedral and polyhedral mesh. Within the same convergence range of the residual criteria (more than $1e-10$ for all the criteria), fast convergence was achieved in just 118 and 160 iterations, for the hexahedral and polyhedral mesh respectively. The tetrahedral mesh, on the other hand, shows a slower convergence to about 320 iterations and with a divergence peak at the beginning of the simulation. The reason for this divergence probably lies in the mesh quality and more specific in the poor orthogonality of some elements. Additional to this, the residuals reached a maximum reduction of $1e-01$.

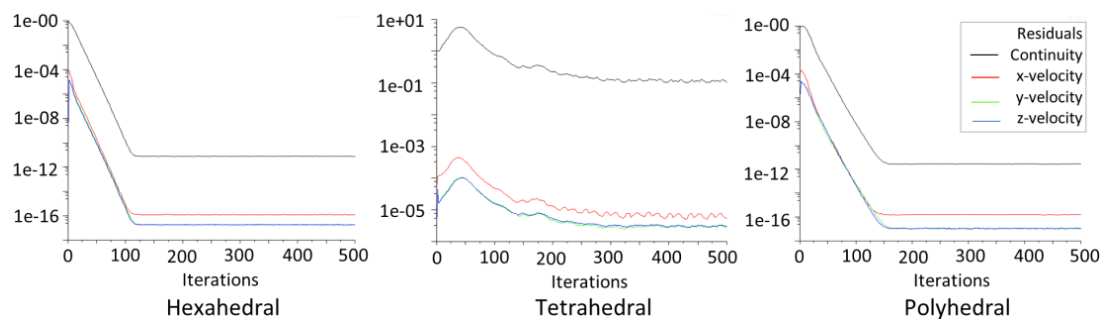


Figure 4-8 Residuals convergence history for the hexahedral, tetrahedral and polyhedral mesh (from left to right).

Finally the results gave information about the memory usage for each simulation. The hexahedral model required 6 Mb, as opposed to 20 Mb and 27 Mb for the polyhedral and tetrahedral mesh respectively. The advantageous performance of the polyhedral cells cannot be overlooked but due to limited use in literature will not be employed for the current case study.

4 Computational Fluid Dynamics

4.3.4 Mesh Recording

When selective meshing is performed, which includes the careful selection of size functions and methods for the geometric model bodies, the sequence of the mesh generation is important. From default, the mesh is generated with the following sequence:

All Tringles → Quad Dominant → MultiZone Quad/Tri

The sequence of meshed bodies can be controlled by using mesh recording, allowing the selection of those bodies that need to be meshed first. In Figure 4-9, it is compared the selective mesh of the case study model generated with automatic mesh (top) and with mesh recording sequence (bottom). Mesh recording can be advantageously be used in case of design experimentation, where the same model is assessed against different dimensional characteristics, and the mesh quality needs to be of the same level of quality as the initial design case.

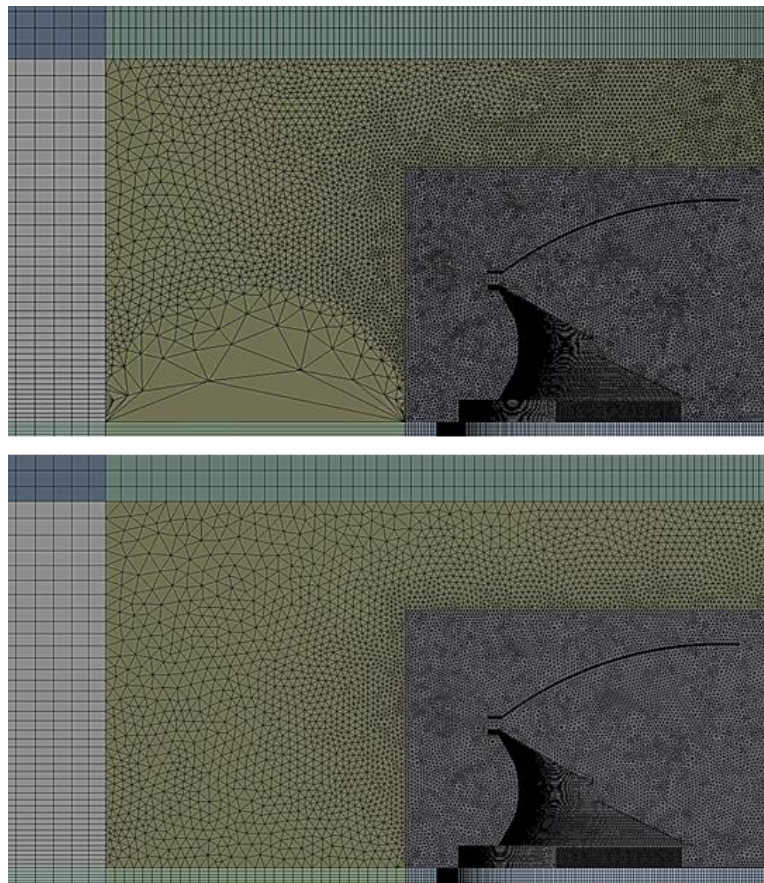


Figure 4-9 Mesh generation using automatic method (top) and recording sequence meshing method (bottom).

4 Computational Fluid Dynamics

4.4 Equation discretisation

As described earlier, the turbulent atmospheric flow can be described by the three governing equations for mass conservation, momentum conservation and energy conservation. In CFD studies, for a homogeneous, isotropic, incompressible, ideal fluid, the continuity (4.4) the Navier-Stokes equations (4.5) of the following form are used:

$$\text{div}(\vec{v}) = 0 \quad (4.4)$$

$$\rho \frac{dv}{dt} + \rho \text{div}(v\vec{v}) = G_x - \frac{\partial p}{\partial x} + \mu \bar{V}^2 v \quad (4.5)$$

where the first term in Equation 4.5 describe the local change of velocity in time and the second term the change in velocity due to movement in the fluid. The terms on the right part of the equation, from left to right are the body force, the pressure change and the dissipative viscous forces (Versteeg and Malalasekera, 1995).

4.4.1 The structure of the turbulent Boundary Layer (BL)

A turbulent boundary layer is a balanced environment of production, transport and dissipation of the turbulent kinetic energy (Kline et al., 1967). In terms of the energy cascade, turbulence kinetic energy is produced in the lowest levels of the BL, but turbulence is transferred from the larger turbulence eddies to the smaller ones, till the viscous forces dominate the flow and the energy is dissipated into viscosity. Figure 4-10 illustrates the gradation of layers in a turbulent BL. On the outer layer, the flow is fully turbulent, with dominant large eddies. The inner layer is subdivided in three categories, depending on the viscous effects that are present. In the log-law layer the inertial forces are dominant over the viscous effects. The buffer layer is an intermediate layer, where the viscous and turbulent effects are equally important. Finally, the linear sublayer (or viscous layer) is located close to the wall boundary and the flow is solely dominated by the viscous effects.

4 Computational Fluid Dynamics

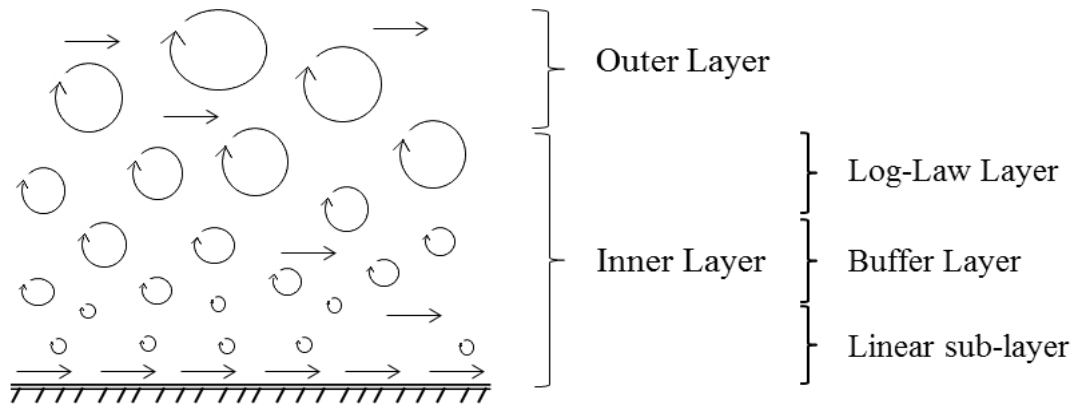


Figure 4-10 The structure of the turbulent boundary layer.

On the studies of the built environment the whole spectrum of the inner layer is evaluated, with major focus on the solid wall boundaries, including the ground surfaces and the building envelope that connect the open urban environment with the building environment. According to Reynolds (1974), every wall layer with approximate constant surface shear stress, τ_w , can be accurately represented by the behaviour of the flow in pipes. Thus, the law of the wall, which shows the relationship between the distance from the wall and the fluid velocity, can be applied in all turbulent flows, independent Reynolds number, by employing the dimensionless values of velocity, u^+ (Equation 4.6) and distance, y^+ (Equation 4.7).

$$u^+ \equiv \frac{U}{u^*} = \frac{U}{\sqrt{\tau_w/\rho}} \quad (4.6)$$

$$y^+ = \frac{u^*y}{\nu} \quad (4.7)$$

where the u^* is the friction velocity that represents the velocity fluctuations in the wall-bounded flow and y the distance from the nearest wall. As illustrated in Figure 4-11, the wall boundaries on the viscous sublayer can be characterised with no slip conditions, since the dominant viscous forces restrain the velocity and flow development (Hanjalić et al., 2003). The viscous layer lies between $0 < y^+ < 5$ and the velocity follows linear development ($u^+ = y^+$). The buffer layer lies between $5 < y^+ < 30$ and it is the intermediate layer prior the logarithmic one, where the velocity profile follows a logarithmic law as in Equation 4.8:

4 Computational Fluid Dynamics

$$u^+ = \frac{1}{\kappa} \ln(E_c y^+) \quad (4.8)$$

where κ is the von Karman constant ($\kappa \approx 0.4$) and E_c is a universal constant equal to 9.8 for fully turbulent flows of high Reynolds numbers. The y^+ value in the logarithmic layer lies between $30 < y^+ < 500$ (Versteeg and Malalasekera, 1995).

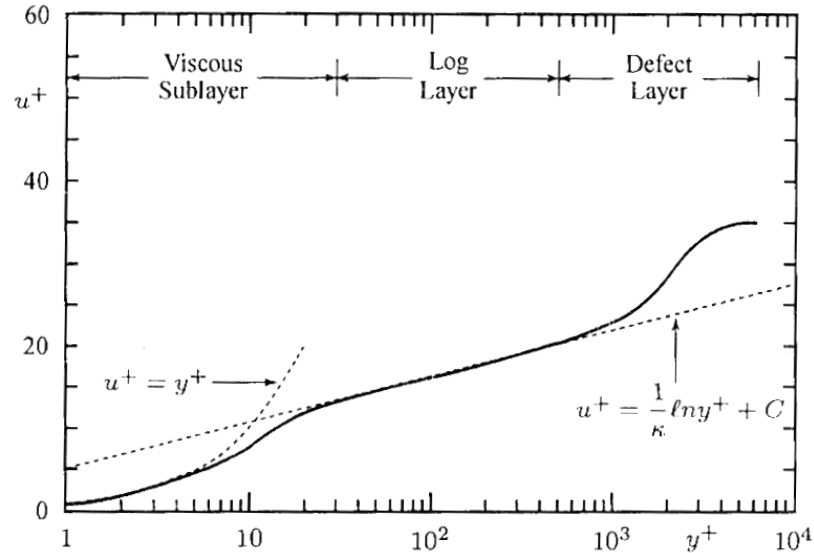


Figure 4-11 Dimensionless velocity profile for a turbulent boundary layer (Wilcox, 1993).

In order to estimate the near wall behaviour, the viscous and buffer layers may be either solved with low Reynolds number modelling, or be approximated with wall functions that are integrated in turbulence models. For the simulation software used, the law of the wall for velocities is based on the wall unit y^* , which is approximately equal to y^+ in equilibrium turbulent boundary layers (ANSYS Inc, 2013). In case of wall-bounded turbulent flows, different type of wall functions serve different study purpose and mesh requirements. More specifically, standard wall functions require a lower limit of $y^* \sim 11.225$, in order to avoid the deterioration of the wall functions and the applicability of the log law. Scalable wall functions are employed in refined meshes that result in $y^* < 11.225$, forcing the employment of the log law, in combination with standard wall functions for $y^* > 11.225$. Finally, enhanced wall functions require a very fine mesh, with the first near-wall node placed at $y^+ \approx 1$. Similarly to enhanced wall functions, hand, the low Reynolds number modelling requires very fine cells to resolve the near-wall region and the y^+ value to be situated in the viscous sublayer ($y^+ < 4$).

4 Computational Fluid Dynamics

Commonly, the wall unit y^+ is a good indicator of the solution accuracy and the adequacy of the mesh resolution near the wall. However, in studies of the urban environment, the y^+ value is equal to several thousands, which poses several questions of the use of y^+ as an accuracy criterion during turbulence model and grid performance verification studies.

4.4.2 Modelling turbulence

There are three developed numerical methods that allow the study of the turbulent eddies in the boundary layer:

Direct numerical simulations (DNS) involve the exact calculation of the unsteady Navier-Stokes equations, including the computation of the fluctuating velocity components from the smaller to the largest eddy scales. Great advantage of the method is the exclusion of any equation modelling.

Large eddy simulations (LES) include calculation of the filtered Navier-Stokes equations, resolving the large eddies and modelling of the smaller sub-grid scales of motion (Piomelli and Balaras, 2002).

Reynolds-averaged Navier-Stokes (RANS) involves modelling of all the turbulent eddies scales by solving the time-averaged Navier-Stokes equations.

In wind engineering and building aerodynamics, the DNS is inapplicable, due to the large computational resources that it requires, along with its application only in simple geometries, since a very fine mesh is required to capture the energy dissipation, resolving the Kolmogorov length scales (Versteeg and Malalasekera, 2007). The LES is computational demanding, since the large eddies need to be modelled precisely in time and space, requiring fine grids and small time-steps, adding to the computational time, effort and memory (Piomelli et al., 2003). The commonly used and adopted for the built environment are the RANS equations with proven high accuracy and reliability, after validations with wind tunnel and in-situ experiments. They also offer the advantage of conducting a wider number of numerical cases in less time without compromising the results' performance (Blocken et al., 2016).

The derived mean average continuity and RANS equations for incompressible flow conditions are presented below:

4 Computational Fluid Dynamics

$$\frac{\partial \bar{u}_i}{\partial x_i} = 0 \quad (4.9)$$

$$\frac{\partial \bar{u}_i}{\partial t} + \bar{u}_j \frac{\partial \bar{u}_i}{\partial x_j} = -\frac{1}{\rho} \frac{\partial \bar{p}}{\partial x_i} + \frac{\partial}{\partial x_j} (2\nu \bar{s}_{ij} - \overline{u'_j u'_i}) \quad (4.10)$$

where \bar{u}_i and \bar{p} are the mean components of velocity and pressure, respectively, $\overline{u'_j u'_i}$ are the Reynolds stresses and \bar{s}_{ij} the mean strain-rate tensor given by:

$$\bar{s}_{ij} = \frac{1}{2} \left(\frac{\partial \bar{u}_i}{\partial x_j} + \frac{\partial \bar{u}_j}{\partial x_i} \right) \quad (4.11)$$

In RANS equations, the first computational node is placed outside the viscous sublayer and in order to capture the near wall turbulence effects different turbulence models are employed, providing near wall velocity estimations. Depending on the case study and the required level of accuracy, different turbulence models have been developed. For the studies of building aerodynamics, natural ventilation performance and flow distribution at the interior of stadium structures the following three turbulence models have been used and their performance will be assessed in a turbulence model assessment study; the standard k - ε model, the realisable k - ε model and the Spalart-Allmaras model, as described below.

4.4.3 The Standard k - ε model (SKE)

The SKE (Launder and Spalding, 1974) is a two-equation turbulence model that determines both turbulence length and time scales, by solving two separate transport equations. It is one of the most widely used and validated turbulence models for flow and heat transfer simulations, due to its acceptable level of accuracy, robustness and computational economy. The model relies on two additional transport equations of the kinetic turbulence (4.12), k , and the energy dissipation (4.13), ε , given by:

4 Computational Fluid Dynamics

$$\rho \frac{\partial k}{\partial t} + \rho \frac{\partial}{\partial x_i} (k v_i) = \frac{\partial}{\partial x_j} \left(\left(\mu + \frac{\mu_t}{\sigma_k} \right) \frac{\partial k}{\partial x_j} \right) + G_k + G_b - \rho \varepsilon - Y_M + S_j \quad (4.12)$$

①
②
③

$$\rho \frac{\partial \varepsilon}{\partial t} + \rho \frac{\partial x}{\partial x_i} (\varepsilon v_i) = \frac{\partial}{\partial x_j} \left(\left(\mu + \frac{\mu_t}{\sigma_\varepsilon} \right) \frac{\partial \varepsilon}{\partial x_j} \right) + C_{1\varepsilon} \frac{\varepsilon}{k} (G_k + C_{3\varepsilon} G_b) - \rho C_{2\varepsilon} \frac{\varepsilon^2}{k} + S_\varepsilon \quad (4.13)$$

①
②
③

where term 1 is the local variation of k and ε with time, term 2 is the advection term, and term 3 represents the diffusion, G_k the generation of k due to mean velocity gradients, G_b the generation of k due to buoyance and $\rho\varepsilon$ expresses the dissipation of k , Y_M represents the contribution of the fluctuating dilatation in compressible turbulence to the overall dissipation rate ($Y_M = 2\rho\varepsilon M^2$, M is the Mach number), and S_k and S_ε are user-defines source terms. The constants $\sigma_k = 1.0$, $\sigma_\varepsilon = 1.3$ are turbulent Prandtl numbers for k and ε respectively, $C_\mu = 0.09$, $C_{1\varepsilon} = 1.44$, $C_{2\varepsilon} = 1.92$, and μ_t expresses the turbulence viscosity, defined as:

$$\mu_t = \rho C_\mu \frac{k^2}{\varepsilon} \quad (4.14)$$

The constant values have been determined through a series of experimental studies on fundamental turbulent flows; including the encountered shear flows and decaying isotropic grid turbulence and cases of high Reynolds numbers. Thus, the SKE model is considered a semi-empirical model, with main disadvantages the overestimation of turbulence of k and underestimation of the reverse flow areas (Tominaga et al., 2008). However, this is highly dependent on the case study; the complexity of the model and the main objective of the study. In studies of the built environment, the standard k - ε turbulent model has been used widely in wind comfort studies (Mirzaei and Haghghat, 2010; Zhang et al., 2011; Ramponi et al., 2015), assessment of natural ventilation (Montazeri, 2011; Mora-Pérez et al., 2015) and wind performance studies in buildings (Han, 1989; Baskaran and Stathopoulos, 1994; Cóstola and Alucci, 2007; Asfour, 2010; Montazeri and Blocken, 2013).

4.4.4 The Realizable k - ε turbulence model (RKE)

The realizable k - ε model (Shih, 1995) differs over the standard k - ε model in two factors. The code has been modified to remove unphysical values of variables, such

4 Computational Fluid Dynamics

as negative normal stresses and also the value of C_μ is not constant, but a function of the turbulence fields, mean strain and rotation rates (Moshfegh and Nyireddy, 2004).

$$\rho \frac{\partial k}{\partial t} + \rho \frac{\partial}{\partial x_j} (kv_j) = \frac{\partial}{\partial x_j} \left(\left(\mu + \frac{\mu_t}{\sigma_k} \right) \frac{\partial k}{\partial x_j} \right) + G_k + G_b - \rho \varepsilon - Y_M + S_k \quad (4.15)$$

$$\rho \frac{\partial \varepsilon}{\partial t} + \rho \frac{\partial}{\partial x_j} (\varepsilon v_j) = \frac{\partial}{\partial x_j} \left(\left(\mu + \frac{\mu_t}{\sigma_\varepsilon} \right) \frac{\partial \varepsilon}{\partial x_j} \right) + C_{1\varepsilon} \frac{\varepsilon}{k} C_{3c} G_b - \rho C_{2\varepsilon} \frac{\varepsilon^2}{k + \sqrt{\nu \varepsilon}} + \rho C_{1\varepsilon} S\varepsilon + S_\varepsilon \quad (4.16)$$

where $C_1 = \max \left[0.43, \frac{\eta}{\eta + 5} \right]$, $\eta = Sk/\varepsilon$, $S = \sqrt{2S_{ij}S_{ij}}$ and $\sigma_k = 1.0$, $\sigma_\varepsilon = 1.3$, $C_{1\varepsilon} = 1.44$, $C_{2\varepsilon} = 1.9$.

The advantages of the RKE over the SKE have been proved in swirling flows and areas of flow separation (Suryan et al. 2013), in buoyant flows in street canyons (Allegrini et al., 2014) and in wind engineering studies of large urban scale (Janssen et al., 2012). The realisable k - ε model has been used to describe flow distributions at the stadium interior, due to their geometric similarities to urban canyons (van Hoof and Blocken, 2010a).

4.4.5 The Spalart-Allmaras model (SA)

The SA model is one-equation turbulence model developed by Spalart and Allmaras (1992) to perform aerospace case studies. It solves only a modelled transport equation for the kinematic eddy turbulence viscosity, ν , and it does not calculate the turbulence kinetic energy, k . The transport equation is given below:

$$\begin{aligned} & \textcircled{1} \quad \textcircled{2} \\ & \frac{\partial(\rho\nu)}{\partial t} + \frac{\partial}{\partial x_i} (\rho\nu u_i) \\ & = G_\nu + \frac{1}{\sigma_\nu} \left[\frac{\partial}{\partial x_j} \left\{ (\mu + \rho\nu) \frac{\partial \nu}{\partial x_j} \right\} + C_{b2} \rho \left(\frac{\partial \nu}{\partial x_j} \right)^2 \right] - Y_\nu + S_\nu \\ & \textcircled{3} \quad \textcircled{4} \quad \textcircled{5} \quad \textcircled{6} \end{aligned} \quad (4.17)$$

where term 1 expresses the rate of turbulence viscosity change, term 2 transport of ν by convection, term 3 the production of ν , term 4 the transport of ν by turbulence diffusion, term 5 the rate of production of ν and term 6 the rate of dissipation. The SA model has proven its accuracy in aerospace and aeronautic studies, in wind

4 Computational Fluid Dynamics

turbine studies (Belamadi et al., 2016; Zaghi et al., 2016), in prediction of ventilation rates and aerodynamic characteristics of livestock trailers (Gilkeson et al., 2009), as it can successfully predict the flow result for boundary layers under adverse pressure gradients.

4.5 Verification and Validation

Computational Fluid Dynamics is indisputably a powerful tool that approximates the interactions occurring between the simulation models and the environment. However, simulation results are mainly based on simplifications of real systems, which are modelled under time and space compression (Bellinger, 2004). For this reason, it is important to ensure the accuracy of the results before their adaptation. Two fundamental principles that determine whether the correct governing equations have been solved and that the governing equations are solved correctly are well known as verification and validation.

Verification is the process of assessing the numerical error and the uncertainty of the calculation results. It can be divided along solution and code verification. For solution verification, Roache (1994) developed the Grid Convergence Index (GCI) technique, originated from Richardson Extrapolation (RE). The GCI is based on the generation of different mesh sizes with constant grid refinement ratio and uniform order of accuracy in all space and time directions. If these criteria are fulfilled, then it is possible to determine the discretisation error in a fine and coarse grid solution according to the following equations:

$$E_1[\text{fine grid}] = \epsilon / (r^p - 1) \quad (4.18)$$

$$E_2[\text{coarse grid}] = r^p * \epsilon / (r^p - 1) \quad (4.19)$$

where $E_{1,2}$ are fine (E_1) and coarse (E_2) grid Richardson error estimator and ϵ is an estimator of the numerical solution difference, calculated by Equation 4.20:

$$\epsilon = (f_2 - f_1) / f_1 \quad (4.20)$$

where f_1, f_2 are numerical solutions generated from fine and coarse grids respectively, r is the grid refinement ratio (ideally equal to 2), and p is the order of accuracy (1 for first and 2 for second order discretisation scheme).

The solution is of high level of accuracy when $E_1 \ll 1$ (Roache, 1994). In literature, ϵ is commonly used as the only error estimator for the grid independency studies.

4 Computational Fluid Dynamics

However, this error is a simple variance estimation between the initial and coarse, and initial and fine grid solutions, without taking under consideration neither the grid ratio nor the order of accuracy, which may lead to conservative error estimation.

For case studies that do not comply with the requirements for $r = 2$ and $p = 2$, a safety factor is introduced to ensure the numerical accuracy of the discretised domain (Roache, 1997):

$$GCI_1^{fine} = F_s |E_1| \quad (4.21)$$

$$GCI_2^{coarse} = F_s |E_2| \quad (4.22)$$

where F_s is a safety factor in the range of [1,3]. A value of $F_s = 3$ is commonly used that sets $GCI = \epsilon$, when $r = 2$ and $p = 2$, which as mentioned earlier is a conservative but accurate error estimation for that particular case. For more complex studies a value of $F_s = 1.25$ is recommended (Roache, 1998).

An important consideration prior the performance of the mesh independency study that facilitates the selection of the best grid assessment method is the evaluation of the convergence ratio, R , which denotes the classification of the computational nodes and it is based on the ratio of the solution change for the different meshes (Franke and Frank, 2008). R is given by Equation 4.23:

$$R = \frac{f_2 - f_1}{f_3 - f_2} \quad (4.23)$$

where f_1, f_2, f_3 are the comparative solutions generated from the fine, the medium and the coarse meshes respectively, and R is the value that defines the discretisation convergence and can be classified as:

1. Monotonic convergence: $0 < R < 1$
2. Oscillatory convergence: $R < 0, |R| < 1$
3. Monotonic divergence: $R > 1$
4. Oscillatory divergence: $R < 0, |R| > 1$

The GCI presented in Equations 4.21-4.22 is applicable for structural grids that allow uniform refinement and coarsening ($r = \text{constant}$). However, in case of large and complex geometries it is not always feasible to produce grids with the same refinement/ coarsening ratio. As an example of this, a fully structured grid refined by a ratio of 2 would lead to a grid 8 times larger, which can be computational too

4 Computational Fluid Dynamics

expensive and also time consuming. For this reason, the effective ratio value, r_{eff} , is used, which is dependent on the total number of elements, given by Equation 4.24 (Roache, 1994):

$$r_{eff} = (N_1/N_2)^{1/D} \quad (4.24)$$

where N_1 , N_2 are the number of cells in fine and coarse grids and D is the dimensionality of the problem ($D = 1$ for 1D, $D = 2$ for 2D and $D = 3$ for 3D models). The GCI is then calculated by using the Equation 4.21-4.22.

Inaccuracies on the order of convergence, p , may also be observed, commonly due to the grid quality, the non-linearity of the solution, the turbulence modelling or other cause. Thus, the exact value of p may be calculated using three meshes using Equation 4.25 for cases of constant r and by Equation 4.26 for cases of non-constant (Stern et al., 2001):

$$p = \frac{\ln(\epsilon_{32}/\epsilon_{21})}{\ln(r)} \quad (4.25)$$

$$p_k = \frac{\ln(\epsilon_{32}/\epsilon_{21})}{\ln(r_{k_{21}})} + \frac{1}{\ln(r_{k_{21}})} \left[\ln(r_{k_{32}}^{p_k} - 1) - \ln(r_{k_{21}}^{p_k} - 1) \right] \quad (4.26)$$

where ϵ is the comparative solution change for the medium-fine, ϵ_{21} , and the coarse-medium meshes, ϵ_{32} , as described in Equation 4.20.

The code verification is associated with the evaluation of the error (Roache, 2002). In other words it should be proven that “*the computational implementation accurately represents the conceptual model and its solution*” (Oberkampf and Trucano, 2002). The code verification requires that the algorithms produce accurate solutions of the discrete algebraic equations and that they converge to the correct numerical results in all circumstances (Oberkampf and Trucano, 2002).

The validation of the CFD models determines the degree of accurate representation of a real system. Models’ validation is based on comparison of the obtained results with either other similar CFD studies or real experiment data. It is recommended to validate the CFD codes and turbulence models to be used prior their integration to the final flow problem (Casey and Wintergerste, 2000).

4 Computational Fluid Dynamics

4.6 ABL flow simulation

In building aerodynamics, depending on the purpose of the study, might require the consideration of variable turbulent length scales, during the transition from urban to building scale. Thus, the need for an accurate approach of the flow phenomena, led to an in depth study of the interactions between the urban and the building environment, whilst also highlighting the challenges facing the accurate simulation of the ABL flow characteristics.

On the CFD studies of the urban environment, the mean ABL velocity profile is assumed to follow a logarithmic production that when it is fully-developed it can be described by the Equation 3.3, suggested by Richards and Hoxey (1993), followed by the mean turbulent kinetic energy (Equation 4.27) and dissipation rate profiles (Equation 4.28):

$$k = \frac{u_{ABL}^{*2}}{\sqrt{C_\mu}} \quad (4.27)$$

$$\varepsilon = \frac{u_{ABL}^{*3}}{\kappa(y + y_0)} \quad (4.28)$$

where u_{ABL}^* is the ABL friction velocity, y the height, y_0 the aerodynamic roughness length and κ the von Karman constant (usually 0.40-0.42). Equations 4.27-4.28 are the analytical solutions of the standard k - ε when the constant values of the turbulence model are mathematical based on the Equation 4.29:

$$\kappa^2 = (C_{\varepsilon 2} - C_{\varepsilon 1})\sigma_\varepsilon\sqrt{C_\mu} \quad (4.29)$$

The results produced from the simulation studies on ABL flow showed that the homogeneity of the flow is not properly maintained along the domain, even if the aforementioned requirements and recommendations were taken into consideration. More specifically, the profile of the turbulent kinetic energy appears to have a large peak close to the wall and specifically on the second cell from the ground (Hargreaves and Wright, 2007). This occurs due to a large shear production “feeds into the Reynolds stress” (Zhang and Yang, 2009). The improvements on the ABL flow simulation were based either on the modification of the wall functions or the inlet ABL flow profile, as summarised in the following paragraphs.

4 Computational Fluid Dynamics

In order to deal with the incompatibility between the ABL boundary conditions and the standard wall functions, a modification of the k - ε model using User Define Scalars was proposed by Hargreaves and Wright (2007). The changes on the ground law of the wall were performed in agreement with the ABL preconditions for homogeneity. The results indicated that the homogeneity of the flow was not retained along the whole the domain (total domain length = 10,000 m), but it showed a relative improvement between the 2,500 m to 4,000 m. The peak on the turbulent kinetic energy profile was relatively larger than the one in the previous study case, but the velocity profile showed a smaller decay along the domain in comparison to the one with the unmodified turbulence model.

Parente et al. (2011) were able to solve the wall function-arising problem and remove the peak produced in the turbulent kinetic energy profile by modification of the wall function based on the aerodynamic roughness. The modification enabled the calculation of the turbulent kinetic energy at the wall spaced over a distance equal to the aerodynamic roughness ($y_P + y_0$). Thus equilibrium was achieved between the production and the dissipation rate, preserving the universal logarithmic law of the wall (Balogh et al., 2012).

Zhang and Yang (2009) moderated the turbulence standard k - ε model, so the turbulence kinetic energy and dissipation rate will be equal when logarithmic wind profile is applied on the inlet boundary condition. The resulted ABL inlet profiles of U , k and ε that were suggested are the following:

$$U(x) = \frac{u_*}{\kappa} \ln \left(\frac{y + y_0}{y_0} \right) \quad (4.30)$$

$$k(x) = u_*^2 \sqrt{\frac{C_1 \ln \left(\frac{y + y_0}{y_0} \right) + C_2}{C_\mu}} \quad (4.31)$$

$$\varepsilon(x) = \frac{u_*^3 \sqrt{C_1 \ln \left(\frac{y + y_0}{y_0} \right) + C_2}}{\kappa(y + y_0)} \quad (4.32)$$

where C_1 and C_2 are adjustable constants that represent the nonlinear experimental data of the turbulence development on the vertical direction of the domain. The results of the study showed a well-maintained homogeneity of both velocity and turbulent quantities along the flow domain and highlighted the need to use the revised k - ε model, three-equations, four-equations or LES for accurate pressure

4 Computational Fluid Dynamics

estimations, because the standard k - ε model tends to overestimate the wind pressure coefficient and turbulent kinetic energy directly upstream of the building structures.

The homogeneity of the neutral ABL profile was also studied by Richards and Norris (2011) achieved to prevent kinetic energy anomaly, by applying shear stress values (τ_{xz}) on the north and south sides of the cells' faces and resulting to equilibrium. They also concluded to the fact that the peak of the turbulence kinetic energy on the second cell is not related to the k - ε model, as mentioned by Hargreaves and Wright (2007), but to the discretisation process used in calculating the production term.

4.6.1 Computational requirements

The simulation of the ABL, as mentioned earlier, is produced mainly by the RANS approach, using the standard k - ε turbulence model. Due to the limitations in Wind Engineering modelling studies, particularly related with the inhomogeneity of the ABL flow profile over terrain types with different aerodynamic roughness, there have been established some guidelines that tend to produce fully developed and equilibrium ABL flow profiles. On theoretical basis, these requirements are outlined hereafter:

1. A fine grid close to the ground boundary level with a recommended height of first cell equal or less than 1m, as depicted in Figure 4-12. The vertical mesh resolution is necessary for studies that examine the flow distribution close to ground level, such as pedestrian wind comfort studies (Blocken et al., 2007). However, ABL flow research studies have shown that the y^+ may exceed the value of 10,000 (Hargreaves and Wright, 2007). This creates some doubts on the accuracy of the logarithmic law of the wall, because it is applicable for y^+ values ranging from 30 to 500 or even 1,000 (Blocken et al., 2007). Because the results produced seem to comply with the reality, it entails the need for a new y^+ limit values for the case of ABL flows when rough walls are used (Hargreaves and Wright, 2007).

4 Computational Fluid Dynamics

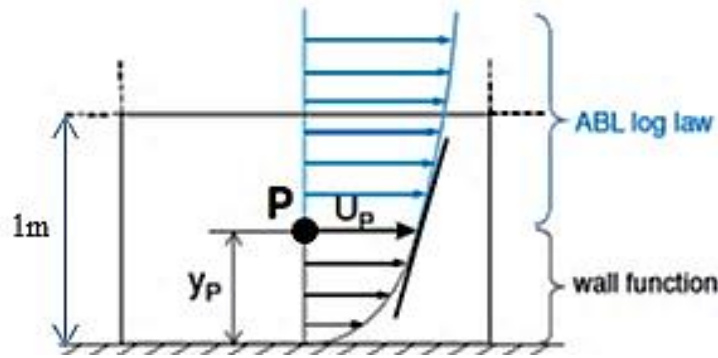


Figure 4-12 Representation of the log-law ABL velocity profile on the first cell and mean velocity at the centre point of the cell (Blocken et al., 2007).

2. Homogeneity of the ABL flow throughout the computational domain. The flow is disturbed not only from the high Reynolds numbers, but also and more importantly from the aerodynamic roughness. For this reason wall functions are employed using roughness modifications (Blocken et al., 2007).
3. The value of y_p , which is half the height of the first cell (as shown in Figure 4-12), to be more than the roughness height k_s of the ground ($y_p > k_s$).
4. A known mathematical relationship between the roughness length (y_0) and roughness height (k_s). The mathematical formulas used in literature and in software are the following:

(Hargreaves and Wright, 2007)	$k_s = 20 * y_0$	(4.33)
-------------------------------	------------------	--------

(Blocken et al., 2007)	$k_s = 30 * y_0$	(4.34)
------------------------	------------------	--------

(Fluent)	$k_s = 9.793 * y_0 / C_s$	(4.35)
----------	---------------------------	--------

(Ansys CFX)	$k_s = 29.6 * y_0$	(4.36)
-------------	--------------------	--------

The preconditions (1) and (3) are difficult to be fulfilled simultaneously, when terrains of high roughness are to be modelled. For instance, modelling open country with low vegetation and aerodynamic roughness length of $y_0 = 0.03$ m (Wieringa, 1992) will produce values of roughness height $0.6 \text{ m} \leq k_s \leq 0.9 \text{ m}$, based on the aforementioned formulas, resulting to minimum cell height of 1.2 m. This value conflicts with the first condition of first cell height and for this reason it is suggested to use finer grid on the areas of interest and coarser to the rest of the domain, as depicted in Figure 4-13 for a bluff body located in the middle of the domain.

4 Computational Fluid Dynamics

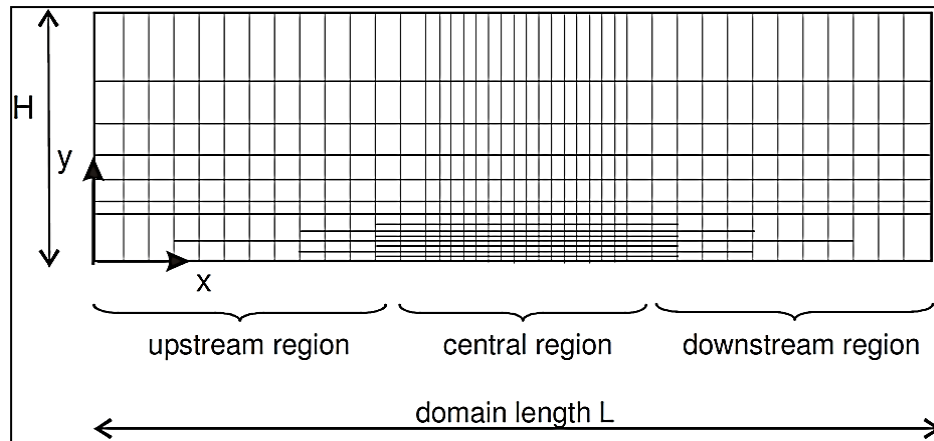


Figure 4-13 Structure of the computational grid for the simulation of a bluff body at the centre of the longitudinal axis (Blocken et al., 2007).

4.6.2 Computational recommendations

Due to potential implications on the accuracy of the studies that may be caused due to insufficient compliance with the four modelling parameters, there have been developed and tested techniques that tend to compensate the modelling and numerical errors. They are mainly related to the size of the computational domain and the applied inlet boundary conditions.

The computational domain, in the assessment of the ABL without any bluff bodies included, should be long enough to allow for the flow to become fully developed and obtain horizontal homogeneity. This condition however may require domain length of more than 10,000 m (Blocken et al., 2007). For this reason, it is recommended to apply periodic conditions at the inlet and outlet that represent the symmetry of the flow between the two boundaries, allowing for pressure drop, full-development and avoiding reverse flow problems. Symmetry should be applied to the side and top boundaries, in order to allow for parallel flow (Franke et al., 2004). Alternatively, on the side walls should be applied slip wall boundary condition with zero shear stress values in any direction and on the top domain a constant shear stress $\tau_w = \rho u_{ABL}^{*2}$ on the flow direction. The later condition is also suggested by Hargreaves and Wright (2007) to produce a horizontally homogeneous ABL velocity profile.

When bluff bodies are to be modelled, the size of the domain should allow for the inflow to become fully-developed and homogeneous before impinging the model. Thus, for a given model with total height H , the domain should have $5H$ length upstream, $10H$ length downstream, $6H$ length height and the lateral extensions

4 Computational Fluid Dynamics

should be of that distance that will comply with a final 3 % blockage ratio³ (Franke et al., 2004), as depicted in Figure 4-14 below:

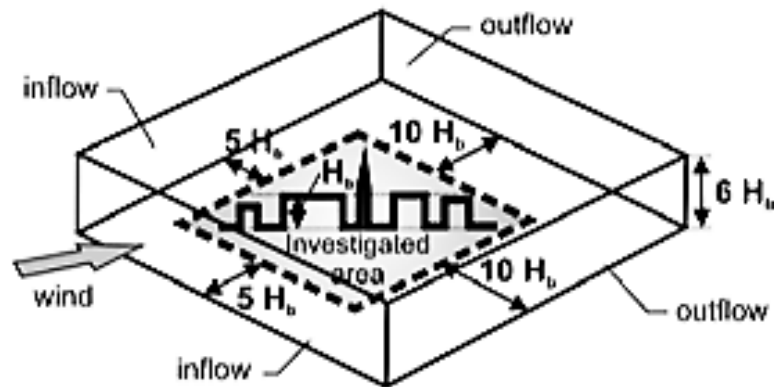


Figure 4-14 Dimensions of the computational domain around the studied area (Franke et al., 2004).

In order to ensure a horizontally homogeneous impinging profile, Blocken et al. (2007) suggested the simulation of the empty computational domain first, with the absence of the building model. By applying similar boundary conditions and roughness characteristics on the identical spatial discretised domain, the simulation would allow the investigation of maintaining the homogeneity along the domain. In cases that the velocity profile was deviating, then the generated mean equilibrium profiles of U , k , ε in the outlet could be exported and imported as inlet profile for the modelling of the original case, including the building model.

In case of CFD validation studies with ABL wind tunnel experiments, different considerations should be taken into account. As reported by Blocken et al. (2008), Blocken et al. (2007) and Franke et al. (2004), in ABL wind tunnel facilities it is almost impossible to achieve horizontal homogeneity along the test section, due to continuous geometrical alterations of the facility and the spatial limitation of the top boundary that prevents fully diffusion of turbulence energy to occur (McVehil et al., 1967).

As shown in Figure 4-15a, the generated vertical profile at the end of the ground roughness blocks is different with the one generated at the turntable, where the building model will be placed. In order to produce CFD studies that will accurately reproduce the developed velocity profile in the wind tunnel, it is recommended to model the empty computational domain first. The domain geometry should be identical to the one of the wind tunnel test section. Great care should be given to the

³ Blockage ratio is the ratio of the projected frontal-area of the building in the flow direction to the free cross section of the computational domain.

4 Computational Fluid Dynamics

inlet boundary conditions, in order to produce a velocity profile at the position of the model similar to the one at the middle of the turntable, as shown in Figure 4-15b. The matching of the profiles is detrimental for the correct validation of the case study and the minimisation of errors due to the unintended streamwise gradients (Blocken et al., 2008).

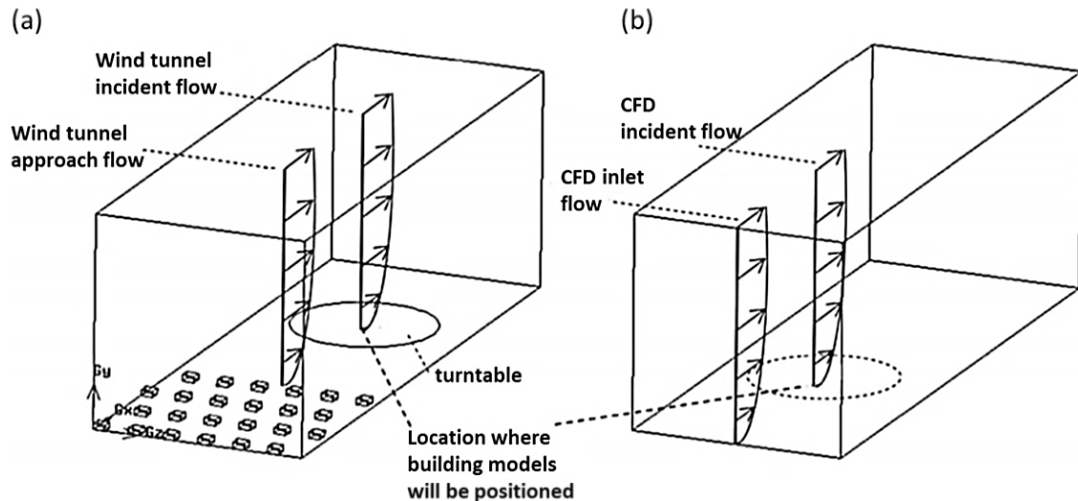


Figure 4-15 Schematic representation of an empty ABL wind tunnel (a) and the empty computational domain (b) and the position at the turntable where the incident flow profiles require similarity (Blocken et al., 2008).

4.7 CFD stadium parameterisation

The aerodynamic study of the stadium model is particularly difficult to perform, regarding the number of the aforementioned requirements and recommendations for the generation of reliable and accurate results. The main difficulties are posed to the development of a computational model that will allow the successful simulation with the available computational means and the development of a methodology that will be easily validated with the ABL wind tunnel experimentation.

4.7.1 Computational domain and discretisation

The computational domain that represents the environment around the stadium model was selected similar to the actual wind tunnel test section, where the experimental validation study was performed. The geometrical similarities between the domains offer two main advantages: 1) the potential blockage effects generated by the wind tunnel geometry would be also simulated by the CFD simulations and 2) the inlet velocity profile would be represented by the CFD generated results of the wind tunnel test section, preventing potential inlet boundary condition inconsistencies.

4 Computational Fluid Dynamics

The computational domain used for the stadium simulations is illustrated in Figure 4-16 and has similar dimensions to the wind tunnel test section starting exactly after the end of the ground blocks baseboard and extended till the end of the test section. More specifically, the domain is $2.4 \times 3.81 \times 1.88 \text{ m}^3$ ($W \times L \times H$). The recommendations for CFD simulation of building structures by Franke et al. (2004) may be violated, regarding the lateral, frontal and rear wall boundary distances, but the purpose of the study was to represent and validate the flow environment developed in the wind tunnel facility, with no intension to scale up the stadium model. The generated domain resulted to a blockage ratio of 3.4 % and 2.9 % for the wind angle of 0 and 90 degrees respectively, which is smaller than the recommended value of 5 % for wind tunnel experimentation studies (Biagini et al., 2007).

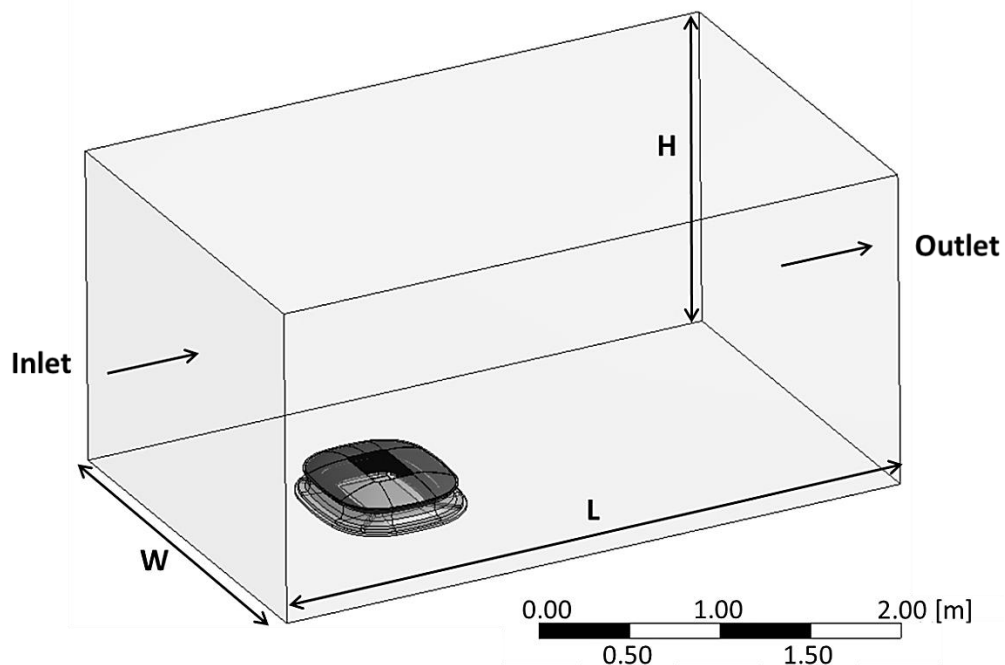


Figure 4-16 Description of the computational domain used for the simulation of the stadium model.

The primarily considered parameters for the domain discretisation were the complexity of the stadium model and the recommendations for grid consistency, continuity and convergence. Due to the difficulties in creating a fully hexahedral structured mesh and regarding the multidimensional characteristics of the model to be considered, a hybrid hexahedral-tetrahedral mesh solution was achieved by creating sweepable bodies and bodies of influence. More specifically, as illustrated in Figure 4-17a, the model was segmented in total 26 sweepable bodies, in addition to the creation of one body of influence for a more controlled and smooth transition

4 Computational Fluid Dynamics

towards the stadium walls. Symmetry was also applied to the domain in order to reduce the computational cost, assuming flow with mirror symmetry (Figure 4-17b).

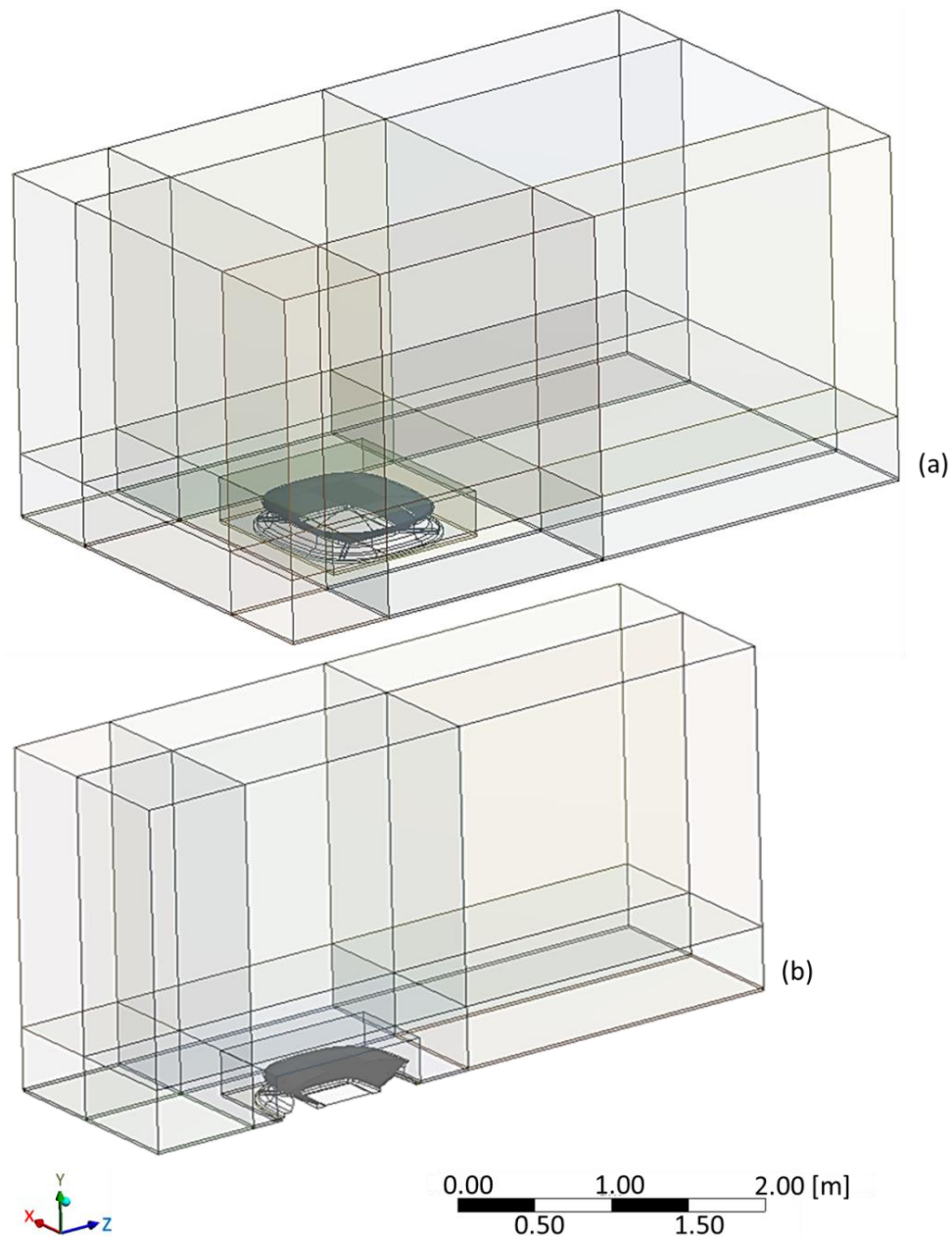


Figure 4-17 Illustration of the discretised computational domain (a) and the symmetric domain for simulation (b).

The segmented bodies were discretised after employing individual edge sizing functions with the required bias ratio to create higher resolution close to the areas of interest, including the top, bottom and side boundary walls of the wind tunnel test section. The bias also allowed controlled grid continuity along the three-dimensional space. The body of influence was designed 1 m wide, 0.9 m long and 0.25 m high to enclose tightly the stadium model and was meshed with cell size equal to 0.0035 m. For the generation of the grid, the mesh recording option, as described in

4 Computational Fluid Dynamics

Section 4.3.4, was employed that controlled the beginning of the mesh construction from the outer and hexahedral to the inner and tetrahedral domain.

Figure 4-18 and Figure 4-19 illustrate the generated grid, which is composed by fully structural hexahedral cells in the outer domain and unstructured conformal tetrahedral cells around the stadium model walls. The total mesh size of 35,904,441 is a computationally expensive model, which satisfies the mesh requirements of Blocken et al. (2007) for structures in the built environment, including finer mesh on the front, rear and lateral sides of the building model, to capture the areas of flow recirculation.

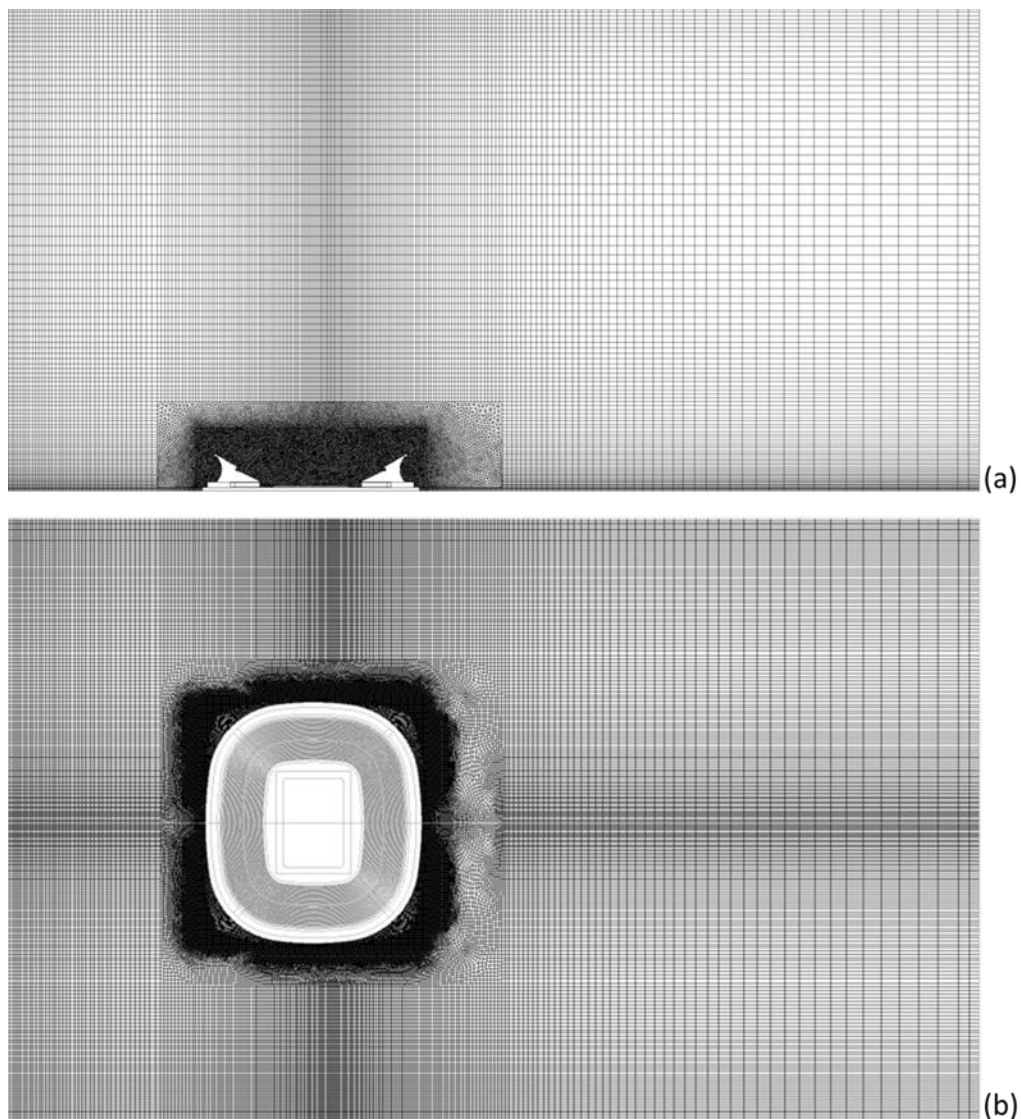


Figure 4-18 Side and top view of the generated grid for the computational domain.

4 Computational Fluid Dynamics

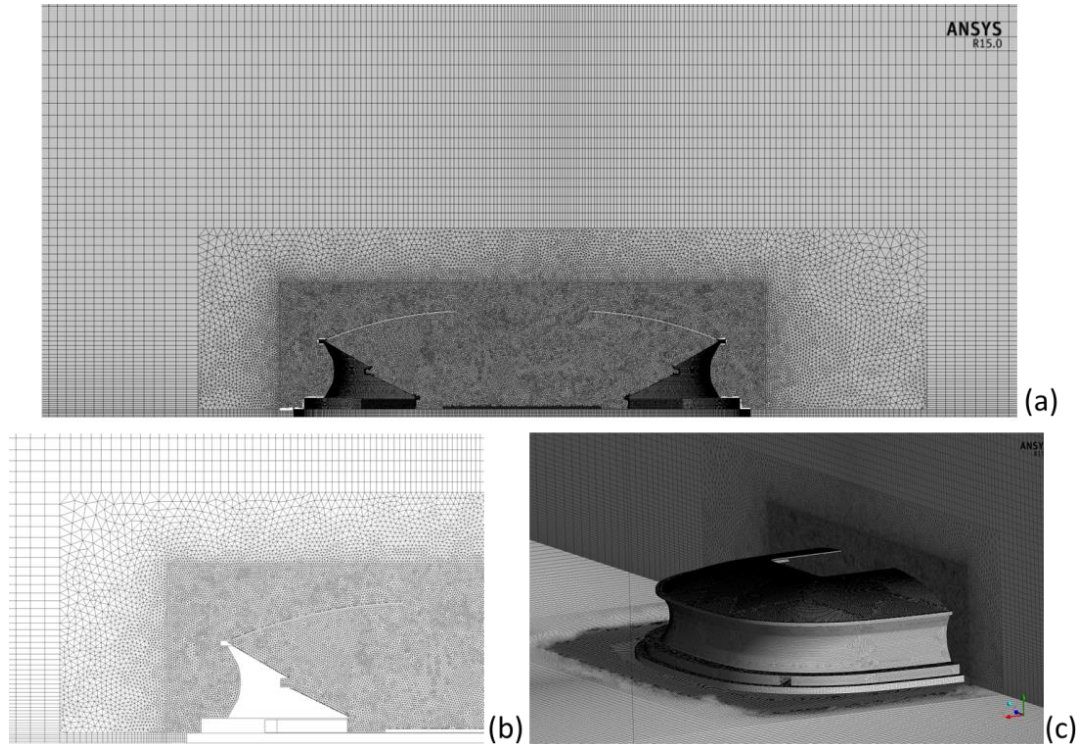


Figure 4-19 Computational mesh on the symmetry plane of the domain (a, b) and on the stadium walls (c).

The quality of the mesh was also assessed after generating information on the cell properties. The values of aspect ratio, orthogonality and skewness are given in Table 4.2, indicating a grid of acceptable quality, with only a very small percentage of the cells to exceed the threshold values.

Table 4.2 *Quality measures for the generated mesh.*

Quality measure	Statistics	Details
Aspect ratio	(max, avg) = (28.5, 1.96)	45 % > 5
Orthogonality	(min, avg) = (0.18, 0.87)	1.5 % < 8
Skewness	(max, avg) = (0.97, 0.2)	3.3 % > 0.15

4.7.2 Simulation set-up

The preliminary stadium analysis involved the use of the Semi-Implicit Method for Pressure-Linked Equations (SIMPLE) algorithm for pressure-velocity coupling and the standard $k-\varepsilon$ turbulence model with standard wall functions. At the inlet, the velocity plane profile generated from the simulation of the ABL wind tunnel facility was used to minimise any inconsistencies caused by the blockage effect (see Appendix 0). Turbulence parameters of turbulence intensity and length scale were also set with values equal to $I = 3.5\%$ and $\ell = 0.168\text{ m}$ respectively, adopted from the wind tunnel results and the characteristics length of the wind tunnel test section.

4 Computational Fluid Dynamics

At the outlet, zero static pressure was set with turbulence parameters similar to the inlet. The domain and the stadium walls were set with a roughness height, k_s , equal to 0.001 m and roughness constant, C_s , equal to 0.5. Second-order discretisation schemes were applied to the pressure, momentum and the transport equations. The solution stabilisation was controlled by disabling the convergence criteria and defining a velocity monitor point at the centre of the stadium bowl, 0.05 m above the pitch level. The parameterisation of the simulation is summarised in Table 4.3. To compensate the computationally costly and time consuming simulation, a parameterisation file was created in batch mode and submitted for execution to the High Performance Computing (HPC) facilities of the University of Sheffield.

Table 4.3 Solver settings for the simulation study of the stadium model.

Turbulent Model	Standard k - ϵ model with standard wall functions
Boundary Conditions	
Inlet	Velocity profile for $U_{inlet} = 7$ m/s
Turbulence Parameters	$I = 3.5\%$ & $\ell = 0.168$ m
Outlet	Pressure-outlet with zero pressure
Turbulence Parameters	$I = 3.5\%$ & $\ell = 0.168$ m
Walls (all)	$k_s = 0.001$ & $C_s = 0.5$
Solution Methods	SIMPLE; Second Order for pressure, momentum and turbulence transport equations
Convergence Criterion	None (to control end of calculation)

4.8 Grid verification

The grid verification study aims to determine a computational mesh that will generate accurate solution values with the minimum computational cost. Four different meshes were tested to ensure mesh independency of the solution. Due to the expected large computational memory required for the solution a series of mesh recommendations were employed to facilitate the space discretisation process. The sweepable bodies constructed solely by structured hexahedral cells were not modified in size, since the solution is primarily dependent on the grid around the stadium model and secondarily on the test section blockage effects.

More specifically, a coarser mesh was generated by increasing the cell size of the body of influence from 0.003 m to 0.0035 m, resulting to 25,096,036 mixed cells. The change of 0.5 mm led to a total decrease of around 10,800,000 tetrahedral cells. Grid refinement was performed by employing adaptive mesh refinement techniques, at the surfaces more subjective to change, including the external roof surface, the spectator tiers and the pitch area. The mesh in the exact proximity of the selected

4 Computational Fluid Dynamics

surfaces was refined twice with a ratio of 2, resulting to a mesh of 36,875,810 and 41,870,905 mixed cells. The boundary adaptation technique is recommended for the generation of acceptable mesh quality, without imposing additional computational cost on the simulation process (Franke et al., 2004). Figure 4-20 illustrates the grid structure on the roof structure for the four different cell sizes.

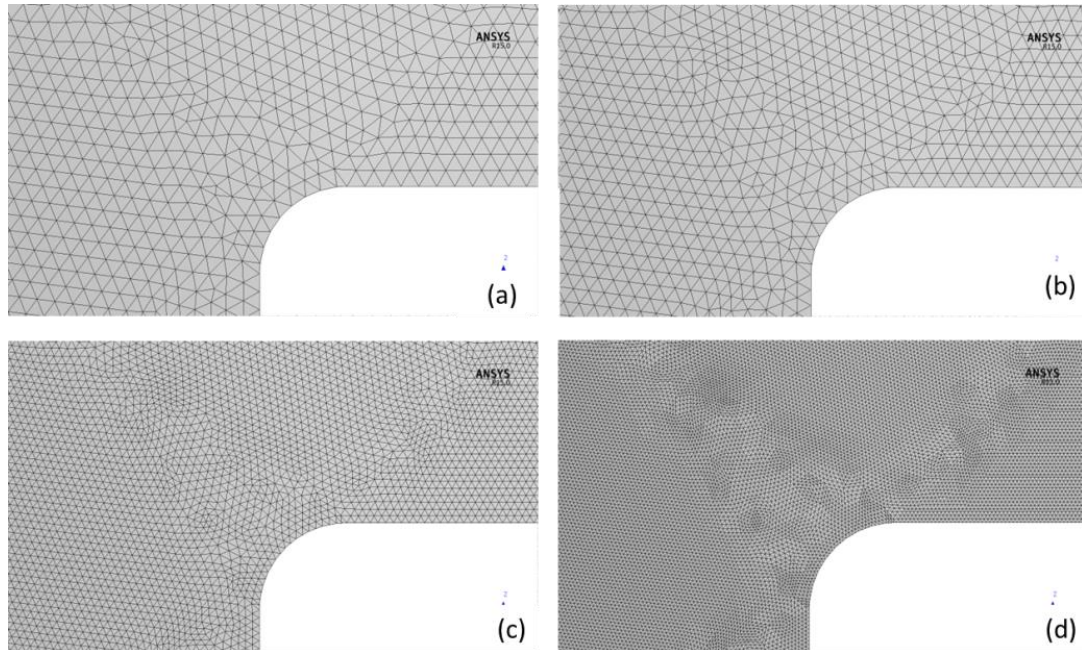


Figure 4-20 Grid structure on the roof surface for the generated meshes; 25,096,036 (a), 35,904,441 (b), 36,875,810 (c) and 41,870,905 (d).

The selection of the optimum mesh size was based on the following four criteria: 1) the assessment of one important flow parameter, 2) the assessment of the dimensionless distance, y^+ , on the stadium walls, 3) the evaluation of the absolute convergence criteria, and 4) the use of the Grid Convergence Index and the Richardson Extrapolation method.

The first assessment criterion involved the calculation of the dimensionless velocity (U/U_{ref}) along a longitudinal line crossing the stadium interior, located on the symmetrical plane 0.105 m above ground level. As reference velocity was selected the undisturbed velocity at roof height, or 0.145 m above ground level. The comparison of the generated results is illustrated in Figure 4-21 for the four grid structures. The dimensionless velocity chart indicates relatively similar trend of the wind behaviour for all meshes. More specifically, the results can be classified in two groups, since for the two coarser and the two finer meshes almost identical velocity values were generated. The highest differences are observed at the area below the oculus configuration, where flow disturbance and recirculation are expected to occur.

4 Computational Fluid Dynamics

The highest deviations of the dimensionless velocity occur at the points A, B and C of Figure 4-21 between the coarse and the finest mesh with percentage differences equal to 5.4 %, 44 % and 64.4 % respectively.

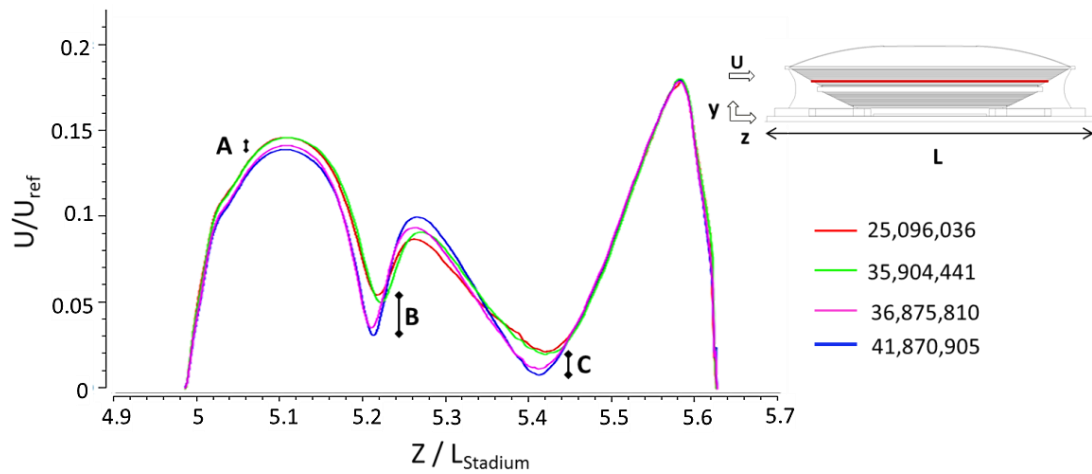


Figure 4-21 Comparison of the dimensionless velocity profiles along a horizontal line crossing the stadium 0.105 m above ground level; $U_{ref} = 5.23$ m/s and $L_{stadium} = 0.96$ m.

The second criterion included the generation of the y^+ values at the stadium interior and exterior walls, as illustrated in Figure 4-22. According to the results, the grid generation resulted in a very fine mesh close to walls. The smallest values were generated for the finest mesh (Figure 4-22d), with an average y^+ equal to 6.88, substantially less than the required value of 11.255 to avoid the deterioration of the standard wall functions. However, small y^+ values were generated for all the constructed grids, which imply the inadequacy of the standard wall functions to determine successfully predictions of the flow properties in the near-wall region.

4 Computational Fluid Dynamics

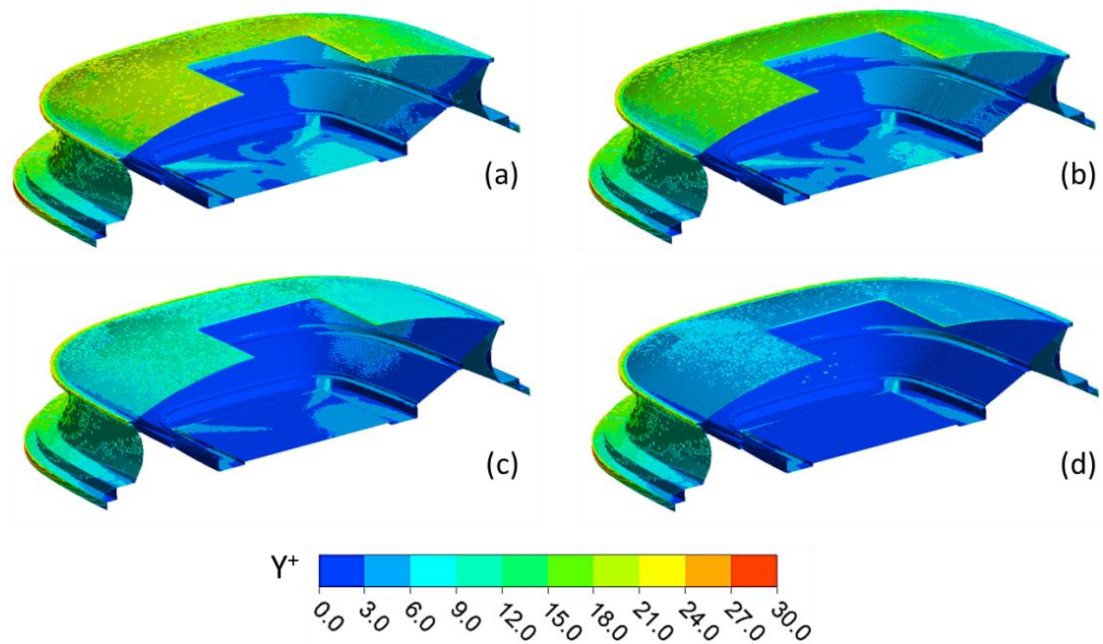


Figure 4-22 Y^+ values on the stadium interior and exterior walls for the generated meshes; 25,096,036 (a), 35,904,441 (b), 36,875,810 (c) and 41,870,905 (d).

The third criterion involved monitoring convergence using the produced residual history. More specifically, the solution stabilisation was monitored with the absolute convergence criteria for the three dimensional components of velocity, the continuity and the turbulence quantities, k and ε . Figure 4-23 presents the generated plots for the four mesh sizes. Smooth convergence history was observed for the residuals of the three meshes (a), (b) and (c), unlike with the finest mesh (d), for which high fluctuations were observed for all the criteria and the solution failed to converge. According to the residuals' error figure, within the first 500 iteration steps the residuals' error drops up to six-orders of magnitude for all the convergence criteria. However, only the three first meshes reached full convergence and the flow became stable after 45,000 iterations for the meshes (a) and (b) and 50,000 iterations for the mesh (c). The finest mesh (d) after 1,000 iteration steps showed a high unstable behaviour and failed to achieve a mesh converged solution and an iterative converged solution.

4 Computational Fluid Dynamics

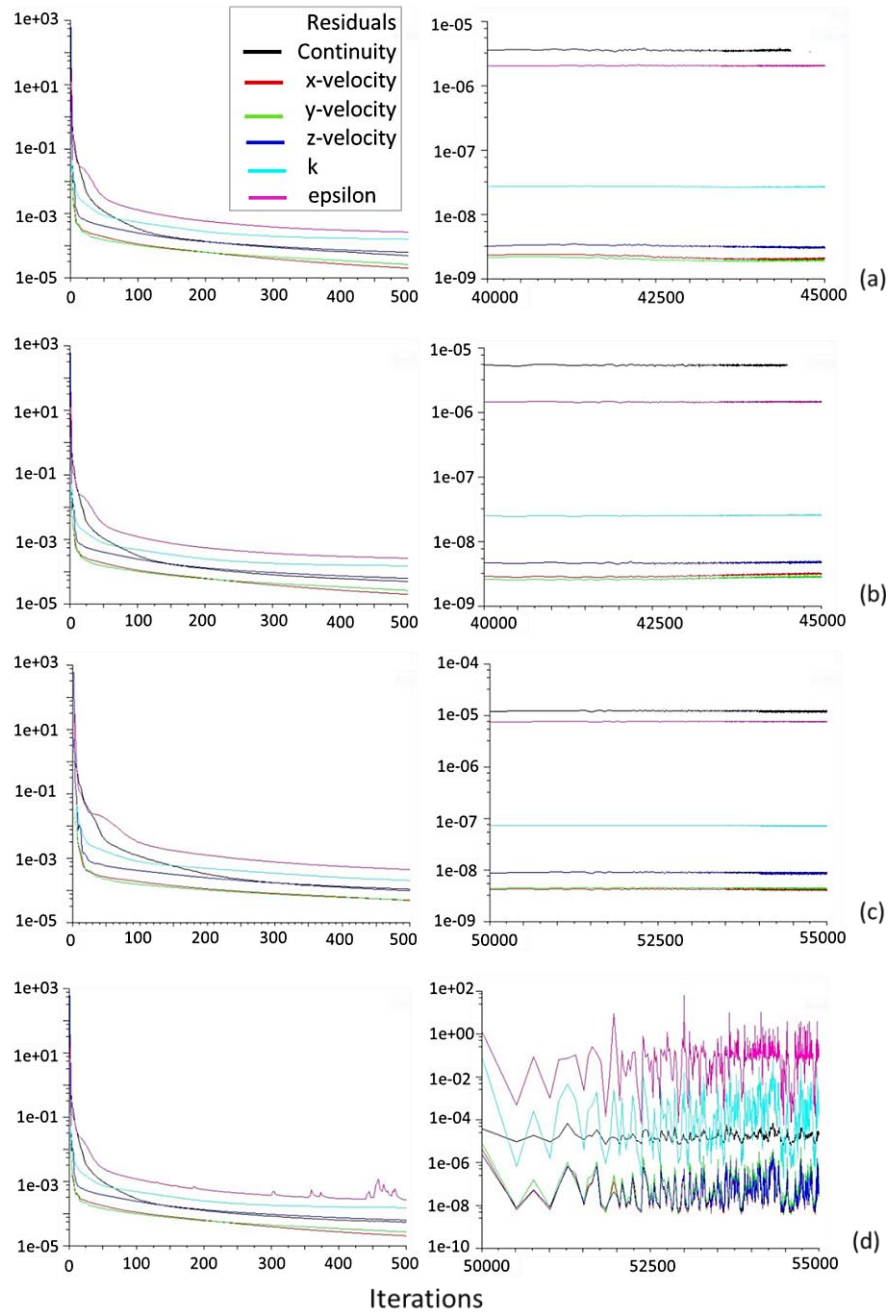


Figure 4-23 Residuals history for the generated meshes; 25,096,036 (a), 35,904,441 (b), 36,875,810 (c) and 41,870,905 (d).

The fourth criterion related the solution independency with the mesh resolution. Since the mesh refinement was performed based on boundary adaptation, the pressure coefficient was selected as the most appropriate solution parameter for comparison. The pressure coefficients were calculated based on Equation 2.4, with $P_{ref} = 0$ Pa, equal to the outlet pressure, as set from the simulation set up and U_{ref} the undisturbed velocity value at roof height, equal to 5.23 m/s for the inlet wind speed case of 8 m/s. The generated C_p values at the Point 15 (as seen in Figure 3-17 for the wind angle of 0°), since that measurement point was identified as an important indicator of the turbulent flow behaviour at the stadium interior. The grid verification included the

4 Computational Fluid Dynamics

calculation of the RE error and the GCI between the coarse-medium, medium-fine and fine-finest meshes according to Equations 4.18-4.22. Due to the inconsistent refinement ratio, Equations 4.23 and 4.25 were used to determine the effective refinement ratio, and the order of convergence.

According to Table 4.4, the generated results indicated that even if the error estimator, $|\epsilon|$, varies between 0.148 % and 2.556 % for the medium and finer mesh, it is not a reliable indicator of solution convergence. The RE error, $|E_{\text{fine}}|$ was found to be equal to 0.55 % for the medium mesh, increasing to 16.77 % for the fine and 28.85 % for the finest mesh size. Finally, the calculation of the GCI (based on the fine grid resolution), using a safety factor $F_s = 1.25$ indicated that the medium mesh with the smallest error of 0.68% can successfully calculate the near wall flow. The high values of both RE error and GCI obtained for the two finest meshes are attributed to the very small effective ratios produced after the boundary adaptation technique. As a result of that, the calculate order of accuracy, p_k , was greatly exceeding the order of accuracy (~ 14) for the selected second order discretisation scheme. According to Eca and Hoekstra (2002) an acceptable range of p_k falls within the interval $[0, 8]$. In cases where p_k exceeds that range then the *GCI* method may not be considered reliable and thus, the theoretical value is recommended to be used (Eca and Hoekstra, 2004). For the current calculation of the $GCI_{(\text{fine})}$ the theoretical value of 2 was used, which generated very large GCI values, equal to 20.96% for the medium-fine and 36.06% for the fine-finest meshes. On the other hand, the GCI value for the coarse-medium meshes was equal to 0.68%, which corresponds to a good grid convergence index result, highlighting the adequacy of the medium mesh to be used for the simulation study.

4 Computational Fluid Dynamics

Table 4.4 Grid independency study based on the four meshes and the RE and GCI techniques.

Variable	Coarse	Medium	Fine	Finest
	25,096,036	35,904,441	36,875,810	41,870,905
C_p [-]	-0.512	-0.511	-0.509	-0.497
r_{eff}	1.127	1.009	1.043	
$ \epsilon $	0.148%	0.302%	2.556%	
ΔC_p	0.0011	0.0022	0.0178	
$ E_{\text{fine}} $	0.55%	16.77%	28.85%	
$GCI_{(\text{fine})}$	0.68%	20.96%	36.06%	

4.9 Summary

In summary, an accurate aerodynamic performance assessment study of building structures requires a holistic approach and understanding of the wind phenomena occurring in the urban environment, both theoretical and computational. Important parameters such as the mesh generation, the selection of the appropriate turbulence model and the assignment of the correct boundary conditions may determine the validity of the results.

The presented CFD parameterisation of the stadium model incorporated the established theoretical requirements and recommendations for flow simulation of structures in the built environment. In order to eliminate the deviation of the results during the validation process, the computational domain was selected to be dimensionally equal to the wind tunnel test section. For the space discretisation, a hybrid mesh was generated that allowed the construction of a computational mesh of high resolution on the areas around the stadium and the domain walls. Four computational grids were generated and assessed against the several computational and convergence criteria, out of which, a medium mesh of 35,904,441 cells was selected as the most appropriate and to be used for the current study. Finally, it was concluded that the standard wall functions are inadequate to support the simulation of the generated mesh and thus, the scalable wall functions were decided to be used for the CFD simulation study, the results of which are presented in the next chapter.

5 Results and Discussion

5.1 Introduction

In the current chapter the results of the CFD stadium study are presented. The wind performance of the structure is assessed under different wind direction and envelope porosity. The generated results involved wind and pressure distributions in both interior and exterior areas of the stadium, with main focus on the occupied areas of players and spectators and the environment on the exact proximity. Finally, the validation of the CFD methodology is performed, including the performance assessment study of three turbulence models and the comparison of the generated results with those acquired from the wind tunnel experimentation study, presented in 3.

5.2 CFD results

The aerodynamic performance of the stadium was assessed via the analysis of the pressure and velocity distributions in both interior and exterior areas of the structural model. Particular emphasis is given to the differences of the developed flow conditions under the two wind directions and the drawn advantages and disadvantages of the pitch orientation and the existence of a horizontal ventilation roof opening. Thereafter, the results generated for the case studies of non-elevated and elevated roof configuration are discussed separately and compared with the reference stadium case study of non-elevated roof and 0° wind angle. The pressure distributions were assessed in dimensionless form by the calculation of pressure coefficients according to Equation 2.4 and the following CFD-Post expression:

$$C_p = \frac{\text{Pressure} - \text{ave}(\text{Pressure})@outlet}{0.5 * 1.225 [\text{kg}/\text{m}^3] * (\text{ave}(\text{Ref. Velocity})@inlet)^2} \quad (5.1)$$

5.2.1 Non-elevated roof configuration

The first set of pressure distribution results included the stadium configuration with non-elevated roof configuration.

5 Results and Discussion

5.2.1.1 Pressure distribution

Figure 5-1 shows the generated pressure coefficients for the external stadium wall surfaces for the wind angle case of 0 (a, ref. case) and 90 (b) degrees. The wind direction, which relates the wind normal to a longer or shorter wall face, created small, but significant differences. For the reference case study of 0 degrees (a) the positive pressure coefficient contours at the front wall were extended towards the ground level, contrary to the case of 90 degrees (b), where the maximum values of pressure coefficients were limited below the roof extension. The pressure coefficients along the external walls varied by 1.53, with a maximum peak of 1.29 observed 0.136 m above the ground level, or exactly at the beginning of the roof geometrical extension. A peak of -0.92 occurred at the side faces of the stadium indicating suction. Negative pressure coefficients were also observed at the rear stadium walls, which were smaller in magnitude and with constant variance (vertical spread). The minimum value of -0.17 occurred at the sides and increased to 0 towards the centre.

Similar results were observed for the wind angle of 90 degrees. Positive pressure coefficients were observed at the front stadium walls, with a maximum of 1.08, 16.3 % smaller than the reference case and a minimum of -0.35 at the front side corners of the structure, which is 62 % higher than the minimum pressure coefficient of the reference case. The C_p values at the leeward walls varied between -0.24 at the sides and 0.034 at the centre of the wall. The positive values observed at the leeward stadium walls weakened the suction and thus in the rear side corners high negative pressures were not present.

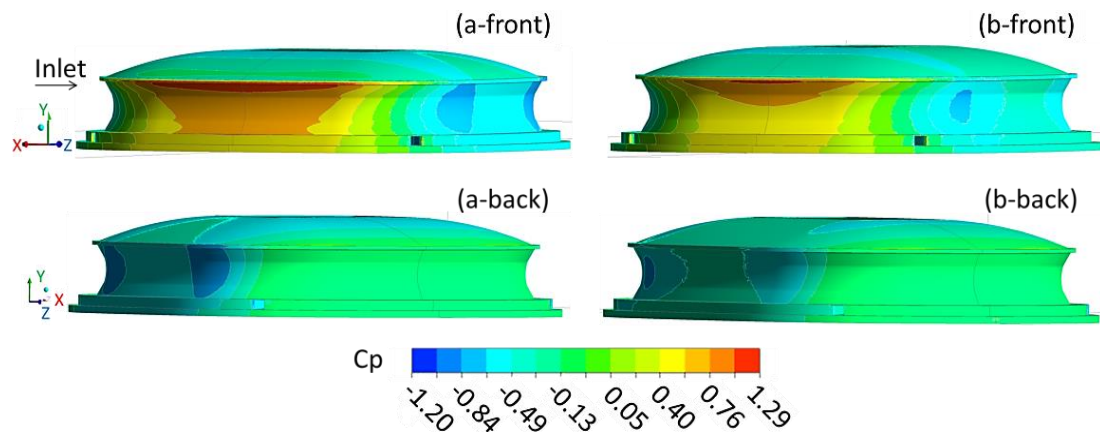


Figure 5-1 C_p contours on the external stadium walls for the non-elevated roof case and the wind angle of 0 (a) and 90 (b) degrees.

5 Results and Discussion

Local pressure coefficients were generated for the roof surfaces and are illustrated in Figure 5-2. The pressure coefficient fluctuations due to wind direction were relatively small. For both cases, the windward and leeward parts of the roof extension were assigned with opposite extreme local pressure coefficients, $C_{p_{windward}} = -1.08$ and $C_{p_{leeward}} = +0.15$. Along the roof structure, negative pressures were developed, with high negative pressure coefficients to be observed at the perimeter of the oculus configuration. The smallest local pressure coefficients were observed at the rear side of the roof opening with values of -1.05 for the wind angle of 0 and -0.77 for the 90 degrees, with a deviation of -26.7% .

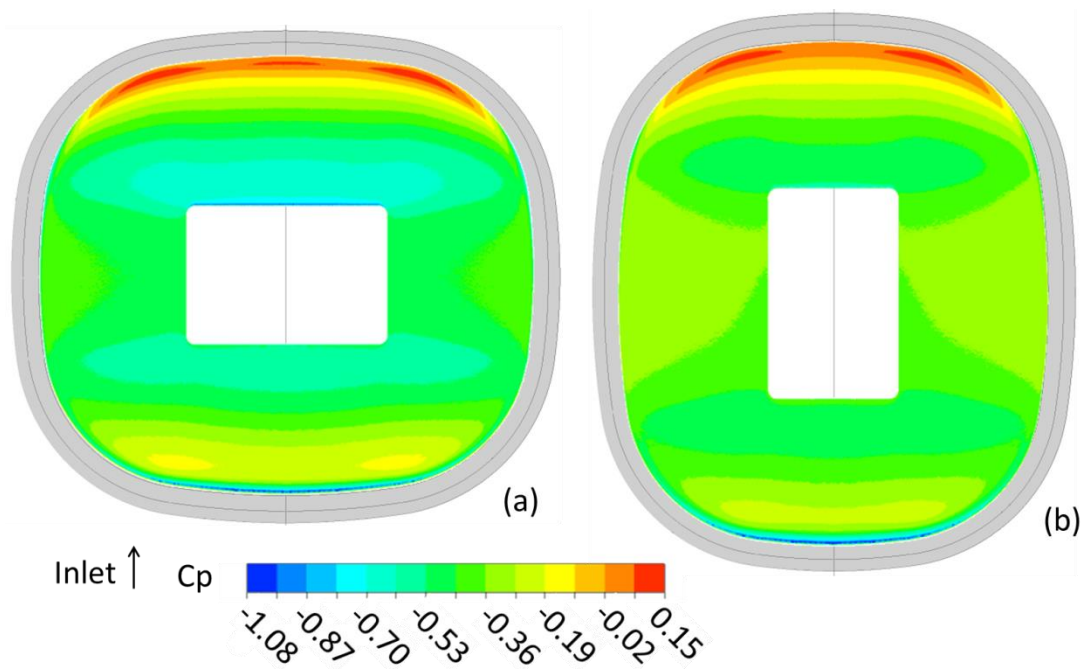


Figure 5-2 C_p contours on the roof wall generated for the closed roof for the wind angle of 0 (a) and 90 (b) degrees.

Solely negative pressure values were developed at the stadium interior walls. The pressure coefficient contours, as shown in Figure 5-3, demonstrated similar patterns of C_p for both wind directions. The peak pressure coefficients were observed at the upper windward spectator tiers with values of -0.34 for the wind angle of 0 degrees and -0.25 (26.4% higher) for the wind angle of 90 degrees and with substantially extended contours towards the sides. For both cases, negative smaller pressure coefficients were observed at the upper spectator tiers, which were increased towards the auxiliary area. The comparison of the average C_p values revealed 28.9% higher negative values for the reference case study, with a pressure coefficient of -0.49 .

At the auxiliary area negative pressure coefficients were generated with an average value of -0.52 and a standard deviation of 0.50 , for the reference case study. For the

5 Results and Discussion

stadium with non-elevated roof and 90° wind angle an average C_p value of -0.39 was obtained, 33 % higher than the reference and a standard deviation of 0.29. For both cases, the highest negative pressure coefficients (suction) occurred at the leeward sides of the auxiliary area, with a C_p value equal to -0.59 for the reference case and -0.46 (28 % higher) for the wind angle of 90 degrees. These suction zones were directly linked to the incoming airflow through the side entrances.

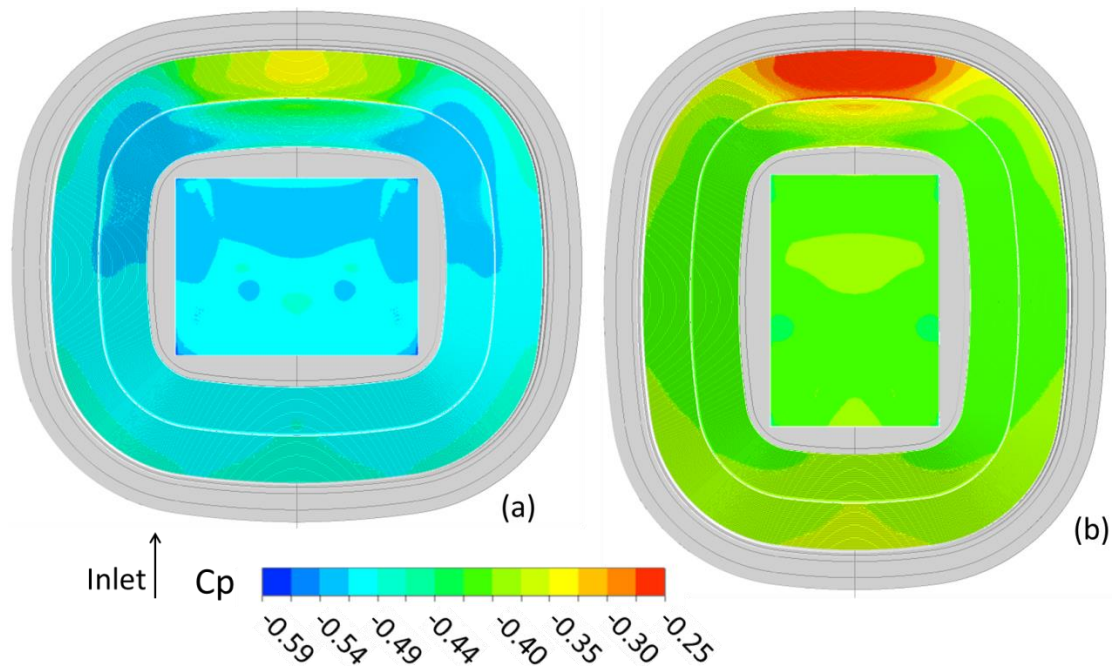


Figure 5-3 C_p contours on the pitch and terraces walls for the non-elevated roof case and the wind angle of 0 (a) and 90 (b) degrees.

5.2.1.2 Airflow distribution

Complementary, and equally important on the stadium aerodynamic performance assessment, is the analysis of the velocity streamlines at the stadium bowl. Figure 5-4 illustrates the streamlines of the dimensionless velocity on the symmetrical plane, for the wind angle of 0 (a) and 90 (b) degrees (see also Figure D-1 and D-2). According to the results, the flow distribution was primarily determined by the oculus roof opening and secondly by the four side entrances. The pitch orientation played an equal and important role on the stadium wind microenvironment.

The mass flow entering the stadium through the roof opening resulted to the creation of a large vertical vortex at the stadium bowl, also reported in van Hoof et al. (2011). For the case of 0 degrees wind angle, the vortex covered the windward spectator tiers and its downwash more than half of the length of the auxiliary area. The areas of maximum wind intensity were observed at the bottom windward roof surface and at

5 Results and Discussion

the lower bottom spectator tiers. The streamlines of the 90 degrees wind angle indicated a more concentrated vortex at the same location, but with limited extension to the windward spectator tiers and the one third of the auxiliary area. Underneath the roof structure, zones of equal intensity were observed, contrary to the bottom spectator tiers, where the downwash flow was substantially weakened when compared with the previous case study.

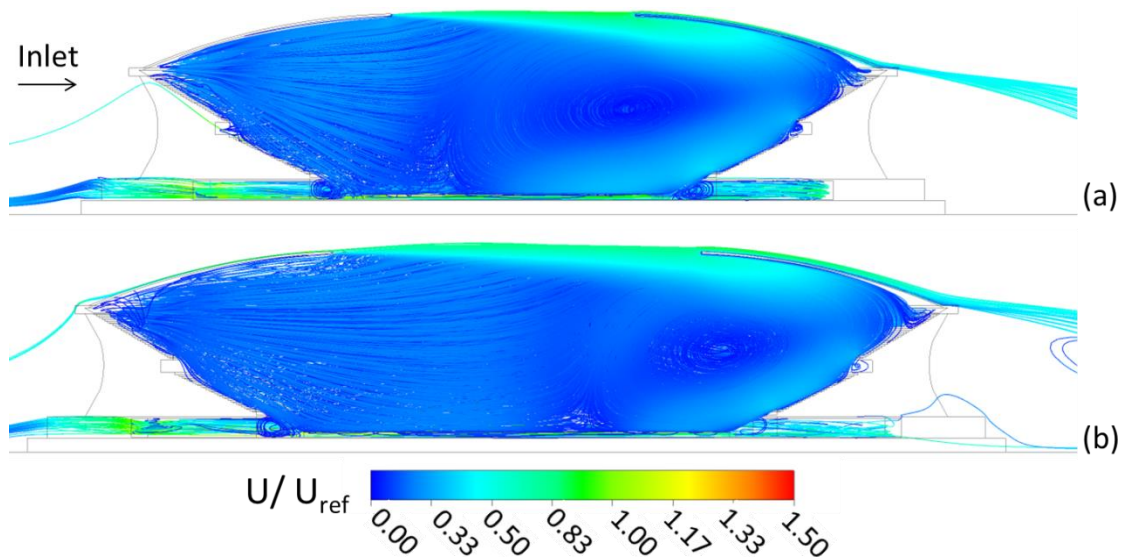


Figure 5-4 Side view of the dimensionless streamlines of velocity for the elevated roof stadium model at 0 degrees (a) and 90 (b) degrees wind angle; $U_{ref} = 5.23$ m/s.

The top view of the velocity streamlines, presented in Figure 5-5, gave further insight into the overall flow distribution. The air flow entering the stadium through the roof opening was spatially separated and was the one that exclusively controlled the microenvironment at the windward spectator tiers. In particular, for the wind angle case of 0 degrees, the primary vortex was expanding horizontally in opposing directions and towards the upper spectator tiers, creating tornado like vortices. This term has been used in Cook (1985) to describe the airflow formation caused in the inner side of a structure with cylinder walls, due to the development of non-uniform pressures.

For the wind angle of 90 degrees, the velocity streamlines were more ‘concrete’ and the airflow behaviour well-defined. In total, two tornado like vortices were present. The one was powered by the primary vortex and was located at the windward corners of the stadium bowl, creating high intensity airflow zones at the upper spectator tiers. The second one was powered by the recirculation zones at the pitch level, where the incoming air stream from the front entrances collided with the recirculation zone of the primary vortex, forcing the flow to move vertically. From

5 Results and Discussion

there, part of the flow exited the stadium bowl through the roof and part of the flow was reattached to the primary vortex, also visible from Figure 5-4b.

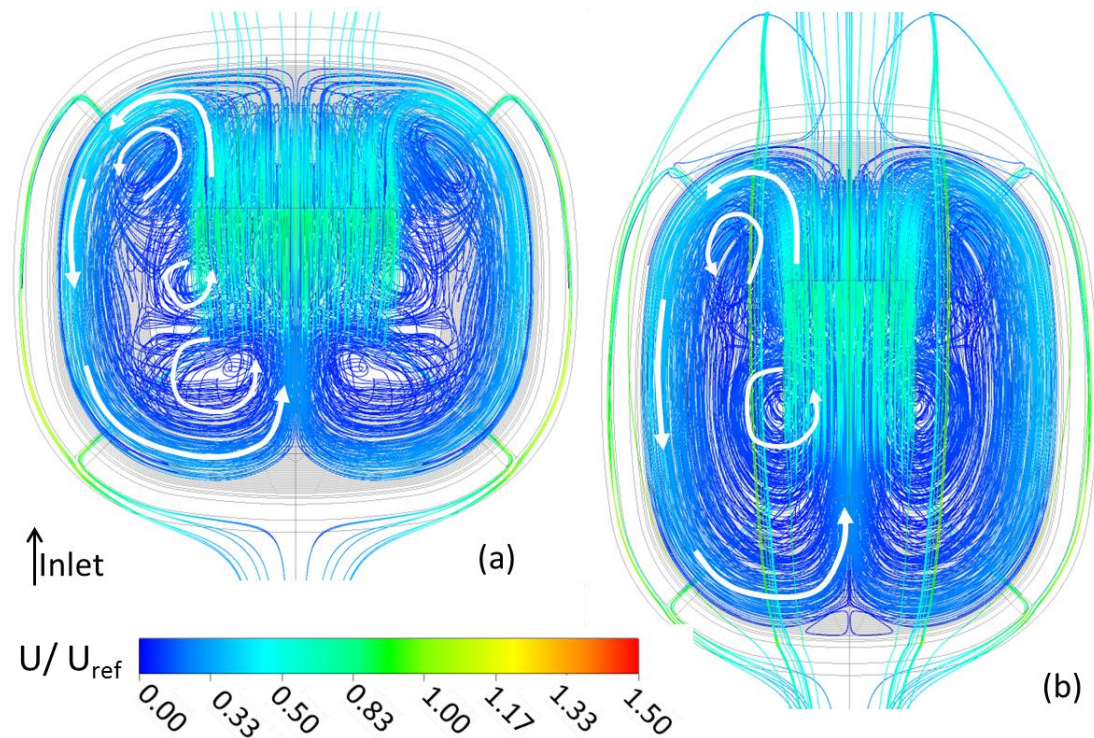


Figure 5-5 Top view of the dimensionless streamlines of velocity for the non-elevated roof stadium model at 0 degrees (a) and 90 (b) degrees wind angle; $U_{ref} = 5.23$ m/s.

The pressure distribution along with the normalised velocity vectors, generated in a horizontal plane 0.01 m above the entrance level, is illustrated in Figure 5-6. According to the results, the induced pressure difference between the external (both windward and leeward) and the internal stadium walls, caused large flows entering the stadium through the side entrance openings. For the case study of 0 degrees wind angle, four vortices were created at the level of the auxiliary area. The incoming air streams through the front side entrances resulted to the development of two vortices, which were small in size due to the collision with the windward downwash of the primary vortex at the pitch area and the vertical vortices created at the leeward spectator terraces. Two vortices were developed due to the air streams entering the stadium bowl via the back side entrances, and were spatially limited on the sides, due to the collision with the primary and the aforementioned small vortices.

For the case of 90 degrees wind angle, absolute smaller negative pressures were developed at the auxiliary area, resulting in the creation of two large vortices powered by the air streams entering the stadium from the four side entrances. The vortices were developed vertically, towards the roof structure and constituted, along with the primary vortex, the core of the flow distribution at the stadium bowl.

5 Results and Discussion

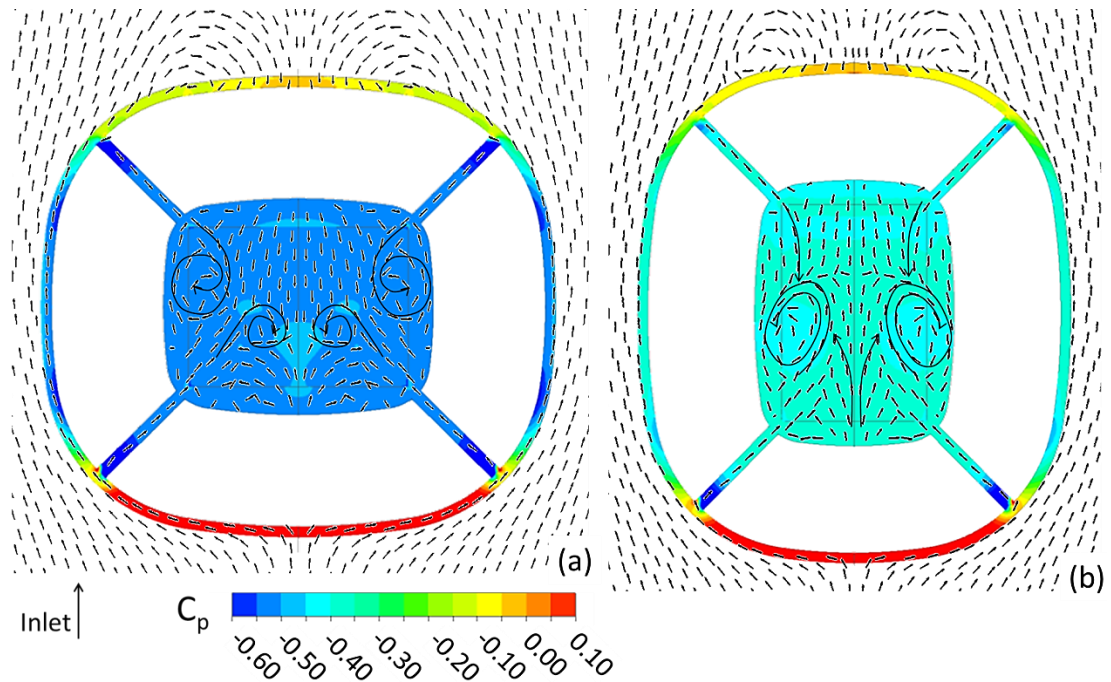


Figure 5-6 C_p contours and normalised velocity vectors on a horizontal plane 0.01 m above the entrances' level, for the non-elevated roof model; 0 (a) and 90 (b) degrees wind angle.

5.2.2 Elevated roof opening

The second first set of pressure distribution results included the stadium configuration with elevated roof.

5.2.2.1 Pressure distribution

According to Figure 5-7, for the stadium configurations with open horizontal ventilation opening between the roof and the upper spectator tiers, similar pressure patterns with the previous cases were observed. For the 0 degrees wind angle, the maximum pressure coefficient, with value of 1.10, and 14.7 % smaller than the one of the reference case study, was observed at the beginning of the extension component at upper spectator tiers (0.136 m above ground level). Suction zones were created at the front and rear sides of the stadium with peak minimum pressure coefficient equal to -0.86, 6.5 % higher than the reference case. On the rear stadium walls, negative pressure coefficients were observed with constant vertical variance between -0.46 to -0.05 from the sides towards the centre.

For the case study of 90 degrees, the maximum peak pressure coefficient value was observed at the same location with identical value (1.10). The side suction areas produced a local negative peak of -0.75, 18 % higher than the reference case study.

5 Results and Discussion

Opposed to the 0 degrees case study, higher pressure coefficients were observed at the rear walls, with a variance between -0.24 and 0.01 from the sides to the centre. It is also worth mentioning that the smallest pressure coefficient value of -1.09 occurred at the top inner surface of the extension component, indicating suction and large flows entering the stadium bowl.

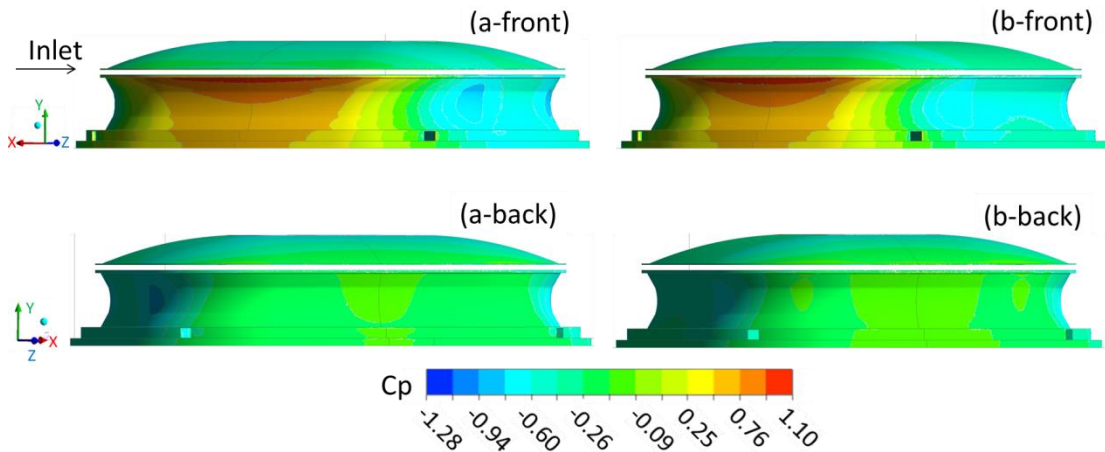


Figure 5-7 C_p contours on the front and back stadium walls for the open roof cases and the wind direction of 0 (a) and 90 (b) degrees.

Local pressure coefficient contours were generated at the roof surface, as shown in Figure 5-8. For both wind angles, the pressure coefficient values were reduced incrementally from the windward and leeward sides towards the centre. More specifically, for the wind case of 0 degrees smaller pressure coefficients values were observed when compared with the reference stadium case study. The minimum peak value of -1.15 (9.5 % smaller) was observed at the rear side of the oculus configuration and also at the windward top surface of the roof extension, indicating suction and large flow movements. The maximum pressure coefficient value of 0.04 was observed at the leeward side walls of the roof structure. For the wind angle of 90 degrees, higher pressure coefficient values are developed. The minimum C_p value of -1.03 (1.9 % higher from reference case) was generated at the rear side of the oculus configuration and -1.09 (1 % smaller from reference case) at the top of the windward roof extension wall. A peak maximum of 0.08 was observed at the leeward extension walls of the roof.

5 Results and Discussion

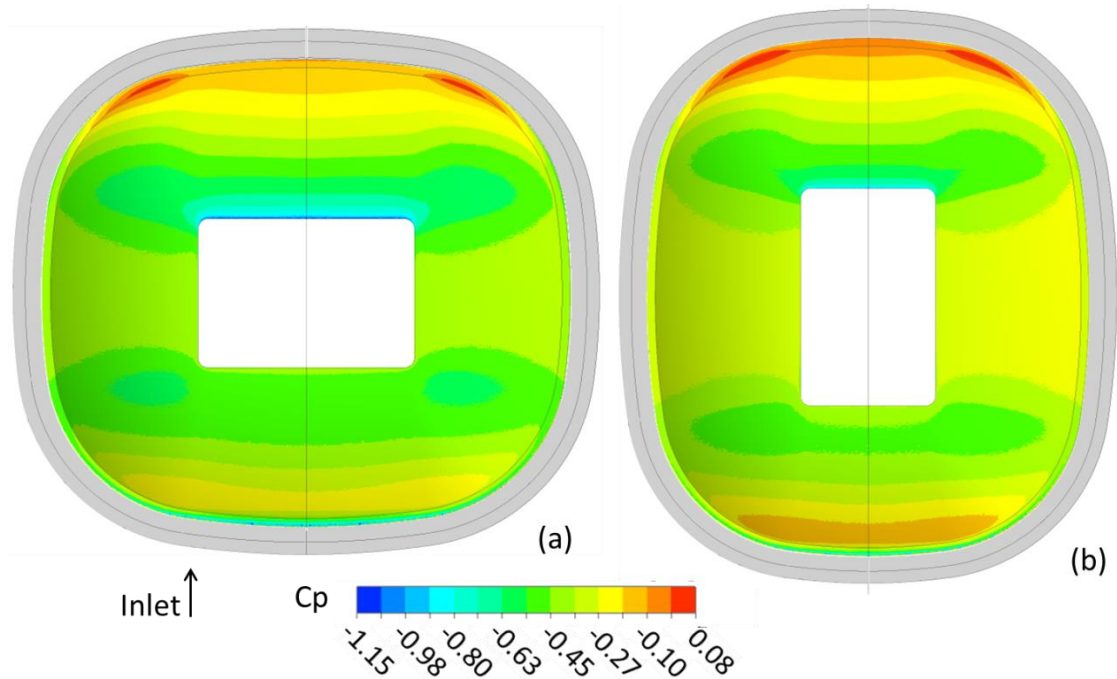


Figure 5-8 C_p contours on the roof wall generated for the open roof for the 0 (a) and 90 (b) degrees wind angle.

The roof elevation revealed considerable differences on the pressure distribution at the stadium interior, when compared with the stadiums with non-elevated roof. In that case, and according to Figure 5-9, the highest negative pressure coefficients were appeared at the highest rows of the leeward and windward upper spectator tiers, indicating intensively ventilated zones and airflow entering the stadium bowl. Smaller negative pressure coefficient values were observed at the corners of the upper windward spectator tiers and the highest rows of the leeward upper lateral spectator tiers, where the airflow exited the stadium bowl. In particular, the highest negative pressure coefficients were equal to -0.44 and -0.39 and the minimum equal to -0.31 and -0.26 for the wind angle of 0 and 90 degrees respectively. The calculated average C_p values revealed that the case of 0° wind angle, with a value of -0.37, produced 24.4 % smaller negative values than the reference case study and 36.7 % smaller negative values for the 90° wind angle, with a value of -0.31.

At the auxiliary area negative pressure coefficient values were generated with an average value of -0.38, which was 27 % higher than the reference case, and a standard deviation of 0.27, for the elevated roof and 0° wind angle. For the stadium with elevated roof and 90° wind angle an average C_p values of -0.32 was obtained, 38.5 % higher than the reference and a standard deviation of 0.20. Again only the leeward corners of the auxiliary area were subject to high negative pressure coefficients with a peak value of -0.43 and -0.38 for the wind angle of 0 and 90

5 Results and Discussion

degrees, which were 27.1 and 35.6 % higher than the C_p values of the reference case study.

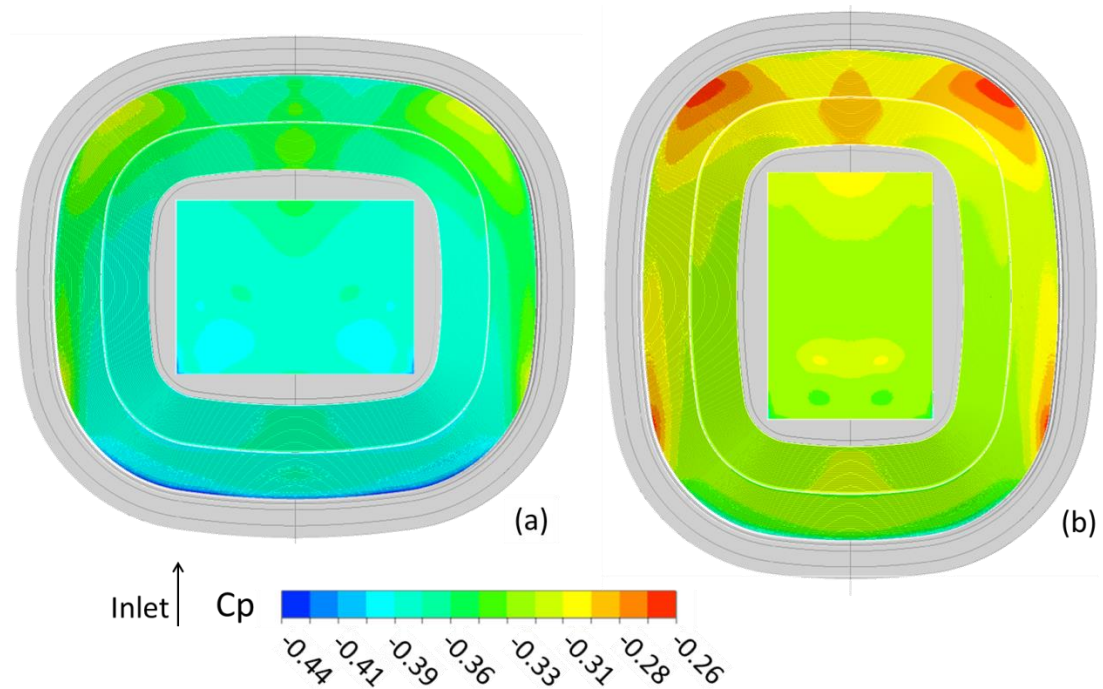


Figure 5-9 C_p contours on the pitch and terraces walls for the open roof case and the wind direction of 0 (a) and 90 (b) degrees.

5.2.2.2 Airflow distribution

Dimensionless velocity streamlines were generated to determine the flow distribution at the stadium bowl. According to Figure 5-10, the horizontal ventilation opening is currently the dominant opening for the interior wind microenvironment development (see also Figures D-3 and D-4). Both wind directions, indicated similar airflow patterns. The wind entered the stadium through the windward and leeward parts of the roof horizontal opening, where the lowest pressure coefficient values were observed (see Figure 5-9). In the leeward stadium walls, particularly, the developed recirculation zones, together with the induced pressure differences, pulled air inwards through the ventilation opening and downwards to the auxiliary area. The side entrances constitute additional air inlets for the stadium interior. The streamlines entering the stadium through the windward horizontal opening, along with the streamlines of the circulated airflow at the stadium interior, appeared to exit the stadium bowl throughout the roof, thereby making the oculus configuration the primary flow outlet for the structure. Finally, it is worth mentioning that even if both wind directions produced similar wind distribution results, in the case of 90 degrees

5 Results and Discussion

wind angle, a small vortex was developed on the windward side of the roof oculus, as a result of the attempt of the recirculated flow to exit from the stadium bowl.

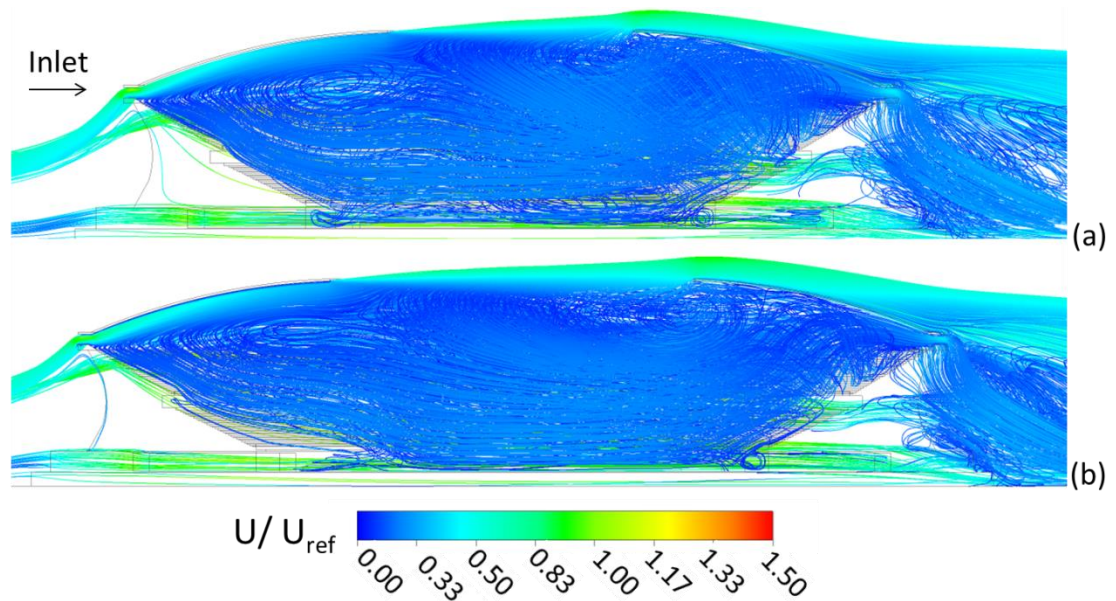


Figure 5-10 Side view of the dimensionless streamlines of velocity for the open roof stadium model at 0 degrees (a) and 90 (b) degrees wind direction; $U_{ref} = 5.23$ m/s.

The top view of the flow distribution at the stadium interior is given in Figure 5-11, by the generation of the backward movement of the velocity streamlines from the oculus configuration. This enabled the identification of the potential air inlet locations via the stadium openings. According to the results, and adding to the aforementioned description of Figure 5-10, the airflow entering the stadium through the windward horizontal ventilation opening was partly exiting the stadium through the roof and partly impinging to the sides of upper windward spectator terraces. The flow collided with the incoming flow through the leeward horizontal ventilation opening and thus two vertical tornado like vortices were created, covering the total area of both upper and bottom tiers. Intensively ventilated zones were developed at the highest rows or the upper spectator tiers, also reported in Biagini et al., (2007).

5 Results and Discussion

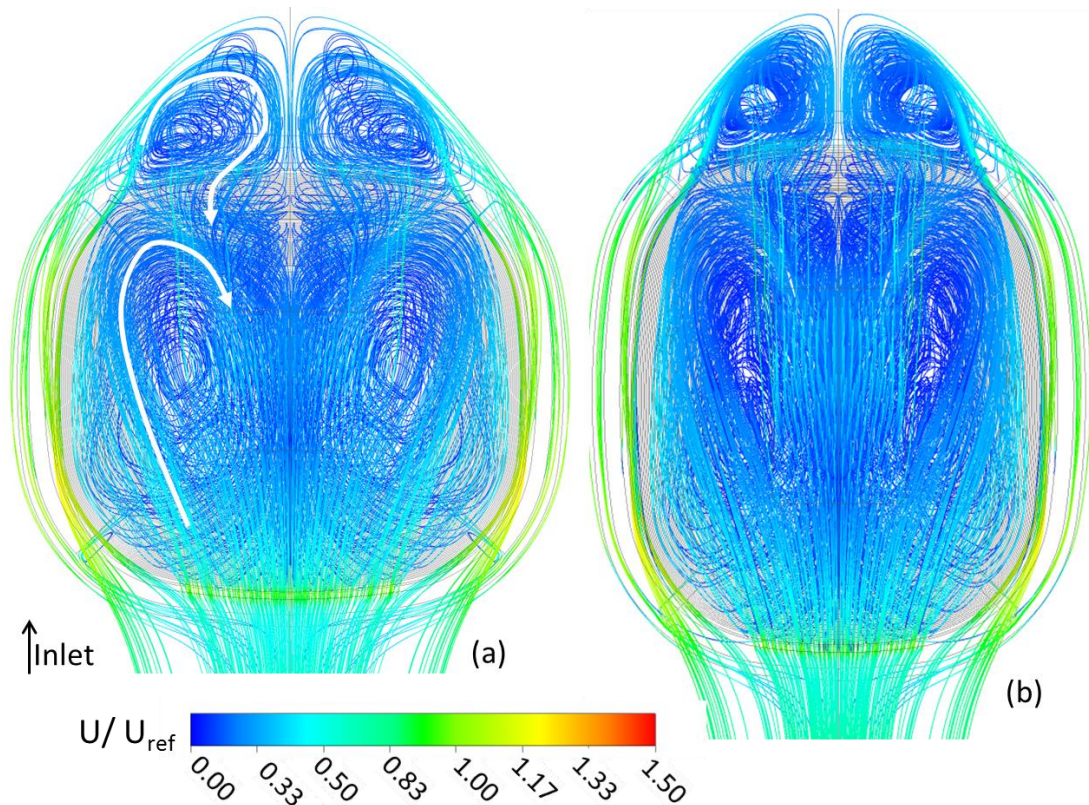


Figure 5-11 Top view of the dimensionless streamlines of velocity for the open roof stadium model at 0 (a) and 90 (b) degrees wind direction; $U_{ref} = 5.23$ m/s.

The flow distribution at the entrance and pitch level is given in Figure 5-12, with the illustration of the normalised velocity vectors and the contours of pressure coefficient. For both wind directions, the induced pressure differences between the exterior and the interior walls caused concentrated suction in all four side entrance openings. In detail, for the wind angle of 0 degrees, the airflow entering through the rear entrances led to the creation of two long vortices located on the right and left sides of the auxiliary area constituting the base of the tornado vortex, illustrated in Figure 5-11a. The smaller in size vortices developed due to the incoming air through the front entrances were concentrated in the leeward side of the auxiliary area, with no further wind impact on the stadium microenvironment.

The velocity vectors generated for the wind angle of 90 degrees coincide well with the streamlines in Figure 5-11b. The air stream entering the stadium through the back side entrances, along with the downwash flow from the leeward horizontal ventilation opening were joined together, forming the lower part of the primary vertical tornado like vortices. The vortices on the leeward auxiliary area were limited in space and strength, due to their collision with the primary vortex formations.

5 Results and Discussion

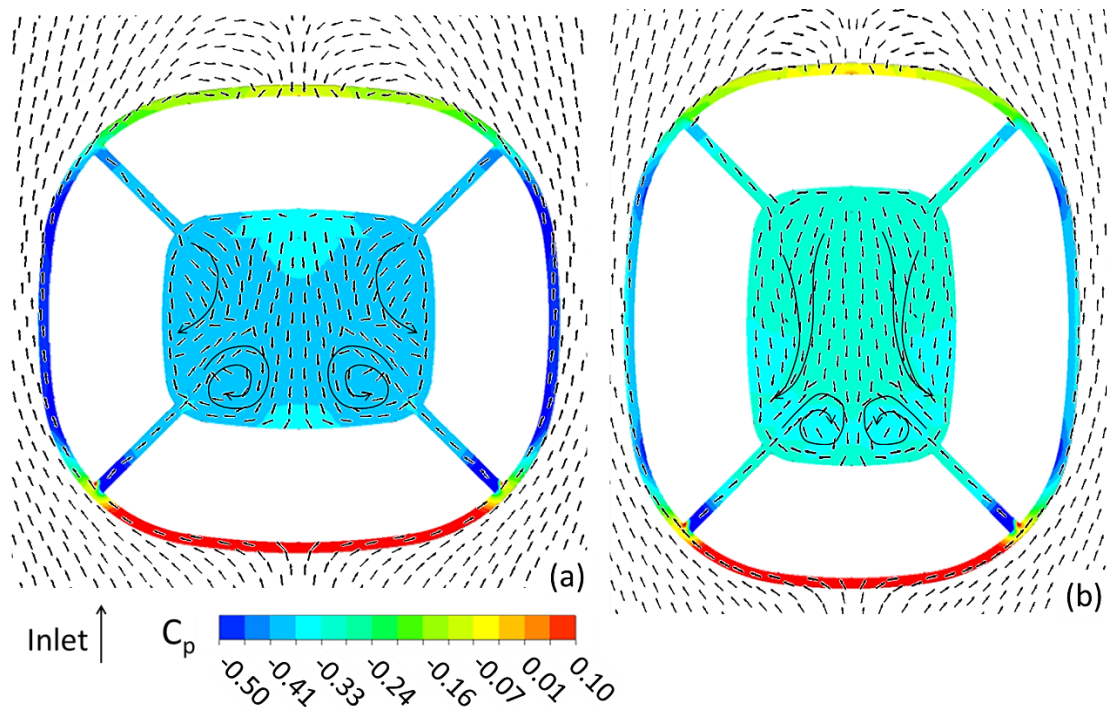


Figure 5-12 C_p contours and normalised velocity vectors on a horizontal plane 0.01 m above the entrances' level, for the elevated roof model; 0 (a) and 90 (b) degrees wind angle.

5.3 Further interpretation of the results

The investigation of the developed wind conditions for users requires the study of the direct interactions between 1) the urban and the stadium scale and 2) the stadium and the human scale. Thus, in the following paragraphs the flow distribution in both external and internal stadium areas is presented, with main focus on the areas in the close proximity to the stadium and the occupied areas of spectators and players.

5.3.1 Wind environmental impact

In large structures, such as sports stadia, it is important to understand their wind behaviour within the concept of the surrounding urban environment (Stathopoulos et al., 1992). The wind environmental impact of the stadium was initially assessed with the generation of pressure coefficient contours on the ground level around the stadium model. As illustrated in Figure 5-13, the pressure distribution around the stadium model is similar for all four configurations. Positive pressure coefficients were developed at the windward ground region with maximum peak of 0.66 and 0.57, 13.6 % smaller, for the case of 0 degrees wind angle and for the closed opening horizontal opening configuration respectively. Negative pressures (suction) were observed at the sides of the stadium walls, the values of which were independent

5 Results and Discussion

roof elevation configuration. A minimum pressure coefficient of -0.44 was observed for the wind angle of 0 degrees and -0.35 for the wind angle of 90 degrees, which is 20.5 % higher. Finally, negative values were present on the ground surfaces at the very close proximity of the rear stadium walls.

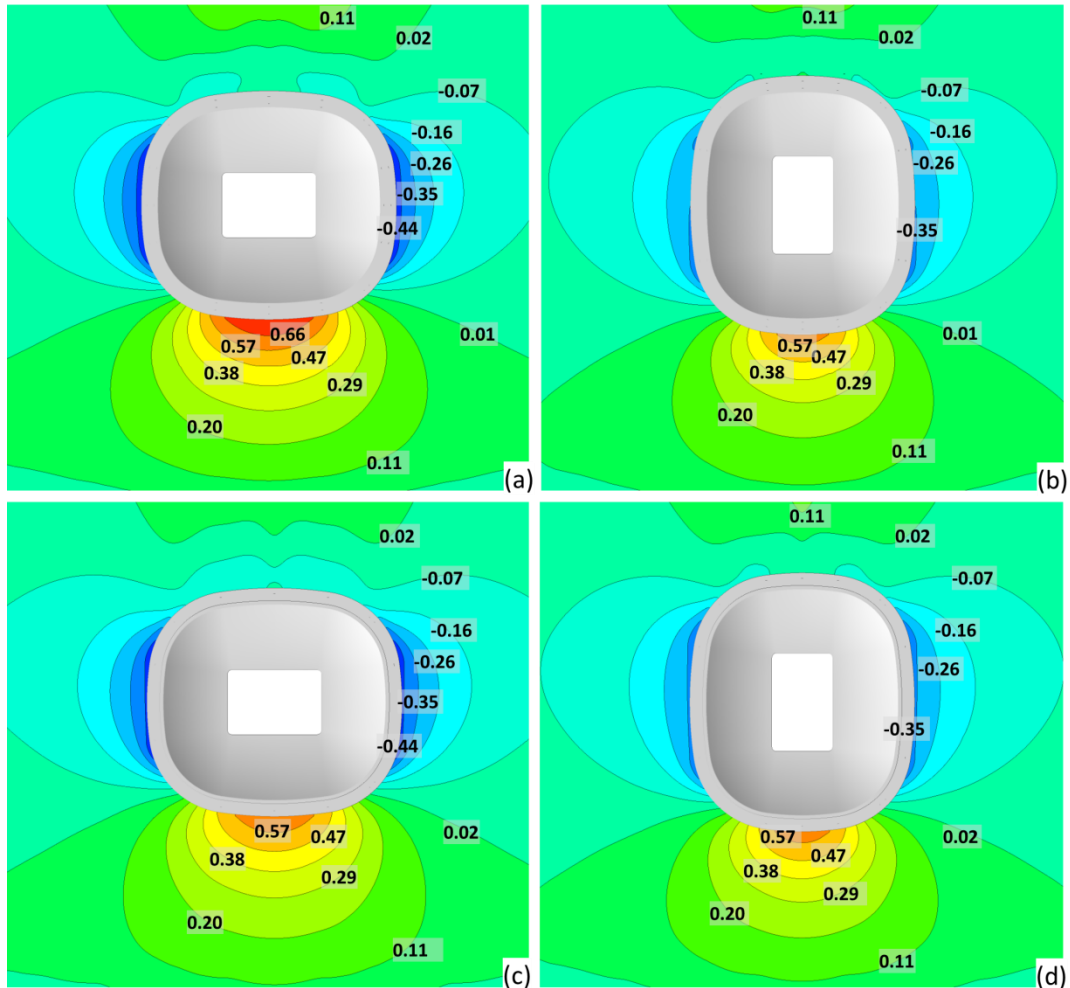


Figure 5-13 Cp contours on the ground level for the configurations: non-elevated roof 0 (a) and 90 (b) degrees and elevated roof 0 (c) and 90 (b) degrees.

Velocity streamlines and vectors were also generated close to the ground level. The results revealed that the flow distribution around the stadium was solely dependent on the geometrical design of the stadium structure. The flow distribution illustrated in Figure 5-14 with the form of velocity streamlines and vectors is similar for both wind directions. Regions of high wind speeds were developed on the lateral sides of the stadiums, which were found to be more intense for the reference stadium case study, with maximum dimensionless velocity value equal to 1.01. For the elevated roof configuration of the same wind direction (0°), the maximum value was found 4.7 % smaller and equal to 0.97. The wind direction change led to a decrease of 9.2 and 9.8 % on the maximum velocities for the non-elevated and elevated roof

5 Results and Discussion

configuration, respectively. Also stated earlier, high negative magnitudes occurred at the sides of the stadiums, which led to suction zones and thus intense airflow streams were developed.

Additional results were obtained for the stagnation points created due to the turbulence field on the building surroundings. Similarly, the horizontal roof opening had no influence on the position of the stagnation points. Nonetheless, in contrast with the expected flow distribution patterns around bluff bodies described in Blocken and Carmeliet (2004) and Shárán (1975), the architectural geometry of the stadium envelope altered significantly the frontal flow patterns. The recirculation zone on the ground level of the windward building wall was not present and replaced by the approaching to the building airflow, resulting to relocation of the front stagnation point, S_f , to a position closer to the building wall, The distance of the S_f from the front of the lower elevational wall of the structure was equal to 0.02 m. The aft stagnation point, S_b , where the rear recirculation zones was separated from the stadium turbulence wake differed in distance regarding the wind direction. For the case of the 0 degrees wind angle the stagnation point was observed 0.287 m away from the elevational lowest level wall of the stadium and 0.274 m, or 4.5 % closer to the stadium, for the case of the 90 degrees wind angle. The width to height ratio explains the longitudinal difference of the two stagnation points. As stated in Leene (1992) an increase in building width, considering constant height, leads to an increase in the turbulence wake at the rear side of the building.

5 Results and Discussion

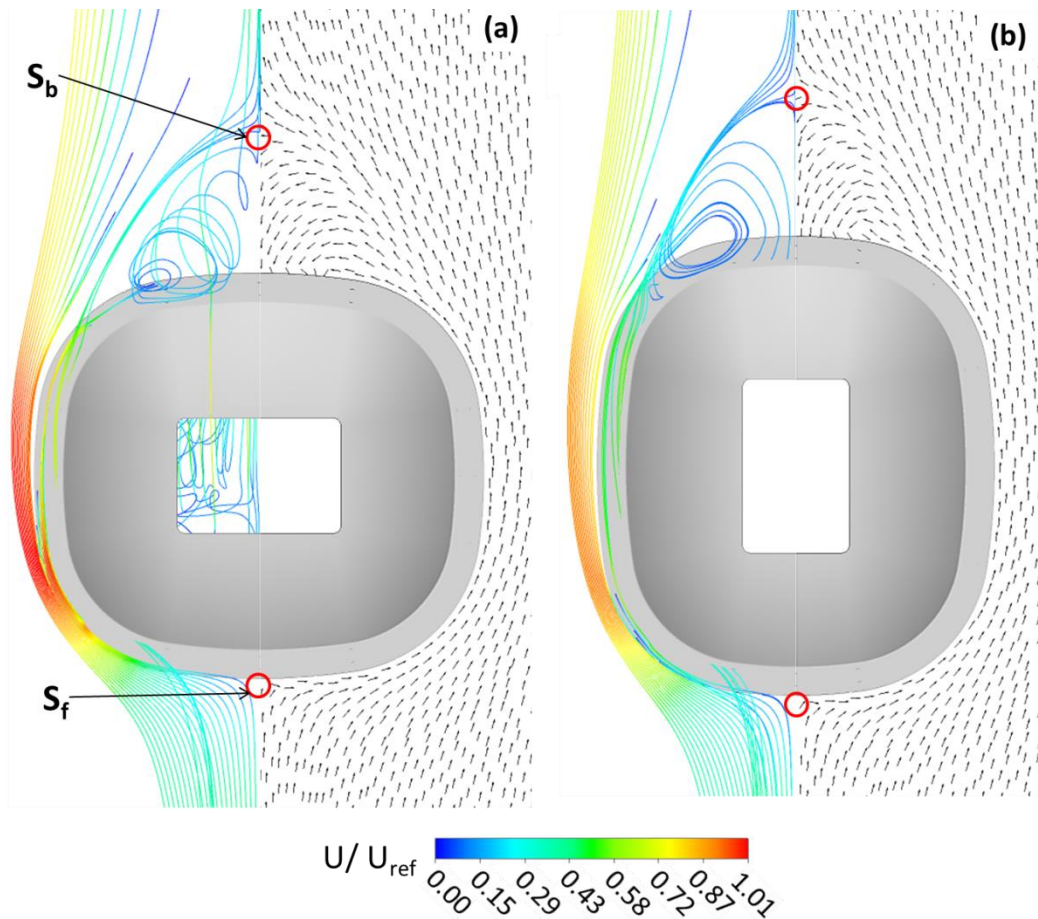


Figure 5-14 Normalised velocity vectors and dimensionless velocity streamlines of the flow around the non-elevated roof stadium model for the 0 (a) and 90 (b) wind angle; S_f and S_b the front and rear stagnation points, $U_{ref} = 5.23$ m/s.

Also discussed earlier, the pressure results on the stadium walls indicated the location of the stagnation point below the extension of the roof structure, which was identical in all four stadium cases. The dimensionless velocity streamlines, given in Figure 5-15, illustrate the concentration of the primary recirculation zone on the concave wall surface. The plot of the dimensionless velocities generated on a vertical line in front of the stadium model, indicated the limitation of the recirculation zone on that area, without creating any backflow effects. Additional recirculation zones of smaller intensity were developed at the front of the each structural elevation level. Moreover, the architectural extension that covers the side entrances successfully operated as a downwash deflector and eliminated the creation of high intensity zones at the entrance level that may promote pedestrian wind safety and comfort.

5 Results and Discussion

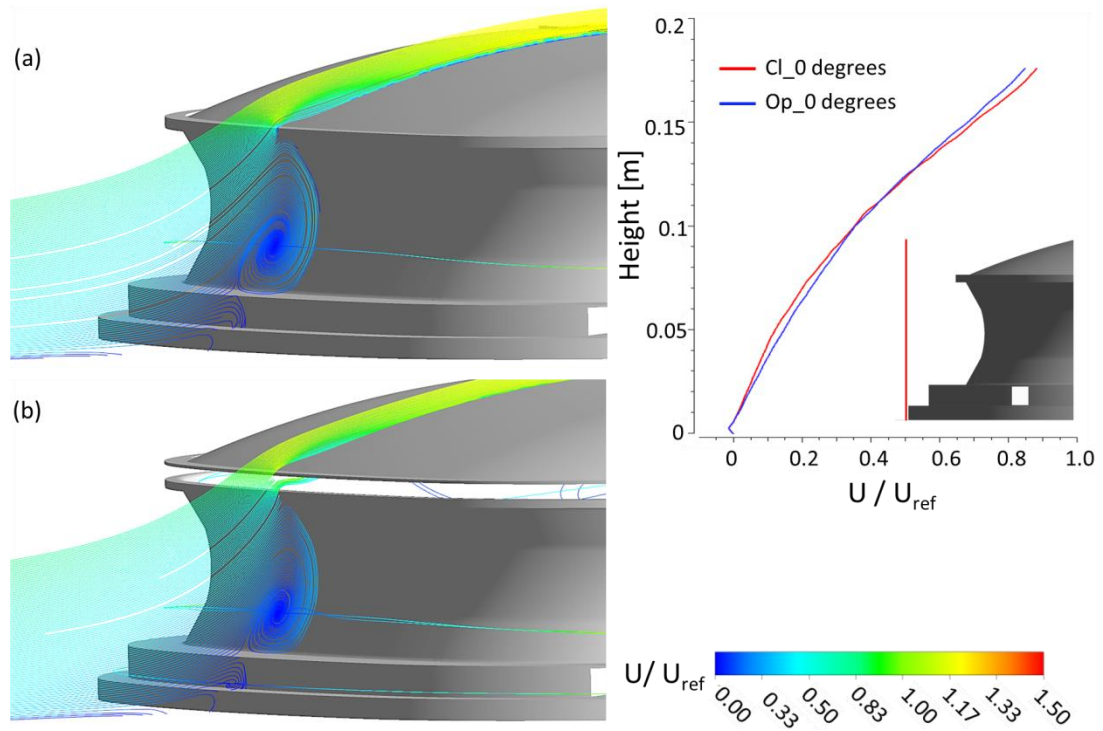


Figure 5-15 Dimensionless velocity streamlines on the front stadium wall for non-elevated (a) and elevated (b) roof configurations and plot of the U/U_{ref} on a vertical line in front of the stadium model; $U_{ref} = 5.23$ m/s.

5.3.2 Wind flow distribution

5.3.2.1 Auxiliary area

Important information on the wind conditions for the players was obtained by the generation of velocity contours and vectors on the area of interest. Figure 5-16 illustrates the generated dimensionless velocity contours and normalised vectors on a horizontal plane 0.003 m above the auxiliary area.

5 Results and Discussion

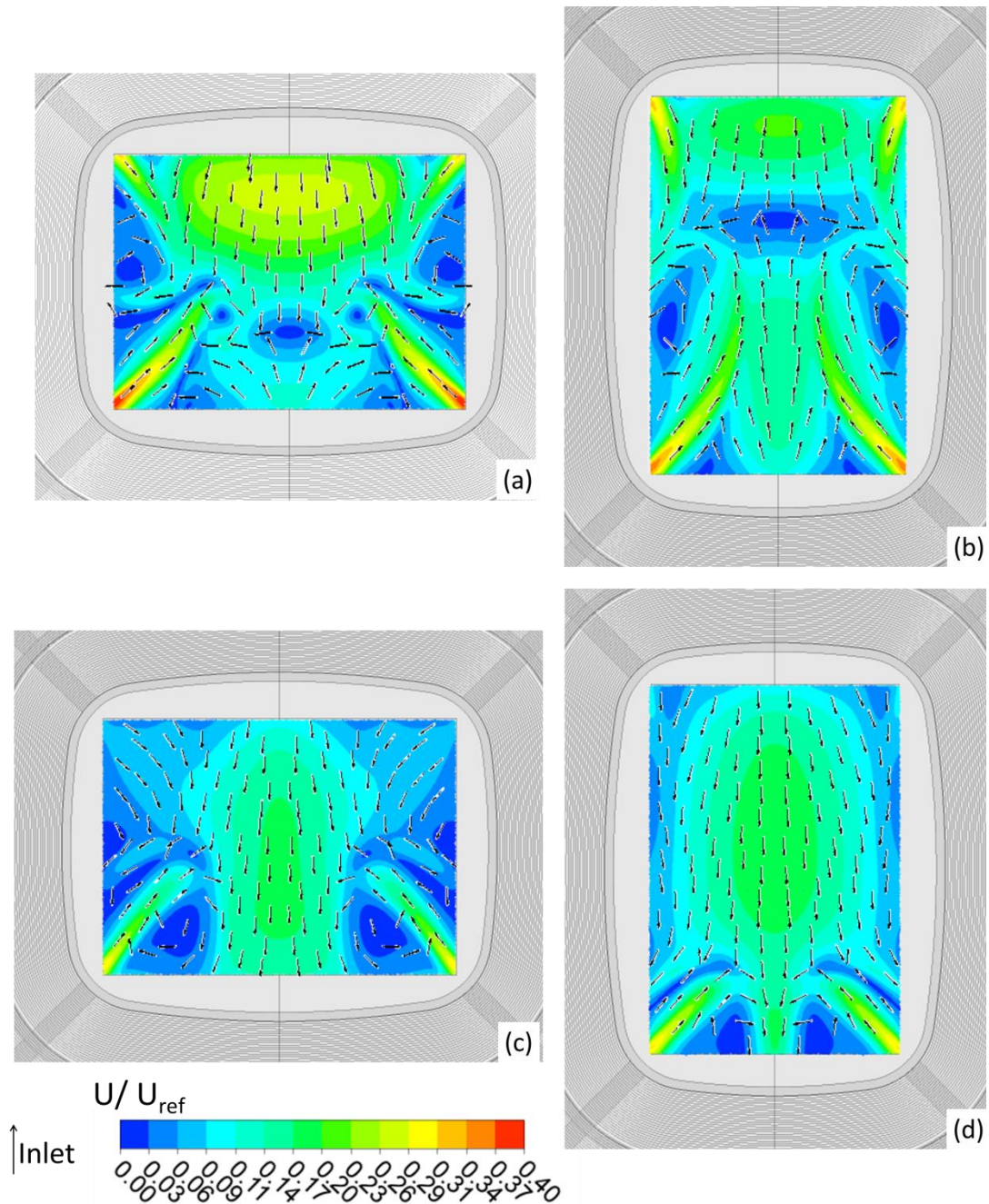


Figure 5-16 Illustration of the dimensionless contours and normalised vector of velocity generated on a horizontal plane 0.003 m above the auxiliary area for the stadium models with non-elevated roof 0° (a) and 90° (b) and the elevated roof 0° (c) and 90° (d) wind angle; $U_{ref} = 5.23$ m/s.

According to the illustrated results, the central airflow recirculation zones along with the airflow streams entering the stadium through the side entrance openings in the form of air jets were the main determinants of the wind environment at the pitch level. More specifically, the reference stadium case (Figure 5-16a) resulted to the highest average dimensionless velocity values of 0.14, with a peak maximum of 0.40 at the corners of the leeward auxiliary area. The stadium model at 90° wind angle (Figure 5-16b) produced 7 % smaller average dimensionless velocity value of 0.13,

5 Results and Discussion

and a 7.5 % smaller maximum peak of 0.37 at the same area. The velocity patterns were similar for the two wind directions with spatial relocation of the ground horizontal vortices. In other words, the primary vortex, as presented in Figure 5-4a, influenced greatly the extent of the incoming air streams through the side doors. Calm zones were developed at the points where the primary vortex collides with the downwash flow from the leeward spectator tiers and at the lateral sides of the auxiliary areas.

The stadiums with elevated roof resulted to different wind flow conditions at the auxiliary area, with substantial less velocity intensity and patterns' complexity. The average dimensionless velocities of 0.09 and 0.12 for the wind angle of 0° and 90° were 35.7 and 14.3 % smaller than the reference case study respectively. Significant was the absence of the air jets at the windward side of the auxiliary area, indicating that the incoming air through the back side openings appears had none influence on the developed flow at the auxiliary area. On the other hand, the incoming air streams via the front side openings had a maximum value of dimensionless velocity equal to 0.31 for both wind directions, which is 22.5 % smaller than the maximum value of the reference case. Taking under consideration the Figure 5-10 and the chaotic velocity streamlines, it was observed that the downwash flow from the windward spectator tiers dominated the largest area of the pitch microenvironment. For the wind direction of the 0° (c), the created air jets were extended up to the centre of the auxiliary area and created lateral calm zones, which added to the heterogeneity of the flow distribution. For the wind direction of 90° (d), the air jets were limited in length and extend to the leeward auxiliary area side.

To investigate further the wind behaviour at the auxiliary area, dimensionless velocity values were generated in a vertical line at the centre of the auxiliary area. According to Figure 5-17, the elevated roof configuration led to similar airflow patterns for the two wind directions. The flow was directed towards the leeward spectator tiers driven by the horizontal flow recirculation at stadium interior and with small vertical deviations. For the case of the non-elevated roof configuration, the wind angle caused great differences on the wind direction. More specifically, for the wind angle of 0° , the flow at the auxiliary area was mainly attributed to the primary vertical vortex, which drove the flow towards the leeward spectator tiers. On the other hand, the wind angle of 90° led to a significantly reduced in length primary vortex, limited to the windward tiers and thus the flow had opposite direction, since

5 Results and Discussion

it was mainly controlled by the downwash flow from the leeward spectator tiers. It can also be observed that the elevated roof configuration led to up to 25 % higher wind speeds at the centre of the auxiliary area when compared with the ones obtained from the non-elevated roof configuration.

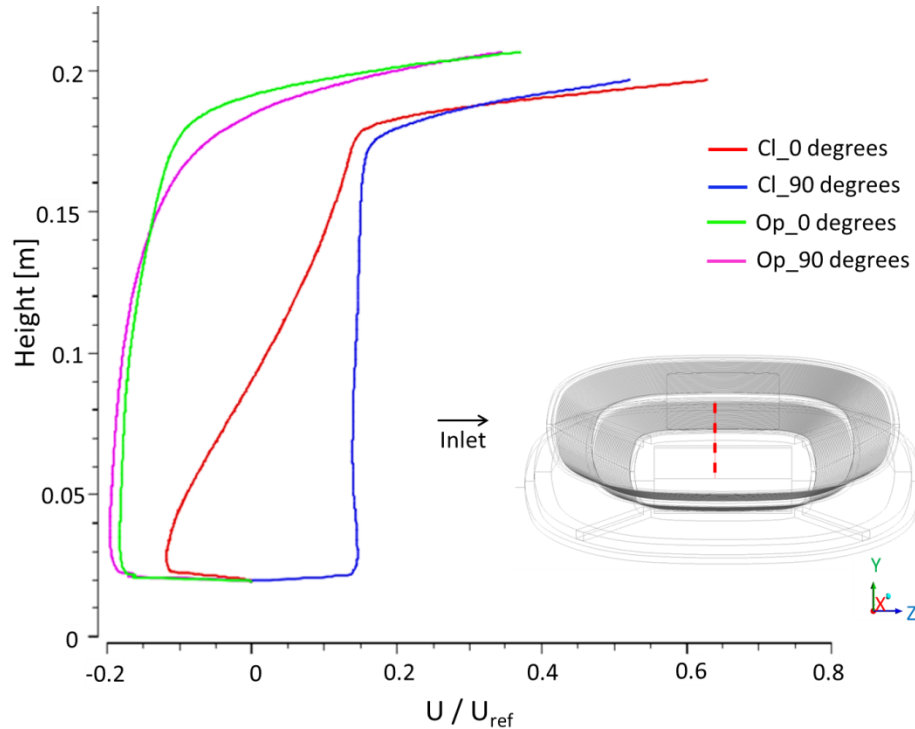


Figure 5-17 Chart of the dimensionless velocity values generated on a vertical line at the centre of the auxiliary area for the four stadium configurations; $U_{ref} = 5.23$ m/s.

5.3.2.2 Spectator tiers

Information on the wind microenvironment at the spectator tiers was obtained with the generation of local dimensionless contours and normalised vectors at the upper and bottom terraces. Figure 5-18 illustrates the results for the non-elevated roof configuration. The velocity contours for both wind directions were similar. The 0° wind angle generated an average value of dimensionless velocity equal to 0.13, which was 8.3 % higher than the average value of the stadium case at 90° wind angle. More specifically, the incoming air flow through the oculus was separated in three parts, including the flow that feeds the primary central vortex and the flow towards the side terraces. The wind travelled parallel to the spectator tiers and contributed to high ventilation zones of up to 0.36 and 0.32 dimensionless velocity values at the upper side windward spectator tiers for the 0° and 90° wind angle respectively. Similar high ventilation zones were also stated in Szucs et al. (2009b). For the upper spectator tiers, the central windward areas were dominated by calm

5 Results and Discussion

zones with dimensionless velocity equal to 0.02, since the flow could not penetrate till the very upper seating rows. The transverse wind created high speed zones in the whole perimeter of the upper tiers and it was attenuated in strength when reaching the leeward terraces' side. The bottom tiers were characterised by high wind speeds at the corners of the windward side of up to 0.26 and 0.22 for the 0° and 90° wind angle and calm zones for the rest of the stadium bowl periphery.

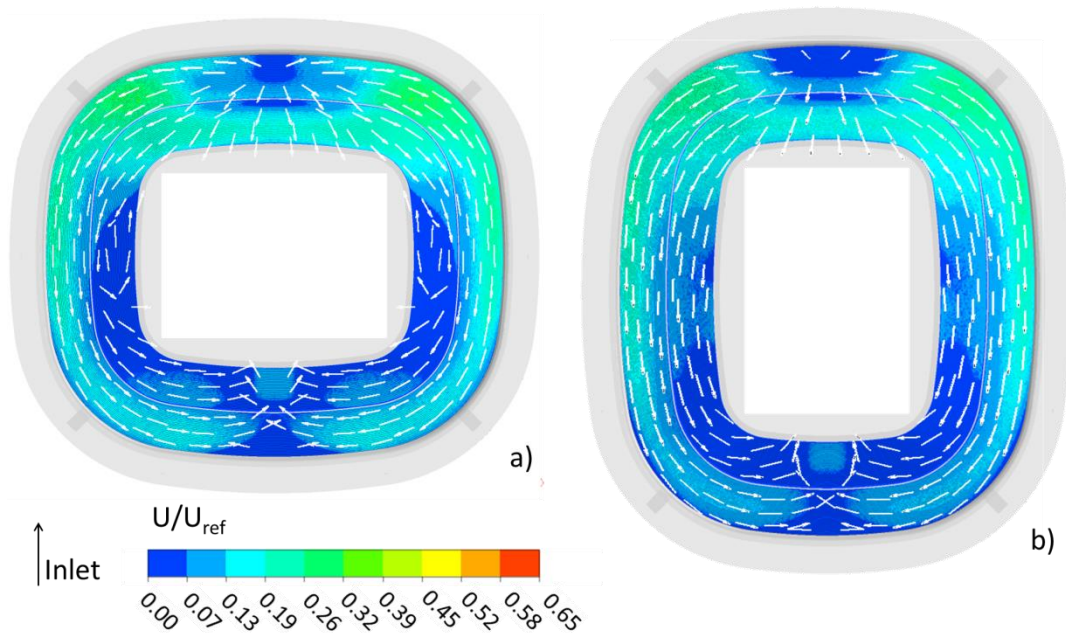


Figure 5-18 Illustration of the dimensionless contours and normalised vectors of velocity generated on a plane 0.003 m above the spectator terraces for the stadium models with non-elevated roof 0° (a) and 90° (b) wind angle; $U_{ref} = 5.23$ m/s.

The elevated roof configuration changed dramatically, the wind environment at the stadium bowl. The existence of the horizontal ventilation opening created additional openings for the airflow to enter and exit the stadium bowl. The generated average dimensionless velocity values were equal to 0.12 and 0.11 for the wind angle of 0° and 90° , and 7.6 and 15.4 % smaller than the average value of the reference stadium case study, respectively. The highest wind speeds were observed at the lateral sides of the upper spectator tiers and influence only the very upper seating rows, also reported by Goliger (2010). The highest values of the dimensionless velocities were equal to 0.65 and 0.63 for the angle of 0° and 90° respectively. It is worth mentioning that even if the average values for the non-elevated roof were higher, the existence of the ventilation opening led to up to 80.5 % higher maximum dimensionless velocity values, as a result of the intense flow streams that are partly traveling on the lateral upper leeward spectator tiers and partly exiting the stadium bowl. For both wind directions the same flow patterns were generated. On the upper terraces, the wind

5 Results and Discussion

distribution was greatly dependent on the envelope porosity, which led to very calm zones on the leeward side, with a minimum value of the dimensionless velocity equal to 0.067, due to the fact that the largest part of the frontal entering flow was driven upwards exiting the stadium via the roof (see Figure 5-10), without interfering with the wind microenvironment of the stadium bowl. The highest speeds were observed at the lateral sides, which were in sequence attenuated at the windward corners. The flow at the windward terraces was added to the entering flow via the horizontal opening at the rear stadium walls and was driven towards the auxiliary area. At the bottom spectator tiers calmer zones were developed. The airflow distribution at the windward side was solely dependent on the upper tiers flow patterns and at the leeward on the central recirculation zone.

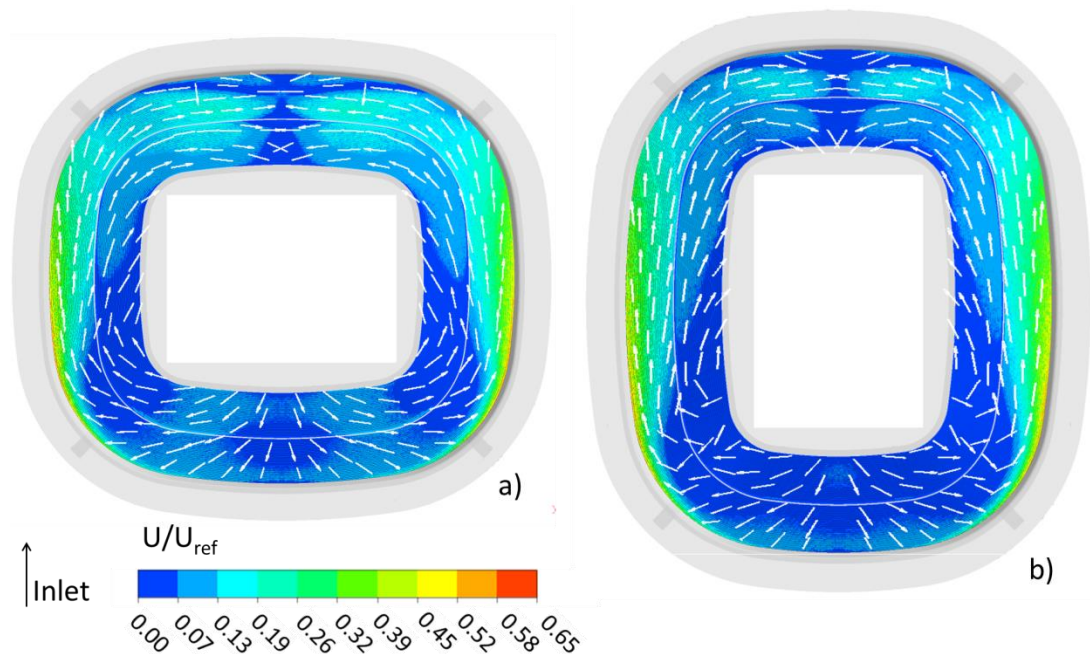


Figure 5-19 Illustration of the dimensionless contours and normalised vectors of velocity generated on a plane 0.003 m above the spectator terraces for the stadium models with elevated roof 0° (a) and 90° (b) wind angle; $U_{ref} = 5.23$ m/s.

The study of the interactions between the stadium and the human scale was also assessed by determining the impact of the developed wind environment on the spectator terraces. Figure 5-20 illustrates the graph of the dimensionless velocities generated on a vertical line in the centre of the windward spectator tiers. According to the results, the stadium configurations with the non-elevated roof contributed to the development of about 60 % and 33 % higher velocities close to the roof boundaries and the bottom spectator tiers respectively, when compared with the elevated roof configuration. Bearing in mind the Figure 5-4 and Figure 5-5, the primary vortex led to intense ventilated zones at the upper spectator tiers and also at

5 Results and Discussion

the lowest levels of the bottom spectator tiers. The graph also enabled the identification of the flow direction. At higher levels the wind was directed towards the windward spectator tiers as a result of both the flow entering the stadium through the oculus and the recirculating flow at the stadium bowl. At the bottom levels, the flow was directed towards the auxiliary area, as a result of the clockwise vortex development.

On the other hand, the presence of the horizontal ventilation opening reduced significantly the velocity intensities at the windward spectator tiers, since the flow is mainly determined by the developed vortices that recirculate the flow at the windward terraces. Another conclusion drawn by the chart was the flow homogeneity along the vertical line. For the wind angle of 0° the line was straight, implying vertical flow homogeneity, whereas for the 90° wind angle, the vertical velocity distribution profile was slightly disturbed on the upper layers by the small vortex developed at the windward oculus side (see description of Figure 5-10). As far as the overall direction of the flow is concerned, the wind was directed away from the windward spectator tiers, as a result of the flow entering from the leeward ventilation opening and the horizontal flow circulation at the terraces.

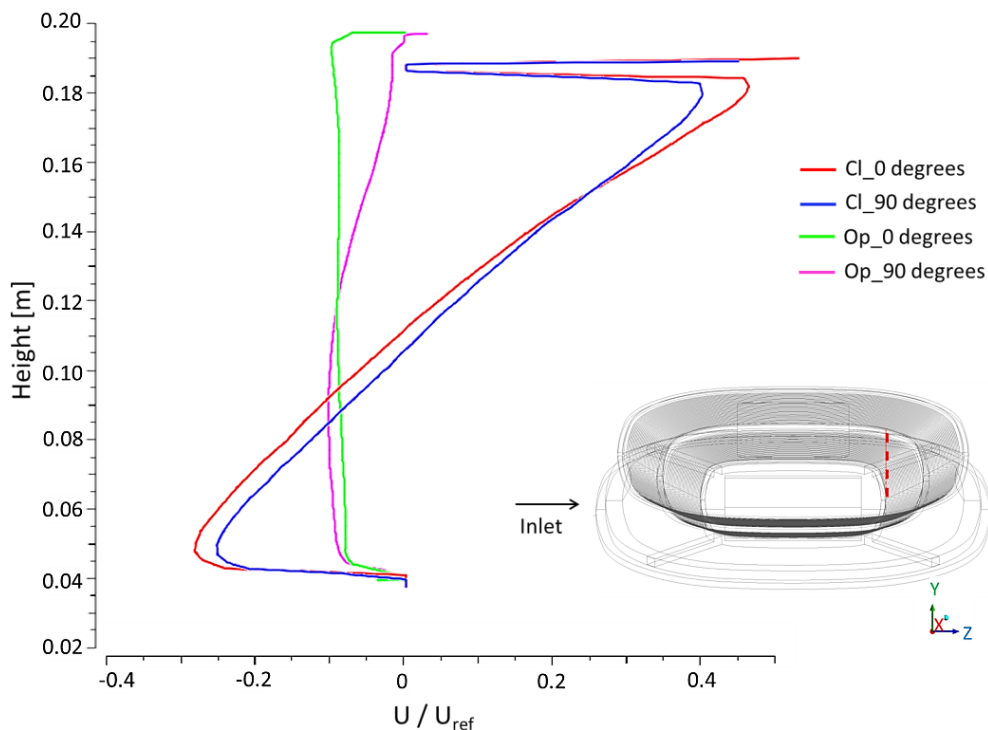


Figure 5-20 Chart of the dimensionless velocity values generated on a vertical line at the front of the windward spectator tiers for the four stadium configurations; $U_{ref} = 5.23$ m/s.

5 Results and Discussion

Figure 5-21 shows the dimensionless velocity values generated on a vertical line at the centre of the leeward spectator tiers. According to the results for the non-elevated roof configuration, the recirculated flow at the leeward spectator tiers was developed homogeneously along the vertical line, with direction towards the stadium centre. On the other hand, the flow distribution for the open ventilation configurations was determined at the upper levels by the incoming flow through the windward horizontal ventilation opening and thus there was a peak of the dimensionless velocity values equal to 0.325 and 0.35 for 0 and 90 degrees wind angle respectively. On the lower levels, the flow was determined by the recirculation zones, which drove the flow towards the leeward spectator tiers. Overall, minor deviations were observed for the case studies of different wind direction.

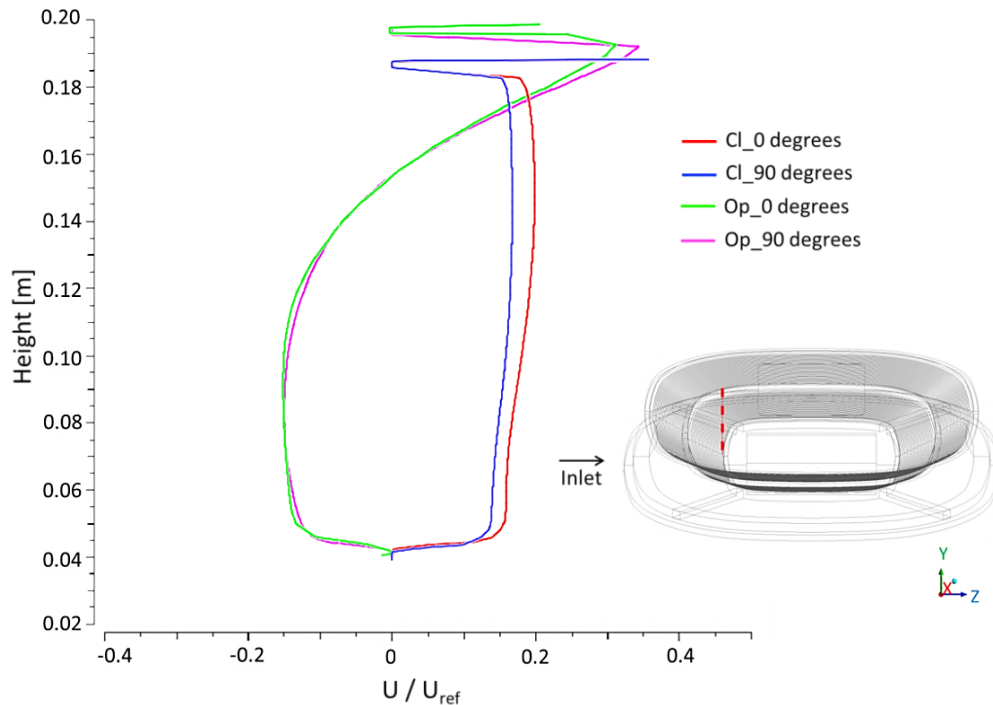


Figure 5-21 Chart of the dimensionless velocity values generated on a vertical line at the front of the leeward spectator tiers for the four stadium configurations; $U_{ref} = 5.23$ m/s.

5.4 Turbulence model validation

Three viscous models were used to assess the performance of the numerical solution: 1) the Spalart-Allmaras model, 2) the standard $k-\varepsilon$ turbulence model and 3) the realisable $k-\varepsilon$ turbulence model. These models have been used in literature to estimate the pressure distribution in aerodynamically designed models and also to assess the airflow distribution in sports stadiums. The simulation set-up was similar to the one presented in Table 4.3, but with the use of scalable wall functions, to

5 Results and Discussion

accurately predict the solution in areas of $y^+ < 11.225$. The turbulence model validation study involved the comparison of 1) the flow distribution at the important areas of the stadium structure, 2) the convergence criteria and 3) the pressure coefficient values at the stadium surfaces.

On the comparison of the flow distribution, the dimensionless velocity contours were generated on the symmetrical plane for the three turbulence model cases. According to the results presented in Figure 5-22, the produced flow regimes differ in strength and turbulence extent. More specifically, for the SA model, the entering flow from the roof appears to create high intensity zones under the windward roof surface, supporting the development of the primary vortex that covers half the length of the auxiliary area and the entire windward spectator tiers. High velocity speeds also appear on the lower bottom terraces and the adjoining playing field area. Overall, when compared with the other two turbulence model cases, the SA model predicts the highest velocity magnitudes at all areas, and particularly at the areas of flow recirculation; i.e. the recirculation zone at the front and the rear side of the stadium model. As far as the extent of the recirculation zones is concerned, the realisable $k-\varepsilon$ turbulence model appears to predict the largest in length zones, particularly on the windward and leeward exterior walls of the stadium structure. Finally, the primary vortex at the stadium interior, for the same turbulence model case, seems to have the smallest velocity values, as opposed to the standard $k-\varepsilon$ and the SA models.

5 Results and Discussion

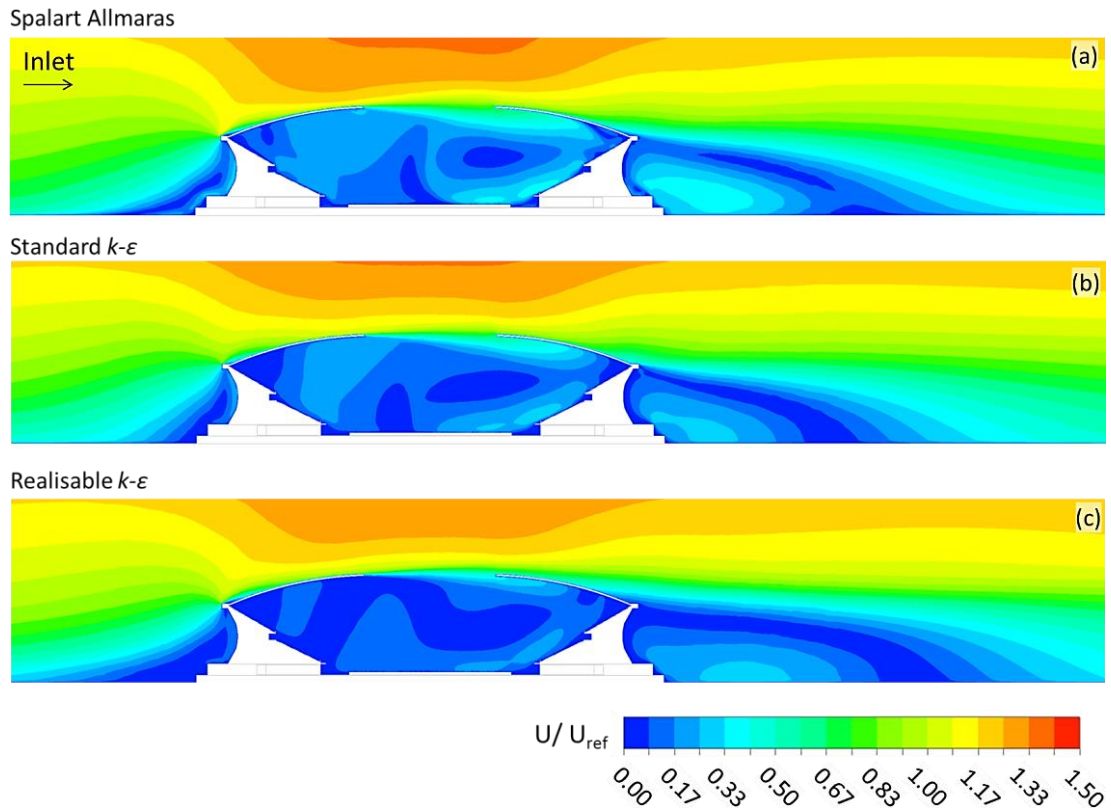


Figure 5-22 Contours of dimensionless velocity generated on the symmetric plane for the Spalart-Allmaras (a), the standard $k-\epsilon$ (b) and the realisable $k-\epsilon$ (c) models; $U_{ref} = 5.23$ m/s.

Complementary to the comparison results of the flow distribution are the dimensionless velocity streamlines that give an overview of the flow distribution at the stadium bowl. According to Figure 5-23, great differences are observed in both wind intensity and flow patterns, especially on the leeward side of the auxiliary area. More specifically, the realisable $k-\epsilon$ model develops less intensity airflow streams at the stadium interior at all areas. The primary vortex is substantially weakened and part of the recirculated flow is incorporated to the flow derived from the leeward terraces. On the other hand the developed flow for the SA and the standard $k-\epsilon$ model is more compact. The primary vortex is separated from the downwash of the leeward spectator tiers. Nonetheless, significant are the differences in the flow intensity, since the SA model produces substantially higher velocity speeds, notably at the lower bottom and the very upper spectator tiers.

5 Results and Discussion

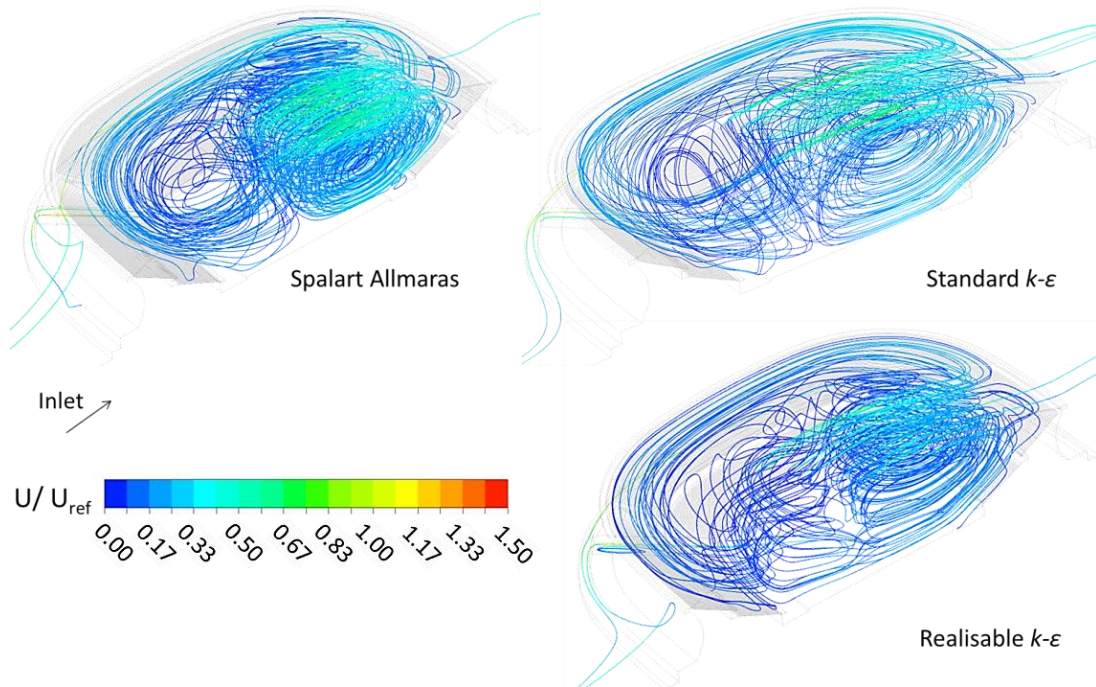


Figure 5-23 Streamlines of the dimensionless velocity for the Spalart-Allmaras, the standard $k-\varepsilon$ and the realisable $k-\varepsilon$ models; $U_{ref} = 5.23$ m/s.

Since the flow distribution results gave only a superficial assessment of the turbulence models' performance, further comparison was conducted with the convergence criteria. Figure 5-24a-f illustrates the convergence history of the scaled residuals, according to which all the residuals values were decreased between 3 and 4 orders of magnitude during the first 250 iterations and between 5 and 10 till the end of the simulation. Additional information on the solution convergence were obtained from the monitored values of the dimensionless velocity set for a point located at the centre of the stadium bowl, 0.053 m above the pitch level (Figure 5-24g-i). More specifically, for the SA model, small fluctuations were observed throughout iterations 39,000 and 45,000, also depicted in the residuals history of turbulence viscosity (ν_t). The standard $k-\varepsilon$ model reached solution stabilisation after 51,000 iterations. Finally, for the realisable $k-\varepsilon$, even if the scaled residuals history implied solution convergence, the solution of the monitor point showed very large fluctuations of increasing scale starting after 40,000 iterations. These fluctuations have previously been reported in literature for flows in buildings, indicating the enforcement of a highly turbulent flow to a steady solution by the RANS models (Ramponi and Blocken, 2012). Nonetheless, the standard $k-\varepsilon$ showed the highest performance out of the three turbulence models, with a smooth solution convergence and a drop of residuals values by at least 8 orders of magnitude to at least 10^{-5} .

5 Results and Discussion

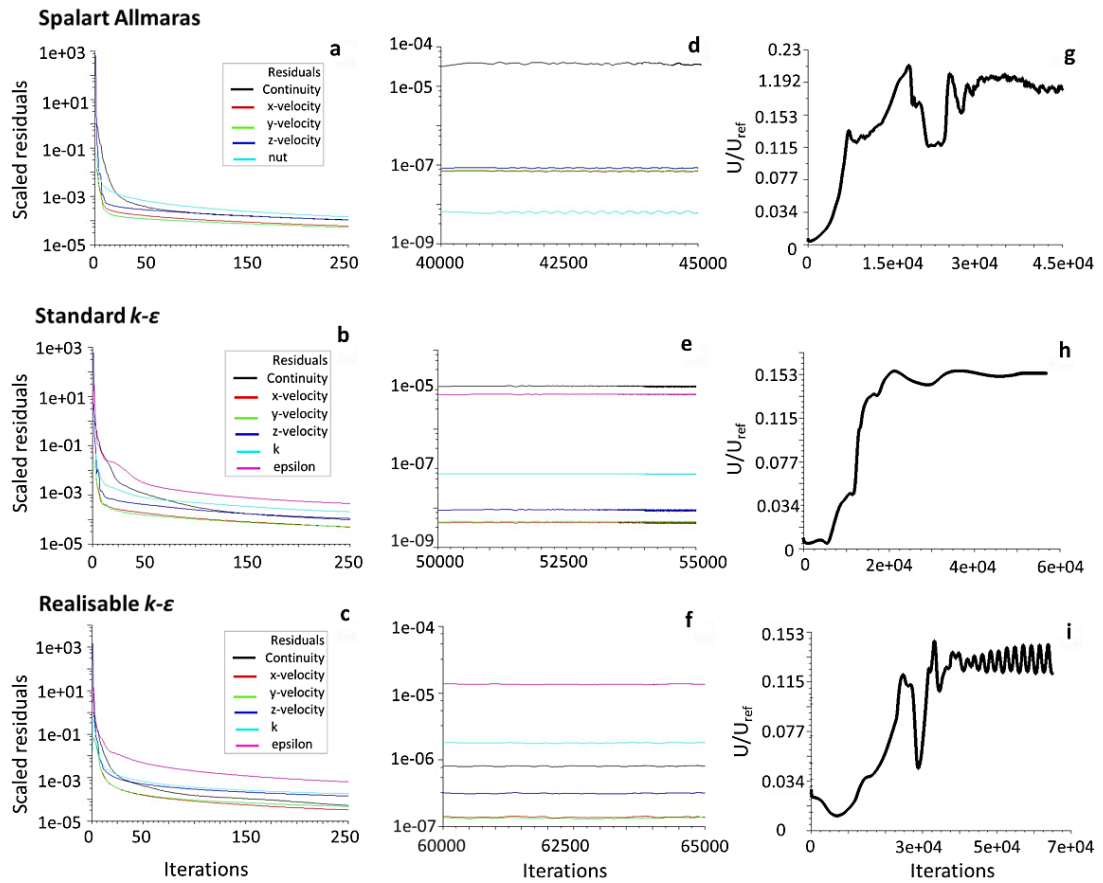


Figure 5-24 Turbulence models results of scaled residuals history for the first 250 iterations (a, b, c) and the last 5,000 iterations of the simulation runs (d, e, f); monitor convergence history of the dimensionless velocity (g, h, i); $U_{ref} = 5.23$ m/s.

The final comparison to conclude to the most appropriate turbulence model involved the comparison of the pressure coefficient values between the CFD simulations and the wind tunnel experimentation. The C_p values were calculated based on Equation 2.4. For the CFD values, P , was the calculated on the stadium surfaces static pressure, P_{ref} was set equal to 0 Pa, equivalent to the outlet pressure and U_{ref} the undisturbed velocity value at roof height. For the wind tunnel values the pressure, P , was calculated after subtracting the static pressure value at the Pitot tube, P_S^{Ref} , from the pressure values obtained by the transducer, P_S^{Tran} .

The comparison of the pressure coefficient values on the roof surface is illustrated in Figure 5-25. According to the results, the Spalart-Allmaras and the standard $k-\epsilon$ model generated almost identical values of C_p with their maximum deviation to occur at the Points 1, 7 and 8 with an equal error of 3.76 %. The realisable $k-\epsilon$ model generated similar results to the Spalart-Allmaras and the standard $k-\epsilon$ model for the points located at the front and lateral sides of the oculus configuration. However, the same model estimated smaller negative values of pressure coefficients at the rear

5 Results and Discussion

side of the oculus and the Points 4 and 12-16 with deviation errors that vary between 19.51 %, for the Points 4 and 14, and 32.57 % for the Point 16. On the comparison of the wind tunnel with the CFD results, the standard $k-\varepsilon$ model appears to have, in average, smaller deviations with total 9 points to produce errors lower than 10 %. The maximum deviation occurs that the Point 7 with an error equal to 30.7 %. Finally, it is also worth-mentioning the advantageous performance of the standard $k-\varepsilon$ and the Spalart-Allmaras models on the estimation of pressure coefficients at the rear side of the oculus, since these points are detrimental indicators of the airflow exiting the stadium bowl.

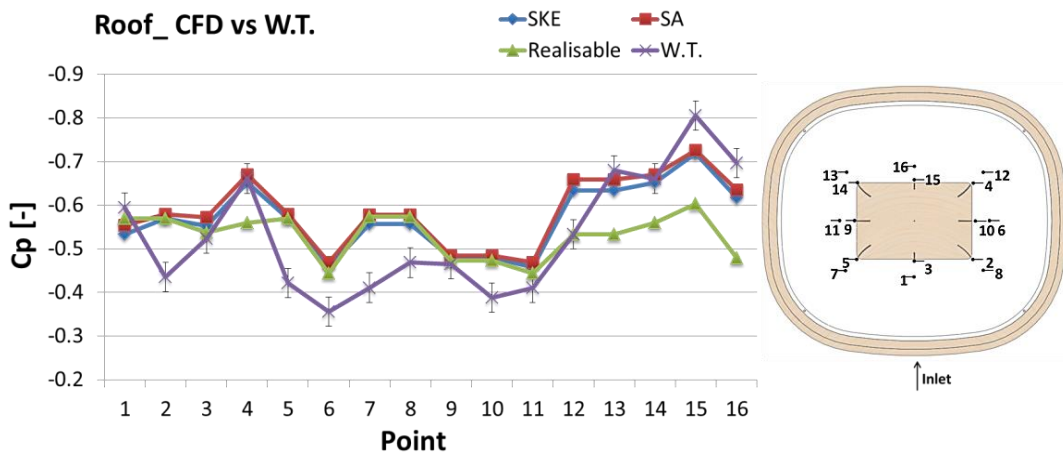


Figure 5-25 Comparative results of the C_p values generated on the roof surface for the stadium model with non-elevated roof, among the three turbulence models and the wind tunnel experiments.

As shown in Figure 5-26, the C_p results generated on the auxiliary area are greatly similar in trend for the three turbulence models. The standard $k-\varepsilon$ and the realisable $k-\varepsilon$ model appear to have the smallest deviations with a maximum error of 3.88 % at the Point 7. The Spalart-Allmaras model overestimates the pressure coefficient results, with a maximum error of 10.38 % at the Point 7 when compared with the realisable $k-\varepsilon$ model. Overall, the wind tunnel results predict smaller negative values of pressure coefficients, with a significant drop at the measuring point 3, which as mentioned in §3.8.2.4, must be caused due to bending of the pressure tap during rotation.

5 Results and Discussion

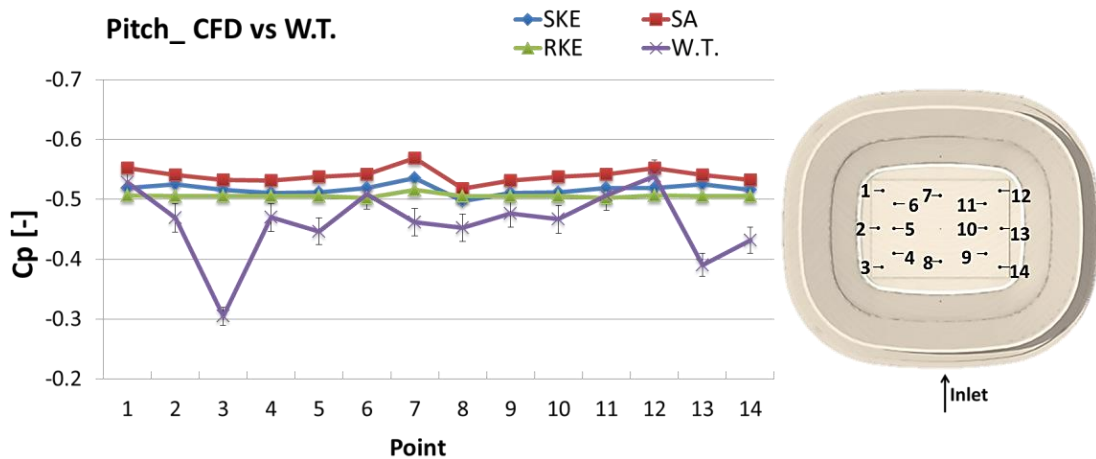


Figure 5-26 Comparative results of the C_p values generated on the auxiliary area of the stadium model with non-elevated roof, among the three turbulence models and the wind tunnel experiments.

Figure 5-27 illustrates the generated pressure coefficients on the surface of the front (windward) and back (leeward) spectator tiers. According to Figure 5-27top, for the windward spectator tiers, the Spalart-Allmaras and the standard $k-\varepsilon$ models provide better pressure coefficient predictions when compared with the wind tunnel measurements, particularly at the Points 6-11, where the primary airflow vortex is developed. Numerical deviations of these two models are observed between Points 6 and 9, where the standard $k-\varepsilon$ model predicts higher negative values, with a maximum deviation error of 16.8 % at the Point 6.

The standard $k-\varepsilon$ model achieves to capture the wind tunnel pressure measurement at the Point 6, located at the centre of the upper tiers, which is primarily influenced by the entering to the stadium bowl airflow. On the other hand, at the Points 5 and 7 located at the highest rows of the upper tiers, the model predicts higher negative C_p values, when compared with the ones from the wind tunnel, with deviation errors equal to 50 and 41 % respectively. Between the Spalart-Allmaras and the wind tunnel measurements, the highest deviations are observed at the Points 5 and 13 with errors equal to 43 and 31 % respectively. The realisable $k-\varepsilon$ predicts higher negative pressures at the Points 6-9, with a maximum deviation error of 78.67 % at the Point 7 when compared with the W.T. prediction. At the rest of the measurement location the realisable $k-\varepsilon$ generates similar results to the standard $k-\varepsilon$ model.

In the case of the results generated for the leeward spectator tiers, all turbulence models predict similar C_p values per measurement point and a relative homogeneous pressure distribution at the entire leeward tiers' area with interval $[-0.534, -0.473]$.

5 Results and Discussion

Out of the three turbulence model, the Spalart-Allmaras gave the largest deviations, followed by the standard $k-\varepsilon$ and the realisable $k-\varepsilon$ models

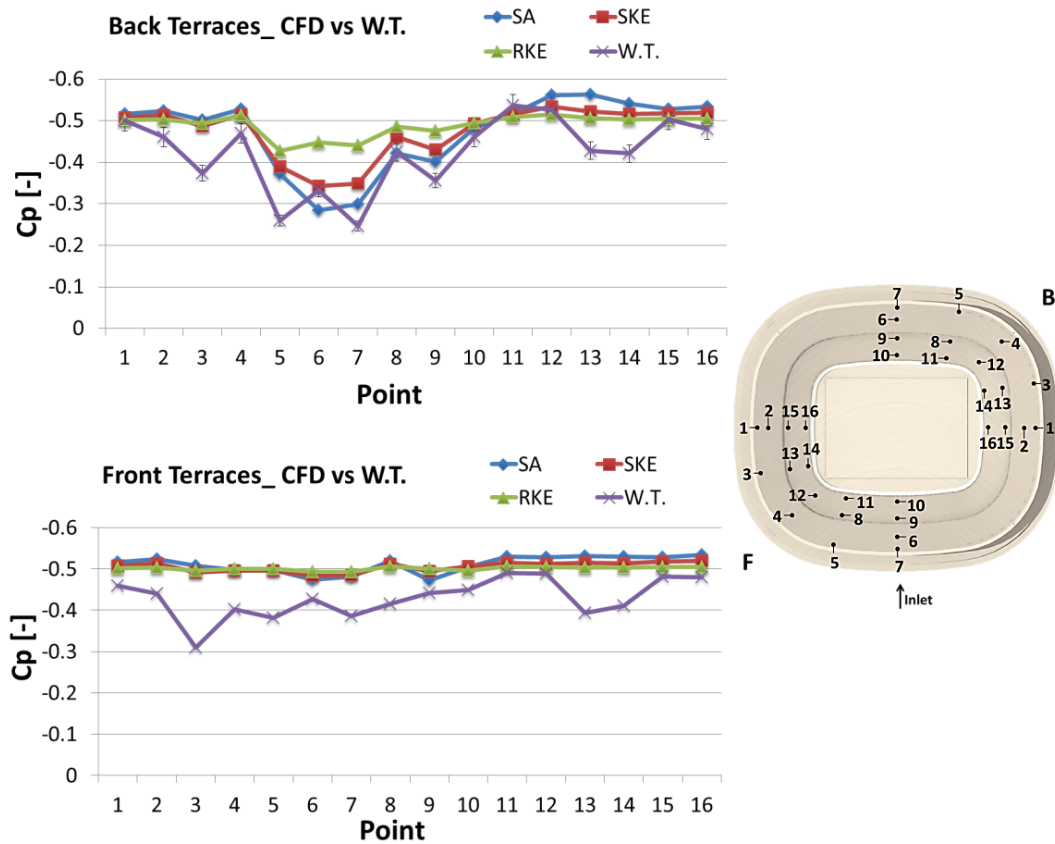


Figure 5-27 Comparative results of the C_p values generated on the back and front spectator terraces of the stadium model with non-elevated roof, among the three turbulence models and the wind tunnel experiments.

According to the aforementioned comparisons, the following conclusion can be drawn:

1. The standard $k-\varepsilon$ model was the only turbulence model with a converged history of the scaled residuals and a monitor point with a steady solution.
2. On the aerodynamic performance evaluation of the stadium structure, attributed to the roof structural component, the standard $k-\varepsilon$ model first and the Spalart-Allmaras model in sequence, showed the best performance. Similar observations, considering the reliability of the Spalart-Allmaras and the standard $k-\varepsilon$ model to predict the pressure coefficients on building surfaces have been reported by Li et al. (2015) and Satwiko et al. (1998) respectively. However, the performance of the SA model against predictions of wind flow turbulent phenomena of the built environment and complex internal flows is not supported enough in literature and thus the model's adaptation should be carefully considered (Spalart and Allmaras, 1992).

5 Results and Discussion

3. The evaluation of the pressure coefficient distribution at the stadium interior highlighted the advantageous performance of the standard $k-\varepsilon$ and the realisable $k-\varepsilon$ models, on their attempt to predict the high turbulent and unstable phenomena at the auxiliary area. However, the realisable $k-\varepsilon$ generated the highest deviations on important studied areas, such as the roof surface and the upper windward terrace areas.
4. Since the study involved both the evaluation of the aerodynamic performance of the structure and the flow distribution at the stadium areas, the standard $k-\varepsilon$ model was selected to conduct the study of the stadium wind environment, since it was the closest to the SA generated pressure coefficient results.

5.5 Limitations

Main limitation of the study is the assumption of a symmetrical flow distribution, considering symmetrical geometry configuration. Adding to the steady state simulation, the flow behaviour is only an average approximation of the real turbulence phenomena developed at the stadium interior. Additional limitations of the validation study are listed below:

1. The static pressure measurement at the Pitot tube was automatically subtracted by the stadium model measurements points, and thus the generated from the CFD study was used to calculate the static pressure at the stadium model. However, the reference static pressure is subject to random error, due to the non-uniformity of the flow in the test section, which cannot be fully represented by the average CFD generated value.
2. The CFD study involved the simulation of the fully detailed stadium structure. On the other hand the wind tunnel results arose from a simplified model, which excluded the grandstand seating details and the protection bars at the front row of each terrace.
3. As mentioned at the limitations of the wind tunnel experimentation study, in order to reduce the roof vibration, six supports were provided, which were also excluded from the CFD simulation study.

5.6 Summary

This chapter presented the CFD generated results of the pressure and flow distribution in both interior and exterior areas of the stadium bowl. Summarising the

5 Results and Discussion

results of the pressure distribution, the wind direction alters slightly the pressure and wind flow patterns at the stadium bowl. However, the presence of a horizontal ventilation opening leads to the development of higher pressure values at the stadium bowl surfaces, which subsequently attenuates the airflow streams entering through the side entrances and the roof.

The airflow distribution at the stadium interior is primarily dependent on the envelope porosity. The non-elevated roof configuration, leads to the development of a more compact flow at the stadium bowl, involving the creation of a primary central vortex, which along with the flow entering through the side openings dominate the wind microenvironment. On the other hand, the roof elevation causes a more chaotic flow distribution, which adds to the ventilation performance of the very upper lateral spectator tiers.

The turbulence model validation study was also presented, which involved the comparison of the Spalart-Allmaras, the standard $k-\varepsilon$ and the realisable $k-\varepsilon$ turbulence models, out of which the standard $k-\varepsilon$ model was selected as the most accurate and computational efficient to describe the aerodynamic performance of the structure and the flow distribution patterns.

6 Design Optimisation

6.1 Introduction

The final objective of the research was to perform a design optimisation study, in order to provide improved microenvironmental conditions for both players and spectators. For the purpose of this, the simulations performed in 5 will be coupled with Design of Experiments (DoE) and Response Surface Methodology (RSM) techniques integrated in the interface of the simulation software. In this chapter, the theoretical background on the Design Exploration techniques and the optimisation algorithms are stated along with their advantages and disadvantages per case study. The key stadium structural parameters are determined and their responses on the wind comfort study at the stadium areas are assessed. Finally, based on multi-objective optimisation algorithms the optimum design solutions are generated for 3D stadium structures.

6.2 Theoretical background

DoE is a valuable technique used to assess the performance of model's parameters upon change. It is a tool to study the change of the behaviour (output) of the model, regarding alterations of the design (input) parameters. It provides an insight into the relationships among the model parameters and the identification of the most influential factors upon change (Wu and Hamada, 2000). In other words, it is an engineering approach to improve and/or optimise a model, by mathematizing its parameters (inputs and outputs).

Hotelling (1941) and Friedman and Savage (1947) were those who laid the groundwork for the exploration of design responses by evaluating the input design parameters. The mathematical equation that describes the unknown functional relationship between the independent design parameters (or variables or inputs), x , and the equivalent dependent design responses (or outputs), y , can be described by the following low-degree polynomial model:

$$y = f(x, \theta) + \varepsilon \quad (6.1)$$

where ε is treated as a statistical error. By employing mathematical and statistical methods, first-order (6.2) and second-order (6.3) polynomial regression models are constructed, based on physical or computer experiments (Myers at al., 1989).

6 Design Optimisation

$$\eta = \beta_0 + \beta_1 x_1 + \dots + \beta_k x_k \quad (6.2)$$

$$\eta = \beta_0 + \sum_{i=1}^k \beta_i x_i + \sum_{i=1}^k \beta_{ii} x_i^2 + \sum_{\substack{i=1 \\ i < j}}^k \sum_{j=1}^k \beta_{ij} x_i x_j \quad (6.3)$$

where η represents a design response (i.e. velocity, pressure, deformation, etc.), x_1, x_2, \dots, x_k are the design variables (i.e. width, radius, load, etc.) and $\beta_0, \beta_1, \dots, \beta_k$ are unknown regression coefficients.

Box and Wilson (1951) introduced a statistical tool that allows simultaneous assessment of several design parameters, aiming at the generation of improved design solutions that satisfy specific design constraints. They defined the experimental region, as the region within which the design inputs vary and their outputs can be retrieved. This region is known as Response Surface and the developed technique Response Surface Methodology (RSM).

The RSM employs mathematical tools to calculate approximate values of the regression coefficients to describe complex experimental or simulation data, obtained for a specific number of sample design points. The best fit approximation function may be used, in sequence, to examine several design combinations, without the need to conduct time-consuming deterministic response analysis. Additional to this, the RSM offers the great advantage of performance assessment of the key design parameters on the design responses, assisting model simplification, results' interpretation and performance of optimisation studies (Friedman, 1996). RSM determines the relationships among variables by performing regression analysis. Depending on the number of the variables related to the problem, different algorithms may be applied, in order to determine the most accurate regression function that will describe the model.

6.3 Optimisation concept and methodology

The CFD analysis and experimental validation that has been performed in 5 has shown that the roof geometry together with the ventilation openings are the main contributors for the climate development at the stadium bowl. Thus, the optimisation study focuses on the investigation of the roof configuration with aim the improvement of the wind comfort conditions for the players and the spectators. For the purpose of the study, the stadium configuration with closed horizontal roof

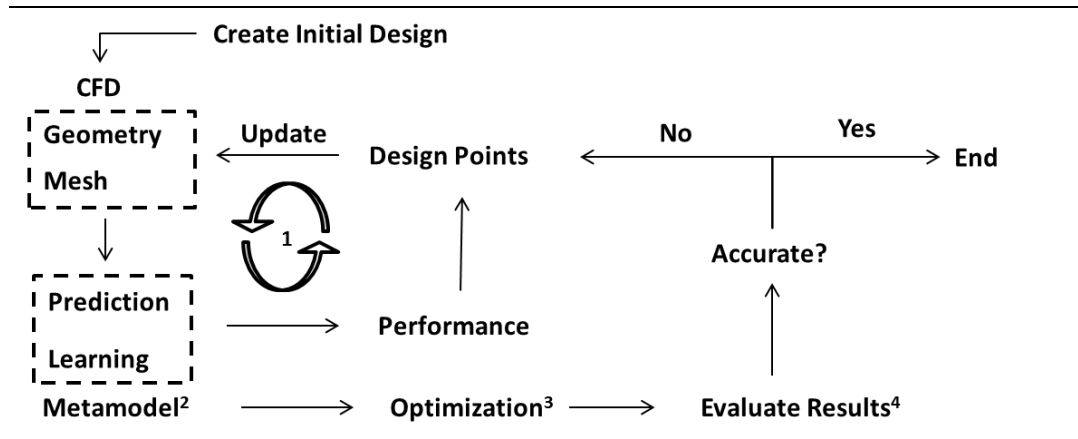
6 Design Optimisation

opening and 0° wind angle was used. The selection of that stadium was based on the fact that the wind conditions could be more easily controlled than the case of the open roof opening and also according to the results, higher velocity magnitudes were generated at the stadium bowl. This was mainly dependent on the developed large vortex towards the windward side of the spectator tiers.

The simulation-based optimisation study was conducted in four main steps. Once the results of the initial design case were obtained, a series of sequential simulation runs was performed generating data, regarding predefined geometrical characteristics of the stadium roof (Step 1). The results were used to formulate a high precision mathematical model that would describe the problem and predict relationships among the design variables (Step 2). The optimisation process was performed according to the selected algorithm and the defined objective sets and thresholds, pursuing design optimality (Step 3). Finally, the proposed solutions were verified with CFD runs and compared with the predicted ones, in order to evaluate the solution and therefore the accuracy of the RSM-based optimisation technique (Step 4). The flowchart in Table 6.1 is a graphical representation of the steps followed for the optimum-seeking stadium roof configuration to create optimum wind comfort conditions. The methodology is fully detailed and validated by Sofotasiou et al., (2016) and it is a computational inexpensive solution to provide quantitative and qualitative results of improved design solutions.

6 Design Optimisation

Table 6.1 Four step methodology of the RSM optimisation study (Sofotasiou et al., 2016).



Step 1. Design of Experiments

- i. Define input parameters: continuous or discrete
- ii. Define output parameters
- iii. Select DoE scheme: Central Composite Design, Box-Behnken Design, etc.
- iv. Select design type: Auto Defined, Face-Centered, etc.
- v. Generate design points

Step 2. Response Surface

- vi. Select a Meta-Model: Standard Response Surface, Kriging, Neural Network etc.
- vii. Generate correlation of parameters, sensitivity results, etc.

Step 3. Goal driven optimisation

- viii. Select optimisation method: Screening, MOGA or NLPQL.
- ix. Define objectives and constrains
- x. Obtain candidate points

Step 4. Robustness Evaluation

- xi. Solution verification

6.3.1 Design of Experiments (DoE) set-up

The three main principles for the implementation of a DoE were described by Shen et al. (2012) as follows:

1. Identify the performance assessment of the dependent variables (outputs) to be optimised, considering the influential role of the most significant independent variables (inputs).
2. Designate the design space (constrains), within which the input parameters will vary.
3. Generate the design points and their response values.

6 Design Optimisation

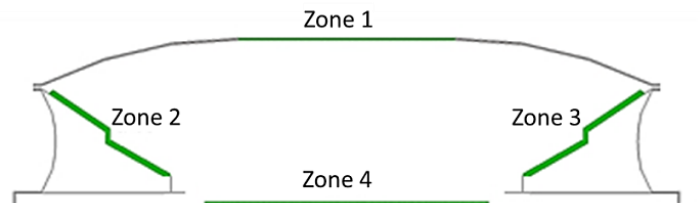
6.3.1.1 Selection of input parameters

According to literature, stadium structures have been extensively studied in order to determine optimum geometrical configurations to provide comfort conditions for both players and spectators (Persoon et al., 2008; Szucs et al., 2009a; Bouyer et al., 2007). The roof dimensional characteristics seem to be the major contributors on the attainment of microenvironmental satisfaction, also demonstrated by the conducted CFD simulations in 5. Thus, the input design parameters were set as: 1) the roof radius, 2) the roof length extension towards the centre of the pitch area, and 3) the roof height.

6.3.1.2 Selection of output parameters

Favourable microenvironmental conditions in semi-outdoor stadium structures, initially reported by Szucs et al. (2007), indicated that aerothermal comfort conditions may be achieved with wind threshold speed values between 0.1 m/s, to ensure minimum air movement, and 3.6 m/s, to prevent wind disturbance and performance impairment. On the basis of these considerations, the output parameters were set as the flow homogeneity values on the spectator tiers and the playing field area and the maximum developed velocity magnitudes at the same areas. The mass flow rate from the roof oculus opening and the minimum velocities at the spectator terraces and the pitch were also selected as additional derived parameters to enable the interpretation of results. In order to control and enable the generation of the results, the areas of interest were separated from the entire fluid domain. As shown in Table 6.2, zones 2, 3 and 4 comprise an area equal to the zone length times 1.8 m on the perpendicular direction, to adequately cover the fluid area on human height level. Zone 1 was 0.5 m thick, similar to roof thickness.

Table 6.2 Separation of the fluid domain into four controllable zonal areas.



Zone	Description
Zone 1	Roof
Zone 2	Leeward
Zone 3	Windward
Zone 4	Auxiliary

The flow homogeneity for ventilated areas is calculated based on the equation of the coefficient of spatial variation, presented in Equation 6.1 (Kindangen et al., 1997):

6 Design Optimisation

$$C_{sv} = \sigma_s \left(\frac{U_i}{U_{ref}} \right) / C_v \quad (6.1)$$

where

C_{sv} = coefficient of spatial variation,

$\sigma_s(U_i/U_{ref})$ = standard deviation of C_v ,

C_v = average velocity coefficient obtained by Equation 6.2:

$$C_v = \frac{1}{n} \sum_{i=1}^n \left(\frac{U_i}{U_{ref}} \right) \quad (6.2)$$

U_i = mean velocity at interior location i (m/s),

U_{ref} = mean outdoor reference velocity at reference height, and

n = number of nodes measured in the area of interest.

The post-processing feature of the simulation software was used for the calculation of the number of nodes in the 4 zones and the generation of the components for the Equation 6.1 and 6.2. The coefficient of spatial variation, C_{sv} , was used as the indicator of the homogeneity at the zonal areas. Values of C_{sv} larger than 1 imply distributions of high-variance, as opposed to values lower than 1 that indicate flow uniformity and velocity magnitudes of low-variance.

The roof mass flow rate was calculated based on Equation 6.3, for a non-uniform flow of an incompressible fluid ($\rho = \text{constant}$), in order to obtain a direct indicator of the flow direction; either incoming or outgoing flow stream to the stadium bowl.

$$Q = \sum_{i=1}^n U_i A_i = \bar{U} A \quad (6.3)$$

where

A = the area of the opening configuration, and

\bar{U} = the mean velocity in the perpendicular direction to the opening area (A).

6.3.1.3 Generation of design points

The design space, within which different design points are evaluated, is defined as the design space that indicates the range of inputs' variability (Cavazzuti, 2013). In the case of the stadium design three input design parameters were selected, in order

6 Design Optimisation

to control symmetric transformations of the roof configuration, presented in Table 6.3. It is worth stating at this point that the design constraints set for the input parameters were subjective, if not arbitrary, selected. The design exploration excluded the option of convex roof configuration, or a roof length that exposes the spectator tiers or partly covers the pitch area.

Table 6.3 Description of the input parameters and the defined constrains for spatial variance.

Input Parameters	Name	Initial Value (m)	Constrains
P1	Roof Radius	200	$100 \text{ m} \leq \mathbf{R} \leq 1000 \text{ m}$
P2	Roof Length	65	$50 \text{ m} \leq \mathbf{L} \leq 65 \text{ m}$
P3	Roof Height	16	$0.5 \text{ m} \leq \mathbf{H} \leq 20 \text{ m}$

The Optimal Space-Filling Design (OSF) scheme was selected for the generation of the design points, because it can describe more accurately nonlinear model parameters and support complex meta-modelling optimisation techniques. The OSF scheme provides an excessive overview of the design space, by equidistributional selection of the input design parameters. The Max-Min Distance design type was selected, which maximises the minimum distance between any two points and saves computational time, without compromising the generation of information throughout the design region.

In total 15 design points were generated, including the initial case study (DP 0), as the most ideal number to balance the computational expenses and solution accuracy. Table 6.4 presents the input parameters of the generated design points based on the OSF scheme, and Figure 6-1 their schematic representation.

6 Design Optimisation

Table 6.4 Description of the input parameters for the generated design points based on OSF scheme.

Design Point	P1_Radius [m]	P2_Length [m]	P3_Height [m]
DP0	200	65	16
DP1	190	62.5	7.65
DP2	790	59.5	2.45
DP3	730	51.5	15.45
DP4	610	52.5	1.15
DP5	430	55.5	19.35
DP6	130	54.5	12.85
DP7	850	58.5	18.05
DP8	490	56.5	11.55
DP9	970	60.5	10.25
DP10	550	64.5	5.05
DP11	310	57.5	3.75
DP12	370	50.5	8.95
DP13	670	63.5	14.15
DP14	910	53.5	6.35

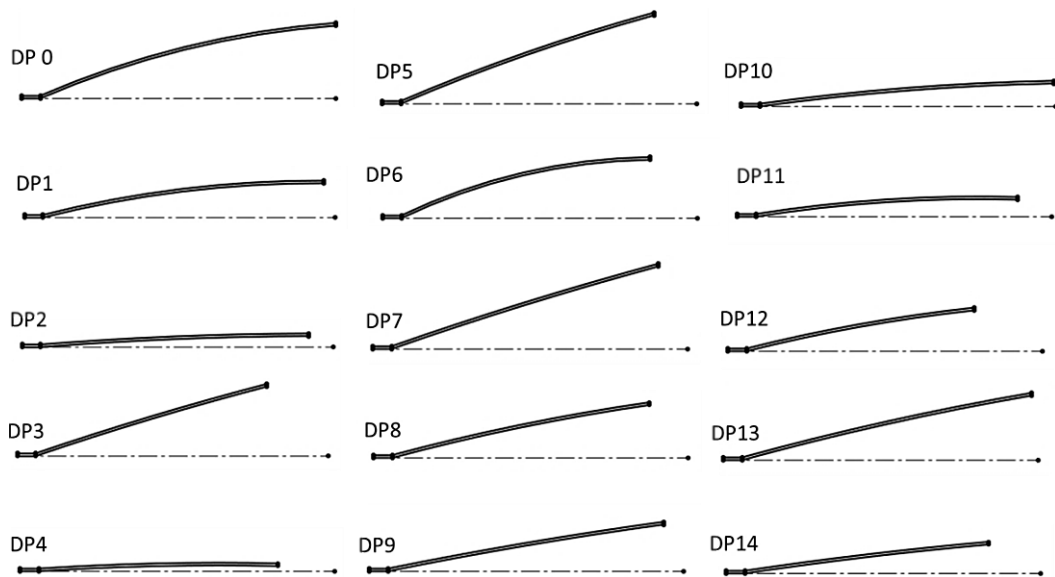


Figure 6-1 Schematic representation of the generated design points.

The calculation of the design point responses (output parameters) was performed with sequential simulation runs, contributing to the most computational time-consuming part of the study, since convergence was achieved for each run. One complete case study required 1 computational hour to generate the mesh file and 120 hours in the High Performance Computer facility of the Department to generate a converged solution (48 processors per study and 2.4 GB memory per processor). The values of the obtained output parameters will form the basis for the non-parametric

6 Design Optimisation

regression model, as part of the RSM meta-model technique and the creation of the design space, where different roof configurations, regardless of the input value, may be examined against their responses.

The generation of the results for the output variables for each design point gave an overview of the behaviour of the homogeneity and the maximum developed velocity values at the stadium interior (see also 0). In Figure 6-2 the coefficients of spatial variation of velocity are presented. According to the results, the homogeneity at the upper spectator tiers does not show a large variance when compared with the initial design case. However, for all design points the C_{sv} values were greater with the DP 5 to show the largest heterogeneity change of about 11.6 %.

At the bottom spectator tiers, the roof design seems to affect more the flow homogeneity conditions. The smallest coefficient values are identified for the design points DP 2, 4, 10 and 11, which according to Figure 6-1 have the smallest roof height. The decrease in roof height resulted to a decrease of 49, 53, 39 and 47 % in flow heterogeneity respectively. Similar deviations were observed at the coefficient of variance for the velocity values at the pitch area. The smallest values of C_{sv} were obtained for the DP 2, 4, 10 and 11 with a decrease of 30, 32, 26 and 29.5 % compared to DP 0.

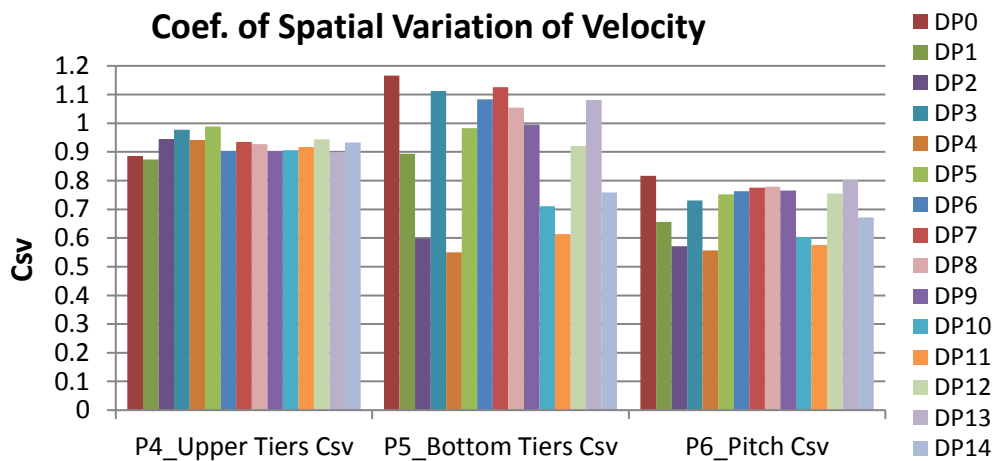


Figure 6-2 Coefficients of spatial variation of velocity at the areas of the upper and bottom terraces and the pitch.

Figure 6-3 shows the variance of the dimensionless maximum velocity with the roof geometrical changes. More specifically, for the upper tiers, the maximum velocities were increased for the roof cases with large radius (or flatter surface). The DP 3, 5 and 7 showed the highest increase with percentages of 23, 30 and 21 % respectively. For the DP 1, 2, 4, 10 and 11 the maximum velocity values were decreased to a

6 Design Optimisation

maximum of 33 % for the DP 10. At the bottom spectator tiers, the maximum velocity showed a decrease for the DP 1(10 %), DP 2 (18 %), DP 4 (12 %), DP 10 (17 %) and DP 11 (15 %). An increase on maximum velocities was noted for the rest of the design points, with the most significant to be the one for the DP 3 with a percentage of 23 % According to Figure 6-1, DP 3 has a very flat roof surface (large radius), a small roof length and a large height, which possibly denotes large mass flow entering the stadium bowl and the development of high speeds at the interior. Finally, similar behaviour of the maximum velocities was observed at the pitch area, where the design points with the smaller roof radius to record lower maximum velocities, compared to the ones with higher and shorter roof length. More specifically, the maximum velocity was decreased by 29 % for the DP 4 and increased by 14 % for the DP 7.

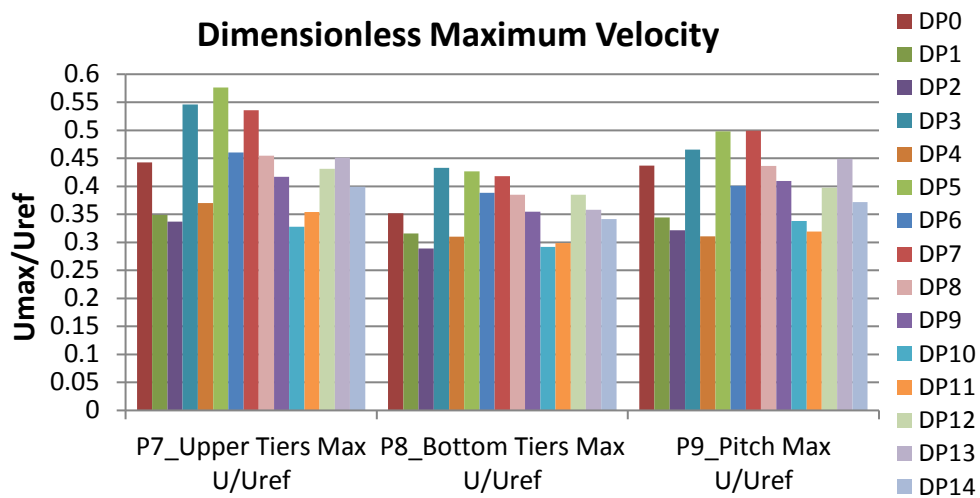


Figure 6-3 Dimensionless maximum velocity values generated at the upper and bottom spectator tiers and the pitch area; $U_{ref} = 5 \text{ m/s}$ taken at the stadium roof height.

6.4 Response Surface Methodology (RSM)

The RSM is based on the accuracy of the meta-models to create approximation functions to describe the output parameters regarding the variance of the inputs. For the current work, the non-parametric regression and the Kriging meta-models were assessed against their performance to describe the DoE data and the accuracy of the predicted optimum design solutions against CFD validation runs.

6.4.1 RSM meta-models

The non-parametric regression meta-modelling algorithm was selected to interpolate the DoE results and find the best function fit for the input-output data. The non-

6 Design Optimisation

parametric regression meta-model is based on the categorisation of noisy data using the Support Vector Machine (SVM) technique. SVM enable non-linear mapping of input-output data (or training data) on a higher-dimensional feature space by the aid of kernel maps. The data are split in non-overlapping classes by the aid of hyperplanes, aiming at the maximisation of their in-between margin. The hyperplanes are used to separate noisy data in groups, by using only those inputs, also known as support vectors that seem to sufficiently represent the outputs. At the same time, as illustrated in Figure 6-4, the hyperplanes are suitably positioned, so as to minimise the distance of the support vectors that fall outside the margin (slack variables ξ).

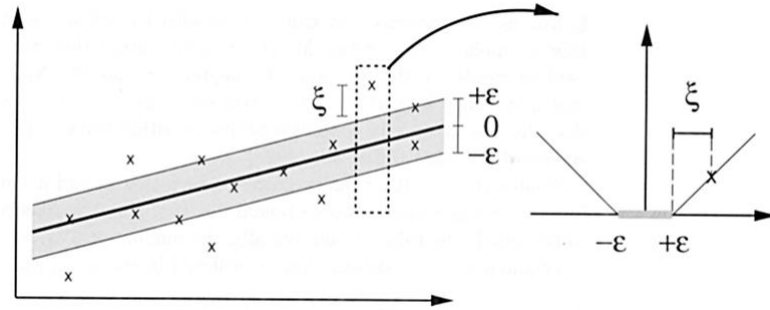


Figure 6-4 Methodology followed by SVM hyperplanes to separate data in classes and minimise the distance of points falling out of the margins (Schölkopf et al., 1999).

Non-parametric regression systems with non-linear responses and noisy results can be described mathematically by the following equations, Equation 6.4 (Vapnik, 2000):

$$f(x) = \langle w, x \rangle + b \quad (6.4)$$

where $f(x)$ is the response of interest, $\langle \dots \rangle$ is the dot product in x and w is a weight factor given by Equation 6.5:

$$w = \sum_{i=1}^n (\alpha_i^* - \alpha_i) \varphi(x_i) \quad (6.5)$$

Threshold b can be described by Equation 6.6:

$$b = -\frac{1}{2} \langle w, (x_r + x_s) \rangle \quad (6.6)$$

where α_i^* , $\alpha_i \geq 0$ are Lagrange variables and x_r and x_s are support vectors.

6 Design Optimisation

The main advantage of non-parametric regression against the parametric one is that the function lacks of rigidity and can be adapted to the equivalent data without compromising form (parabolic, periodic, etc.), generating an inferred function (Wand and Jones, 1995).

The Kriging meta-modelling algorithm is a multidimensional interpolation that covers the whole design space (global model). Kriging meta-model is widely accepted due to its high accuracy in deterministic studies with large number of experimental data (Kleijnen, 2009), however, on the assessment of the goodness of fit and the function verification points, it showed poor performance and thus the generated results are not presented below. However, the predicted optimum design solution gave better results than the non-parametric regression analysis and thus they will be further assessed in the goal driven optimisation section.

6.4.2 Goodness of fit

The goodness of fit gave a first insight into whether the data are adequately represented by the function. Three verification points were used to refine and improve the function fit. As shown in Figure 6-5, the predicted values from the response surface and the observed values from the design points perfectly fit the diagonal line, indicating a very good fit of the model.

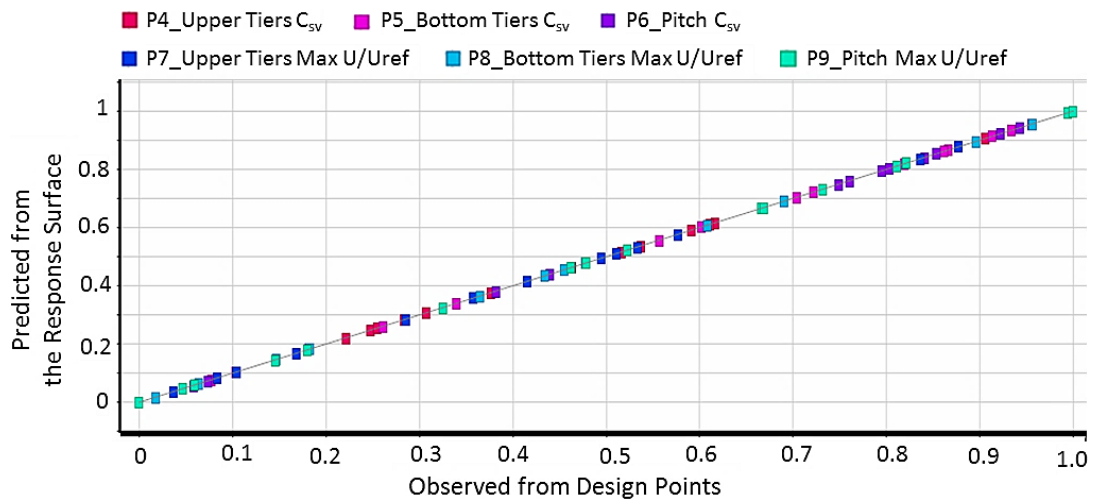


Figure 6-5 Goodness of fit based on non-parametric regression meta-model.

A commonly used indicator, to show in what percentage a design output can be described by the response surface regression equation, is the coefficient of determination (R^2). For linear regression analysis the R^2 can be described by the following equation (6.6), and lies in the interval $[0, 1]$.

6 Design Optimisation

$$R^2 = \frac{\text{Regression sum of squares}}{\text{Total sum of squares}} = \frac{\sum_{i=1}^k (\hat{y}_i - \bar{y})^2}{\sum_{i=1}^k (y_i - \bar{y})^2} \quad (6.6)$$

However, in case of non-parametric regression and non-linear data, the integrity of the function cannot rely on the coefficients of determination (R^2), because the more the parameters involved in the system, the higher the value of the regression sum of the squares will be, which might lead to a value of R^2 greater than 1.0 in some cases (Kvålseth, 1983). Indeed, in current case the values of R^2 for every design output were equal to 1.0, as the software automatically truncates exceeding values to 1.0.

Since non-linear regression aims at minimizing the sum of squares of the points' distances from the fitting curve, the root mean square error (RMSE) can be considered a good estimator value, given by Equation 6.7:

$$RMSE = \sqrt{\frac{1}{n} \sum_{i=1}^n (y_i - \hat{y}_i)^2} \quad (6.7)$$

The closer the value of RMSE is to zero, the better the fit. The values for the output values were varying from 2.1×10^{-11} to 1.6×10^{-4} , indicating a very good fit and a regression function adequate to represent the model.

6.4.2.1 Response surfaces

Three-dimensional graphs of the output responses were generated, enabling the investigation of the effect that two inputs have on a single output. Due to the multidimensional character of the system, few response surfaces are presented that show the complex interrelations between the model parameters. Figure 6-6 presents the generated response surfaces for the dimensionless maximum velocity (P 7) and the C_{sv} at the upper spectator tiers, regarding the alterations in roof height (P 3) and radius (P 1) (Figure 6-6 left) and the roof length (P 2) and radius (P1) (Figure 6-6 right) respectively.

6 Design Optimisation

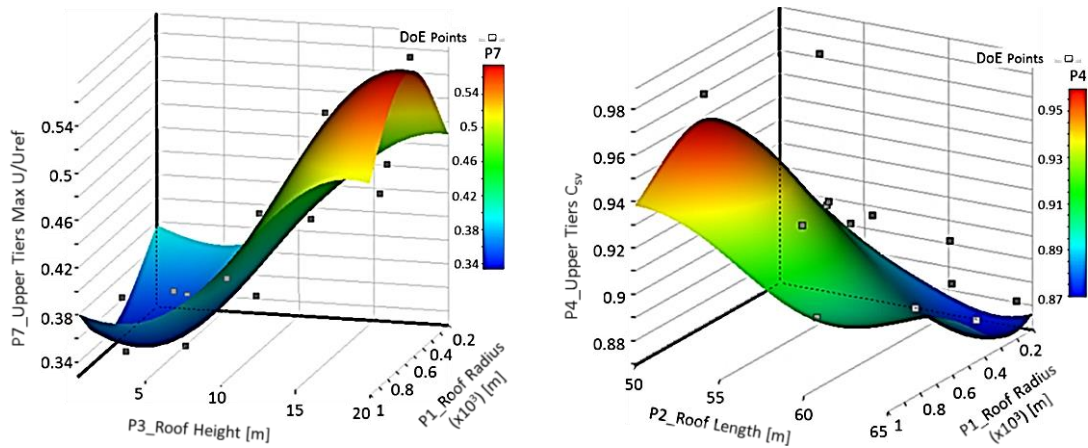


Figure 6-6 Response surfaces for selective sets of input-output parameters within the design space; (left) P7 vs P1 and P3, (right) P4 vs P1 and P2.

In linear correlations between the parameters, the response surface would fit perfectly the design points. However, this is not the case in the current design problem. The system is highly non-linear and the algorithm adopted used weighting factors to create a function of high accuracy that enables the prediction of any response within the input design space.

Results were also generated on local sensitivities and weight factors of every input to the design outputs, allowing assessing the responses' dependence on roof alterations. For the initial case study (DP 0) the roof height (P 3) is the most influential parameter, since by increasing the roof height, all maximum velocities are increased (P 7, P 8 and P 9), along with the heterogeneity at the bottom tiers (P 5) and the pitch (P 6) area. On the other hand the heterogeneity at the upper tiers (P 4) is decreased, without denoting improvement on the wind environment, since the maximum velocity is increased. The roof radius (P 1) and the roof length (P 2) seem to have opposite effect on the design responses, with sensitivity factors substantially smaller than the roof height for almost all of the outputs.

6 Design Optimisation

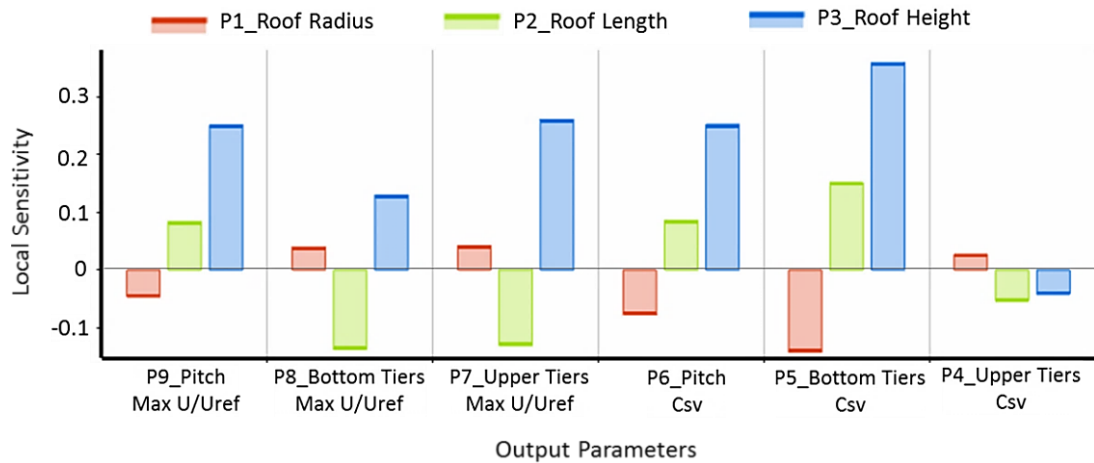


Figure 6-7 Local sensitivities for the initial design case, DP 0.

6.5 Goal driven optimisation (GDO)

As mentioned earlier, the goal driven optimisation results include candidate points generated from both meta-model algorithms. More specifically, the Kriging meta-model was combined with Screening response surface optimisation algorithm and the non-parametric regression with Multi-Objective Genetic Algorithm (MOGA). Both methods are used to conduct the multi-objective optimisation studies, investigating the best solution fit for a predefined set of constraints and objectives. The Screening optimisation is a non-iterative direct sampling method by a quasi-random number generator (ANSYS, 2013). It is based on the generation of a large number of sample design points from the response surfaces and provides several candidate points that satisfy the objectives and constraints. The MOGA belongs to the family of Genetic Algorithms (GA). By employing Pareto sets, a number of design solutions are determined, after assessing multiple populations of points. The algorithm performs an elitist non-dominated sorting according to the set objectives. The theoretical background can be found in Deb et al. (2002); Srinivas and Deb (1994) and Fonseca and Fleming (1993).

The optimisation goal was to improve the stadium aero-comfort conditions, by providing homogeneity and low wind velocities at the zonal areas 2-4 (see Table 6.2). For the purpose of that, six optimisation targets were set, as presented in Table 6.5. The coefficient of spatial variation in all three occupied areas (P4, P5 and P6) was set with a minimisation goal. Low values of C_{sv} will indicate lower flow heterogeneity and velocity variance, which is one of the preconditions for achievement of wind comfort. A minimisation objective was also set for the velocity

6 Design Optimisation

values at the spectator terraces and the pitch area (P 6, P 7 and P 8). The combination of the objectives set will optimally lead to a design solution with reduced airflow interactions between the urban and the stadium interior, offering the ability to control the provision of the most favourable wind environment for players and spectators.

Table 6.5 Optimisation objectives and constraints set for the output parameters.

Output Parameter	Objective	Constraint
P4 _Upper Tiers C_{sv}	Minimise	
P5 _Bottom Tiers C_{sv}	Minimise	-
P6 _Pitch C_{sv}	Minimise	-
P7 _Upper Tiers Max U/U_{ref}	Minimise	-
P8 _Bottom Tiers Max U/U_{ref}	Minimise	-
P9 _Pitch Max U/U_{ref}	Minimise	-

6.5.1 Optimisation results

Several design points that achieved to satisfy the objectives were generated and the best candidates from each optimisation algorithm are presented. The optimum roof configurations from the Screening (CP 1) and the MOGA (CP 2) demonstrate great differences between them, but also in relation to the original. Table 6.6 shows the generated results for the CP 1. The roof of the candidate point has a height equal to 0.5 m and a radius equal to 100 m, which are the lowest constraint values for the corresponding design parameters. The roof length is equal to 65 m, which provides full coverage beyond the auxiliary area, leaving only the playing field exposed. As far as the design outputs are concerned, the optimised design achieved a reduction in flow heterogeneity of about 64.8 % for the bottom spectator tiers (P 5) and 60.8 % for the pitch area (P 6), while in upper spectator tiers (P 4) the flow heterogeneity remains almost at the same level as the initial design case. The presented contours of dimensionless velocity show improvement in the flow behaviour mainly associated with the existence of the primary vortex, which appears to be substantially limited in length and dominance over the developed wind microenvironment at the stadium interior. All maximum velocities have been reduced between 32.3 % and 51.9 %, which is a great achievement towards the optimisation goal.

6 Design Optimisation

Table 6.6 Input and output parameters generated for the CP1 and deviation from initial design case.

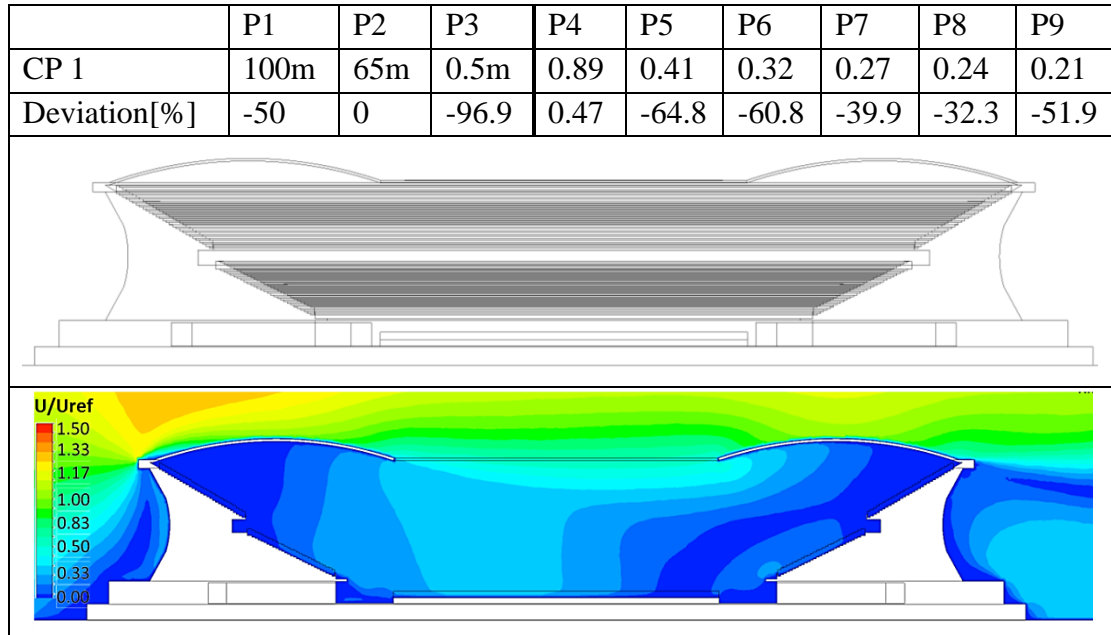


Table 6.7 shows the generated results for the CP 2. The roof geometry has been reduced in length by 6.76 %, in height by 76.6 % and has been increased in radius by 154.75 %. The roof length of 60.6 m provides enough coverage for the spectators, exposing the full auxiliary area. The small height of 3.75 m, in combination to a higher roof radius (509.5 m) diminishes the flow mass entering the stadium that leads to reduced maximum velocity speeds of a minimum of 16.74 % for the bottom spectator tiers and a maximum of 37.35 % for the pitch area. The flow homogeneity was improved up to 45.77 % for the bottom spectator tiers and 29.18 % for the pitch area, as opposed to the upper terraces, where the heterogeneity was increased by only 4.6 %. The generated contours of dimensionless velocity show an advantageous reduction both in strength and extent of the primary vortex that successfully improves the wind conditions for the users.

6 Design Optimisation

Table 6.7 Input and output parameters generated for the CP2 and deviation from initial design case.

	P1	P2	P3	P4	P5	P6	P7	P8	P9
CP 2	509.5m	60.6m	3.75m	0.93	0.63	0.58	0.34	0.29	0.27
Deviation [%]	154.7	-6.76	-76.6	4.6	-45.77	-29.2	-23.3	-16.5	-37.4

6.5.2 GDO verification

The verification of the optimisation results involves the simulation for the candidate points, by performing CFD runs. The verification process is important prior the further analysis of the results, since it will ensure the accuracy of the method, the precision of the response surface to estimate the design responses and the effectiveness of the candidate designs to improve the wind comfort conditions. Figure 6-8 compares the CFD and the RSM-generated results. The CP 1 shows large deviations on the calculation of the C_{sv} for the bottom spectator tiers and the pitch area, with a maximum of 91 % for the latter one. The maximum velocity values for the same areas were deviated to up to 28 %. On the other hand, the CP 2 showed superior performance for all the output parameters. The maximum deviation appeared on the maximum velocity at the bottom spectator tiers with an error value equal to 14.2 %, followed by the C_{sv} at the bottom spectator tiers with a value of 7.6 %.

However, the design output values for the CP1 that were generated using CFD simulations, regardless the deviation errors, are considerably smaller than the output values for the CP 2. It is therefore concluded that the combination of the non-parametric regression and the MOGA algorithm generates results that may actually be reproduced by the CFD simulation with high accuracy, but lack to predict the

6 Design Optimisation

local optimum design solution. The global Kriging meta-model on the other hand considers all the points in the design space, including the extreme values and thus it achieved to predict a design solution with considerable superior performance against the optimisation objectives.

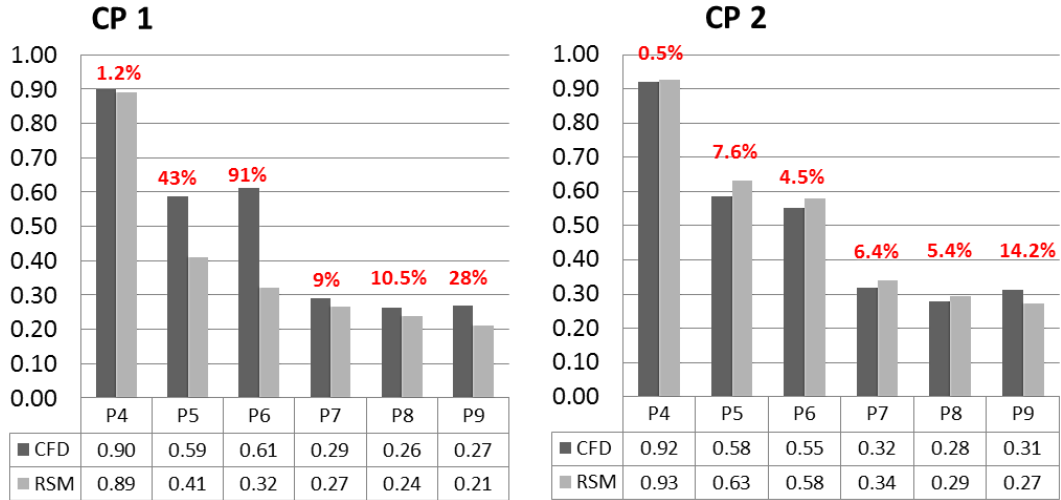


Figure 6-8 RSM vs CFD results for verification for the CP 1 and the CP 2.

6.6 GDO sensitivities

Using correlation analysis, the global sensitivities over the output parameters were generated, by evaluating the entire design space. According to the results in Figure 6-9 all design inputs have strong influence, positive or negative, at the development of the wind environment. Positive sensitivity denotes that as the value of the design parameter increases, the value of the design response will also increase. Negative sensitivity implies that increasing the value of the design parameter, the response value will be decreased.

More specifically, the roof height (P 3) has the greatest impact on the design outputs. Increase in the roof height has positive sensitivity of 0.82, 0.64 and 0.30 in the maximum velocity responses of the auxiliary areas, the bottom and the upper terraces respectively. It also appears to have positive sensitivity of 0.91 and 0.90 for the C_{sv} values of the auxiliary area and the bottom spectator tiers, implying that an increase of the roof height will increase the flow heterogeneity in these areas. On the other hand a negative sensitivity of -0.91 was produced for the C_{sv} value at the upper spectator tiers, which improves the flow homogeneity, without implying reduction of the velocity speeds.

6 Design Optimisation

The roof radius (P 1) is the second most influential parameter, with negative sensitivity for almost all the design outputs, except from the C_{sv} for the upper tiers (P 4), with a positive sensitivity value of 0.78. More specifically, the sensitivities were found equal to -0.62, -0.78 and -0.63 for the maximum velocities at the auxiliary area, the bottom and upper spectator tiers and -0.66 and -0.70 for the C_{sv} values at the auxiliary area and the bottom spectator terraces. It can also be observed that the increase of the roof radius creates opposite effect on the output responses, when compared to the rest of the design inputs.

Finally, the roof length (P 2) has positive sensitivity of 0.78 and 0.34 at the maximum velocities of the pitch area and the bottom tiers respectively. Roof length changes have negligible impact on the maximum velocities at the upper spectator tiers, contrariwise to the flow homogeneity at the same area, which appears to be significantly improved, with a negative sensitivity for the C_{sv} equal to -0.72. Increase of P 2 results also to an increase of the heterogeneity at the bottom tiers and the pitch area, since positive sensitivities were produced equal to 0.78 and 0.73, respectively.

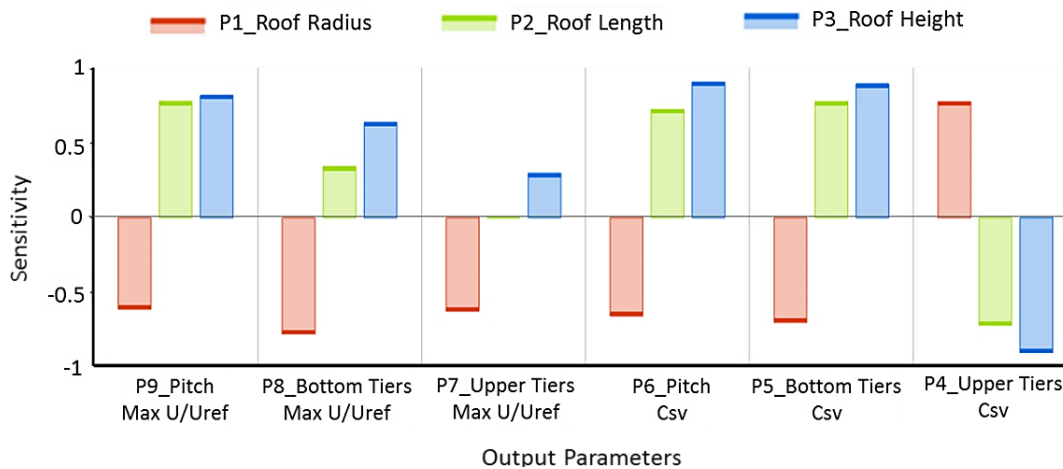


Figure 6-9 Global sensitivity chart of input-output parameters.

6.7 Interpretation of results

The verified optimum solution for the CP 1 is further discussed and compared with the initial design case, in terms of flow homogeneity, wind and pressure distribution patterns. Figure 6-10 illustrates the velocity contours generated for the dimensional velocity at the stadium interior. The major difference on the flow generation is the weakness of the primary velocity vortex, prior covering the entire area of the windward spectator tiers. The vortex has been decreased in size and has been limited in length affecting only the lower bottom spectator tiers. The streamline colours

6 Design Optimisation

indicate remarkable reduction in velocity magnitude of the vortex-generated flow, mainly attributed to the roof alteration, which prevents the development of high-flow acceleration areas.

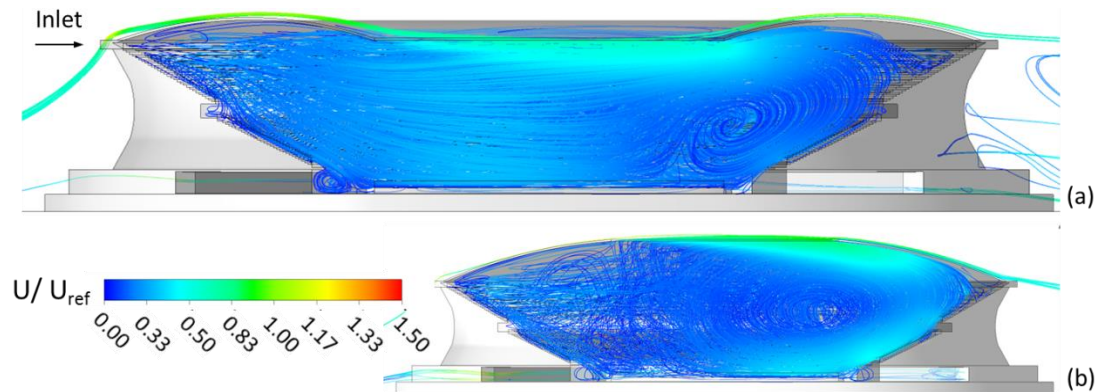


Figure 6-10 Side view of the streamlines of the dimensional velocity developed at the stadium bowl, for the CP 1 (a) and the initial design case (b); $U_{ref} = 5.23 \text{ m/s}$.

Figure 6-11 shows the normalised dimensional velocity vectors and the pressure contours at the vertical plane in the middle of the stadium model for the two roof cases. According to the results, the roof modification has changed dramatically the pressure distribution at the stadium interior. The pressure alteration explains the airflow distribution change at the stadium bowl. The maximum velocities have been reduced up to 25.7 % and 34 % for the bottom and the upper spectator tiers and up to 37 % for the pitch area, which is no longer wind dominated by the central vortex but by the peripheral flow recirculation.

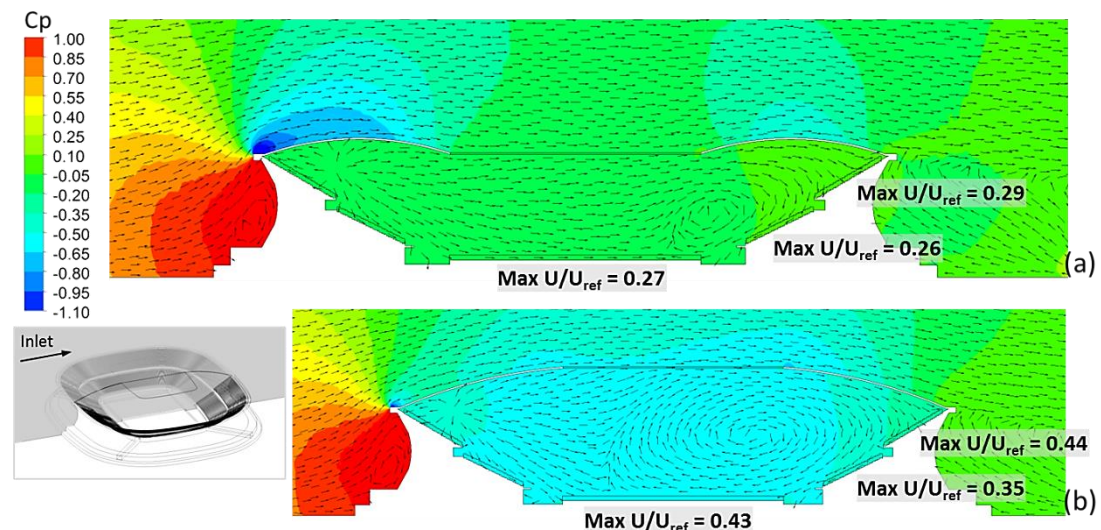


Figure 6-11 User defined pressure coefficient contours and normalised velocity vectors generated at the central plane of the stadium model for the CP 1 (a) and the initial design case (b); $U_{ref} = 5.23 \text{ m/s}$.

According to Figure 6-12, the overall flow distribution at the stadium interior has also been improved. The streamline patterns indicate a homogeneous flow at the

6 Design Optimisation

entire stadium bowl, without the development of intense flow accelerating zones at the upper spectator tiers. The curved roof configuration results in higher pressure values at the interior roof part, which counteract the wind suction decelerating the airflow entering the stadium. This adds to the explanation of the decreased maximum dimensionless velocity values discussed earlier. The flow microenvironment is entirely dominated by two symmetrical vortices with centre on the pitch area, with the vortex on the windward bottom spectator tiers to play secondary role on the overall flow distribution. These findings yield great advantages for the wind comfort of the users who could benefit from a simplified and easier to control flow environment.

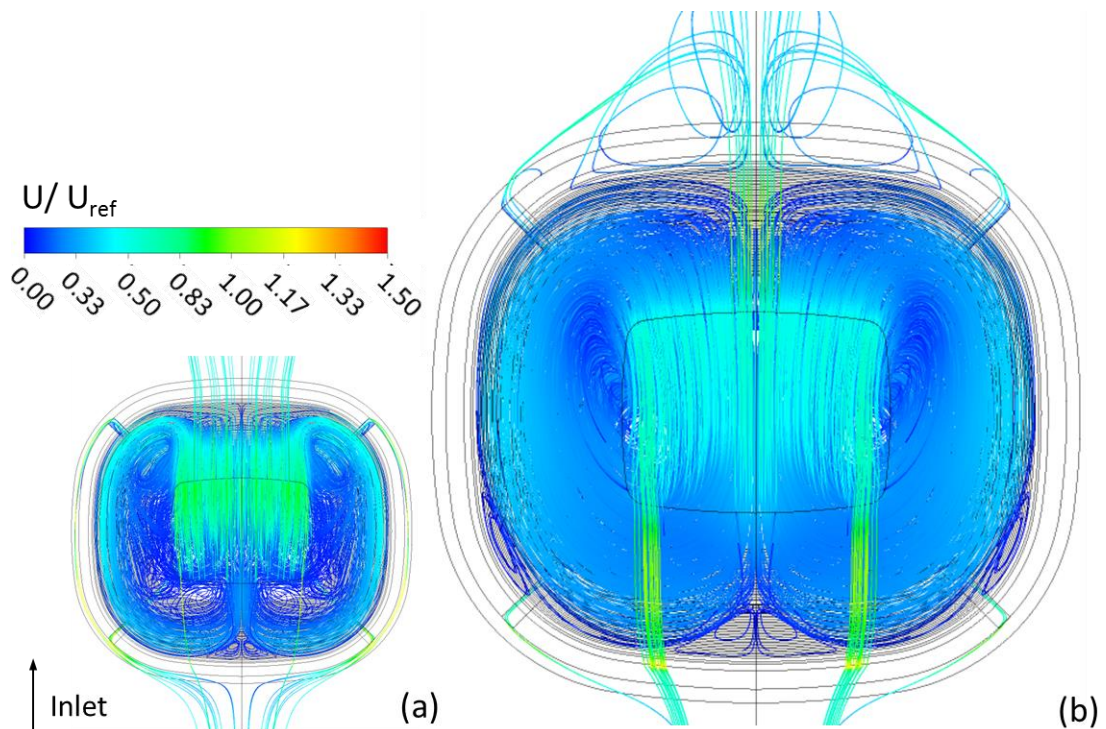


Figure 6-12 Top view of the streamlines of the dimensional velocity developed at the stadium bowl, for the initial design case (a) and the CP 1 (b); $U_{ref} = 5.23$ m/s.

Figure 6-13 illustrates the normalised velocity vectors and the pressure contours for a horizontal plane located 0.01 m above the entrance level. More specifically, the pressure distribution at the exterior of the stadium envelope is the same in both design cases. However, the roof alteration has created significant changes at the pressure values at the stadium interior. The average pressure coefficient at the pitch area for the optimised design is equal to -0.128, which is 76 % higher than the average pressure at the pitch area of the initial design (-0.532). The new pressure environment forces the wind to exit the stadium bowl through the rear side entrances, where the pressures are lower in magnitude. Consequently, the wind flow at the pitch

6 Design Optimisation

is mainly determined by two small vortices, opposite in direction, developed by the collision of the incoming airflow via the front side entrances and the recirculated flow at the windward bottom spectator terraces towards the auxiliary area.

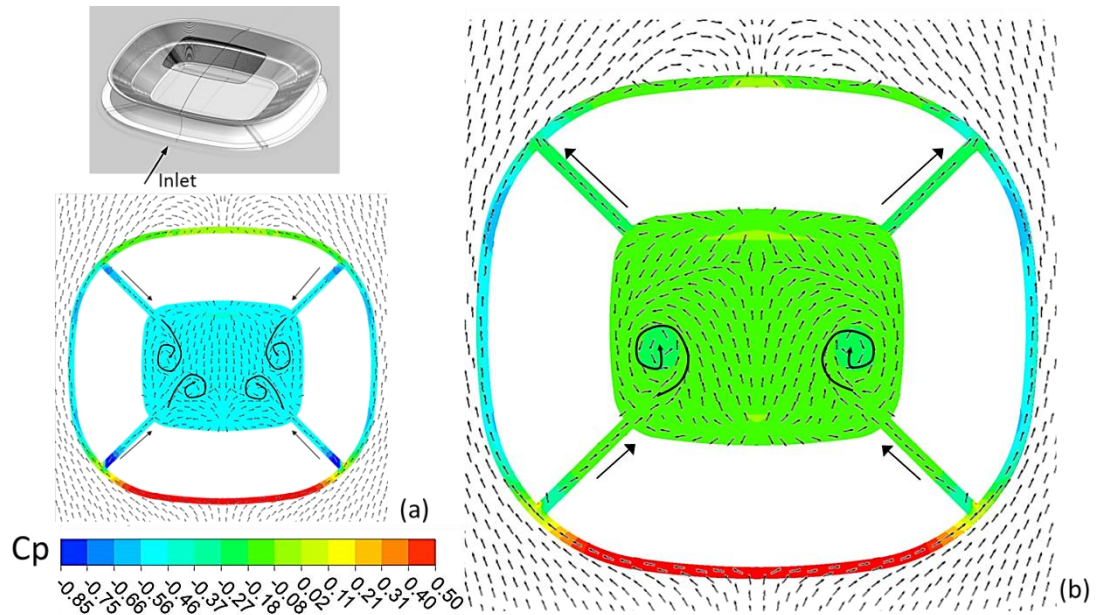


Figure 6-13 User defined C_p contours and normalised vectors of velocity for the initial (a) and the CP 1(b) design, generated at the horizontal plane 0.01 m above the entrance level.

A clear view of the developed velocities at the occupied areas is given in Figure 6-14. The optimised microenvironment has led to an overall decrease of the velocity values at the stadium interior, as a result of the decelerating zones, previously generated via the front side entrances and the intensive flow recirculation zones at the upper spectator tiers. Additional conclusions can be drawn for the flow homogeneity at the studied areas. As opposed to the previous highly heterogeneous velocity patterns on the whole periphery of the stadium bowl, the optimised roof design has resulted in remarkable improvements, by increasing the homogeneity by 49.6 % and 25.2 % for the bottom spectator tiers and the pitch respectively. On the other hand, the heterogeneity at the upper spectator tiers appears to be increased by 1.6 %, implying the inadequacy of the C_{sv} to be the primary factor for the estimation of the microenvironmental wind comfort.

6 Design Optimisation

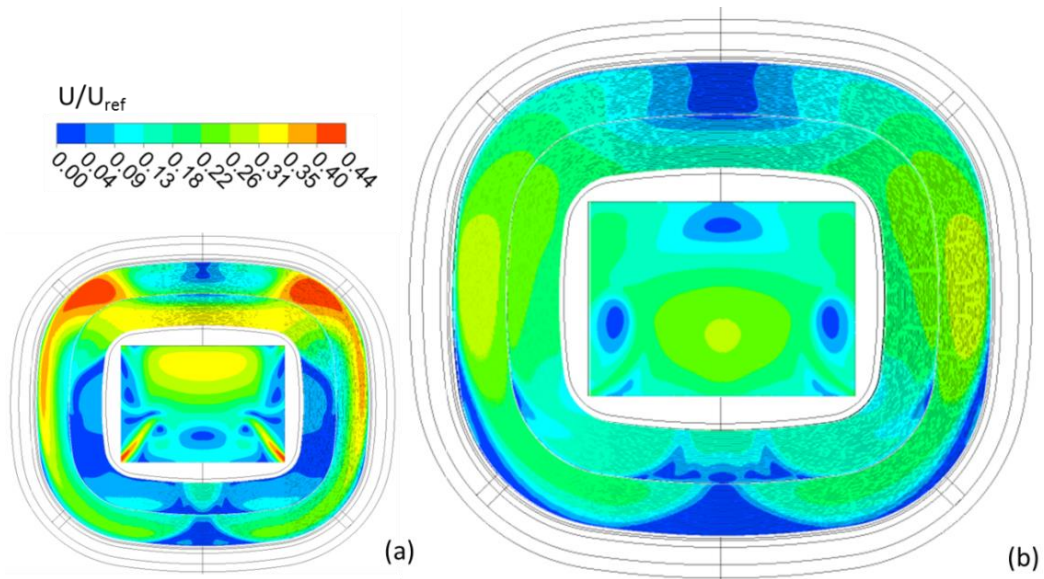


Figure 6-14 Contours of the dimensionless velocity at the spectator tiers and the pitch area, for the initial design case (a) and the CP 1 (b); $U_{ref} = 5.23$ m/s.

6.8 Limitations

The main limitations of the optimisation study are listed below:

1. The design optimisation was aiming at the identification of the local optimum solution and not the global optimum. This arises from the fact that the design variables were varying within specified limits, excluding certain geometrical configurations, such as the concave roof or the roof design inclined towards the terraces.
2. The selection of the optimisation algorithm is important on the identification of the best design solution that satisfies the defined objectives. However, it was shown that not all the available multi-objective algorithms give similar results, and thus it is generally suggested to perform a preliminary study initially with the Screening and in sequence with the MOGA optimisation algorithm to refine the optimisation results.
3. The optimisation goal for flow homogeneity, set by the function of the spatial variation of velocity does not lead to minimum velocity values at the stadium bowl. The C_{sv} implies that the velocity magnitudes are closer to the mean velocity value at the occupied areas, which might be higher than the one at the initial roof configuration. However, it is an important parameter that defines the wind comfort and thus it was included in the optimisation objectives.
4. The study was conducted under a subjective set of input and output parameters that were considered of great importance for the aerodynamic optimisation of the

6 Design Optimisation

stadium model. However, different design solutions may be obtained under different sets of design parameters (inputs and outputs) and objectives.

5. Due to the large computational cost, only 14 design points were generated, which due to the high non-linearity of the problem might be insufficient to represent the design space, upon which the optimisation study was built.
6. Final limitation of the study is the structural feasibility of the optimal design solution, which was not a consideration factor for the current work.

6.9 Summary

In this chapter a 3D optimisation study on the wind comfort conditions of the players and the spectators was performed. By employing coupled CFD-RSM metamodeling optimisation algorithms, selected design parameters of the roof geometry were assessed with reduced computational time and cost, as opposed to traditional deterministic studies. The investigation of different roof configurations was conducted using design experimentation, under variable radius, length and height. Different response surface and optimisation algorithms were assessed and validated against the CFD simulation runs indicating that the non-regression meta-model predicted accurately the design responses but failed to predict the optimum design solution.

7 Conclusions

This research work provided a comprehensive experimental and computational method to assess the aerodynamic performance of a semi-open stadium structure and provide optimum roof configuration solutions that improve the wind comfort of users. The thesis conclusions are presented thereafter, numerically linked to the defined objectives of Section 1.1:

1. The aerodynamic performance study of the stadium structure was performed in an ABL wind tunnel facility. The test section was integrated with vortex and turbulence generators that successfully achieved the simulation of a suburban environment, resulting to a power coefficient of $\alpha = 0.282$, the prediction of the zero plane displacement at $d = 0.035$ m and the boundary layer height at $\delta = 1.0$ m, satisfying the theoretical values described in Simiu and Scanlan (1996).

The pressure coefficient results indicated similar trends per wind direction and envelope porosity at all stadium surfaces. In summary, on the roof structural component the pressure coefficient measurements were compared with the reference stadium case study (non-elevated roof and 0° wind angle). The results revealed that the average C_p values were decreased by 1.3 % for the elevated roof and 0° wind angle and increased by 16.5 % and 12.6 % for the non-elevated and elevated roofs under 90° wind angle. The point of the minimum C_p value was similar for all four stadium cases, located at the centre of the rear oculus configuration. At that point, the elevated roof configuration under 0° wind angle revealed a decrease of the C_p value by 20.4 %, followed by a substantially smaller decrease by 3.5 % for the same roof configuration under 90° wind angle. The rotation of the reference case under 90° led to an increase of the C_p value at the same point by 6.1 % (see Table 3.2).

On the surfaces of the spectator tiers, the highest average pressure coefficient values were generated for the reference case study, followed by the elevated roof under 0° wind angle (-9.0 %), the non-elevated roof under 90° wind angle (-17.0 %) and the elevated roof under 90° wind angle (-22.0 %). On the comparison of the two roof configurations, the non-elevated roof resulted to higher pressure coefficients by up to 31.6 % on the upper windward spectator tiers, indicator of intense flow movements, also reported in literature (Szucs et

7 Conclusions

al., 2009b). Finally, under the wind angle of 90° , the measurement points on the upper windward and leeward spectator tiers were higher in absolute values for the elevated roof configuration by up to 17 %, indicators of higher suction and incoming airflow into the stadium bowl (see Table 3.3).

For the pressure coefficients on the auxiliary area, the reference case study generated the highest in magnitude results, with an average value to be higher by 9.2 %, 16.6 % and 20.1 % from the case of elevated roof and 0° wind angle, non-elevated roof and 90° wind angle and elevated roof and 90° wind angle, respectively (see Table 3.4). The small errors of asymmetry, with an average deviation error of 4 % between the relevant measurement points indicated also the importance of the model positing under the exact wind direction.

2. The computational simulation of the pressure and velocity distributions was performed with CFD tools and steady state RANS turbulence model approach, by employing the standard $k-\varepsilon$ turbulence model, which showed the best performance in the turbulence model validation study. The generated results on the pressure distribution indicated similar pressure distribution patterns at the external stadium walls. The maximum pressure was observed at the roof extension height for all four stadiums, with the reference case to generate a C_p value 16 % higher than the non-elevated roof and 90° wind angle and 14.7 % higher than the stadiums with elevated roof, which produced equal values. At the lateral stadium walls suction zones were present with the minimum C_p values for wind angle of 0° to be approximately 41 % smaller than the ones of 90° wind angle.

On the roof surface similar pressure patterns were obtained for all stadium cases, with decreasing C_p values towards the central roof opening. The highest negative values were observed at the rear side of the oculus configuration, similar to the wind tunnel experimentation. At that area, the reference stadium case study generated 26.7 % higher negative C_p values compared to the non-elevated roof at 90° wind angle, 9.5 % smaller negative values compared to the elevated roof at 0° wind angle and 1% higher negative values compare to the elevated roof at 90° wind angle, as a result of the airflow exiting the stadium bowl.

On the spectator tiers, small deviations of the average pressure coefficients of approximately 22.4 % and 16.1% were observed for the non-elevated and the elevated roof configuration by altering the model orientation, with the smallest negative values to be developed for the case of 0° wind angle for both roof cases.

7 Conclusions

On the comparison of the average C_p values between the four stadium cases, the reference case study generated 28.9, 32.4 and 58.1 % higher negative values compared to the non-elevated roof at 90° and the elevated roof at 0° and 90° respectively. The existence of the ventilation opening led to substantially different pressure distribution patterns, with high suction zones to be observed at the upper windward and leeward terraces of the stadium, where the external airflow enters the stadium bowl. On the other hand, for the stadium with non-elevated roof configuration, the oculus, as the primary ventilation opening, drives the air towards the windward spectator tiers, where the smallest pressure values were observed.

At the auxiliary area the non-elevated roof at 0° wind angle generated the highest negative average C_p values, 25, 27 and 38.5 % higher than the non-elevated roof at 90° , the elevated roof at 0° and the elevated roof at 90° wind angle respectively. For all cases, the highest negative peaks were observed at the leeward corners of the auxiliary area, with a range between -0.59 and -0.38; values that are directly related to the incoming flow through the front side entrances.

The simulation of the wind distribution patterns at the stadium bowl was interpreted with the generation of velocity streamlines. The non-elevated roof configuration contributed to the development of a large vertical vortex at the windward spectator tiers, with extended downwash flow towards the centre of the auxiliary area, which was horizontally separated along the stadium bowl periphery, causing high ventilation zones at the highest rows of the upper spectator tiers. On the other hand, the elevated roof configuration resulted to a more chaotic flow distribution at the stadium interior, since it created several entering and exiting flow passages. The flow at the interior was of opposite direction and of lower intensity when compared with the non-elevated roof case. Finally, the wind direction caused no changes on the wind flow patterns at the spectator tiers, but it created more compact flow streams, as the roof passage became narrower. Differences were observed at the flow distribution at the auxiliary area level. The colliding air streams entering the stadium through the back side entrances and the recirculating flow at the stadium interior had a longer distance to travel, causing relocation of the developed vortices towards the leeward spectator tiers for the non-elevated roof configuration. For the case of

7 Conclusions

the elevated-roof configurations, the previously developed four vortices were merged into two and discharged symmetrically at the centre of the pitch.

3. The wind microenvironment for the users was assessed by the generation of dimensionless velocity contours and vectors at the areas of interest. At the auxiliary area, the flow entering by the front side entrances was present in all four stadium configurations, which might cause disturbance to the players at the corners' areas. At the corners, the structure with non-elevated roof configuration and under 0° wind angle developed the largest dimensionless velocity values, 7.6, 55.5 and 16.7 % higher than the ones of the non-elevated roof at the 90° and the elevated roof at 0° and 90° wind angle respectively. Another important conclusion drawn was that the elevated roof configuration diminished the intensity of the airflow entering the stadium via the back side entrances, as no air jets were appeared to influence the wind conditions at the pitch level. Horizontal vortices were developed in all stadium cases and their extent and intensity was dominated by the air jets through the side openings and the flow collision between the downwash flow from the windward and leeward spectator terraces. At the pitch centre the stadiums with elevated roof configuration resulted to 25% higher dimensionless velocities than the stadiums with non-elevated roof, as a result of the additional airflow entering the stadium via the ventilation opening at the rear side of the structures.

At the areas of the spectator terraces, the stadiums with non-elevated roof configuration resulted to up to 18 % higher average dimensionless velocity values compared to the stadiums with ventilation opening, but up to 50.7 % lower maximum dimensionless velocity values, due to the variations on the flow distribution. The non-elevated roof configuration led to the development of high ventilation zones at the upper spectator corners, fed by the large primary recirculation vortex, whereas at the case study of elevated roof configuration, the horizontal ventilation opening resulted to very high intensity zones at the very upper seats of the lateral leeward spectator terraces and calm zones at the rest of the areas.

4. The interactions between the urban and the stadium environment revealed that the shape of the building and the structural and geometrical characteristics play the most important role on the pressure and velocity distributions at the areas of the exact proximity of the stadium. The results revealed similar pressure distribution patterns between the two wind directions. The 0° wind angle

7 Conclusions

generated 13.6 % higher pressures at the front of the stadium and 20.5 % higher negative pressures at the lateral sides of the structure when compared with the wind angle of 90° .

The velocity streamlines, indicated the similarities of the flow distribution patterns with a simple building bluff building, including the recirculation zones at the underpressure rear stadium areas and the horseshoe vortices at the sides of the building. The change of the wind direction resulted to a 4.5 % longer wake on the rear stadium side for the wind angle of 0° . The high recirculated zones on the lateral side of the structure, indicated that the reference stadium case contributed to the maximum dimensionless velocity values, followed by 4.7, 9.2 and 9.8 % smaller values for the cases of elevated roof and 0° wind angle, non-elevated roof and 90° wind angle and elevated roof and 90° wind angle, respectively.

Finally, the structural extension above the side entrances was an important asset at the wind safety and comfort for the structure, as it attenuated the recirculation zone, created by the downwash flow at the pedestrian level, preventing the disturbance of the wind environment at the stadium entrance level.

5. The correlation analysis of the input design parameters revealed that the wind environment at the stadium bowl in terms of flow homogeneity and velocity speeds was primarily dependent on the roof height with an average absolute sensitivity value of 0.45, followed by the roof radius with a value of 0.43 and the roof length with a sensitivity value of 0.32.

More specifically, an increment of the roof height would lead to increase of all the maximum velocity speeds at the stadium interior, with more sensitive to be the velocity speeds at the auxiliary area with a sensitivity value of 0.82. The flow heterogeneity would also be increased at the auxiliary area and the bottom spectator tiers, but it will be reduced at the upper ones.

The increase of the roof radius was found to create opposite effect on the output parameters when compared with the roof height and length. Such an increase would reduce the maximum velocity speeds at all occupied areas, with an average sensitivity value equal to -0.67 and a standard deviation of 0.09. Equal high negative sensitivity values were observed for the flow heterogeneity at the auxiliary area and the bottom spectator tiers. On the contrary, the roof radius increase would lead to increase of homogeneity at the upper spectator tiers.

7 Conclusions

The roof length resulted to sensitivity results of similar sign with the roof height, but with smaller values of approximately 21 %. The main difference was observed at the response of the maximum velocity speeds at the upper spectator tiers, the value of which appears to be independent of the roof extension length.

6. The multi-objective optimisation results revealed that by reducing the roof height down to 0.5 m and the roof radius to 100 m, maintaining the roof length equal to 65 m, substantial improvements on the wind microenvironment may be achieved. The maximum wind speeds at the bottom and upper spectator tiers were reduced up to 25.7 % and 34 % and 37 % for the pitch area. The flow heterogeneity was slightly increased for the upper spectator tiers to about 1.6 % and decreased to up to 49.6 % and 25.2 % for the bottom spectator tiers and the pitch area.

The changes of the roof altered the pressure development at the stadium interior surfaces, which created a more homogeneous flow around the periphery, highly simplified and easier to control/predict. However, even if the generated roof configuration represents a local optimum design solution, the potentiality of the method to be used for the further investigation of the global optimum solution is highly recommended.

7.1 Future work

This research was based on the fundamental theory of wind comfort, wind engineering and fluid aerodynamics. It produced a wide range of results relevant to stadium's aerodynamic performance, using advanced computer simulation techniques and wind tunnel experimentation and revealed optimum design configurations that improve the interior stadium wind environment by employing coupled CFD-RSM multi-objective optimisation techniques. However, it can be considered an ongoing research, with well-defined foundations and a wide range of study alternatives.

A more detailed investigation of the flow distribution in the stadium environment could consider the ambient temperature parameters and the solar radiation into the simulation study that may significantly alter the results. In reality, the airflow patterns are highly influenced by the temperature and thus, especially in hot-humid climates, temperature considerations must be taken to increase the accuracy of the results. By employing the energy and radiation models, the heat transfer coefficient of the stadium materials could be also calculated and thus their impact on the

7 Conclusions

temperature of the stadium bowl be evaluated. Alternative structural materials could be used, leading to comparative results of their thermal performance.

Additional to this, the integration of under seat cool air jets in the simulation model would be beneficial to evaluate the performance of cooling mechanisms in the semi-open stadia. A more complicated research would involve the incorporation of the human factor, by simulating the human physical processes, under the model-defined environmental conditions. This could be performed by employing the species transport CFD techniques to study the heat and moisture transport from and to human bodies.

As far as the wind tunnel experiments are concerned, additional experimental cases could be performed, by altering the wind direction, integrating Irwin tubes to study pedestrians' and players' wind comfort and/or by changing the roof configuration. Different measurement points would be also beneficial to the research, such as at the four entrances of the stadium, which might cause wind discomfort in case of poor designing.

The simulation of a full scale simulation could be considered too. The transition from a 1:300 scale model to 1:1 scale is a challenging process, since a similar stadium design should be built and in situ experiments should be performed for validation.

Additional work could be performed in the design optimisation study. Different input and output parameters could be selected to study and optimise different structural components and assess different conditions inside and outside the stadium environment.

8 References

- Allegrini, J., Dorer, V. and Carmeliet, J. (2014). Buoyant flows in street canyons: Validation of CFD simulations with wind tunnel measurements. *Building and Environment*, 72, pp.63-74.
- Anderson, J. (1995). *Computational fluid dynamics*. New York: McGraw-Hill.
- Anderson, W. (1992). Grid generation and flow solution method for Euler equations on unstructured grids. [Washington, DC]: National Aeronautics and Space Administration, Office of Management, Scientific and Technical Information Program.
- Announcement of the Alan G. Davenport Wind Loading Chain. (2011). *Journal of Wind Engineering and Industrial Aerodynamics*, 99(10), pp.998-999.
- ANSYS, (2013). Lecture 5 Goal Driven Optimisation. Realise 14.5, ANSYS. Available at:http://innomet.ttu.ee/martin/MER0070/WB/WS10/DX_14.5_L05_Optimization.pdf.
- ANSYS, Inc. (2011) ANSYS Fluent User's Guide, Release 14.0. November. ANSYS, Inc, Southpointe 275 Technology Drive Canonsburg, PA 15317.
- Arens, E. A; Gonzalez, R. and Berglund, L. (1986). Thermal comfort under an extended range of environmental conditions. *ASHRAE Transactions*, 92 Part 1B. UC Berkeley: Center for the Built Environment. Retrieved from: <http://escholarship.org/uc/item/1jw5z8f2>.
- Asfour, O. (2010). Prediction of wind environment in different grouping patterns of housing blocks. *Energy and Buildings*, 42(11), pp.2061-2069.
- Avissar, R., Moran, M., Wu, G., Meroney, R. and Pielke, R. (1990). Operating ranges of mesoscale numerical models and meteorological wind tunnels for the simulation of sea and land breezes. *Boundary-Layer Meteorology*, 50(1-4), pp.227-275.
- Balafas, G. (2014). Polyhedral mesh generation for CFD-analysis of complex structures (Master's thesis). Technical University of Munich.
- Balogh, M., Parente, A. and Benocci, C. (2012). RANS simulation of ABL flow over complex terrains applying an Enhanced k- ϵ model and wall function formulation: Implementation and comparison for fluent and OpenFOAM. *Journal of Wind Engineering and Industrial Aerodynamics*, 104-106, pp.360-368.
- Baniotopoulos, C., Borri, C. and Stathopoulos, T. (2011). *Environmental wind engineering and design of wind energy structures*. Wien: Springer.
- Banta, R. and Blumen, W. (1990). *Atmospheric processes over complex terrain*. Boston, Mass.: American Meteorological Society.
- Barlow, J., Rae, W., Pope, A. and Pope, A. (1999). *Low-speed wind tunnel testing*. New York: Wiley.

8 References

- Baskaran, A. and Stathopoulos, T. (1994). Prediction of wind effects on buildings using computational methods — review of the state of the art. *Canadian Journal of Civil Engineering*, 21(5), pp.805-822.
- Belamadi, R., Djemili, A., Ilinca, A. and Mdouki, R. (2016). Aerodynamic performance analysis of slotted airfoils for application to wind turbine blades. *Journal of Wind Engineering and Industrial Aerodynamics*, 151, pp.79-99.
- Bellinger, G. (2004). Simulation - Time and Space Compression. [online] Systems-thinking.org. Available at: <http://www.systems-thinking.org/simulation/simulation.htm>.
- Bhaskaran, R., and Collins, L. (2002). Introduction to CFD basics. Cornell University-Sibley School of Mechanical and Aerospace Engineering.
- Biagini, P., Borri, C. and Facchini, L. (2007). Wind response of large roofs of stadiums and arena. *Journal of Wind Engineering and Industrial Aerodynamics*, 95(9-11), pp.871-887.
- Biswas, G. and Eswaran, V. (2002). Turbulent flows. Boca Raton, Fla.: CRC Press.
- Blackman, K., Perret, L., Savory, E. and Piquet, T. (2015). Field and wind tunnel modeling of an idealized street canyon flow. *Atmospheric Environment*, 106, 139-153.
- Blocken, B. and Carmeliet, J. (2004). Pedestrian Wind Environment around Buildings: Literature Review and Practical Examples. *Journal of Building Physics*, 28(2), pp.107-159.
- Blocken, B. and Persoon, J. (2009). Pedestrian wind comfort around a large football stadium in an urban environment: CFD simulation, validation and application of the new Dutch wind nuisance standard. *Journal of Wind Engineering and Industrial Aerodynamics*, 97(5-6), pp.255-270.
- Blocken, B., Stathopoulos, T. and van Beeck, J. (2016). Pedestrian-level wind conditions around buildings: Review of wind-tunnel and CFD techniques and their accuracy for wind comfort assessment. *Building and Environment*, 100, pp.50-81.
- Blocken, B., Stathopoulos, T. and Carmeliet, J. (2008). Wind Environmental Conditions in Passages between Two Long Narrow Perpendicular Buildings. *J. Aerosp. Eng.*, 21(4), pp.280-287.
- Blocken, B., Stathopoulos, T. and Carmeliet, J. (2007). CFD simulation of the atmospheric boundary layer: wall function problems. *Atmospheric Environment*, 41(2), pp.238-252.
- Blumberg, D. and Greeley, R. (1993). Field studies of aerodynamic roughness length. *Journal of Arid Environments*, 25(1), pp.39-48.

8 References

- Bouyer, J., Vinet, J., Delpech, P. and Carré, S. (2007). Thermal comfort assessment in semi-outdoor environments: Application to comfort study in stadia. *Journal of Wind Engineering and Industrial Aerodynamics*, 95(9-11), pp.963-976.
- Box, G. E. P., and Wilson K. B. (1951). On the Experimental Attainment of Optimum Conditions. *Journal of the Royal Statistical Society. Series B (Methodological)*, 13(1), pp.1-45.
- Casey, M. and Wintergerste, T. (2000). Best practice guidelines. 1st ed. [Switzerland]: ERCOFTAC.
- Castro, I. and Robins, A. (1977). The flow around a surface-mounted cube in uniform and turbulent streams. *J. Fluid Mech.*, 79(02), p.307.
- Cavazzuti, M. (2013). Optimization methods. Berlin: Springer.
- Cermak, J. E., Davenport A. G., Plate E. J., and Viegas D. X. (1995): *Wind Climate in Cities*. Kluwer Academic, p.23.
- Chaudhry, F. and Cermak, J. (1971). Wind-tunnel modeling of flow and diffusion over an urban complex. Fort Collins: Colorado State University.
- Chen, B., Wu, T., Yang, Y., Yang, Q., Li, Q. and Kareem, A. (2016). Wind effects on a cable-suspended roof: Full-scale measurements and wind tunnel based predictions. *Journal of Wind Engineering and Industrial Aerodynamics*, 155, pp.159-173.
- Cook, N. (1985). *The designer's guide to wind loading of building structures*. Garston: Building Research Establishment.
- Cóstola, D., Alucci, M. (2007). Pressure coefficient simulated by CFD for wind-driven ventilation analysis. *Proceedings of the 7th IBPSA Conference, Beijing, China*, pp. 999-1006.
- Counihan, J. (1969). An improved method of simulating an atmospheric boundary layer in a wind tunnel. *Atmospheric Environment* (1967), 3(2), 197-214.
- Culley, P. and Pascoe, J. (2005). *Stadium engineering*. London: Thomas Telford.
- Dantecdynamics.com. (2017). Single-sensor Miniature Wire Probes. [online].
- De Paepe, W., Pindado, S., Bram, S. and Contino, F. (2016). Simplified elements for wind-tunnel measurements with type-III-terrain atmospheric boundary layer. *Measurement*, 91, pp.590-600.
- Deb, K., Pratap, A., Agarwal, S. and Meyarivan, T. (2002). A fast and elitist multiobjective genetic algorithm: NSGA-II. *IEEE Transactions on Evolutionary Computation*, 6(2), pp.182-197.
- Dyrbye, C. and Hansen, S. (1997). *Wind loads on structures*. Chichester: J. Wiley.
- Eça, L. and Hoekstra, M. (2004). A verification exercise for two 2-D steady incompressible turbulent flows. In: Neittaanmäki, P., Rossi, T., Majava, M., Pironneau, O. (Eds.), *Proceedings of the ECCOMAS 2004, Jyväskylä, Finland*.

8 References

- Eça, L. and Hoekstra, M. (2002). An evaluation of verification procedures for CFD applications. In: Proceedings of the 24th Symposium on Naval Hydrodynamics, Fukuoka, 2002.
- Eiseman, P. (1985). Grid Generation for Fluid Mechanics Computations. *Annual Review of Fluid Mechanics*, 17(1), pp.487-522.
- European Standard. (2005) EN 1991-1-4:2005: E. Eurocode 1 : Actions on structures – Part 1-4: General actions – Wind actions. Brussels, European Committee for Standardization.
- Faber, P., Drewnick, F., Veres, P., Williams, J. and Borrmann, S. (2013). Anthropogenic sources of aerosol particles in a football stadium: Real-time characterization of emissions from cigarette smoking, cooking, hand flares, and color smoke bombs by high-resolution aerosol mass spectrometry. *Atmospheric Environment*, 77, pp.1043-1051.
- Fiala, D. and Lomas, K. (1999). Application of a computer model predicting human thermal responses to the design of sports stadia.
- FIFA. 2011. Football Stadiums: Technical recommendations and requirements - 5th Edition. [e-book] FIFA.
- Foncesa, C. and Fleming, P. (1993). Genetic algorithms for multiobjective optimization: Formulation, discussion and generalization. In: Fifth International Conference on Genetic Algorithms. San Mateo, CA: Morgan Kauffman, pp.416-423.
- Franke, J. and Frank, W. (2008). Application of generalized Richardson extrapolation to the computation of the flow across an asymmetric street intersection. *Journal of Wind Engineering and Industrial Aerodynamics*, 96(10-11), pp.1616-1628.
- Franke, J., Hirsch, C., Jensen, A.G., Krüs, H.W., Schatzmann, M., Westbury, P.S., Miles, S.D., Wisse, J.A., Wright, N.G. (2004). Recommendations on the use of CFD in wind engineering. In: Proceedings of the International Conference on Urban Wind Engineering and Building Aerodynamics. In: van Beeck JPAJ (Ed.), COST Action C14, Impact of Wind and Storm on City Life Built Environment. von Karman Institute, Sint-Genesius-Rode, Belgium, 5–7 May 2004.
- Friedman, L. (1996). *The Simulation Metamodel*. Boston, MA: Springer US.
- Friedman; M. and Savage L., J. (1947). *Planning Experiments Seeking Maxima*. Techniques of Statistical Analysis, M. H. and W. A. C. Eisenhart and Wallis, Eds. N.York-London: McGraw-Hill, pp. 363–72.
- Garratt, J. R. (1994). *The atmospheric boundary layer*. Cambridge: Cambridge University Press, pp. 86.
- Gilkeson, C., Thompson, H., Wilson, M., Gaskell, P. and Barnard, R. (2009). An experimental and computational study of the aerodynamic and passive

8 References

- ventilation characteristics of small livestock trailers. *Journal of Wind Engineering and Industrial Aerodynamics*, 97(9-10), pp.415-425.
- Goliger, A. M. (2010). Wind-tunnel testing of sports stadia to optimize their use and safety. *Journal of the South African Institute of Civil Engineering*, 52(1), pp.28-35.
- Han, T. (1989). Computational analysis of three-dimensional turbulent flow around a bluff body in ground proximity. *AIAA Journal*, 27(9), pp.1213-1219.
- Hanjalić, K., Nagano, Y. and Tummers, M. (2003). *Turbulence, heat and mass transfer 4*. 1st ed. New York: Begell House.
- Hansen, S. V. (1993). Surface roughness lengths. ARL Technical Report U. S. Army, White Sands Missile Range, NM 88002-5501.
- Hargreaves, D. and Wright, N. (2007). On the use of the k– model in commercial CFD software to model the neutral atmospheric boundary layer. *Journal of Wind Engineering and Industrial Aerodynamics*, 95(5), pp.355-369.
- Hohman, T., Buren, T., Martinelli, L. and Smits, A. (2015). Generating an artificially thickened boundary layer to simulate the neutral atmospheric boundary layer. *Journal of Wind Engineering and Industrial Aerodynamics*, 145, pp.1-16.
- Holmes, J. (2001). *Wind loading of structures*. London: Spon Press.
- Hotelling, H.(1941). Experimental Determination of the Maximum of a Function. *The Annals of Mathematical Statistics*, vol. 12, no. 1, pp. 20–45.
- Houghton, E. and Carruthers, N. (1976). *Wind forces on buildings and structures*. New York: Wiley.
- Irwin, H. (1981). The design of spires for wind simulation. *Journal Of Wind Engineering And Industrial Aerodynamics*, 7(3), 361-366.
- Janssen, W., Blocken, B. and Van Wijhe, H.J., 2012. Experimental and computational analysis of microscale wind environmental conditions in the Port of Rotterdam. Doctoral dissertation, International Environmental Modelling and Software Society (iEMSs).
- John, G. and Sheard, R. (2000). *Stadia*. 3rd ed. Boston: Architectural Press.
- Katz, A. and Sankaran, V. (2012). High aspect ratio grid effects on the accuracy of Navier–Stokes solutions on unstructured meshes. *Computers & Fluids*, 65, pp.66-79.
- Kim, J. and Chung, J. (2014). Untangling polygonal and polyhedral meshes via mesh optimization. *Engineering With Computers*, 31(3), 617-629.
- Kindangen, J., Krauss, G. and Depecker, P. (1997). Effects of roof shapes on wind-induced air motion inside buildings. *Building and Environment*, 32(1), pp.1-11.
- Kleijnen, J. (2009). Kriging metamodeling in simulation: A review. *European Journal of Operational Research*, 192(3), pp.707-716.

8 References

- Kline, S., Reynolds, W., Schraub, F. and Runstadler, P. (1967). The structure of turbulent boundary layers. *J. Fluid Mech.*, 30(04), p.741.
- Kozmar, H. (2009). Scale effects in wind tunnel modeling of an urban atmospheric boundary layer. *Theoretical and Applied Climatology*, 100(1-2), pp.153-162.
- Kowalski, N., Ledoux, F. and Frey, P. (2014). Block-structured Hexahedral Meshes for CAD Models Using 3D Frame Fields. *Procedia Engineering*, 82, pp.59-71.
- Kvålseth, T. (1983). Note on the R^2 measure of goodness of fit for nonlinear models. *Bulletin of the Psychonomic Society*, 21(1), pp.79-80.
- Launder, B. and Spalding, D. (1974). The numerical computation of turbulent flows. *Computer Methods in Applied Mechanics and Engineering*, 3(2), pp.269-289.
- Laws, E. M. and Livesey, J. L. (1978). Flow through screens. *Annual Review of Fluid Mechanics*, 10, pp.247-266.
- Leene, J. A. (1992). Building wake effects in complex situations. *Journal of Wind Engineering and Industrial Aerodynamics*, 41(44), pp.2277-2288.
- Lestinen, S., Koskela, H., Jokisalo, J., Kilpeläinen, S. and Kosonen, R. (2016). The use of displacement and zoning ventilation in a multipurpose arena. *International Journal of Ventilation*, 15(2), pp.151-166.
- Levinson, D. and Christensen, K. (1996). *Encyclopedia of world sport*. Santa Barbara, Calif.: ABC-CLIO.
- Li, B., Liu, J., Luo, F. and Man, X. (2015). Evaluation of CFD Simulation Using Various Turbulence Models for Wind Pressure on Buildings Based on Wind Tunnel Experiments. *Procedia Engineering*, 121, pp.2209-2216.
- Libii, N. (2011). *Wind Tunnels in Engineering Education*. Available at: http://cdn.intechopen.com/pdfs/16674/InTech-Wind_tunnels_in_engineering_education.pdf
- Lomas, K., Eppel, H., Cool, M. and Mardaljevic, J. (1997). Ventilation and thermal performance of design options for Stadium Australia. In: *The 5th International IBPSA (International Building Performance Simulation Association)*. [online] IBPSA.
- Malkawi, A., Srinivasan, R., Yi, Y. and Choudhary, R. (2005). Decision support and design evolution: integrating genetic algorithms, CFD and visualization. *Automation in Construction*, 14(1), pp.33-44.
- Marighetti, J., Wittwer, A., De Bortoli, M., Natalini, B., Paluch, M. and Natalini, M. (2000). Fluctuating and mean pressure measurements on a stadium covering in wind tunnel. *Journal of Wind Engineering and Industrial Aerodynamics*, 84(3), pp.321-328.
- Mei, W. and Qu., M. (2016). Evaluation and Analysis of Wind Flow for a Football Stadium. *Procedia Engineering*, 145, pp.774-781.

8 References

- Mirzaei, P. and Haghghat, F. (2010). A novel approach to enhance outdoor air quality: Pedestrian ventilation system. *Building and Environment*, 45(7), pp.1582-1593.
- Mitchell, M. (2002). *An introduction to genetic algorithms*. New Delhi: Prentice-Hall of India.
- Myers, R., Khuri, A. and Carter, W. (1989). Response Surface Methodology: 1966–1988. *Technometrics*, 31(2), pp.137-157.
- McVehil, G., Ludwig, G. and Sundaram, T. (1967). On the feasibility of modeling small scale atmospheric motions. Buffalo, N.Y.: Cornell Aeronautical Laboratory.
- Meroney, R. N. (1980). Physical Simulation of Dispersion in Complex Terrain and Valley Drainage Flow Situations. Proceedings of the 11th NATO-CCMS Int. Tech Meeting on Air Pollution Modeling and Its Application. Amsterdam, the Netherlands pp. 303-322.
- Mochida, A., Murakami, S. and Kato, S. (1994). The similarity requirements for wind tunnel model studies of gas diffusion. *Wind Engineers, JAWE*, 1994(59), pp.23-28.
- Montazeri, H. (2011). Experimental and numerical study on natural ventilation performance of various multi-opening wind catchers. *Building and Environment*, 46(2), pp.370-378.
- Montazeri, H. and Blocken, B. (2013). CFD simulation of wind-induced pressure coefficients on buildings with and without balconies: Validation and sensitivity analysis. *Building and Environment*, 60, pp.137-149.
- Mora-Pérez, M., Guillén-Guillamón, I. and López-Jiménez, P. (2015). Computational analysis of wind interactions for comparing different buildings sites in terms of natural ventilation. *Advances in Engineering Software*, 88, pp.73-82.
- Moshfegh, B. and Nyiredy, R. (2004). Comparing RANS models for flow and thermal analysis of pin fin heat sinks, Proceedings of the 15th Australasian Fluid Mechanics Conference, December 2004, Sydney, Australia.
- Moulinec, C., Benhamadouche, S., Laurence, D. and Peric, M. (2005). LES in a U-Bend Pipe Meshed By Polyhedral Cells. In ERCOFTAC International Symposium on Engineering Turbulence Modelling and Measurements. Sardinia, Italy.
- Muzaferija, S. and Gosman, D. (1997). Finite-Volume CFD Procedure and Adaptive Error Control Strategy for Grids of Arbitrary Topology. *Journal of Computational Physics*, 138(2), 766-787.
- Niemann, H. (1993). The boundary layer wind tunnel: an experimental tool in building aerodynamics and environmental engineering. *Journal Of Wind Engineering And Industrial Aerodynamics*, 48(2-3), 145-161.

8 References

- Nishioka, T., Ohtaka, K., Hashimoto, N. and Onojima, H. (2000). Measurement and evaluation of the indoor thermal environment in a large domed stadium. *Energy and Buildings*, 32(2), pp.217-223.
- Ng, K., Kadirgama, K. and Ng, E. (2008). Response surface models for CFD predictions of air diffusion performance index in a displacement ventilated office. *Energy and Buildings*, 40(5), pp.774-781.
- Nguyen, A., Reiter, S. and Rigo, P. (2014). A review on simulation-based optimization methods applied to building performance analysis. *Applied Energy*, 113, pp.1043-1058.
- Norton, T., Grant, J., Fallon, R. and Sun, D. (2010). Optimising the ventilation configuration of naturally ventilated livestock buildings for improved indoor environmental homogeneity. *Building and Environment*, 45(4), pp.983-995.
- Oberkampf, W. and Trucano, T. (2002). Verification and validation in computational fluid dynamics. *Progress in Aerospace Sciences*, 38(3), pp.209--272.
- Parente, A., Gorré, C., van Beeck, J. and Benocci, C. (2011). A Comprehensive Modelling Approach for the Neutral Atmospheric Boundary Layer: Consistent Inflow Conditions, Wall Function and Turbulence Model. *Boundary-Layer Meteorology*, 140(3), pp.411-428.
- Parr, A. and Zaretsky, M. (2011). *New directions in sustainable design*. London: Routledge.
- Persoon, J., van Hooff, T., Blocken, B., Carmeliet, J. and de Wit, M. (2008). On the impact of roof geometry on rain shelter in football stadia. *Journal of Wind Engineering and Industrial Aerodynamics*, 96(8-9), pp.1274-1293.
- Perić, M. (2004). Flow Simulation Using Control Volumes Of Arbitrary Polyhedral Shape, ERCOFTAC, Bulletin No. 62, pp.1787-1806.
- Passe, U. and Battaglia, F. (2015). *Designing Spaces for Natural Ventilation*. Hoboken: Taylor and Francis.
- Piomelli U., Balaras, E. (2002). Wall-layer models for large-eddy simulations, *Annual Review of Fluid Mechanics*, 34, pp.349-374.
- Piomelli, U., Balaras, E., Pasinato, H., Squires, K. and Spalart, P. (2003). The inner-outer layer interface in large-eddy simulations with wall-layer models. *International Journal of Heat and Fluid Flow*, 24(4), pp.538-550.
- Preuss, H. (2013). The contribution of the FIFA World Cup and the Olympic Games to Green Economy. *Sustainability*, 5(8), pp.3581-3600.
- Ramponi, R. and Blocken, B. (2012). CFD simulation of cross-ventilation for a generic isolated building: Impact of computational parameters. *Building and Environment*, 53, pp.34-48.
- Ramponi, R., Blocken, B., de Coo, L. and Janssen, W. (2015). CFD simulation of outdoor ventilation of generic urban configurations with different urban densities and equal and unequal street widths. *Building and Environment*, 92, pp.152-166.

8 References

- Reid, W. and Travers, J. (1991). Wind tunnel testing of sports stadiums. *Construction and Building Materials*, 5(3), pp.120-122.
- Reynolds, A. (1974). *Turbulent flows in engineering*. London: John Wiley.
- Richards, P. and Hoxey, R. (1993). Appropriate boundary conditions for computational wind engineering models using the k- ϵ turbulence model. *Journal of Wind Engineering and Industrial Aerodynamics*, 46-47, pp.145-153.
- Richards, P. and Norris, S. (2011). Appropriate boundary conditions for computational wind engineering models revisited. *Journal of Wind Engineering and Industrial Aerodynamics*, 99(4), pp.257-266.
- Ristić, S., Isaković, J., Ilić, B. and Ocofoljić, G. (2004). Review of methods for flow velocity measurement in wind tunnels. *Scientific Technical Review*, 54(3-4), pp.60-71.
- Roache, P. (1994). Perspective: a method for uniform reporting of grid refinement studies. *Journal of Fluids Engineering*, 116(3), pp.405-413.
- Roache, P. (1997). Quantification Of Uncertainty In Computational Fluid Dynamics. *Annu. Rev. Fluid Mech.*, 29(1), pp.123-160.
- Roache, P. (1998). *Fundamentals of computational fluid dynamics*. Albuquerque, N.M.: Hermosa Publishers.
- Roache, P. (2002). Code verification by the method of manufactured solutions. *Journal of Fluids Engineering*, 124(1), pp.4-10.
- Rotach, M. W. (1991). *Turbulence within and above an urban canopy*. ETH Diss. 9439. Published as ZGS, Heft 45, Verlag vdf, Ztirich, 1991.
- Sachs, P. (1978). *Wind forces in engineering*. Oxford: Pergamon Press.
- Satwiko, P., Locke, N. and Donn, M. (1998). Reproducing the real pressure coefficient using a Computational Fluid Dynamic program: How close is close enough? Proceedings of the 32th Annual Conference of the Australia and New Zealand Architectural Science Association. 15 – 17 July 1998, University of Wellington, New Zealand.
- Schölkopf, B., Burges, C. and Smola, A. (1999). *Advances in kernel methods*. Cambridge, Mass.: MIT Press, p.11.
- Shárán, V. (1975). On characteristics of flow around building models with a view to simulating the minimum fraction of the natural boundary layer. *International Journal of Mechanical Sciences*, 17(9), pp.557-563.
- Shen, X., Zhang, G. and Bjerg, B. (2012). Investigation of response surface methodology for modelling ventilation rate of a naturally ventilated building. *Building and Environment*, 54, pp.174-185.
- Shen, X., Zhang, G. and Bjerg, B. (2013). Assessments of experimental designs in response surface modelling process: Estimating ventilation rate in naturally ventilated livestock buildings. *Energy and Buildings*, 62, pp.570-580.

8 References

- Shih, T. H. (1995). A new k -epsilon eddy viscosity model for high Reynolds number flows. *Computers in Fluids*, 24, pp.227–238.
- Simiu, E., and Scanlan, R.H (1996). *Wind effects on structures*. New York: Wiley.
- Snyder, W. (1972). Similarity criteria for the application of fluid models to the study of air pollution meteorology. *Boundary-Layer Meteorol*, 3(1), pp.113-134.
- Snyder, W. (1981). *Guideline for fluid modeling of atmospheric diffusion*. Research Triangle Park, N.C.: Environmental Sciences Research Laboratory, Office of Research and Development, U.S. Environmental Protection Agency.
- Sofotasiou, P., Hughes, B. and Calautit, J. (2015). Qatar 2022: Facing the FIFA World Cup climatic and legacy challenges. *Sustainable Cities and Society*, 14, pp.16-30.
- Sofotasiou, P., Calautit, J., Hughes, B. and O'Connor, D. (2016). Towards an integrated computational method to determine internal spaces for optimum environmental conditions. *Computers & Fluids*, 127, pp.146-160.
- Soligo, M., Lankin, J. and Irwin, P. (2000). Environmental loads and microclimate impacts on sport facilities. In: *The 1st International Conference, Stadia 2000*.
- Souza, A. (2003). *How to understand computational fluid dynamics jargon*. Glasgow: NAFEMS.
- Spalart, P. and Allmaras, S. (1992). One-equation turbulence model for aerodynamic flows, *AIAA Paper 92-0439*.
- Spiegel, M., Redel, T., Zhang, Y., Struffert, T., Hornegger, J. and Grossman, R. et al. (2011). Tetrahedral vs. polyhedral mesh size evaluation on flow velocity and wall shear stress for cerebral hemodynamic simulation. *Computer Methods In Biomechanics And Biomedical Engineering*, 14(1), pp.9-22.
- Srinivas, N. and Deb, K. (1994). Multiobjective Optimization Using Nondominated Sorting in Genetic Algorithms. *Evolutionary Computation*, 2(3), pp.221-248.
- Stamou, A., Katsiris, I. and Schaelin, A. (2008). Evaluation of thermal comfort in Galatsi Arena of the Olympics “Athens 2004” using a CFD model. *Applied Thermal Engineering*, 28(10), pp.1206-1215.
- Stathopoulos, T., Wu, H. and Bédard, C. (1992). Wind environment around buildings: A knowledge-based approach. *Journal of Wind Engineering and Industrial Aerodynamics*, 44(1-3), pp.2377-2388.
- Stavrakakis, G., Zervas, P., Sarimveis, H. and Markatos, N. (2012). Optimization of window-openings design for thermal comfort in naturally ventilated buildings. *Applied Mathematical Modelling*, 36(1), pp.193-211.
- Stavrakakis, G., Karadimou, D., Zervas, P., Sarimveis, H. and Markatos, N. (2011). Selection of window sizes for optimizing occupational comfort and hygiene based on computational fluid dynamics and neural networks. *Building and Environment*, 46(2), pp.298-314.

8 References

- Stavrakakis, G., Zervas, P., Sarimveis, H. and Markatos, N. (2010). Development of a computational tool to quantify architectural-design effects on thermal comfort in naturally ventilated rural houses. *Building and Environment*, 45(1), pp.65-80.
- Stern, F., Wilson, R., Coleman, H. and Paterson, E. (2001). Comprehensive Approach to Verification and Validation of CFD Simulations—Part 1: Methodology and Procedures. *Journal of Fluids Engineering*, 123(4), p.793.
- Suryan, A., Kim, H. and Setoguchi, T. (2013). Comparative study of turbulence models performance for refueling of compressed hydrogen tanks. *International Journal of Hydrogen Energy*, 38(22), pp.9562-9569.
- Szucs, A. (2004). Stadia in the environment - environment in stadia. In: *The 21st International Conference of Passive and Low Energy Architecture (PLEA)*, Eindhoven, The Netherlands, p. 169-174. ISBN 90-386-1636-8.
- Szucs, A., Moreau, S. and Allard, F. (2007). Spectators' aerothermal comfort assessment method in stadia. *Building and Environment*, 42(6), pp.2227-2240.
- Szucs, A., Moreau, S. and Allard, F. (2009a). Aspects of stadium design for warm climates. *Building and Environment*, 44(6), pp.1206-1214.
- Szucs, A., Allard, F., Moreau, S. (2009b). Open Stadium Design Aspects for Cold Climates. In: *The 26st Conference on Passive and Low Energy Architecture (PLEA)*, Quebec City, Canada.
- Tecele, A., Bitsuamlak, G. and Jiru, T. (2013). Wind-driven natural ventilation in a low-rise building: A Boundary Layer Wind Tunnel study. *Building And Environment*, 59, 275-289. <http://dx.doi.org/10.1016/j.buildenv.2012.08.026>
- Thompson, P., Tolloczko, J. and Clarke, J. (1998). *Stadia, arenas and grandstands*. London: E & FN Spon.
- Thuillier, R. and Lappe, U. (1964). Wind and Temperature Profile Characteristics from Observations on a 1400 ft Tower. *Journal of Applied Meteorology*, 3(3), pp.299-306.
- Tominaga, Y., Mochida, A., Murakami, S. and Sawaki, S. (2008). Comparison of various revised $k-\epsilon$ models and LES applied to flow around a high-rise building model with 1:1:2 shape placed within the surface boundary layer. *Journal of Wind Engineering and Industrial Aerodynamics*, 96(4), pp.389-411.
- Tritthart, M. and Gutknecht, D. (2007). Three-Dimensional Simulation of Free-Surface Flows Using Polyhedral Finite Volumes. *Engineering Applications Of Computational Fluid Mechanics*, 1(1), 1-14.
- Tropea, C., Yarin, A. and Foss, J. (2007). *Springer handbook of experimental fluid mechanics*. 1st ed. Berlin: Springer.
- Ucuncu, M., Woolf, D. and Zikri, M. (2010). Thermal Comfort of Spectators in Stadia Built in Hot Climates. In: *Adapting to Change: New Thinking on Comfort, Windsor*, 9-11 April. London: Network for Comfort and Energy Use in Buildings, p.8.

8 References

- Uehara K., Wakamatsu S., Ooka R. (2003). Studies on critical Reynolds number indices for wind-tunnel experiments on flow within urban areas. *Boundary-Layer Meteorology* 107 pp.353–370.
- Vapnik, V. (2000). *The nature of statistical learning theory*. New York: Springer.
- van Hooff, T. and Blocken, B. (2012). Full-scale measurements of indoor environmental conditions and natural ventilation in a large semi-enclosed stadium: Possibilities and limitations for CFD validation. *Journal of Wind Engineering and Industrial Aerodynamics*, 104-106, pp.330-341.
- van Hooff, T. and Blocken, B. (2010a). Coupled urban wind flow and indoor natural ventilation modelling on a high-resolution grid: A case study for the Amsterdam ArenA stadium. *Environmental Modelling & Software*, 25(1), pp.51-65.
- van Hooff, T. and Blocken, B. (2010b). On the effect of wind direction and urban surroundings on natural ventilation of a large semi-enclosed stadium. *Computers & Fluids*, 39(7), pp.1146-1155.
- van Hooff, T. and Blocken, B. (2009). CFD analysis of natural ventilation in large semi-enclosed buildings — Case study: Amsterdam Arena football stadium. In Paper presented at Eleventh International IBPSA Conference Glasgow, Scotland, 27–30 July.
- van Hooff, T., Blocken, B. and van Harten, M. (2011). 3D CFD simulations of wind flow and wind-driven rain shelter in sports stadia: Influence of stadium geometry. *Building and Environment*, 46(1), pp.22-37.
- Veres, P., Faber, P., Drewnick, F., Lelieveld, J. and Williams, J. (2013). Anthropogenic sources of VOC in a football stadium: Assessing human emissions in the atmosphere. *Atmospheric Environment*, 77, pp.1052-1059.
- Versteeg, H. and Malalasekera, W. (1995). *An introduction to computational fluid dynamics*. Harlow, Essex, England: New York.
- Versteeg, H. and Malalasekera, W. (2007). *An introduction to computational fluid dynamics*. 1st ed. Harlow, England: Pearson Education Ltd.
- Wand, M. and Jones, M. (1995). *Kernel smoothing*. London: Chapman & Hall.
- Wang, B. and Malkawi, A. (2015). Genetic algorithm based building form optimization study for natural ventilation potential. In: 14th Conference of International Building Performance Simulation Association. [online] Available at: <http://www.ibpsa.org/proceedings/BS2015/p2197>.
- Wieringa, J. (1992). Updating the Davenport roughness classification. *Journal of Wind Engineering and Industrial Aerodynamics*, 41(1-3), pp.357-368.
- Wilcox, D. (1993). *Turbulence modeling for CFD*. La C nada, CA: DCW Industries, Inc.
- Willemsen, E. and Wisse, J. (2007). Design for wind comfort in The Netherlands: Procedures, criteria and open research issues. *Journal of Wind Engineering and Industrial Aerodynamics*, 95(9-11), pp.1541-1550.

8 References

- Wu, C. and Hamada, M. (2000). *Experiments*. New York: Wiley.
- Xue, Y., Zhai, Z. and Chen, Q. (2013). Inverse prediction and optimization of flow control conditions for confined spaces using a CFD-based genetic algorithm. *Building and Environment*, 64, pp.77-84.
- Zaghi, S., Muscari, R. and Mascio, A. (2016). Assessment of blockage effects in wind tunnel testing of wind turbines. *Journal of Wind Engineering and Industrial Aerodynamics*, 154, pp.1-9.
- Zhang, J. and Yang, Q. (2009). Study of Horizontally Homogeneous Atmosphere Boundary Layer Based on Standard k-e Model. 2009 International Conference on Engineering Computation. [online] Available at: <http://dx.doi.org/10.1109/icec.2009.30>.
- Zhang, W., Mak, C., Ai, Z. and Siu, W. (2011). A Study of the Ventilation and Thermal Comfort of the Environment Surrounding a New University Building under Construction. *Indoor and Built Environment*, 21(4), pp.568-582.
- Zhou, L. and Haghghat, F. (2009a). Optimization of ventilation system design and operation in office environment, Part I: Methodology. *Building and Environment*, 44(4), pp.651-656.
- Zhou, L. and Haghghat, F. (2009b). Optimization of ventilation systems in office environment, Part II: Results and discussions. *Building and Environment*, 44(4), pp.657-665.

Appendix A

A.1 Hot Wire Probe Calibration

The single hot wire probes were calibrated for two positions in total. Figure **Error! No text of specified style in document.-1** illustrates the hot wire to be positioned parallel and Figure **Error! No text of specified style in document.-2** vertical to the inlet flow. The generated hot wire responses fit perfectly the calibration curve out of which the generated coefficients (a, b and c) were used to analyse the velocity experimental data in the MATLAB.

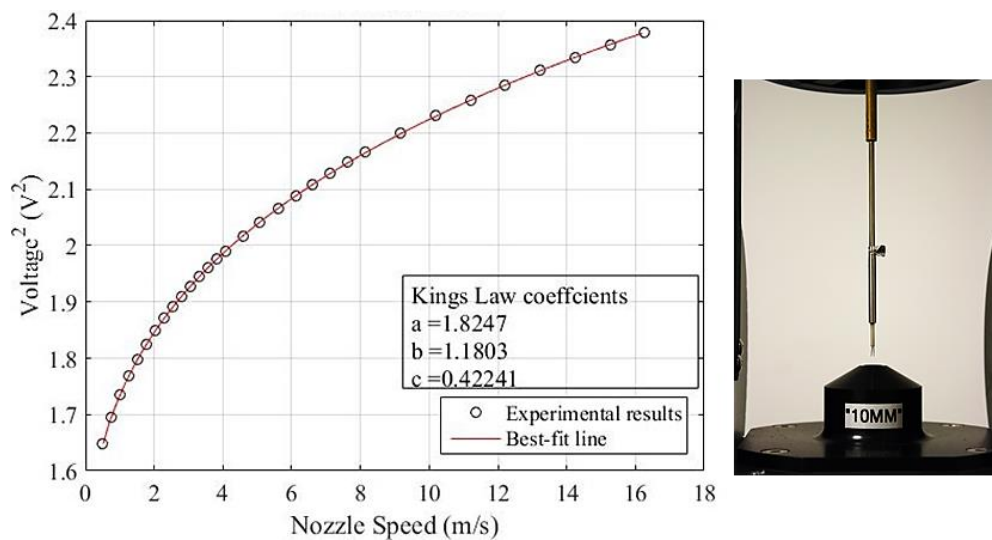


Figure **Error! No text of specified style in document.-1** Velocity calibration curve for the horizontal position of the single hot wire probe in steady flow.

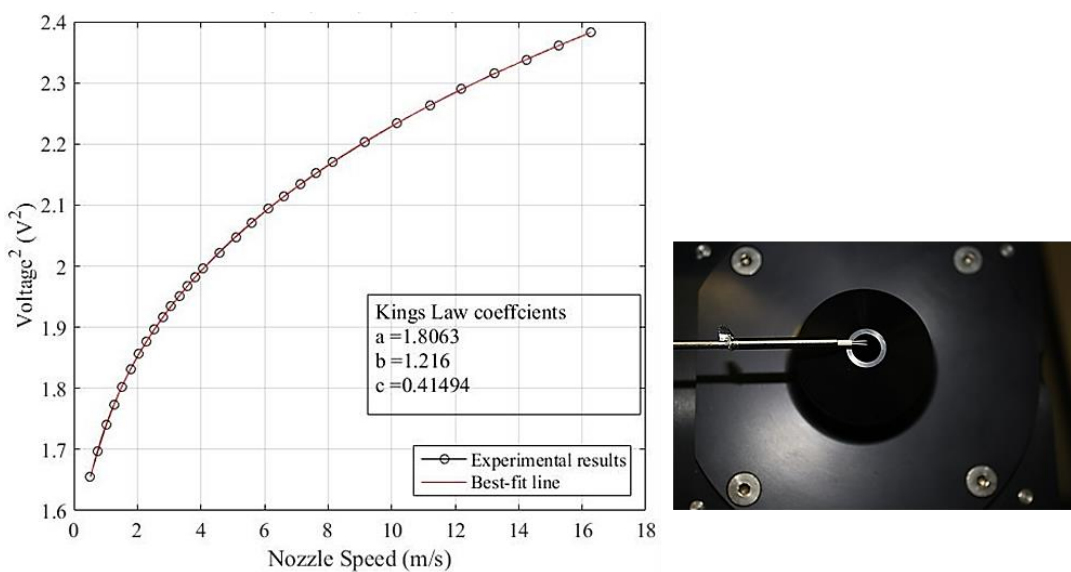





Figure **Error! No text of specified style in document.-2** Velocity calibration curve for the vertical position of the single hot wire probe in steady flow.



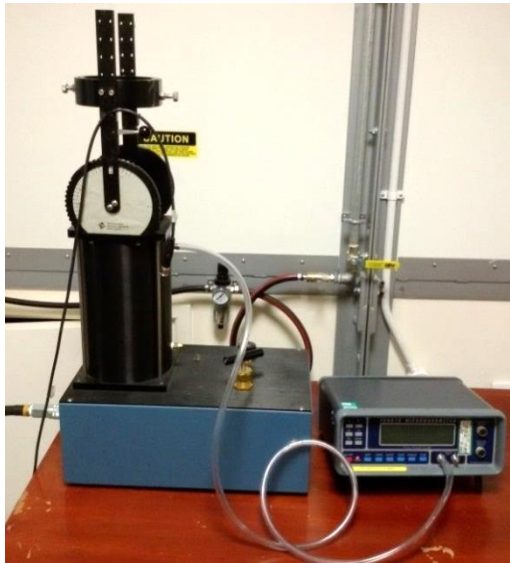
Appendix A

Table A-1 Analytical description of the wind tunnel equipment used for the study.

Instrument Characteristic	Description
1. Standard Pitot Tube	
	
Pitot coefficient	0.99, unless calibrated
Sensitivity	Low to misalignment, up to 15 degrees
Material	304 stainless steel
Feature 1	Shortened stem and enlarged impact
Feature 2	6 static pressure holes on the stem
2. Single hot wire anemometer	
	
Sensor material	Platinum-plated tungsten
Sensor dimensions	5 μm dia, 1.25 mm long
Sensor resistance R20 (approx.)	3.4 Ω
Temperature coefficient of resistance (TCR) α 20 (approx.)	0.36 % / $^{\circ}\text{C}$
Sensor temperature Max. / Min.	300 $^{\circ}\text{C}$ / 150 $^{\circ}\text{C}$
Velocity Max. / Min.*	500 m/s / 0.05 m/s
*Influence from natural convection up to approximately 0.20 m/s	
3. T-Thermocouple probe	
	
Wires' material	Copper-Nickel
Temperature range	-250 $^{\circ}\text{C}$ to 900 $^{\circ}\text{C}$
Std. limits of error	Greater of 1.7 $^{\circ}\text{C}$ or 0.75 %
Spec. limits of error	Greater of 0.5 $^{\circ}\text{C}$ or 0.4 %
Calibration	No calibration requirement

Appendix A

Table A-1(Continued).

Instrument Characteristic	Description
4. <i>Pressure scanner</i>	
	
Accuracy	$\pm 0.5\%$ FS (5 psi & up)
Operating temperature	0°C to 60°C
Max. reference pressure	250 psig (1725 kPa)
Calibration	Factory calibrated
5. Low pressure microprocessor micromanometer	
	
Accuracy	25 % of reading between 10 % of lowest range and full scale, \pm one digit below 10 %
Pressure transducer resolution	0.001 Pascal
Measurement capabilities	Air velocity, volume flow, temperature and absolute pressure
6. TSI air velocity calibrator	
	
Used for the calibration of the hot-wire anemometer in a wide range of velocities. The calibrator is integrated with a micromanometer and a thermocouple probe to provide accurate measurements of velocity.	

Appendix A

A.2 Description of the ABL wind tunnel facility

Thereafter are presented the full dimensional drawings of the wind tunnel facility and the constructed elements to be used for the generation of a suburban atmospheric boundary layer, described as follows:

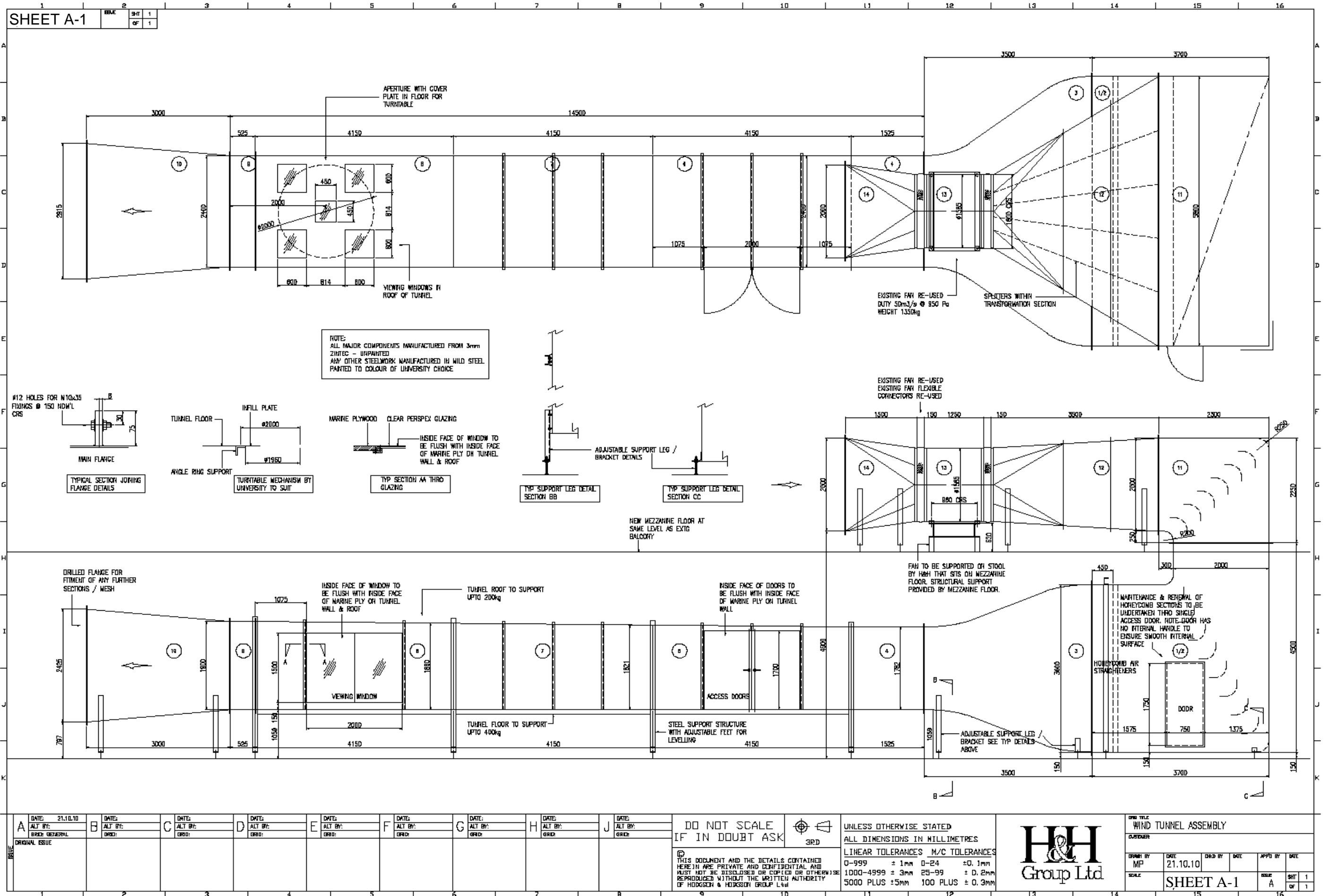
Sheet A-1 illustrates the top and side views of the wind tunnel facility of the University of Nottingham. They are the original drawings, obtained from the Department of Civil Engineering.

Sheet A-2 illustrates the dimensional characteristics of the fence to be used as a vortex generator for the development of artificial turbulence and enable the formation of the ABL velocity profile.

Sheet A-3 illustrates the dimensional characteristics of the spires to be used as vortex generators for the generation of artificial turbulence.

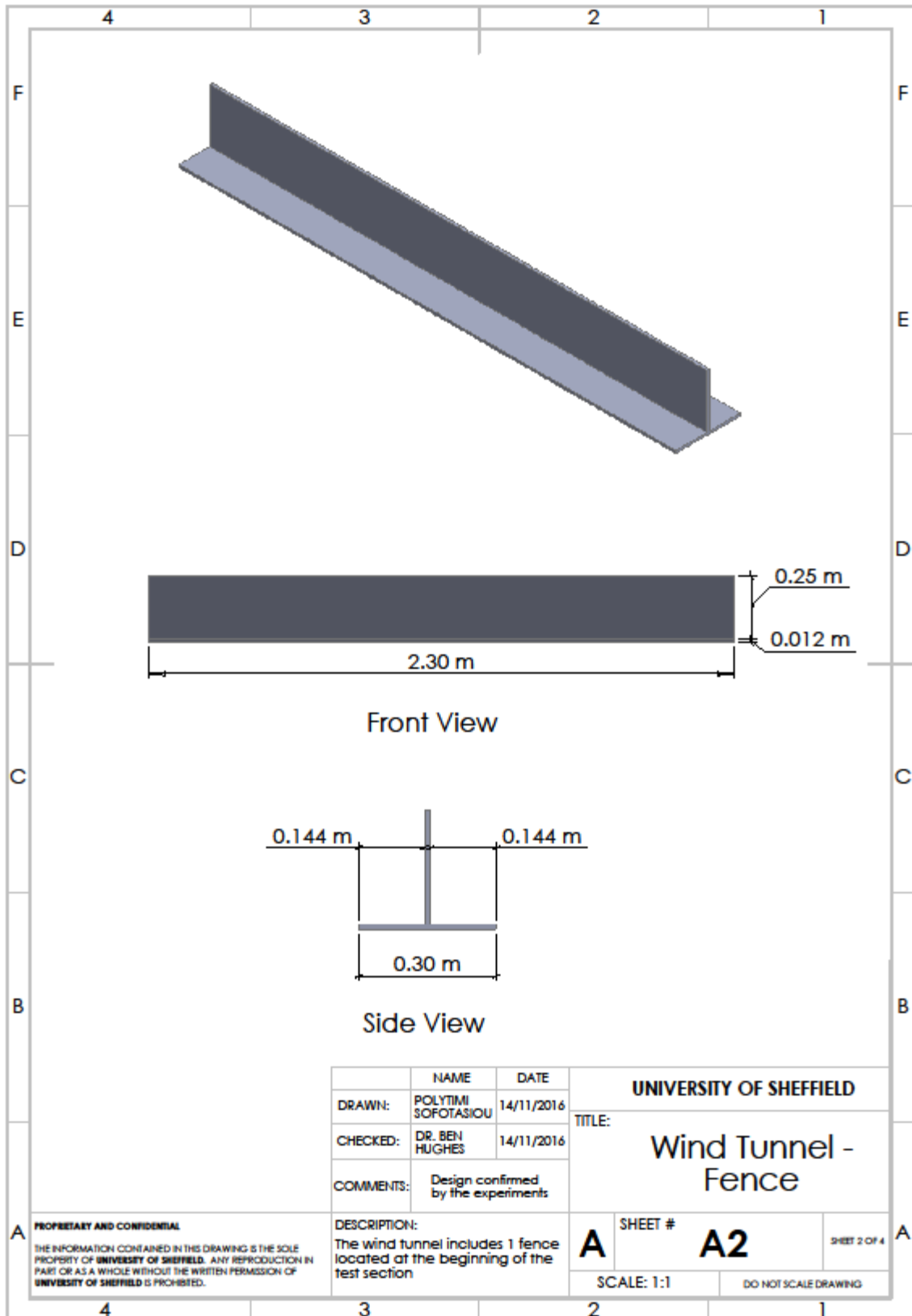
Sheet A-4 illustrates the ground surface element blocks to be used for the representation of a suburban environment in scale 1:400.

Appendix A



A	DATE: 21.10.10 ALT BY: BRIC GENERAL DRD: ORIGINAL ISSUE	B	DATE: ALT BY: DRD:	C	DATE: ALT BY: DRD:	D	DATE: ALT BY: DRD:	E	DATE: ALT BY: DRD:	F	DATE: ALT BY: DRD:	G	DATE: ALT BY: DRD:	H	DATE: ALT BY: DRD:	J	DATE: ALT BY: DRD:	DO NOT SCALE IF IN DOUBT ASK	3RD	UNLESS OTHERWISE STATED ALL DIMENSIONS IN MILLIMETRES	H&H Group Ltd	WIND TUNNEL ASSEMBLY
																		LINEAR TOLERANCES M/C TOLERANCES 0-999 ± 1mm 0-24 ± 0.1mm 1000-4999 ± 3mm 25-99 ± 0.2mm 5000 PLUS ± 5mm 100 PLUS ± 0.3mm		DRAWN BY: MP DATE: 21.10.10 SCALE: SHEET A-1 OF 1		

Appendix A

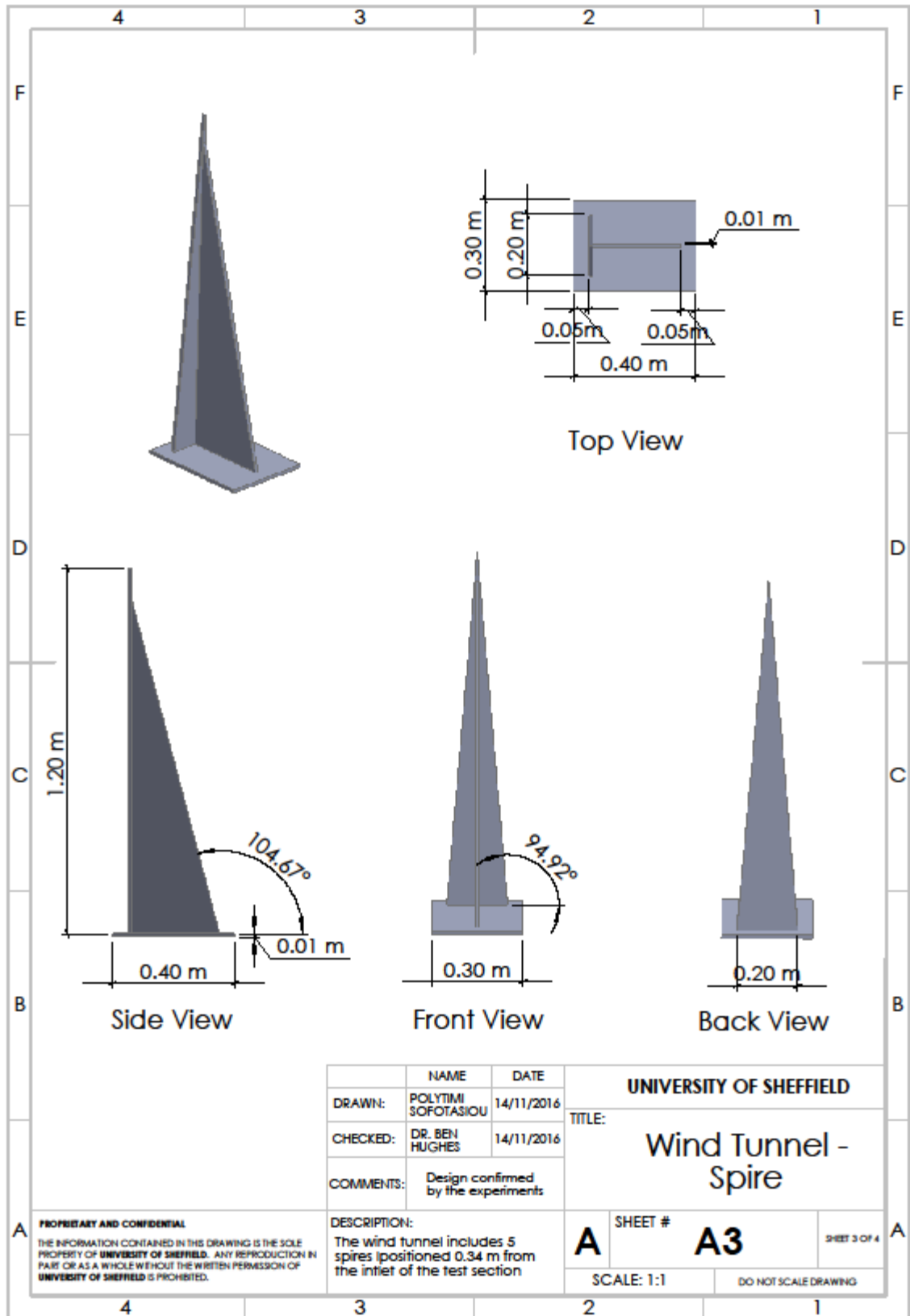


Front View

Side View

	NAME	DATE	UNIVERSITY OF SHEFFIELD	
DRAWN:	POLYTIMI SOFOTASIOU	14/11/2016		
CHECKED:	DR. BEN HUGHES	14/11/2016	TITLE:	
	COMMENTS:		Wind Tunnel - Fence	
	Design confirmed by the experiments			
PROPRIETARY AND CONFIDENTIAL THE INFORMATION CONTAINED IN THIS DRAWING IS THE SOLE PROPERTY OF UNIVERSITY OF SHEFFIELD. ANY REPRODUCTION IN PART OR AS A WHOLE WITHOUT THE WRITTEN PERMISSION OF UNIVERSITY OF SHEFFIELD IS PROHIBITED.	DESCRIPTION:		SHEET #	SHEET 2 OF 4
	The wind tunnel includes 1 fence located at the beginning of the test section		A	
		SCALE: 1:1	DO NOT SCALE DRAWING	

Appendix A



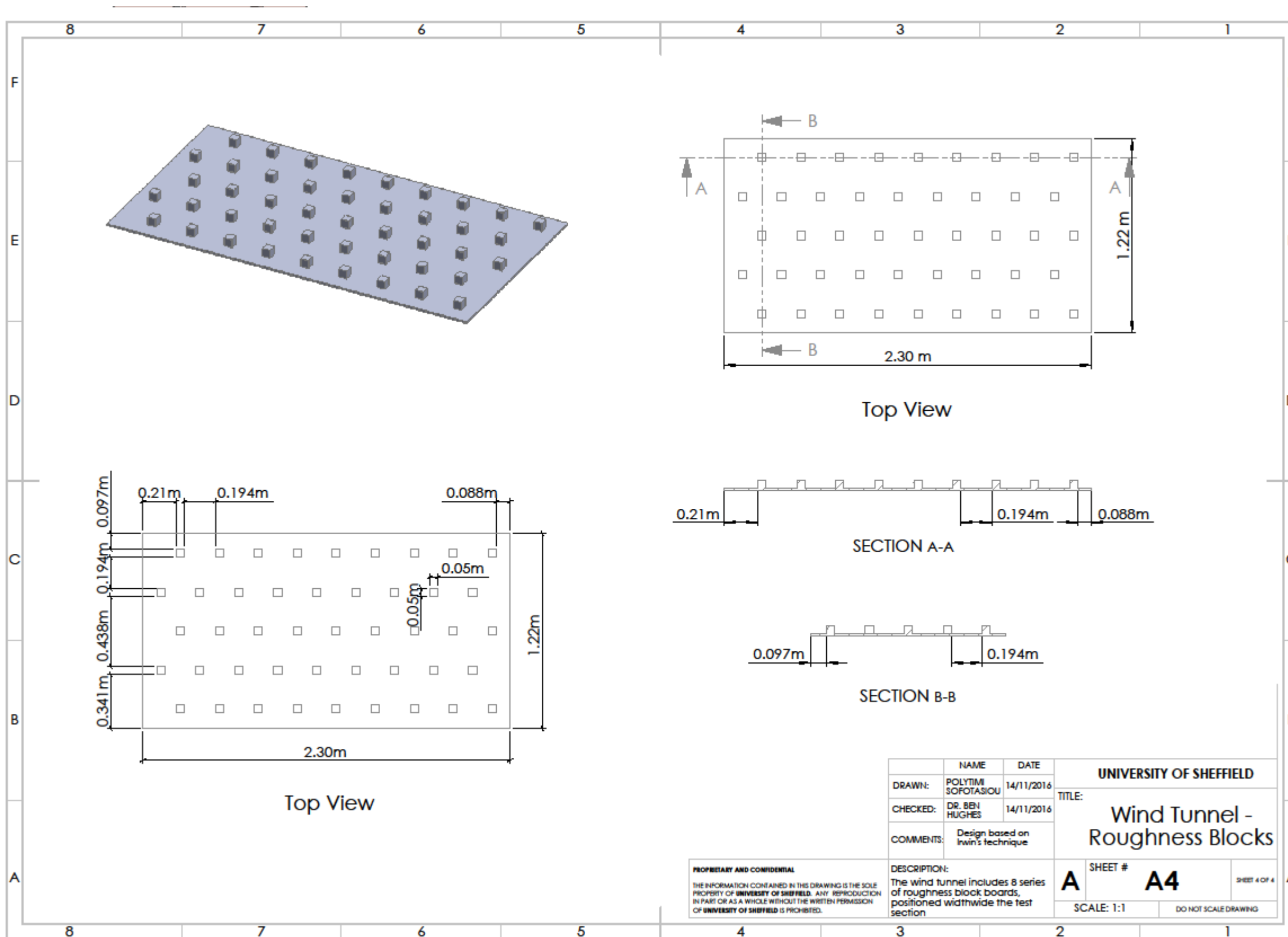
	NAME	DATE
DRAWN:	POLYTIMI SOFOTASIOU	14/11/2016
CHECKED:	DR. BEN HUGHES	14/11/2016
COMMENTS:	Design confirmed by the experiments	

UNIVERSITY OF SHEFFIELD
 TITLE:
Wind Tunnel - Spire

PROPRIETARY AND CONFIDENTIAL
 THE INFORMATION CONTAINED IN THIS DRAWING IS THE SOLE PROPERTY OF UNIVERSITY OF SHEFFIELD. ANY REPRODUCTION IN PART OR AS A WHOLE WITHOUT THE WRITTEN PERMISSION OF UNIVERSITY OF SHEFFIELD IS PROHIBITED.

DESCRIPTION:
 The wind tunnel includes 5 spires positioned 0.34 m from the inlet of the test section

SHEET # **A3** SHEET 3 OF 4
 SCALE: 1:1 DO NOT SCALE DRAWING



NAME		DATE	UNIVERSITY OF SHEFFIELD	
DRAWN:	POLYTIMI SOFOTASIOU	14/11/2016	TITLE: Wind Tunnel - Roughness Blocks	
CHECKED:	DR. BEN HUGHES	14/11/2016		
COMMENTS:	Design based on Irwin's technique		SHEET # A4 SHEET 4 OF 4	
PROPRIETARY AND CONFIDENTIAL		DESCRIPTION:		SCALE: 1:1
THE INFORMATION CONTAINED IN THIS DRAWING IS THE SOLE PROPERTY OF UNIVERSITY OF SHEFFIELD. ANY REPRODUCTION IN PART OR AS A WHOLE WITHOUT THE WRITTEN PERMISSION OF UNIVERSITY OF SHEFFIELD IS PROHIBITED.		The wind tunnel includes 8 series of roughness block boards, positioned wide across the test section		DO NOT SCALE DRAWING

Appendix A

A.3 CFD Modelling of the ABL Wind Tunnel Facility

In order to reduce the computational cost and memory for the conduction of the CFD simulation, the test section of the ABL wind tunnel facility was simulated first to generate the plane velocity profile to be used as inlet boundary condition at the study of the stadium model.

The computational domain as shown in Figure A-3, involved the construction of the full scale ABL wind tunnel test section integrated with the fence, the spires and the ground roughness blocks.

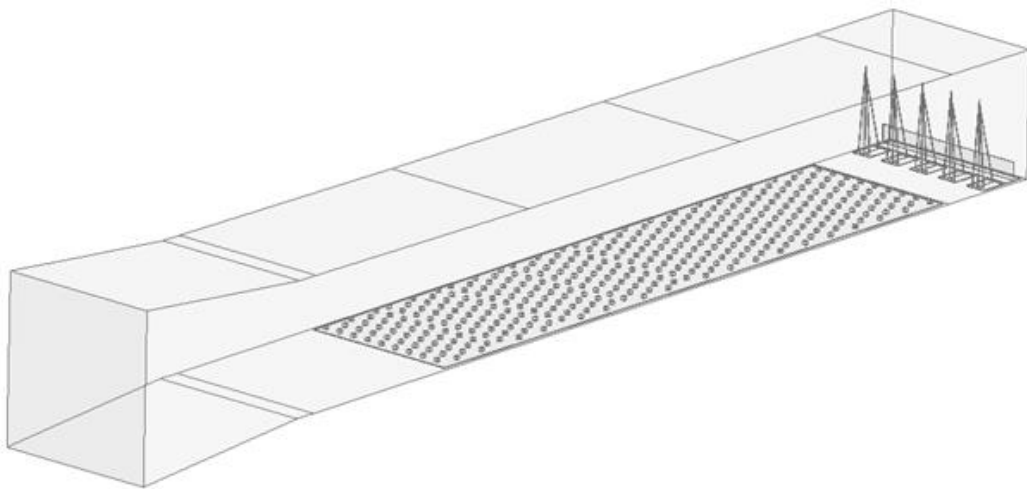


Figure Error! No text of specified style in document.-3 Illustration of the computational domain for the ABL wind tunnel test section.

The computational grid produced an initial mesh size of 5,298,019 hybrid cells, after segmenting the computational domain in 48 bodies to allow the creation of sweepable bodies, where possible, for the generation of structured hexahedral cells. The obtained grid is illustrated in Figure A-4.

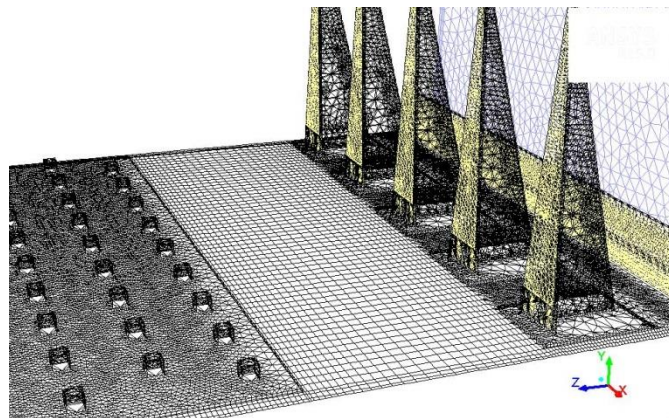


Figure Error! No text of specified style in document.-4 Illustration of the initial generated computational mesh of 5,298,019 hybrid cells.

Appendix A

The grid independency study was performed using boundary adaptation techniques for the fence, the spires, the element blocks and the ground wall, with an increasing ratio of 2. The generated meshes included a medium mesh of 7,187,314 cells and a fine mesh of 16,584,306 cells. The parameterisation of the CFD simulation for the grid independency study is presented in Table A-2 below:

Table Error! No text of specified style in document.-2 Analytical description of the wind tunnel equipment used for the study.

Turbulent Model	Standard k- ϵ model with standard wall functions,
Boundary Conditions	
Inlet	Constant profile: 10 m/s
Outlet	Pressure-outlet with zero pressure
Walls (domain)	$k_s = 10^{-3}$, $C_s = 0.5$
Fence, Spires, Roughness elements	$k_s = 10^{-5}$, $C_s = 0.5$
Solution Methods	SIMPLE; Second Order for pressure, momentum and turbulence transport equations
Convergence Criterion	None (to control end of calculation)

The comparative results focused on the adequacy of the grid resolution to capture the zero-plane displacement at the last row of the ground roughness elements. According to the results illustrated in Figure A-5, the medium and fine meshes predicted the zero-plane displacement at a height equal to 0.03 m, and thus the medium mesh was selected to be used for the simulation study of the facility.

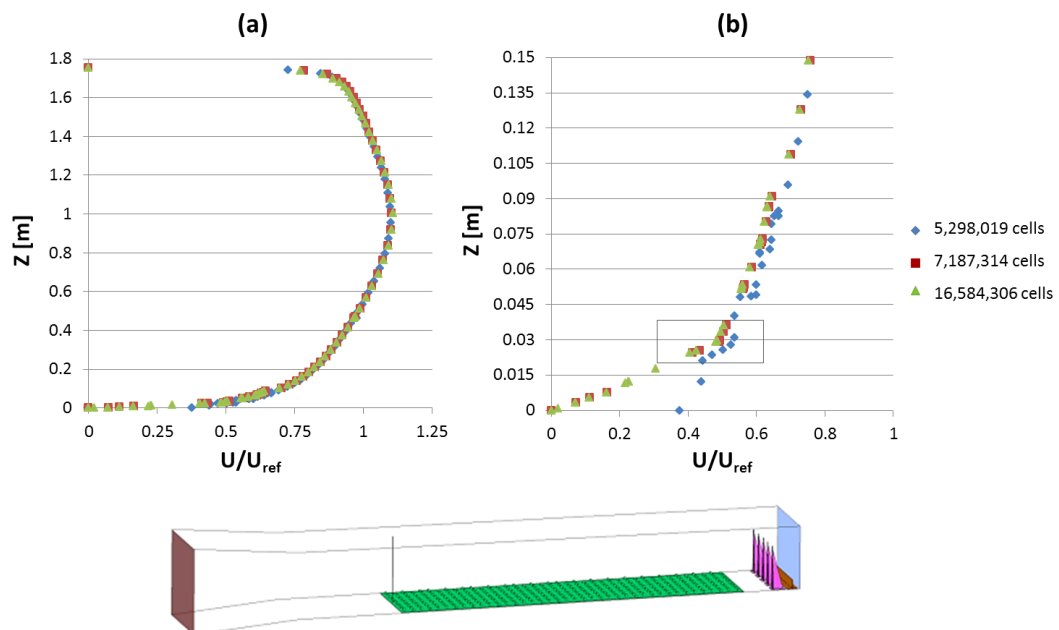


Figure Error! No text of specified style in document.-5 Illustration of the initial generated computational mesh of 5,298,019 hybrid cells.

Appendix A

The results on the velocity distribution that were generated with the Standard $k-\varepsilon$ model were compared with experimental data and additional one and two-equation turbulence models. The turbulence model performance study involved the comparison of the Spalart-Allmaras, the Realisable $k-\varepsilon$, the Renormalisation Group $k-\varepsilon$ and the Shear-Stress $k-\omega$ turbulence models.

Appendix B

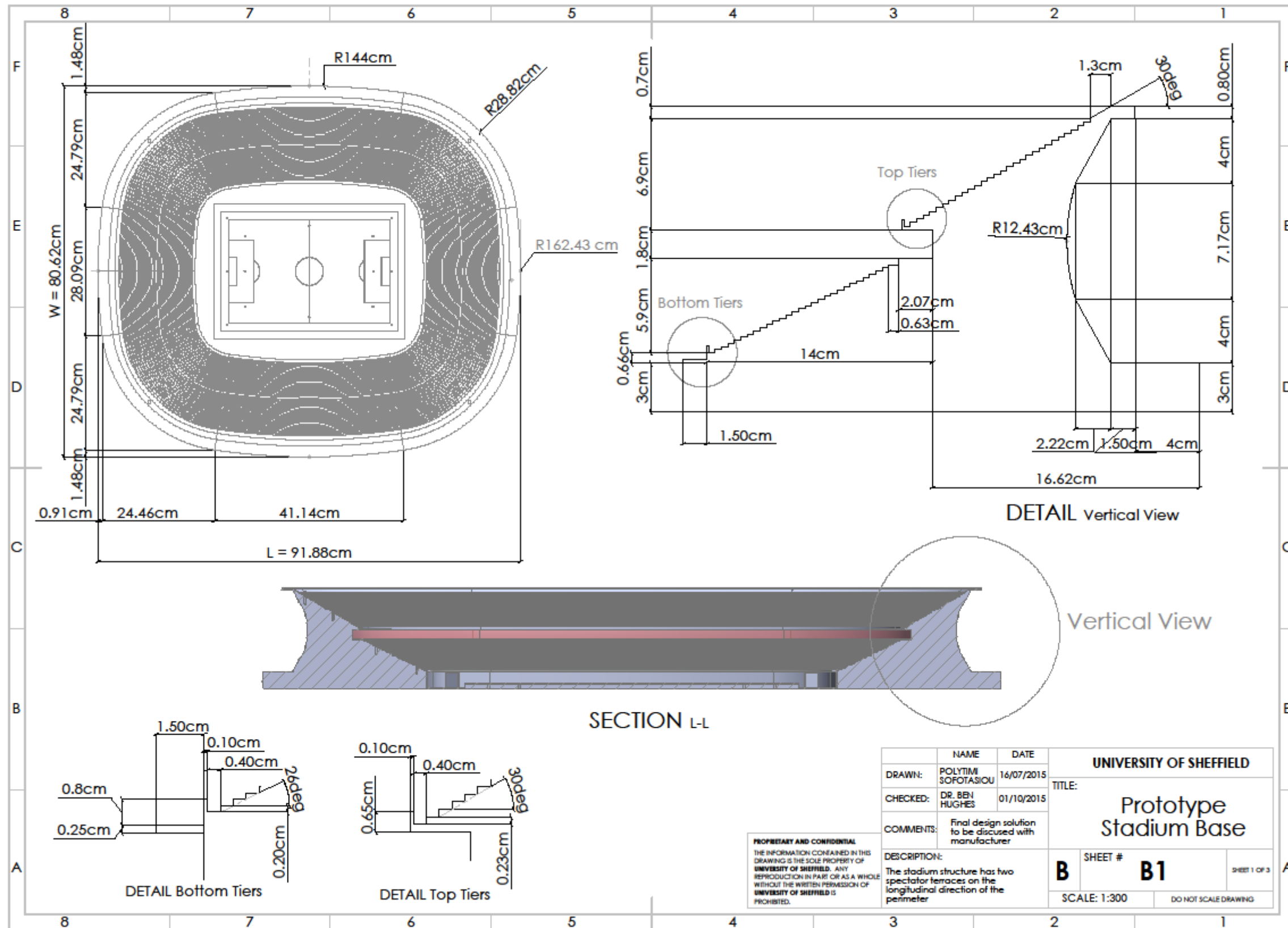
B.1 Description of the scaled stadium model

Thereafter are presented the 1:300 scale stadium drawings that were used for the construction of the wind tunnel stadium model. The locations of the pressure taps are also indicated with the same numbering that was used in 3.

Sheet B-1 illustrates the dimensional characteristics of the stadium base. The spectator tiers were represented by a sloped surface of same angle, in order to reduce the construction cost.

Sheet B-2 illustrates the locations of the pressure taps at the auxiliary area and at the spectator terraces.

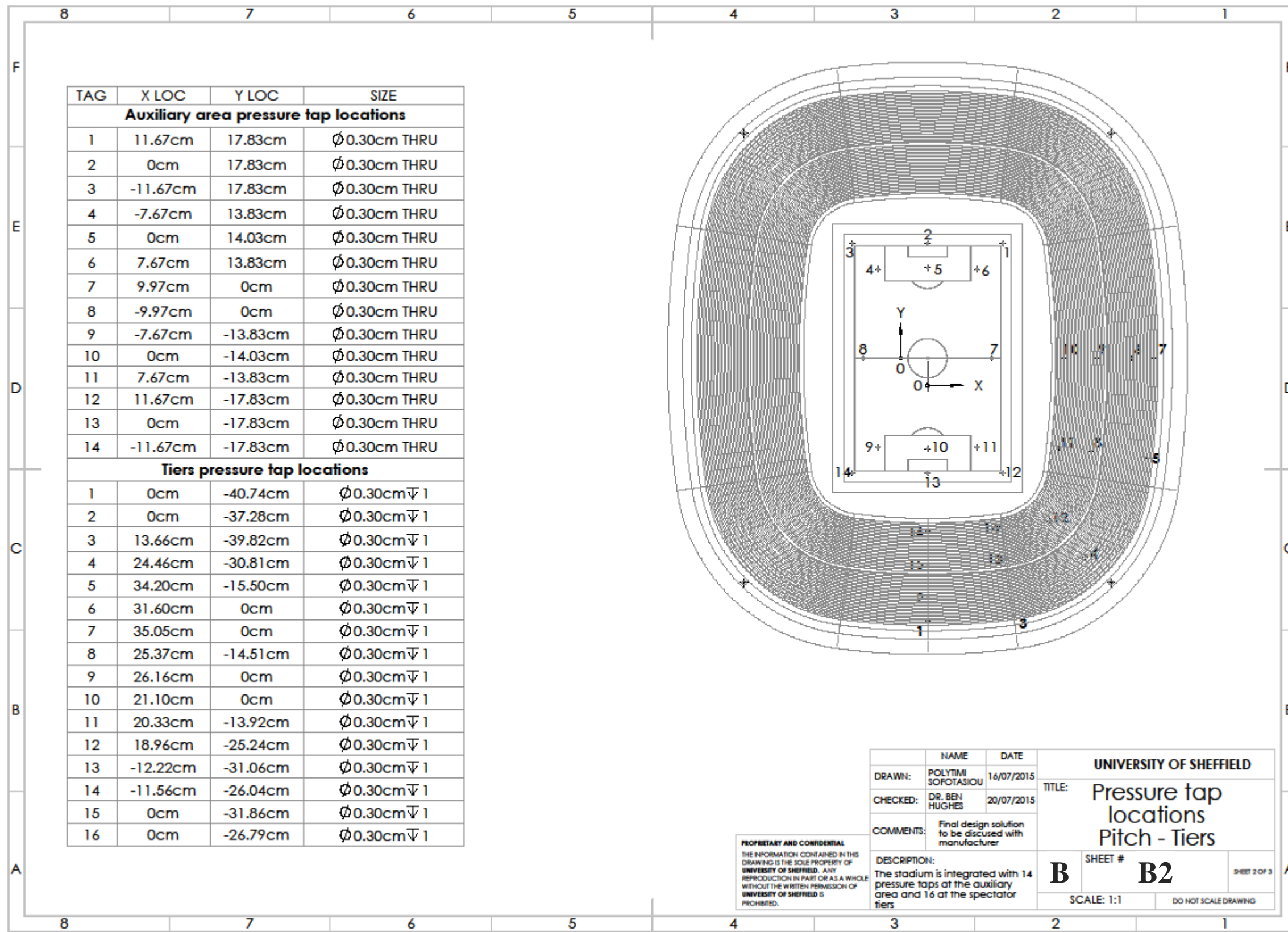
Sheet B-3 illustrates the roof structural component, along with the locations of the pressure taps.



PROPRIETARY AND CONFIDENTIAL
 THE INFORMATION CONTAINED IN THIS
 DRAWING IS THE SOLE PROPERTY OF
 UNIVERSITY OF SHEFFIELD. ANY
 REPRODUCTION IN PART OR AS A WHOLE
 WITHOUT THE WRITTEN PERMISSION OF
 UNIVERSITY OF SHEFFIELD IS
 PROHIBITED.

NAME		DATE	UNIVERSITY OF SHEFFIELD	
DRAWN:	POLYTIMI SOFOTASIOU	16/07/2015	TITLE:	
CHECKED:	DR. BEN HUGHES	01/10/2015	Prototype Stadium Base	
COMMENTS:	Final design solution to be discussed with manufacturer			
DESCRIPTION:	The stadium structure has two spectator terraces on the longitudinal direction of the perimeter			
SHEET #		SHEET 1 OF 3		
B		B1		
SCALE: 1:300		DO NOT SCALE DRAWING		

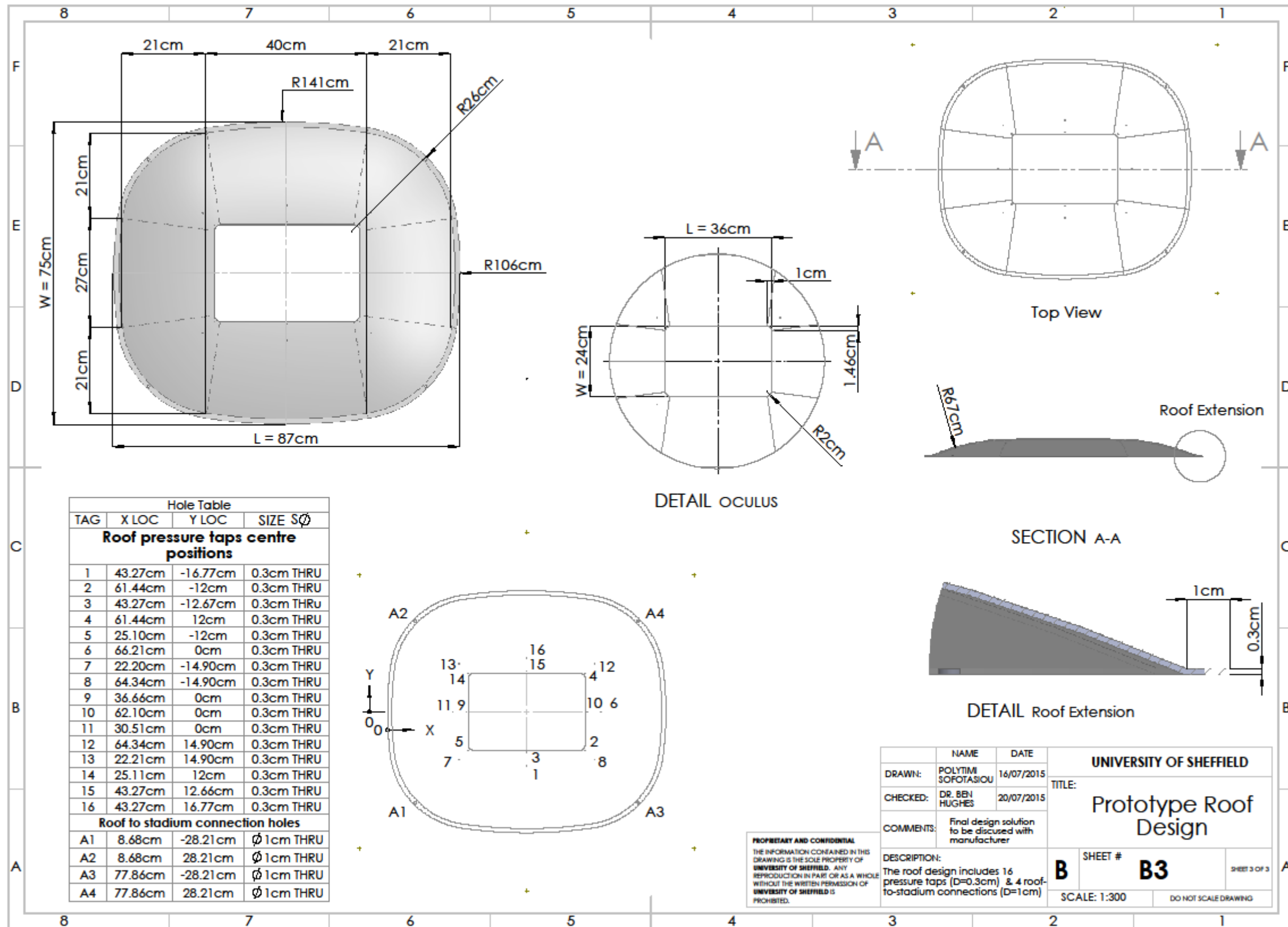
Appendix B



PROPRIETARY AND CONFIDENTIAL
 THE INFORMATION CONTAINED IN THIS DRAWING IS THE SOLE PROPERTY OF UNIVERSITY OF SHEFFIELD. ANY REPRODUCTION IN PART OR AS A WHOLE WITHOUT THE WRITTEN PERMISSION OF UNIVERSITY OF SHEFFIELD IS PROHIBITED.

	NAME	DATE	UNIVERSITY OF SHEFFIELD	
DRAWN:	POLYTIMI SIFOTASIOU	16/07/2015		
CHECKED:	DR. BEN HUGHES	20/07/2015	TITLE: Pressure tap locations Pitch - Tiers	
COMMENTS:	Final design solution to be discussed with manufacturer			SHEET # B2
DESCRIPTION:	The stadium is integrated with 14 pressure taps at the auxiliary area and 16 at the spectator tiers			
			SCALE: 1:1	DO NOT SCALE DRAWING

SHEET 2 OF 3



Appendix B

B.2 Wind Tunnel Results

Thereafter are presented the results of mean pressure coefficients, acquired for the wind speeds of 6 m/s, 10 m/s and 11 m/s. The corresponding values of reference velocity, U_{ref} , measured at roof height were equal to 3.55 m/s, 5.72 m/s and 6.19 m/s. Each figure compares two wind directions (0° and 90°) and two roof configurations (the non-elevated or closed roof and the elevated or open roof).

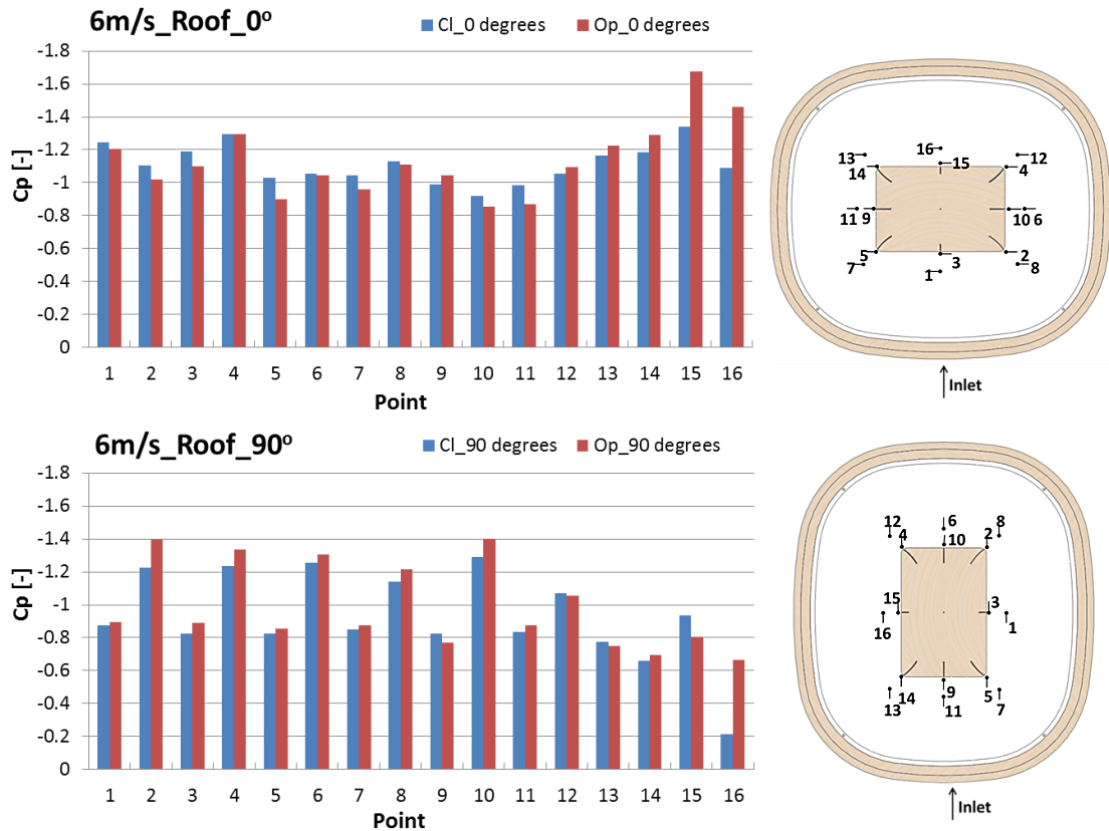


Figure Error! No text of specified style in document.-1 Cp results on the roof surface for the cases of 0° (top) and 90° (bottom) wind angle for the elevated (Op) and the non-elevated (Cl) roof configuration; $U_{ref} = 3.55$ m/s.

Appendix B

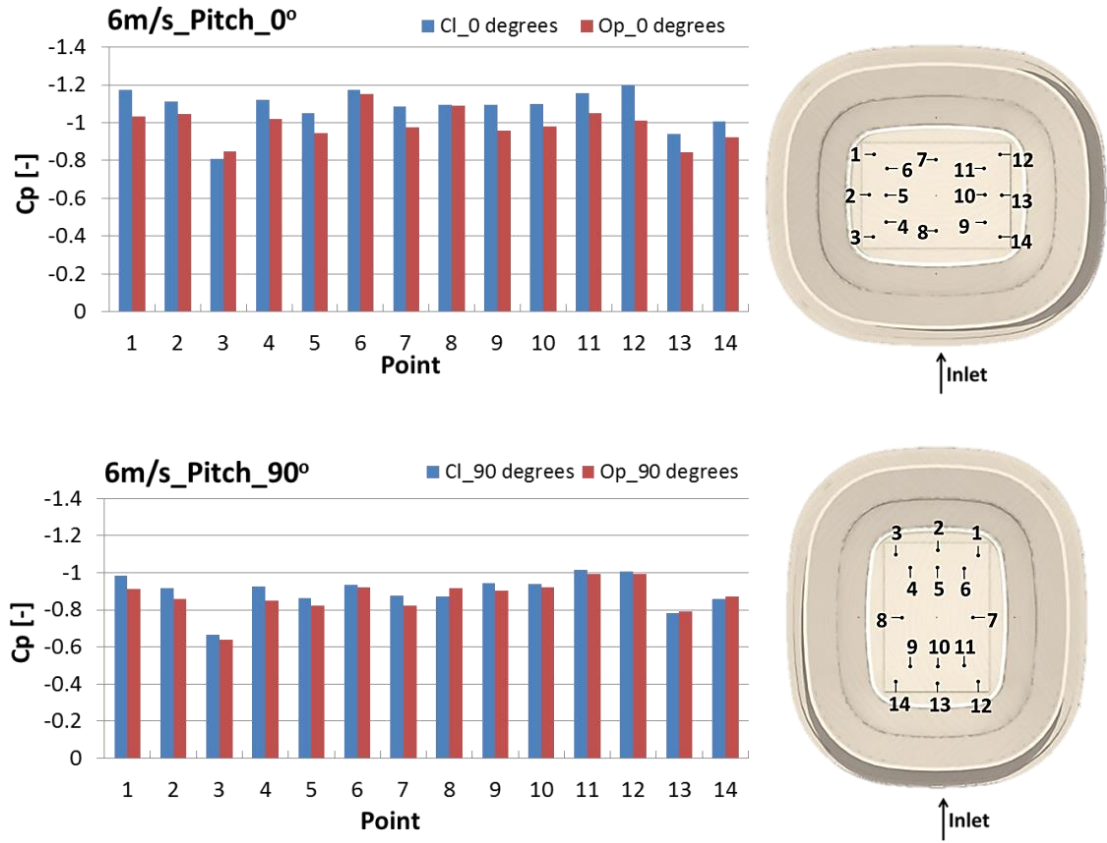


Figure *Error! No text of specified style in document.*-2 C_p results on the pitch surface for the cases of 0° (top) and 90° (bottom) wind angle for the elevated (Op) and the non-elevated (Cl) roof configuration; $U_{ref} = 3.55$ m/s.

Appendix B

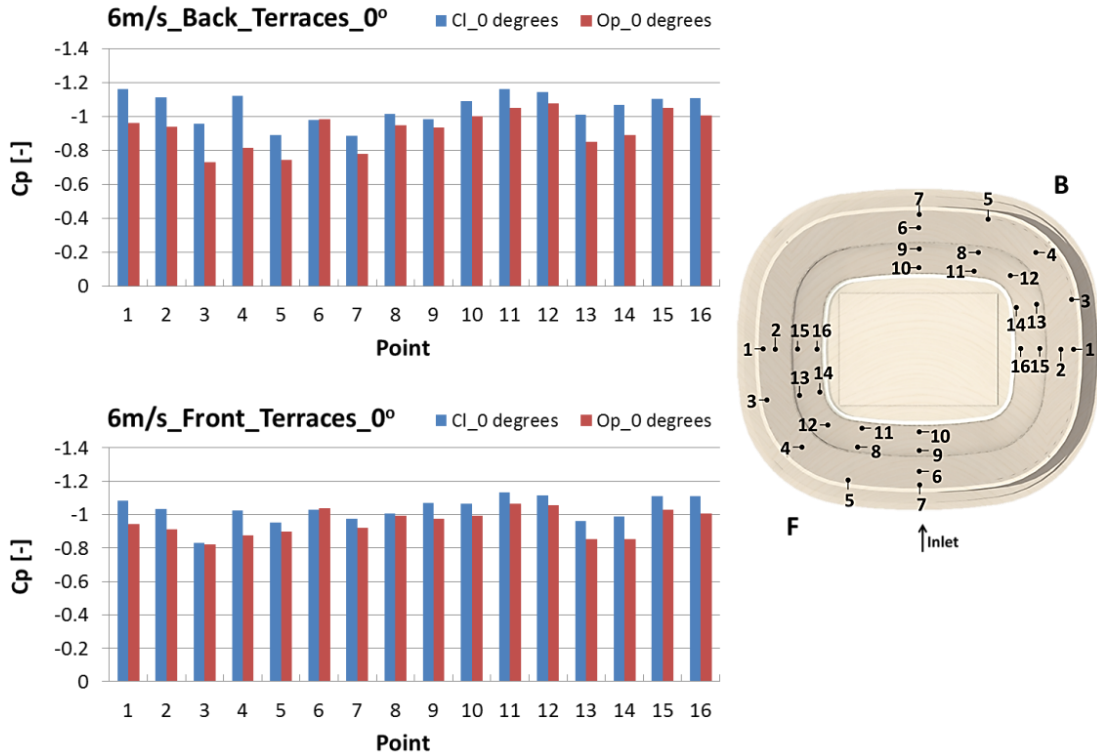


Figure Error! No text of specified style in document.-3 Cp results on the terraces' surface for the case of 0° wind direction for the elevated (Op) and the non-elevated (Cl) roof configuration; $U_{ref} = 3.55$ m/s.

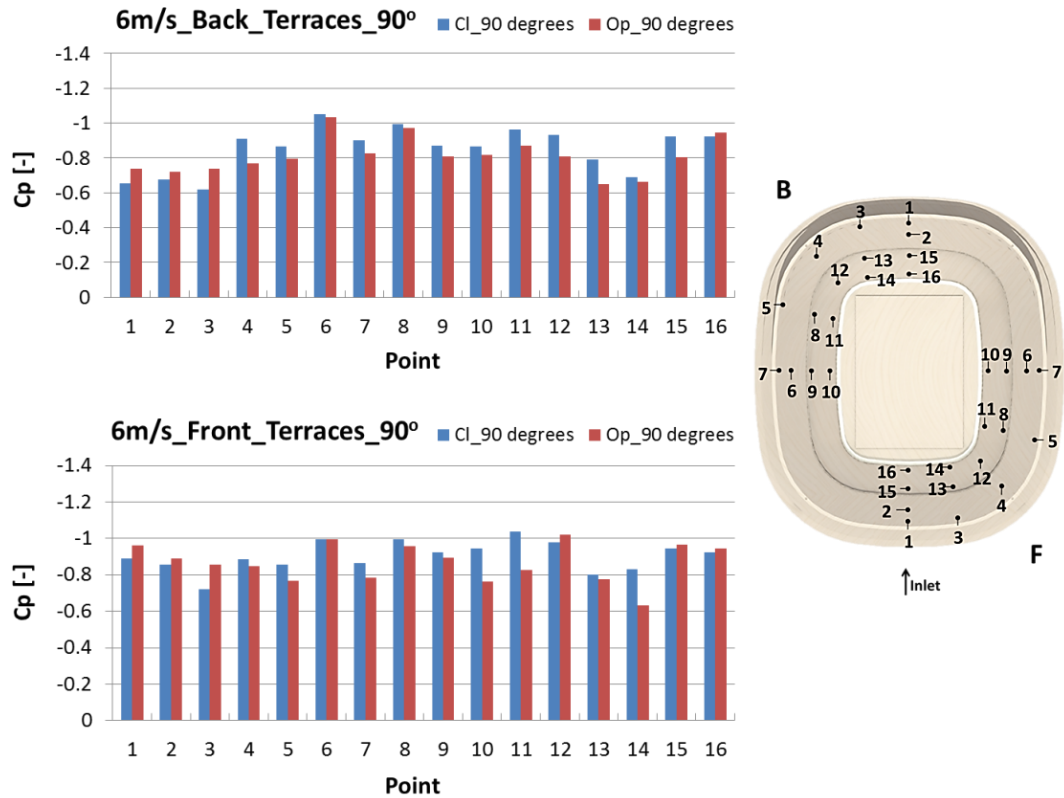


Figure Error! No text of specified style in document.-4 Cp results on the terraces' surface for the case of 90° wind direction for the elevated (Op) and the non-elevated (Cl) roof configuration; $U_{ref} = 3.55$ m/s.

Appendix B

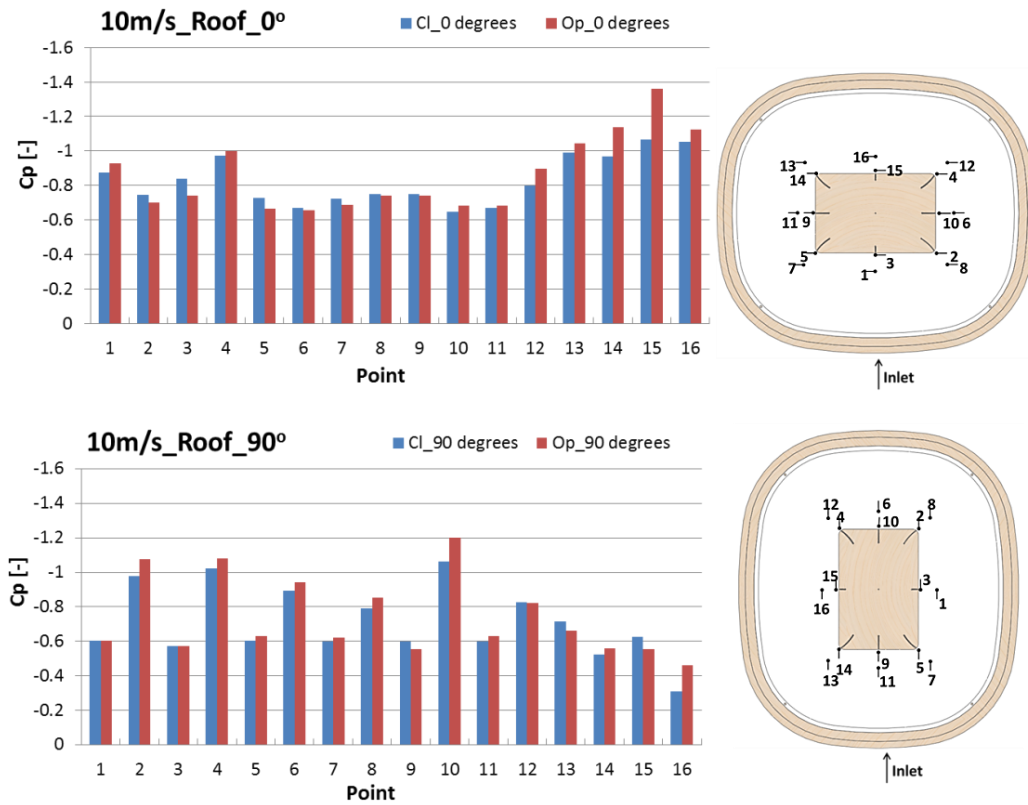


Figure **Error! No text of specified style in document.** -5 Cp results on the roof surface for the cases of 0° (top) and 90° (bottom) wind direction for the elevated (Op) and the non-elevated (Cl) roof configuration; $U_{ref} = 5.72$ m/s.

Appendix B

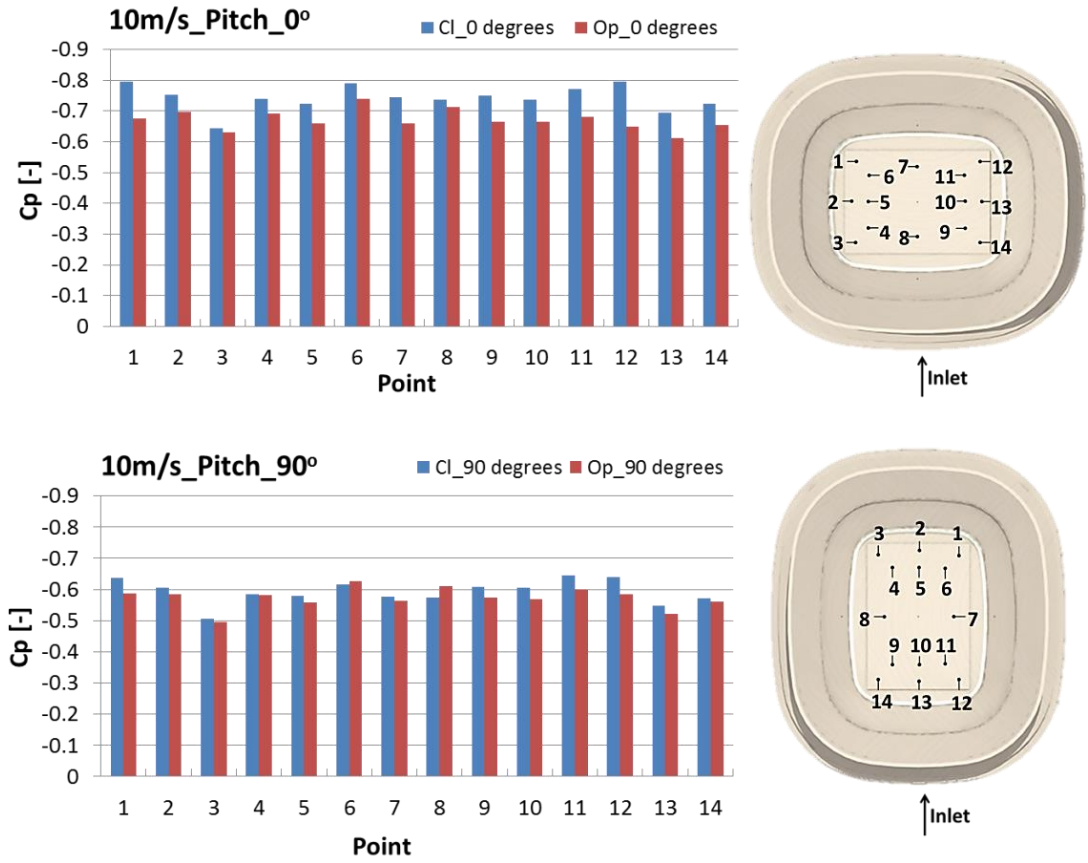


Figure Error! No text of specified style in document.-6 Cp results on the pitch surface for the cases of 0° (top) and 90° (bottom) wind direction for the elevated (Op) and the non-elevated (Cl) roof configuration; $U_{ref} = 5.72$ m/s.

Appendix B

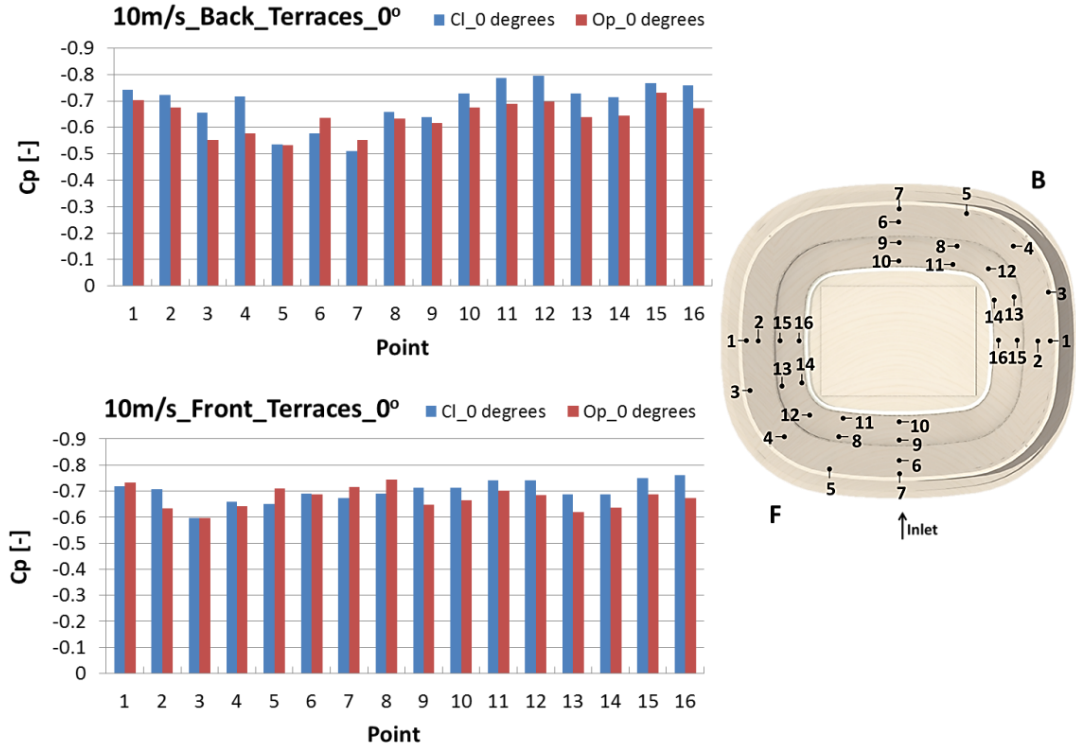


Figure Error! No text of specified style in document.-7 Cp results on the terraces' surface for the case of 0° wind direction for the elevated (Op) and the non-elevated (Cl) roof configuration; $U_{ref} = 5.72$ m/s.

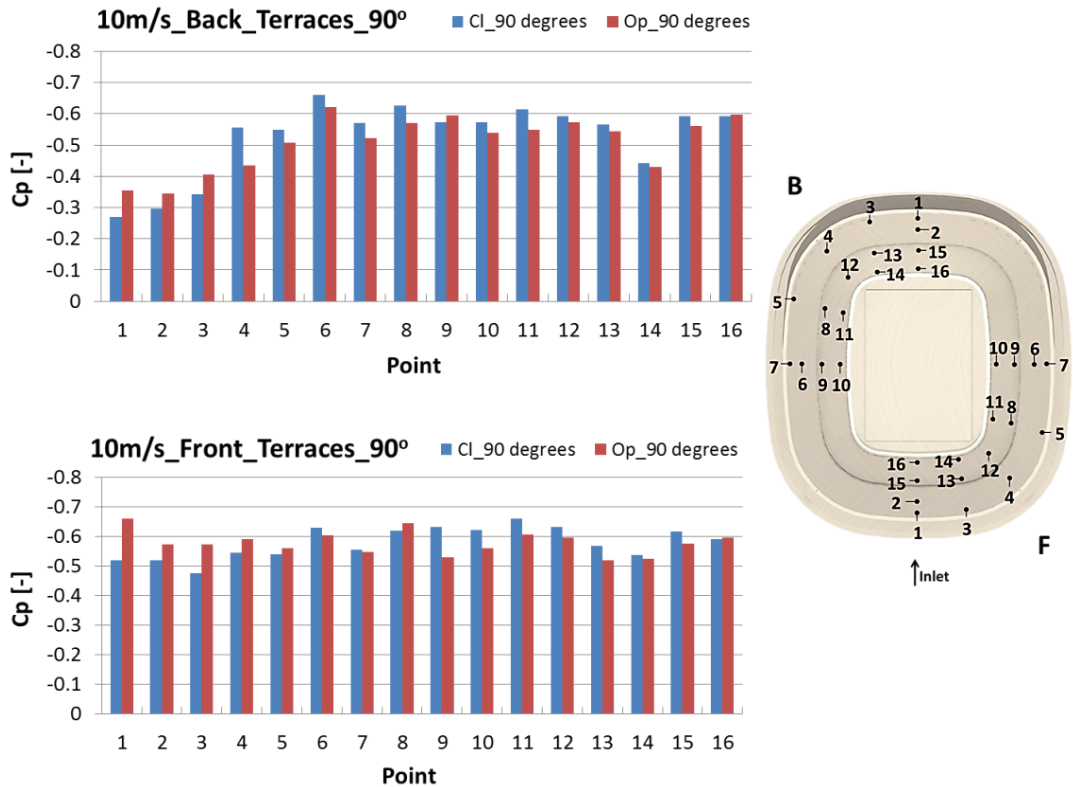


Figure Error! No text of specified style in document.-8 Cp results on the terraces' surface for the case of 90° wind direction for the elevated (Op) and the non-elevated (Cl) roof configuration; $U_{ref} = 5.72$ m/s.

Appendix B

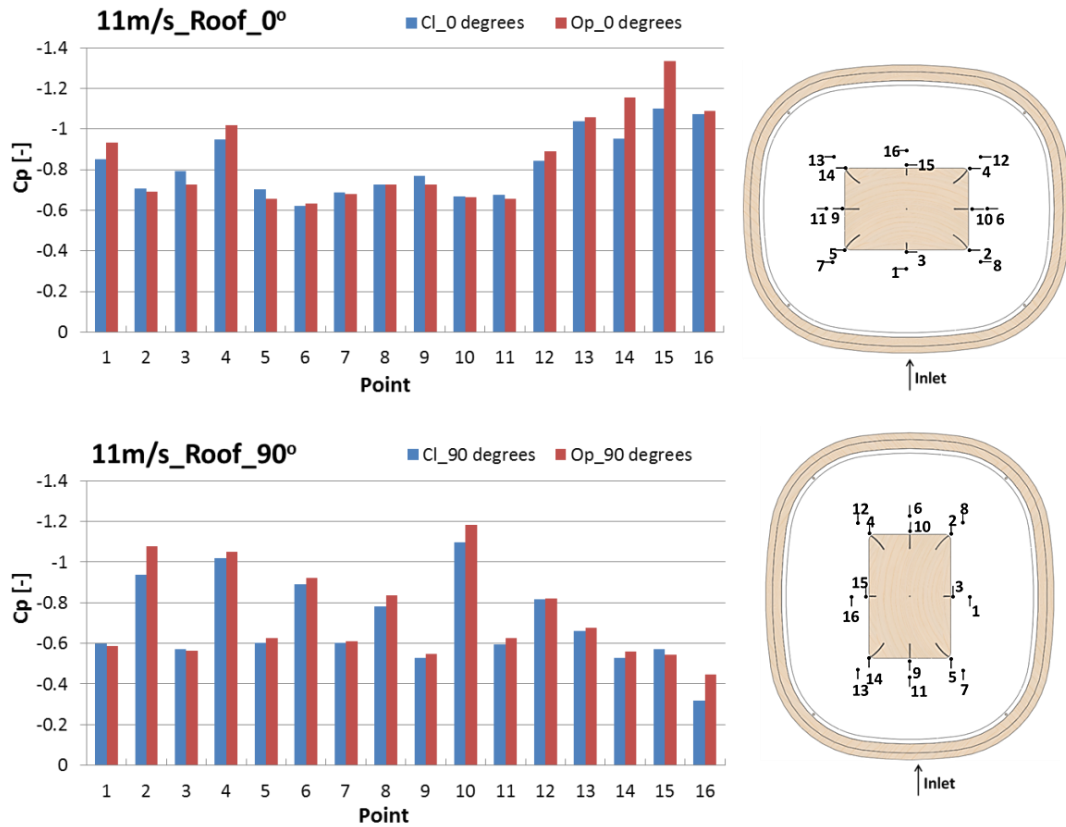


Figure Error! No text of specified style in document.-9 Cp results on the roof surface for the cases of 0° (top) and 90° (bottom) wind direction for the elevated (Op) and the non-elevated (Cl) roof configuration; $U_{ref} = 6.19$ m/s.

Appendix B

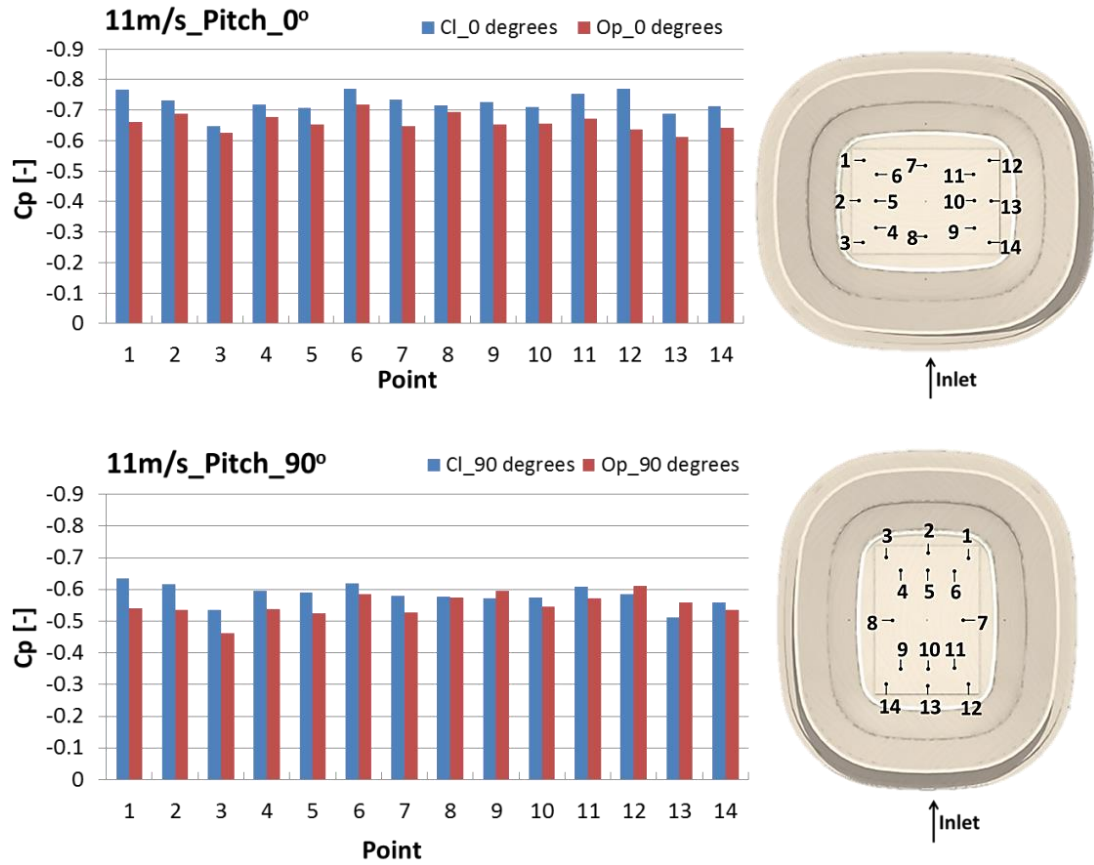


Figure Error! No text of specified style in document. -10 Cp results on the pitch surface for the cases of 0° (top) and 90° (bottom) wind direction for the elevated (Op) and the non-elevated (Cl) roof configuration; $U_{ref} = 6.19$ m/s.

Appendix B

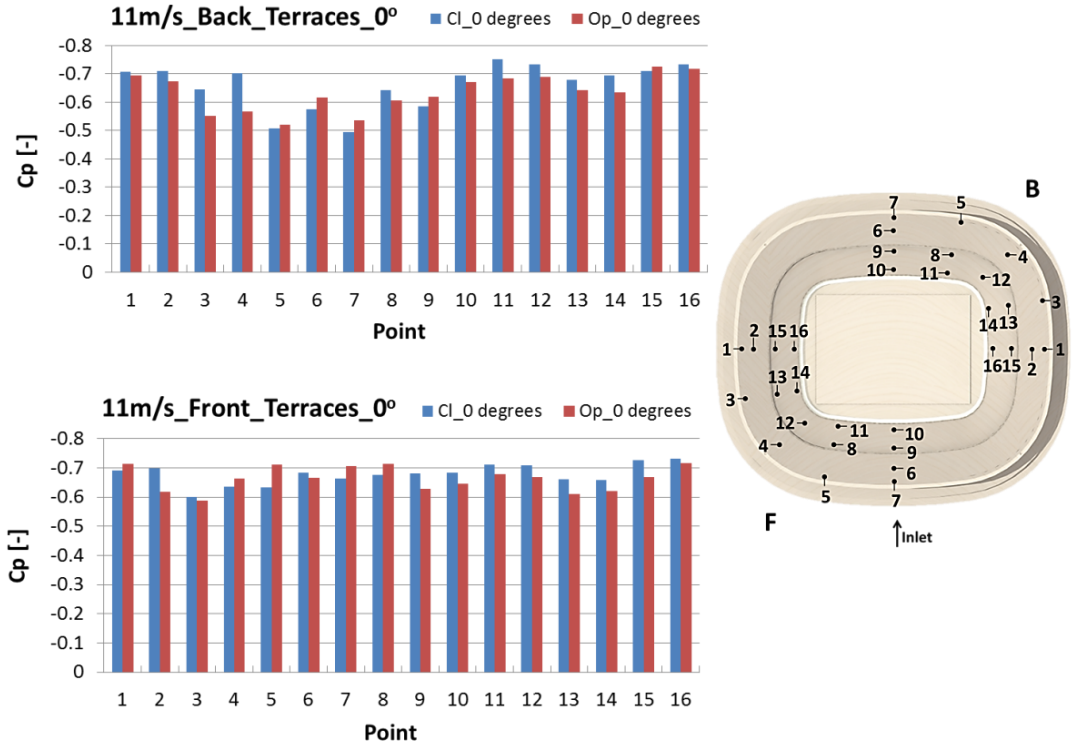


Figure Error! No text of specified style in document.-11 Cp results on the terraces' surface for the case of 0° wind direction for the elevated (Op) and the non-elevated (Cl) roof configuration; $U_{ref} = 6.19$ m/s.

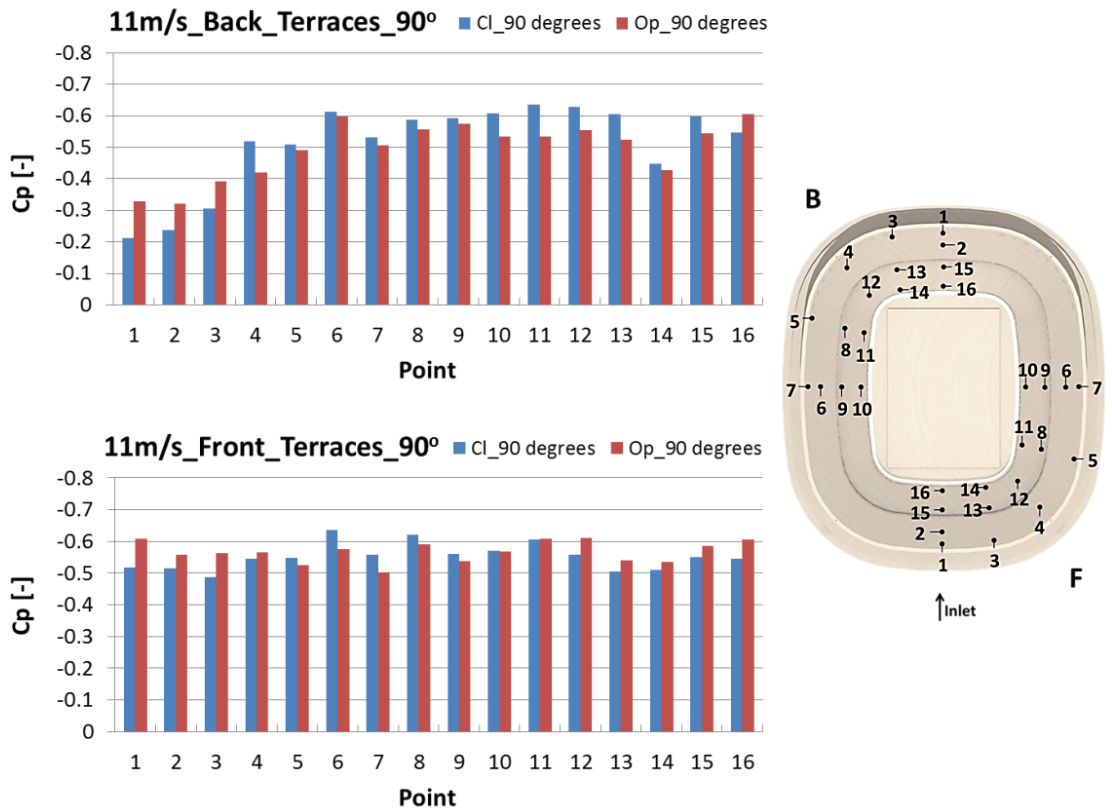


Figure Error! No text of specified style in document.-12 Cp results on the terraces' surface for the case 90° wind direction for the elevated (Op) and the non-elevated (Cl) roof configuration; $U_{ref} = 6.19$ m/s.

Appendix B

Appendix C

C.1 Element Shapes

Figure C-1 illustrates the different element shapes that can be used in ANSYS Mesh to perform space discretisation. There are two types for the two-dimensional geometries and five for the three-dimensional geometries.

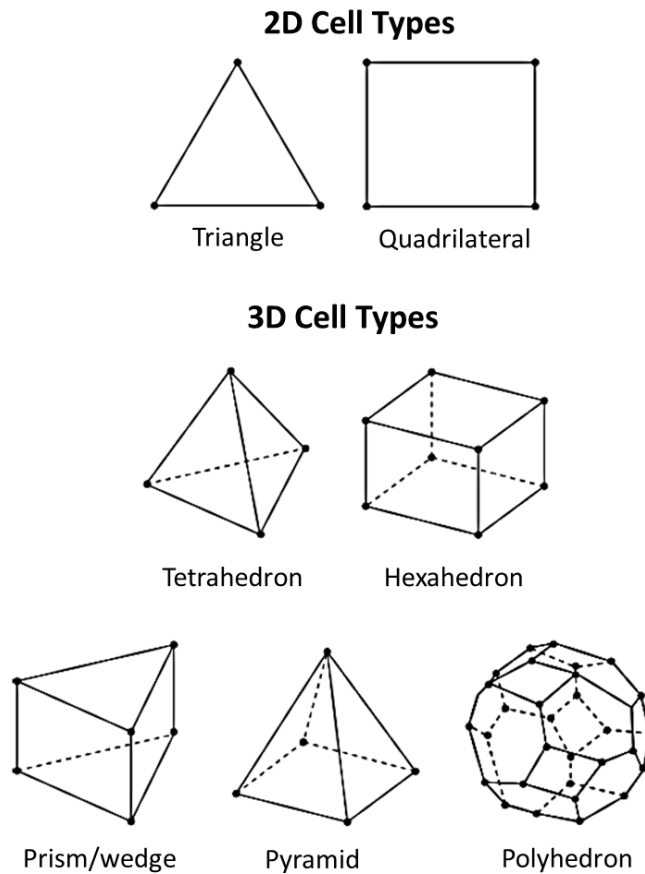
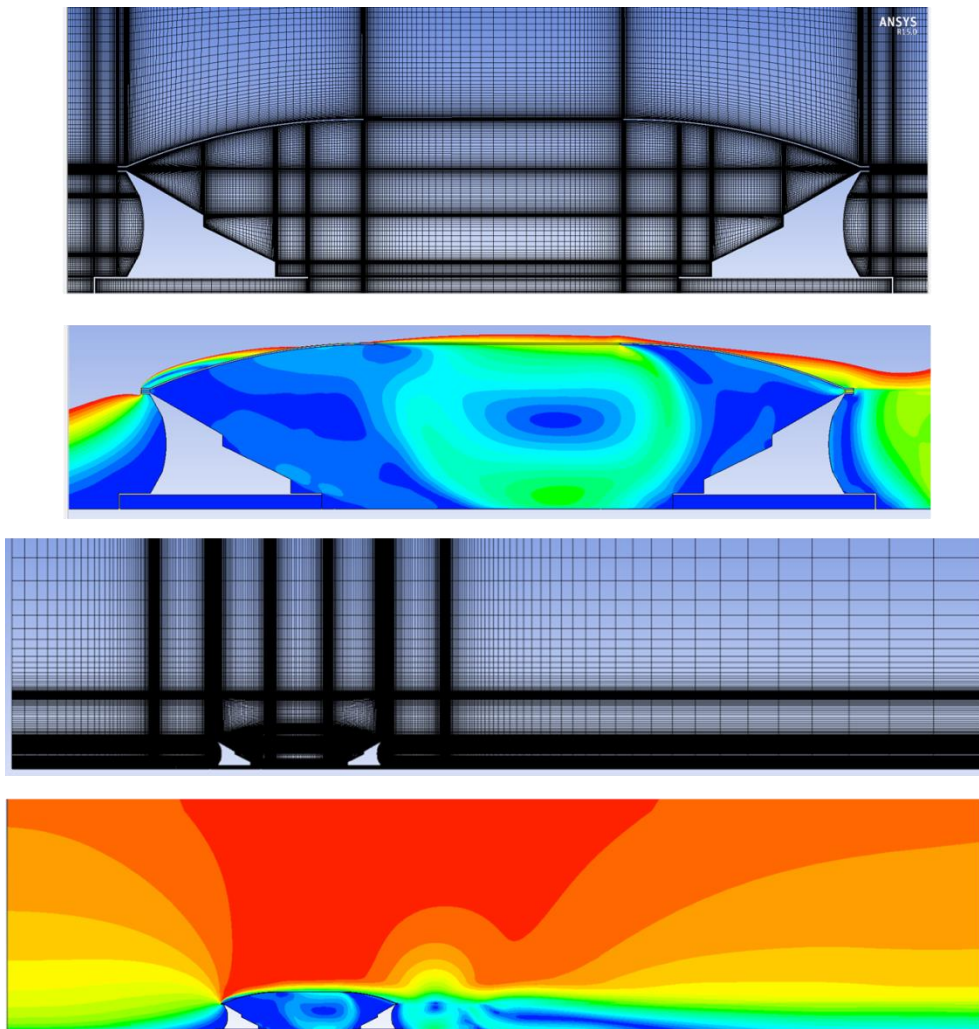


Figure **Error! No text of specified style in document.-1** Cell types used in ANSYS for 2D and 3D geometries (ANSYS, Inc., 2011).

C.2 Conformal Hexahedral Mesh

Figure **Error! No text of specified style in document.**-2 illustrates an initial attempt to generate a fully structural hexahedral mesh was performed for a two-dimensional stadium structure. The geometry was designed in full scale and the constructed mesh was based on the creation of sweepable bodies using the slice tool. However, the multi-dimensional characteristics of the model couldn't satisfy the maximum cell aspect ratio of 2:1. The discrepancies are obvious on the areas of flow recirculation on the leeward side of the stadium model. The high aspect ratio cannot generate accurately results of the turbulent motion in the high flow heterogeneous regions, and thus different mesh types, hybrid or tetrahedral, should be considered for similar geometries.



*Figure **Error! No text of specified style in document.**-2 Computational grid and velocity contours on a 2D stadium model.*

Appendix D

Thereafter are presented some complementary figures of the generated CFD results on the airflow distribution at the stadium interior for the four case studies.

Appendix D

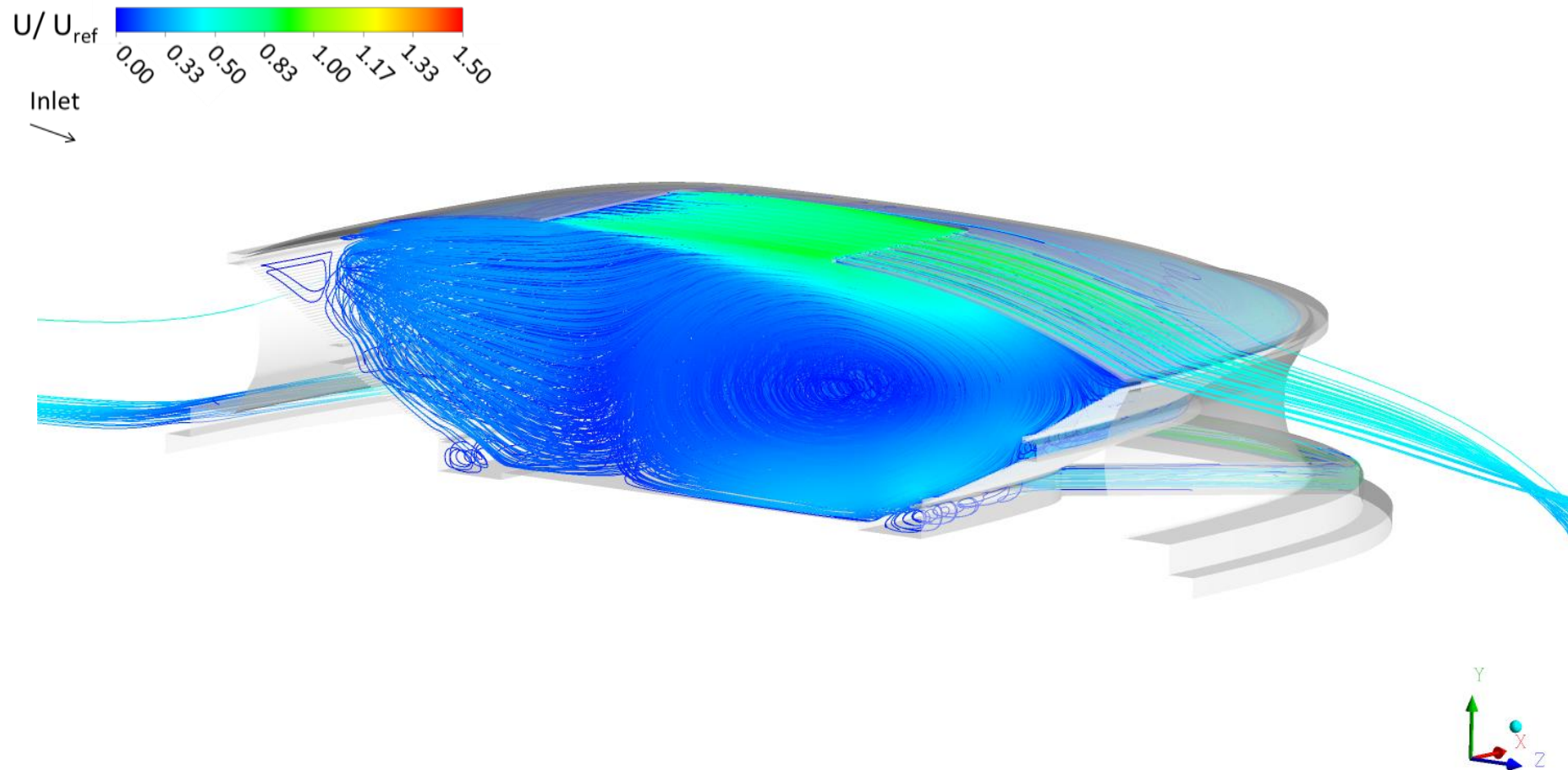


Figure **Error! No text of specified style in document.**-1 Streamlines generated for the stadium case of 0° wind angle and non-elevated roof configuration; $U_{ref} = 5.23$ m/s.

Appendix D

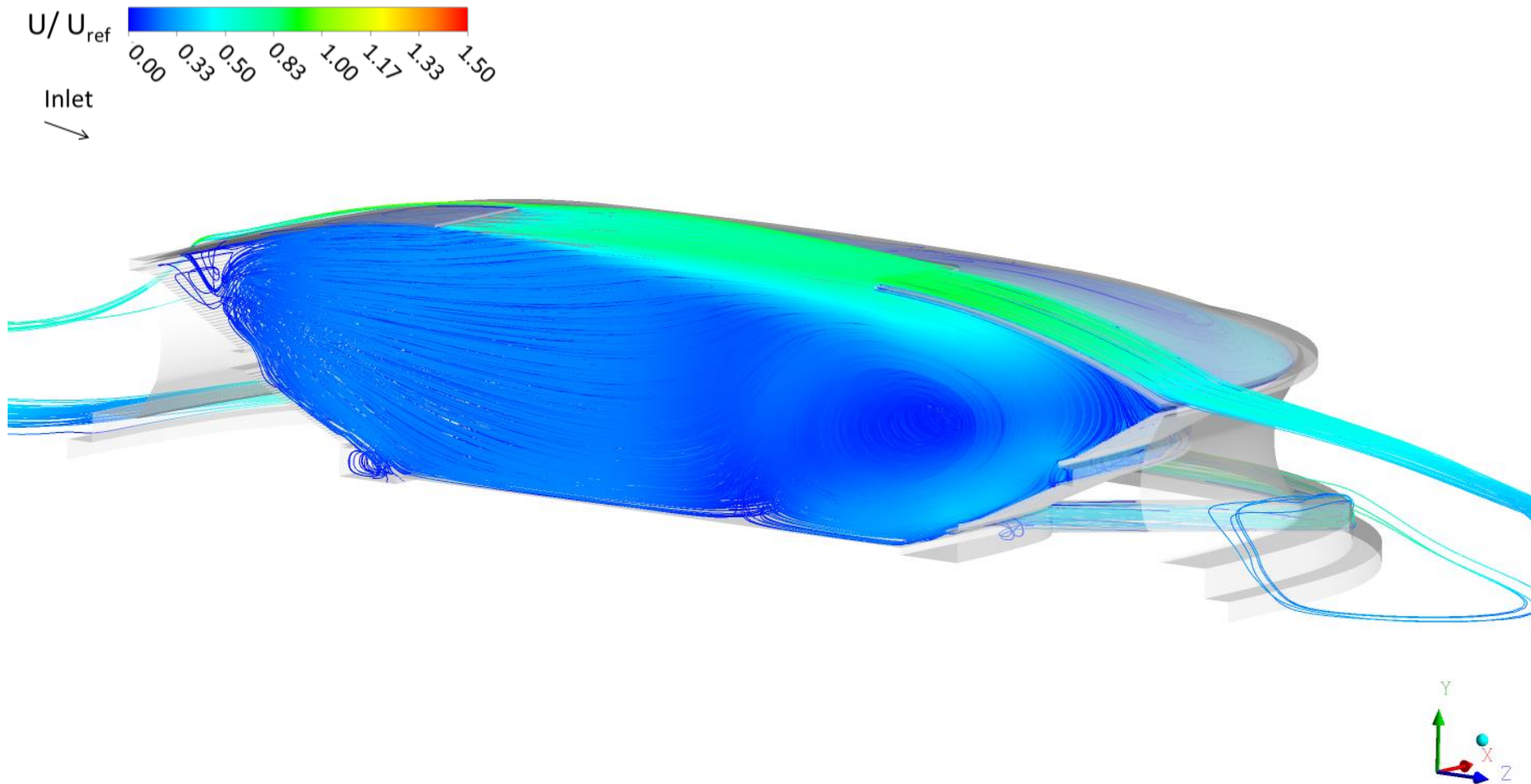


Figure **Error! No text of specified style in document.**-2 Streamlines generated for the stadium case of 90° wind angle and non-elevated roof configuration; $U_{ref} = 5.23$ m/s.

Appendix D

Appendix D

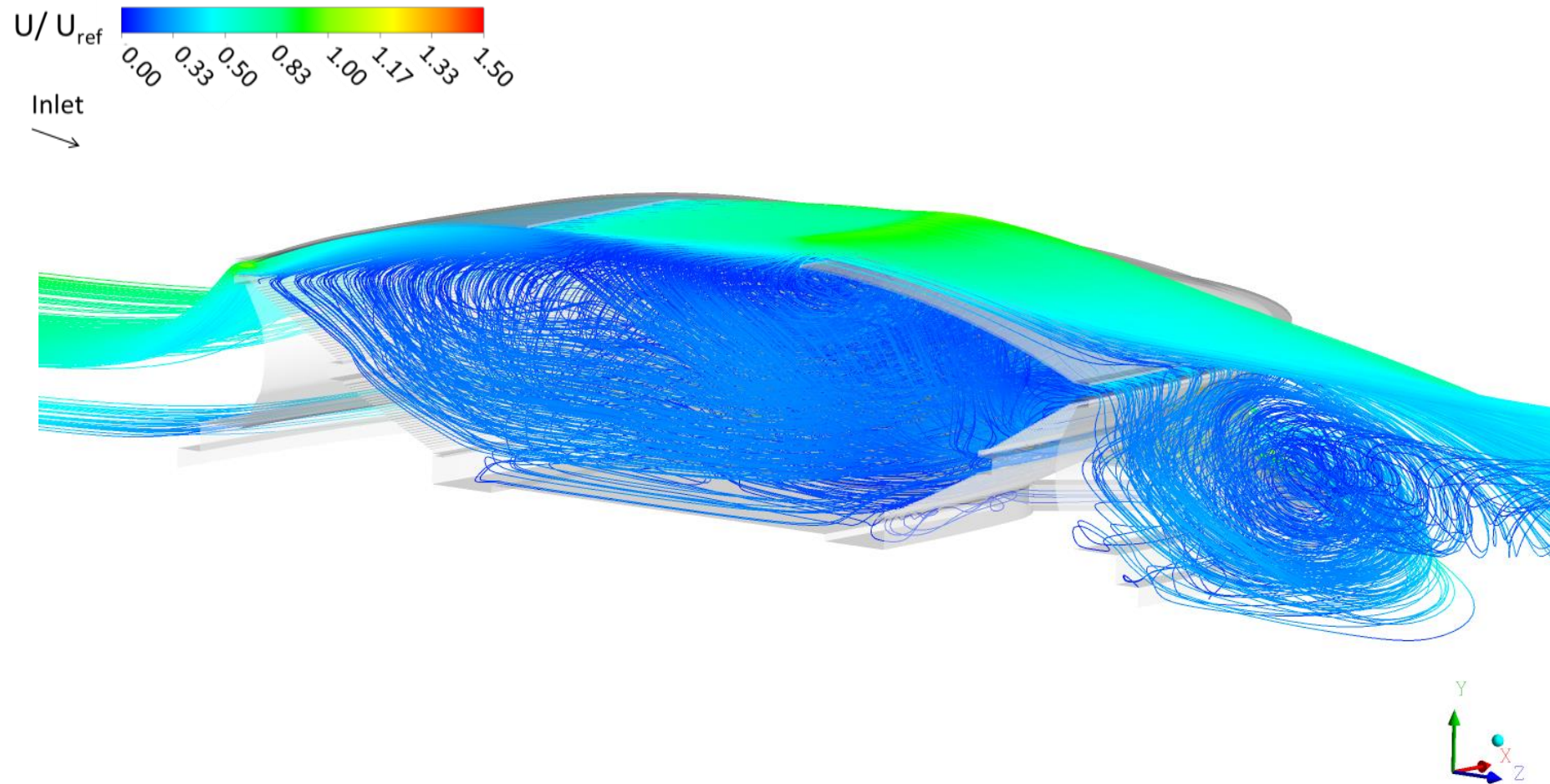


Figure **Error! No text of specified style in document.**-3 Streamlines generated for the stadium case of 0° wind angle and elevated roof configuration;
 $U_{ref} = 5.23$ m/s.

Appendix D

Appendix D

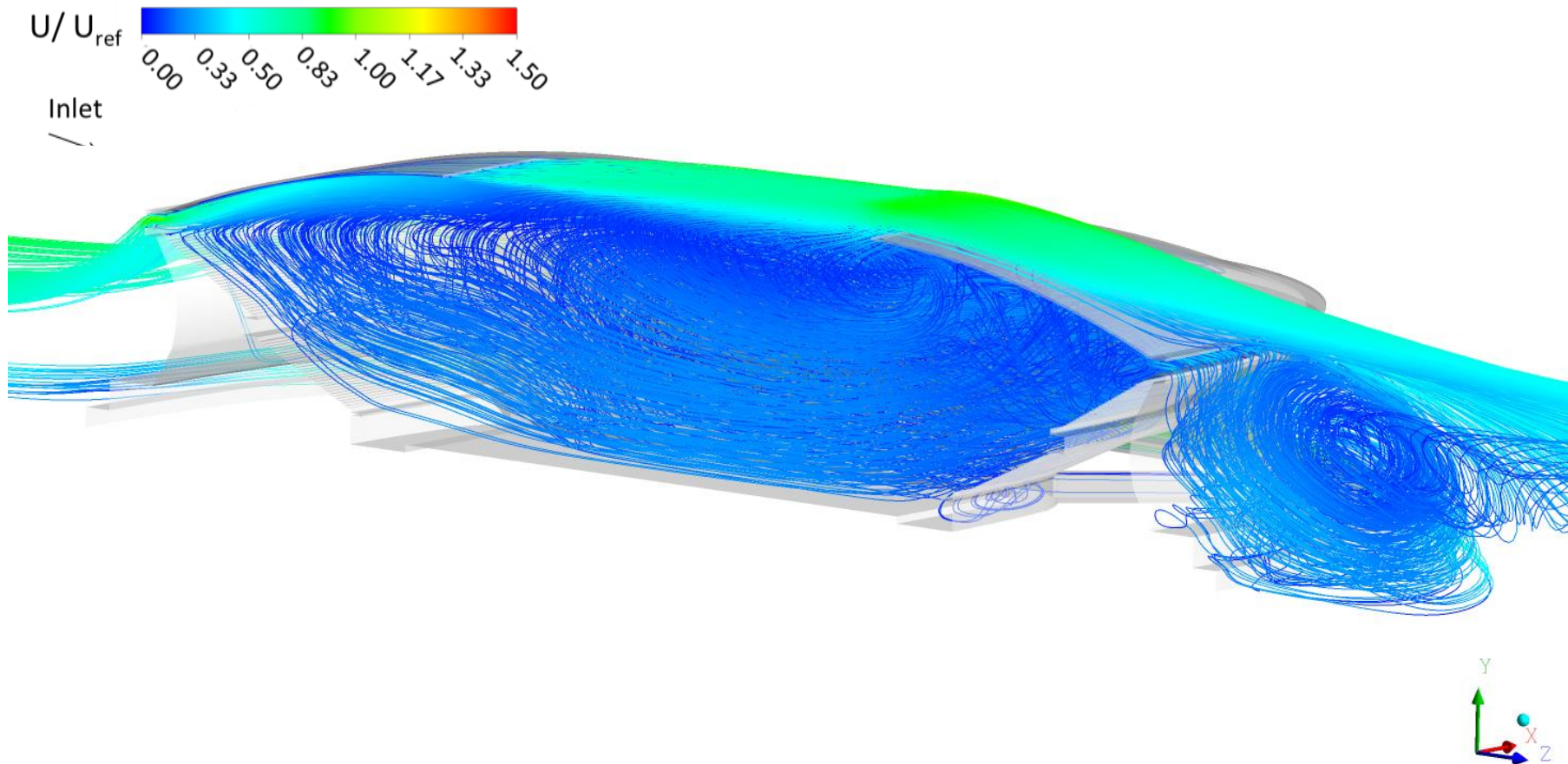


Figure Error! No text of specified style in document.-4 Streamlines generated for the stadium case of 90° wind angle and elevated roof configuration; $U_{ref} = 5.23$ m/s.

Appendix E

Thereafter are presented the CFD-generated results per design point, as part of the Response Surface Methodology. The method included the generation of the design points' output variables that formed the response surfaces for the identification of the most favourable roof configuration to optimise the stadium internal wind environment. The following figures aim to give an insight into the local pressure coefficients' distribution on the stadium surfaces (roof and envelope), the terraces and the auxiliary area. Additional results of the dimensionless velocity streamlines are also presented.

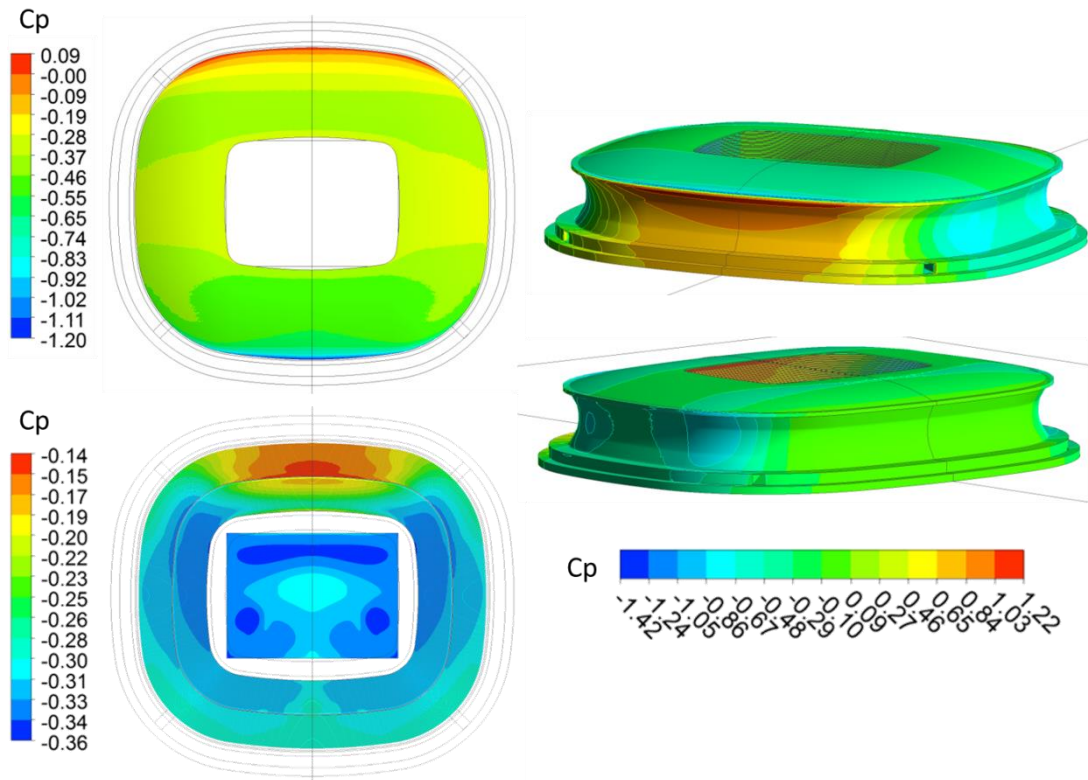


Figure Error! No text of specified style in document.-1 Local C_p values on the exterior and interior stadium surfaces for the DP 1.

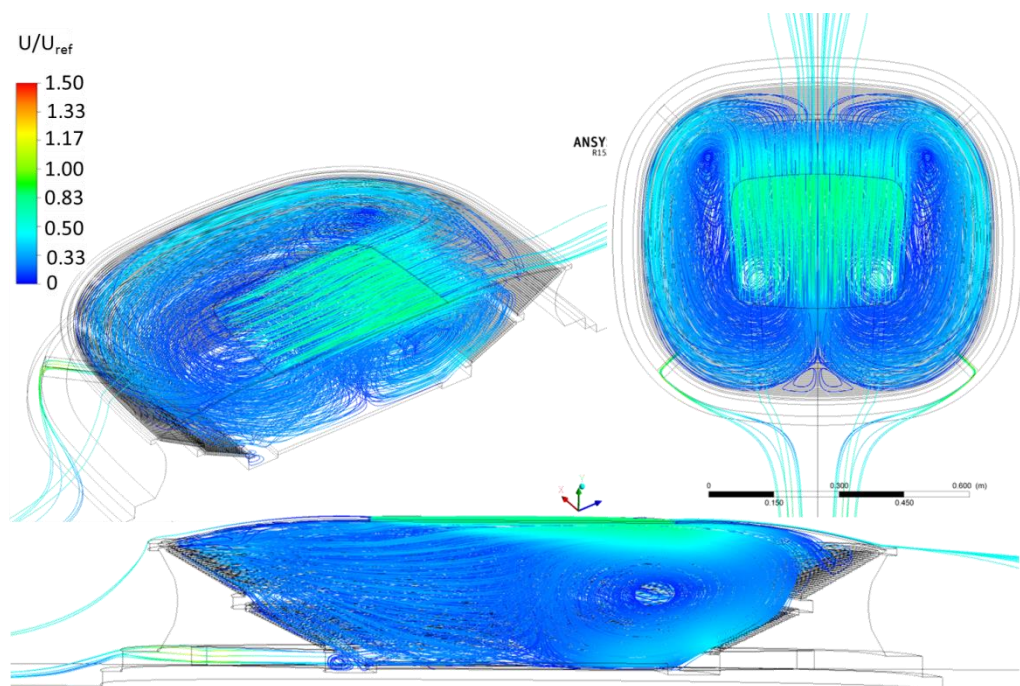


Figure Error! No text of specified style in document.-2 Dimensionless velocity streamlines for the DP 1; $U_{ref} = 5.23$ m/s.

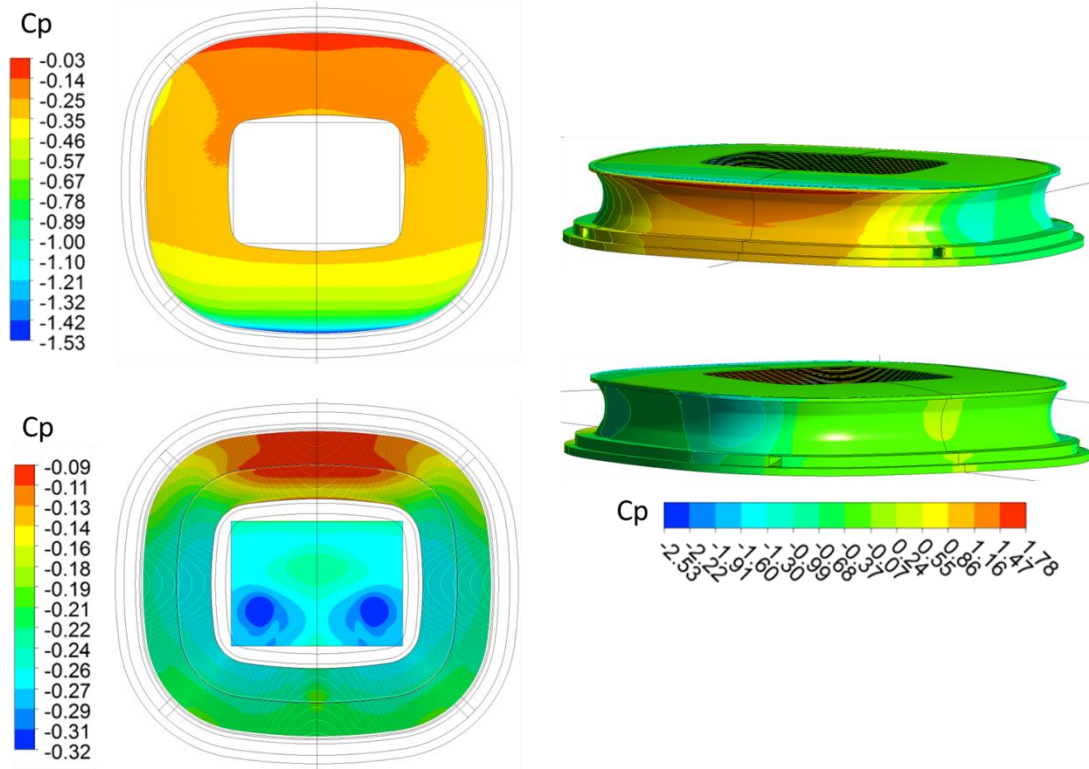


Figure Error! No text of specified style in document.-3 Local C_p values on the exterior and interior stadium surfaces for the DP 2.

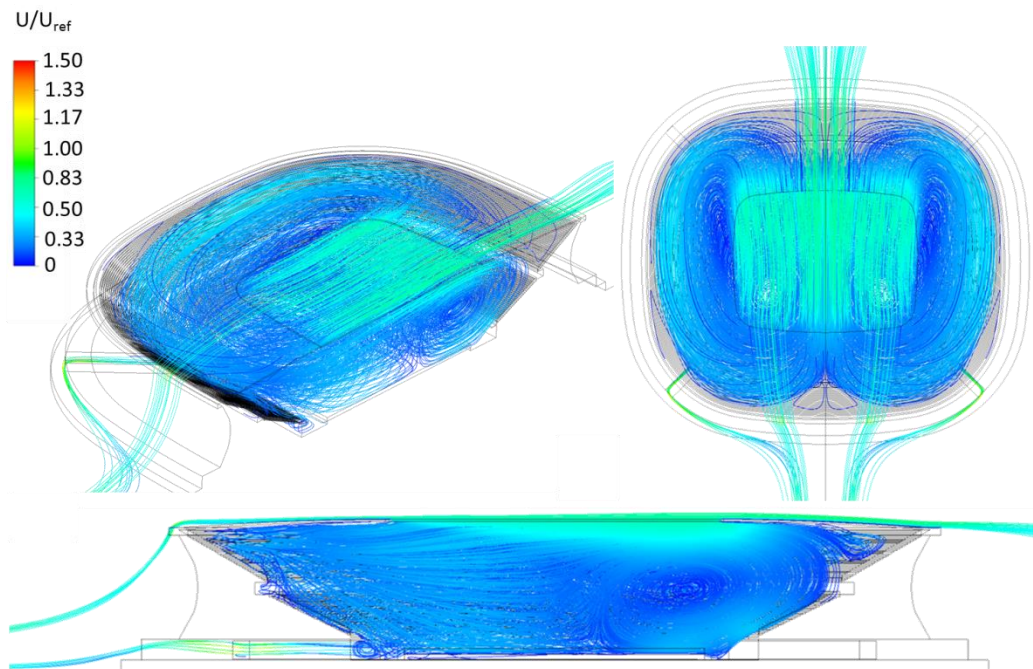


Figure Error! No text of specified style in document.-4 Dimensionless velocity streamlines for the DP 2; $U_{ref} = 5.23$ m/s.

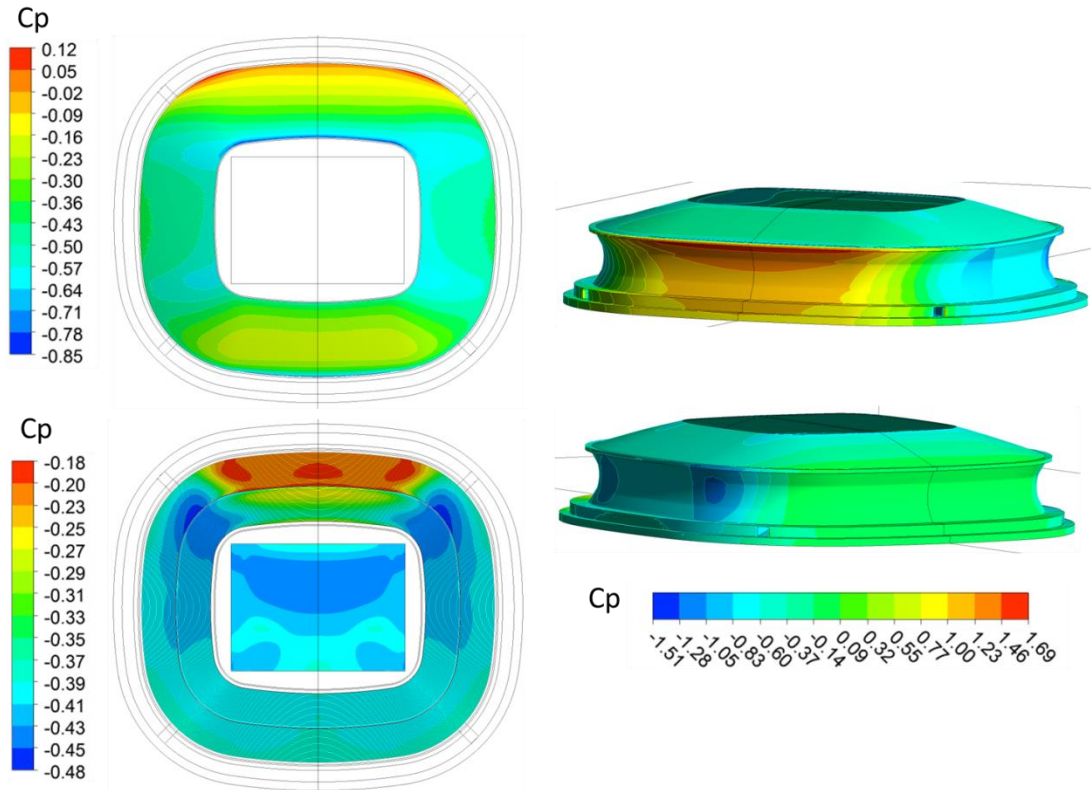


Figure Error! No text of specified style in document.-5 Local C_p values on the exterior and interior stadium surfaces for the DP 3.

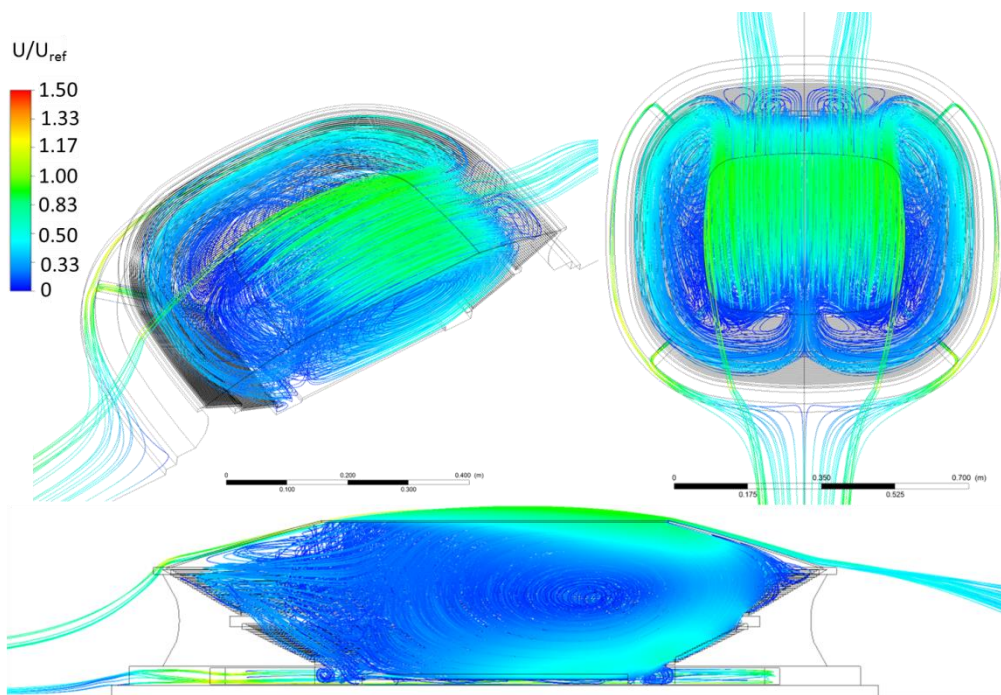


Figure Error! No text of specified style in document.-6 Dimensionless velocity streamlines for the DP 3; $U_{ref} = 5.23$ m/s.

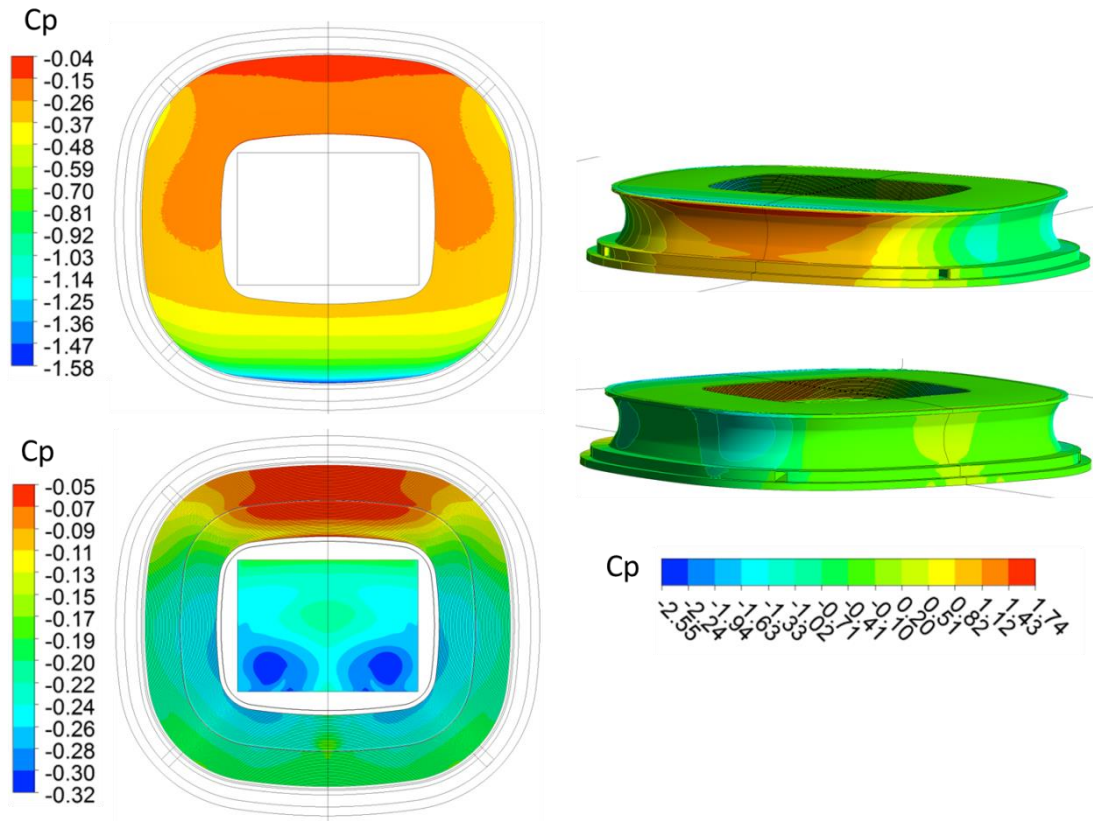


Figure Error! No text of specified style in document.-7 Local C_p values on the exterior and interior stadium surfaces for the DP 4.

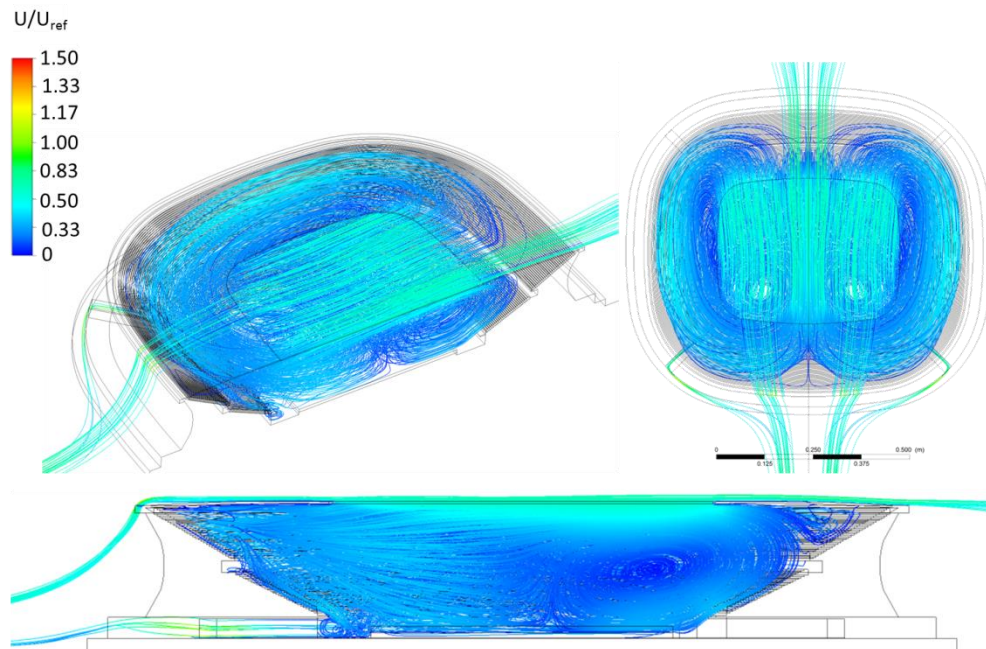


Figure Error! No text of specified style in document.-8 Dimensionless velocity streamlines for the DP 4; $U_{ref} = 5.23$ m/s.

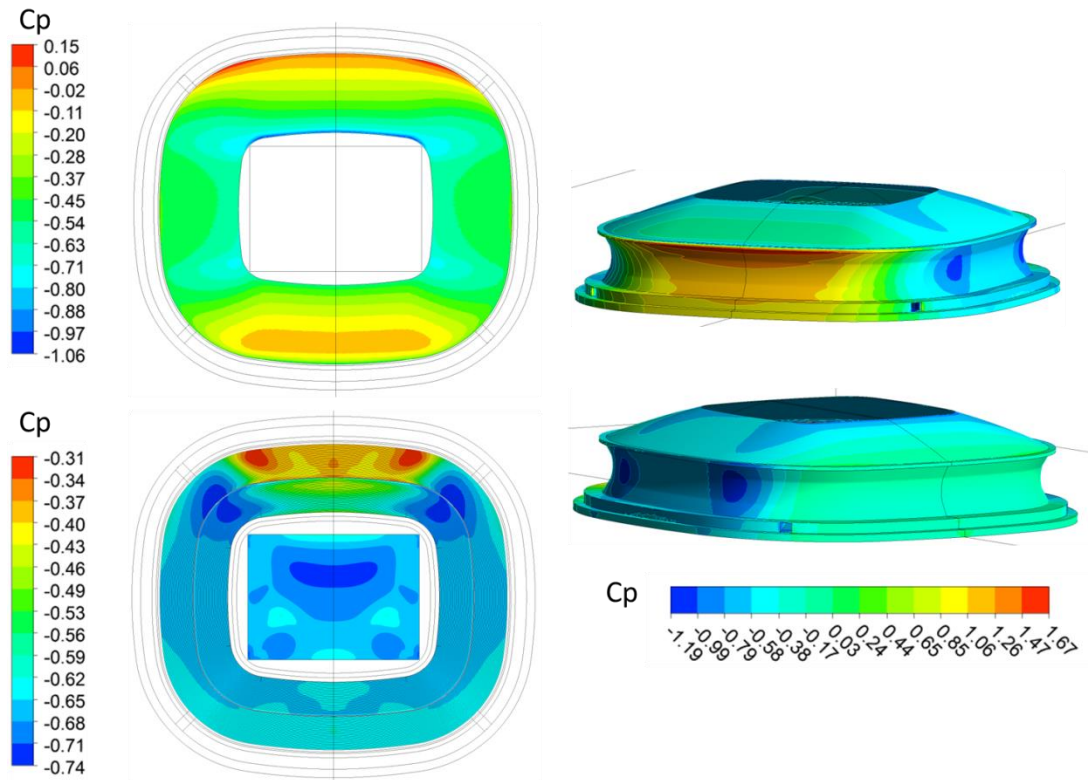


Figure Error! No text of specified style in document.-9 Local C_p values on the exterior and interior stadium surfaces for the DP 5.

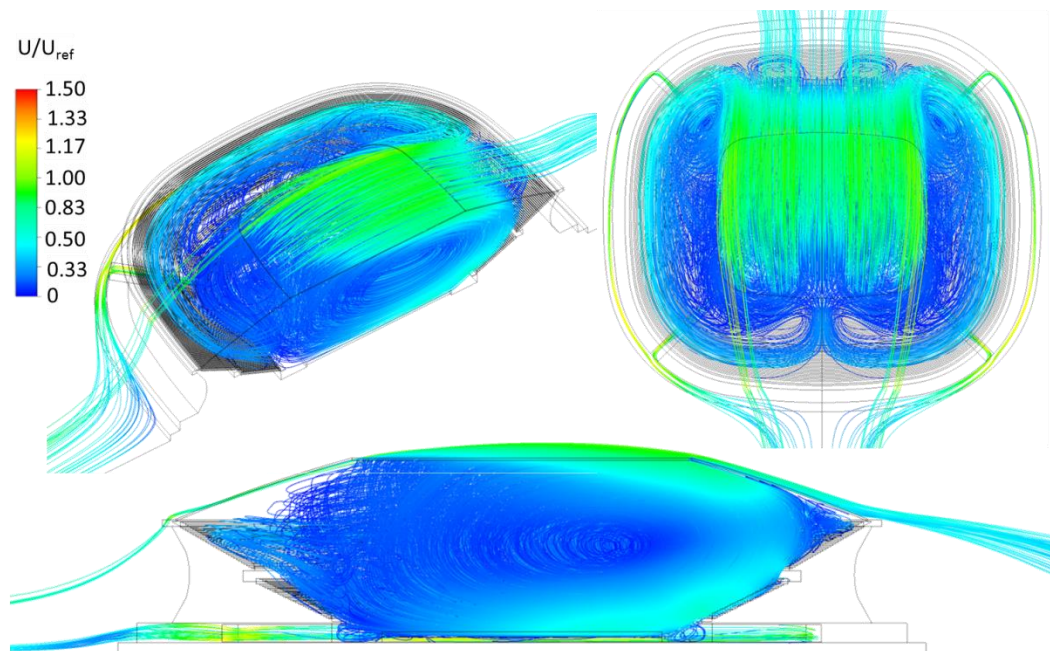


Figure Error! No text of specified style in document.-10 Dimensionless velocity streamlines for the DP 5; $U_{ref} = 5.23$ m/s.

Appendix E

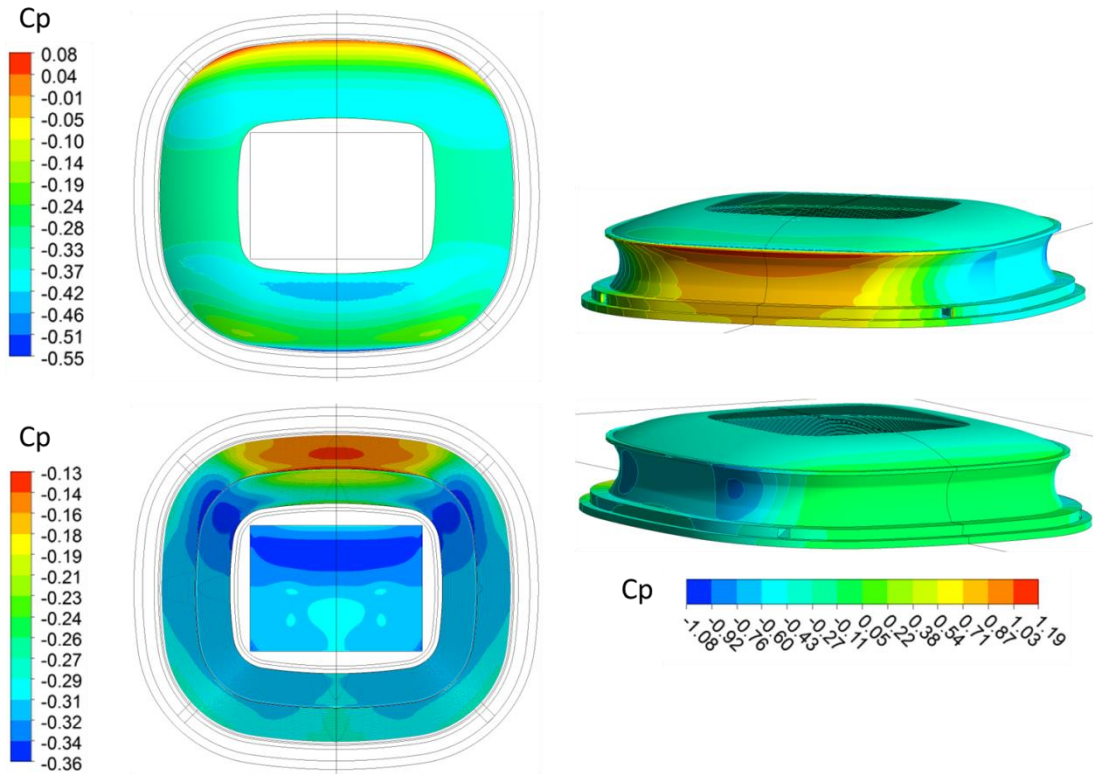


Figure Error! No text of specified style in document.-11 Local C_p values on the exterior and interior stadium surfaces for the DP 6.

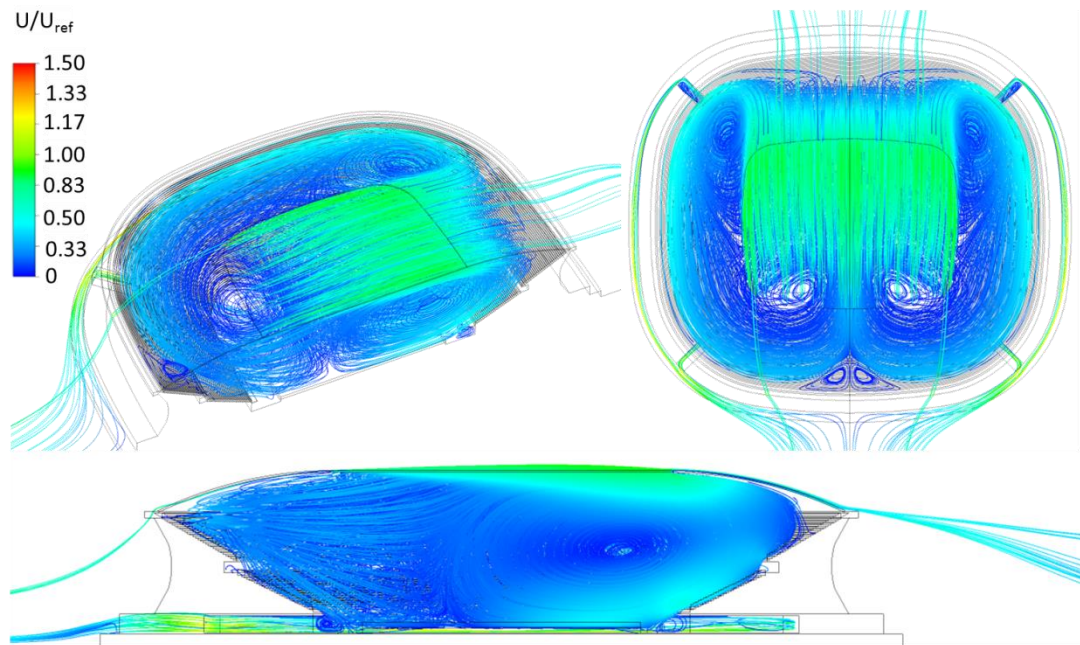


Figure Error! No text of specified style in document.-12 Dimensionless velocity streamlines for the DP 6; $U_{ref} = 5.23$ m/s.

Appendix E

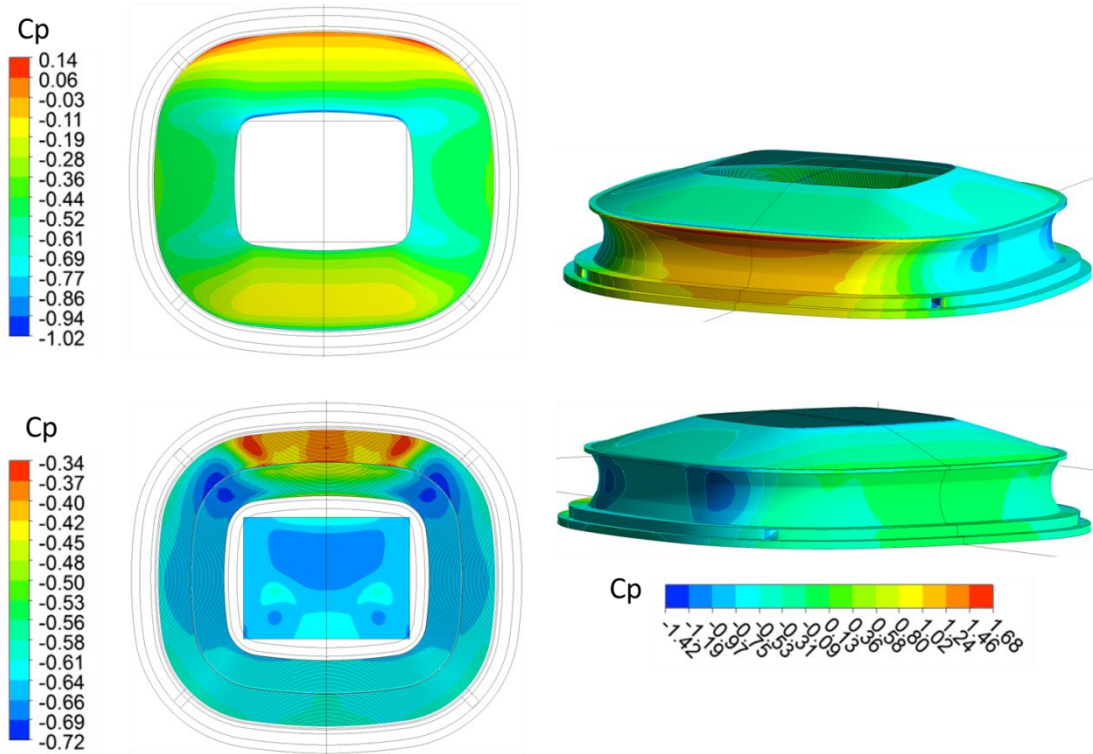


Figure Error! No text of specified style in document.-13 Local C_p values on the exterior and interior stadium surfaces for the DP 7.

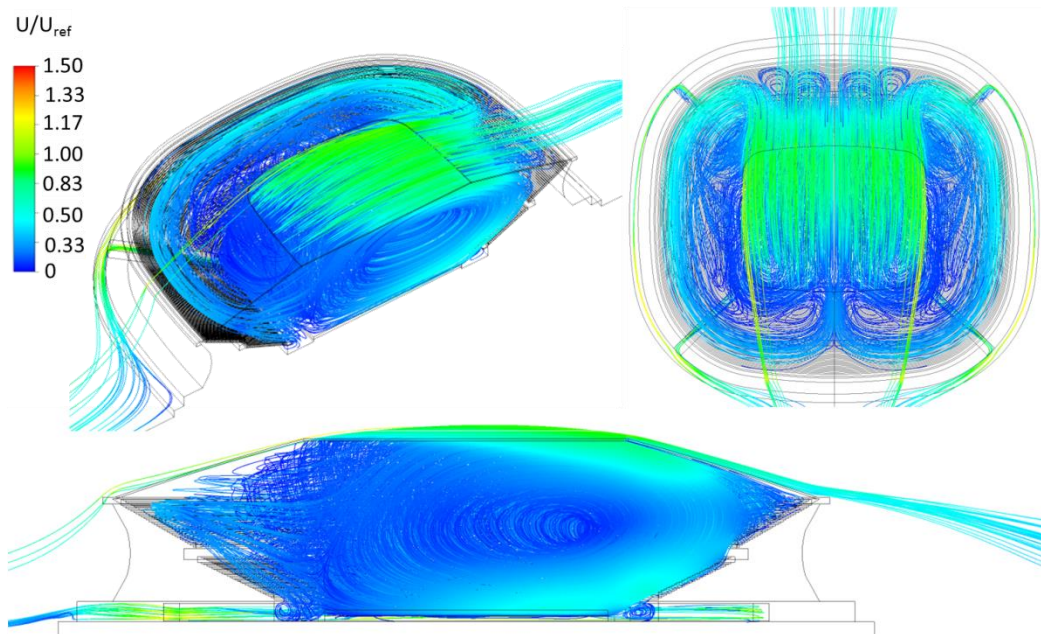


Figure Error! No text of specified style in document.-14 Dimensionless velocity streamlines for the DP 7; $U_{ref} = 5.23$ m/s.

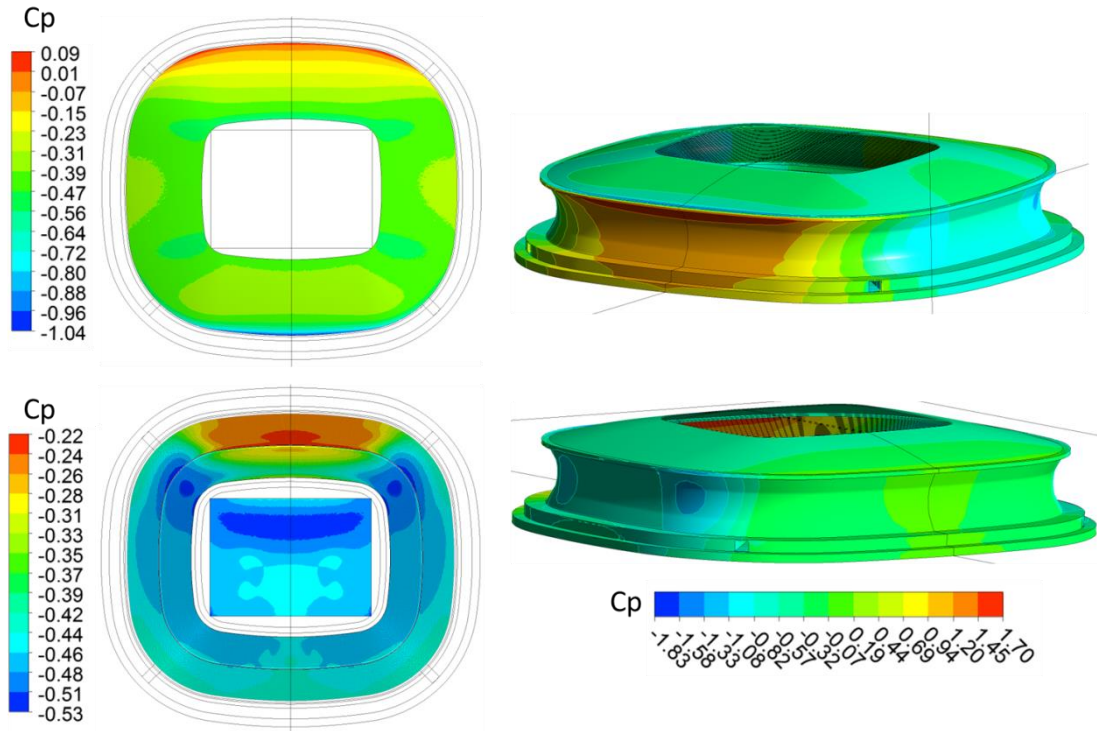


Figure Error! No text of specified style in document.-15 Local C_p values on the exterior and interior stadium surfaces for the DP 8.

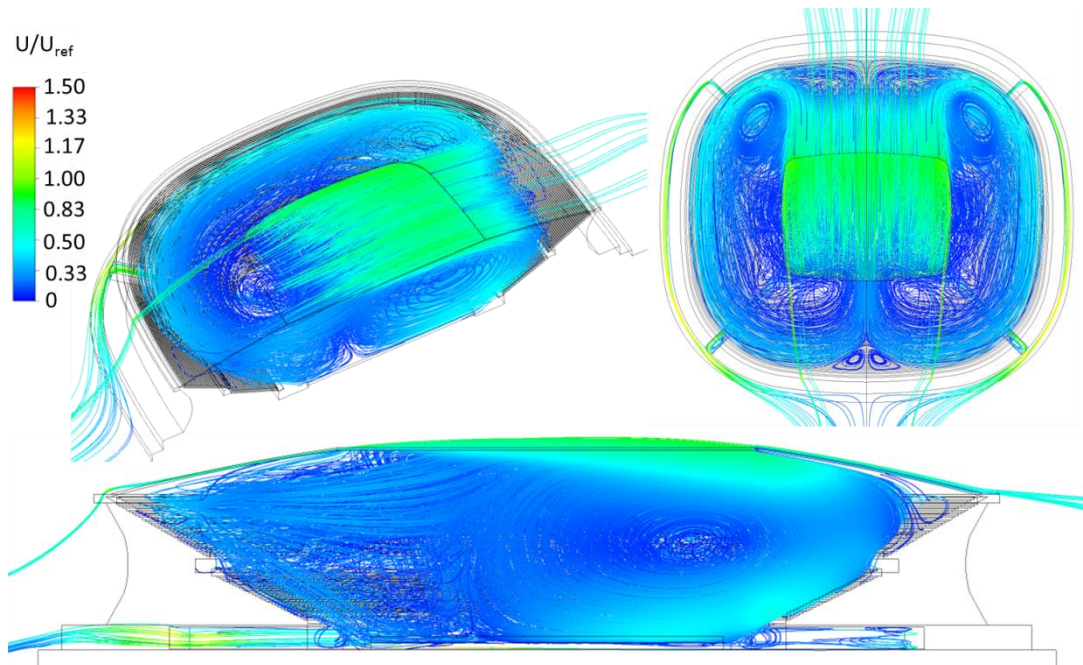


Figure Error! No text of specified style in document.-16 Dimensionless velocity streamlines for the DP 8; $U_{ref} = 5.23$ m/s.

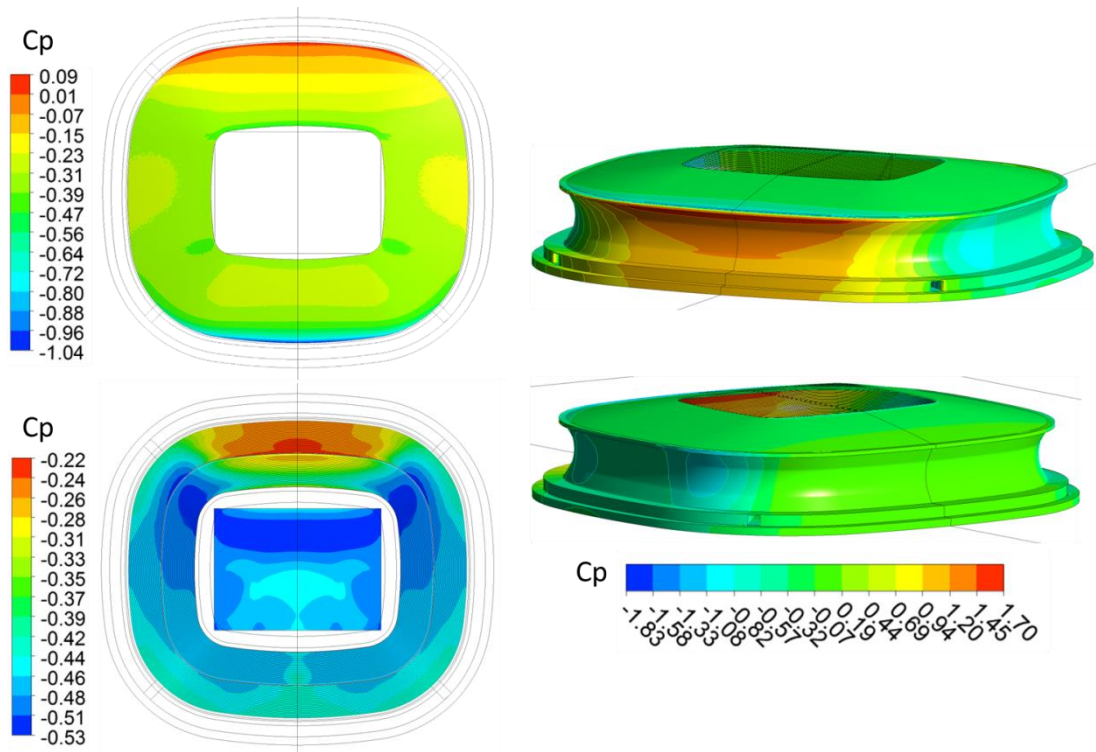


Figure Error! No text of specified style in document.-17 Local C_p values on the exterior and interior stadium surfaces for the DP 9.

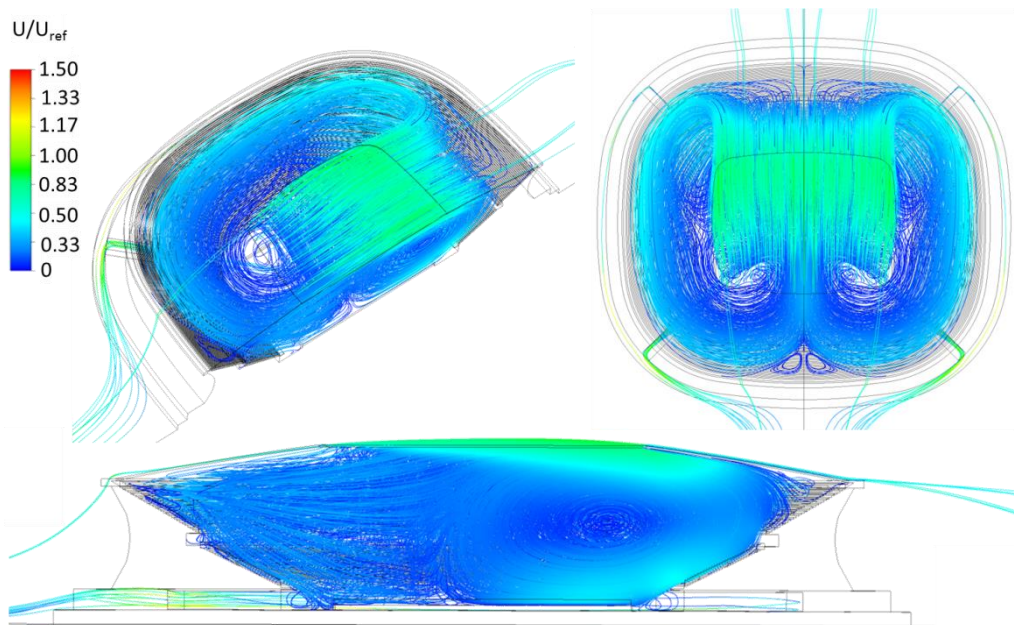


Figure Error! No text of specified style in document.-18 Dimensionless velocity streamlines for the DP 9; $U_{ref} = 5.23$ m/s.

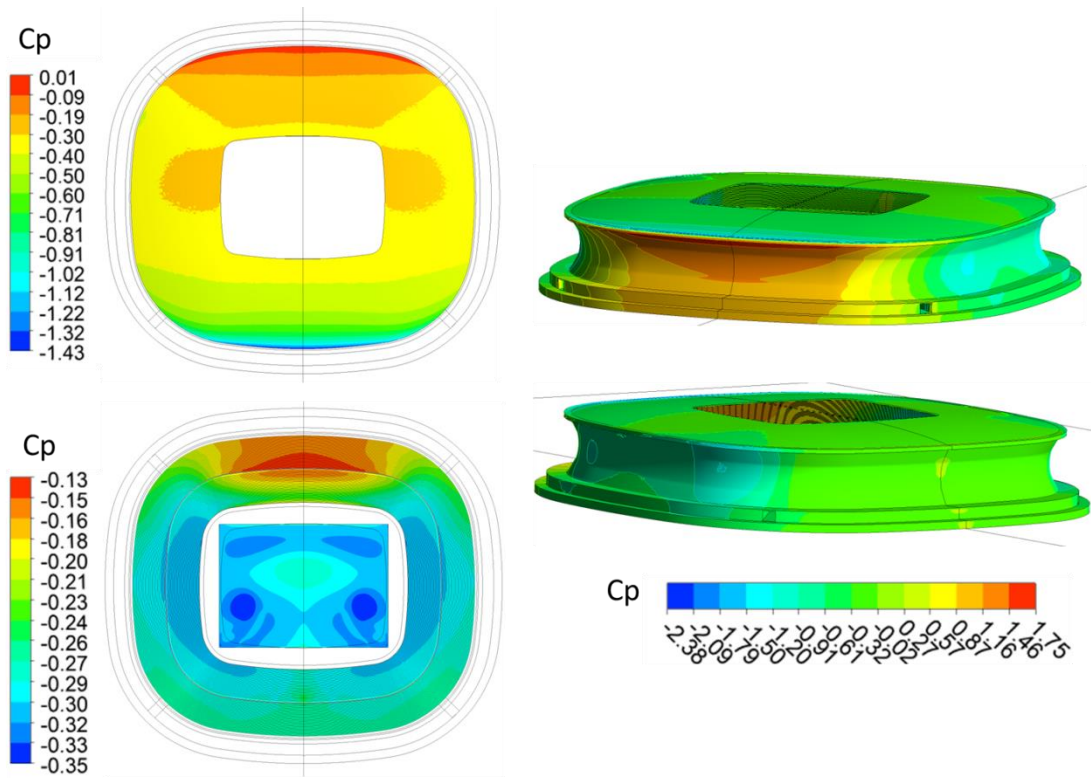


Figure Error! No text of specified style in document.-19 Local C_p values on the exterior and interior stadium surfaces for the DP 10.

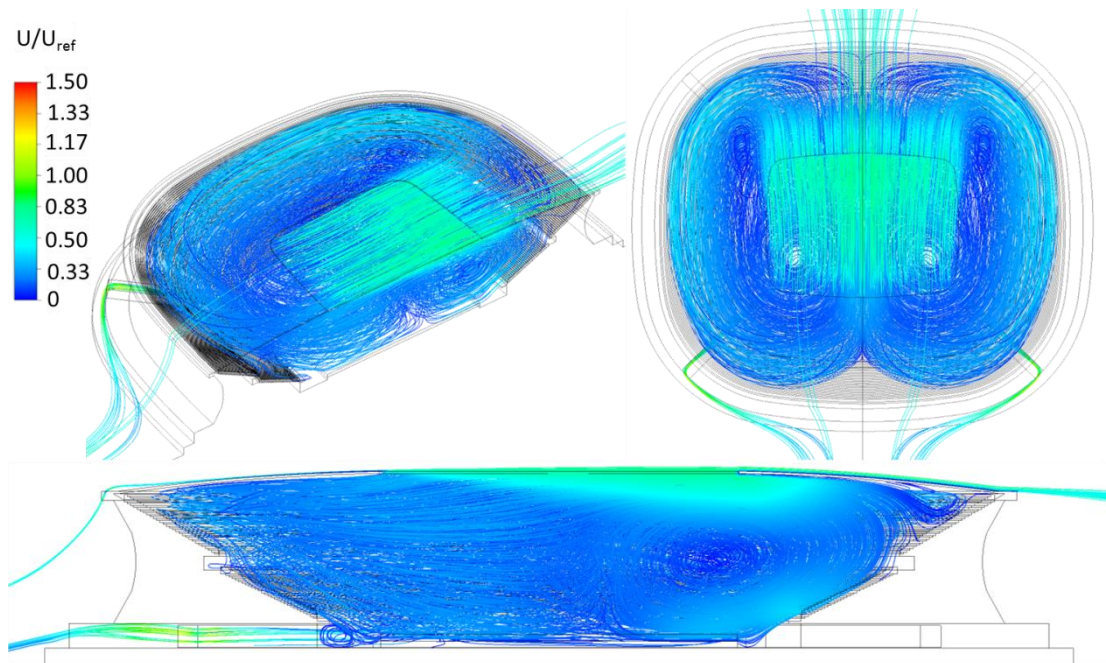


Figure Error! No text of specified style in document.-20 Dimensionless velocity streamlines for the DP 10; $U_{ref} = 5.23$ m/s.

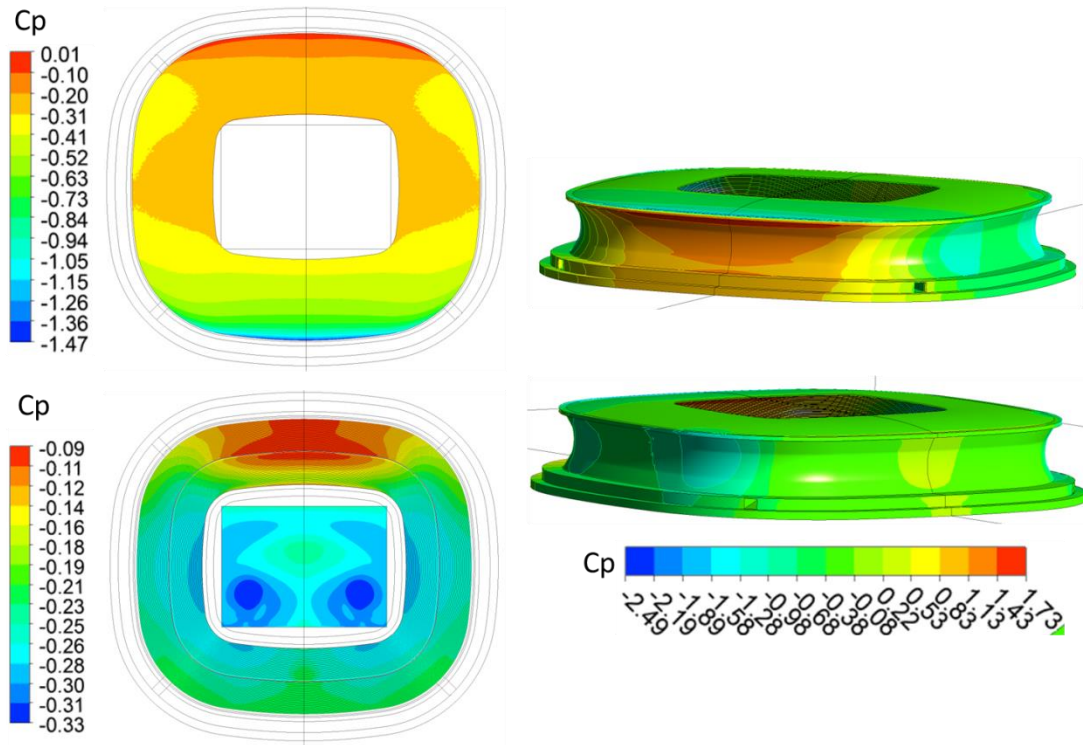


Figure Error! No text of specified style in document.-21 Local C_p values on the exterior and interior stadium surfaces for the DP 11.

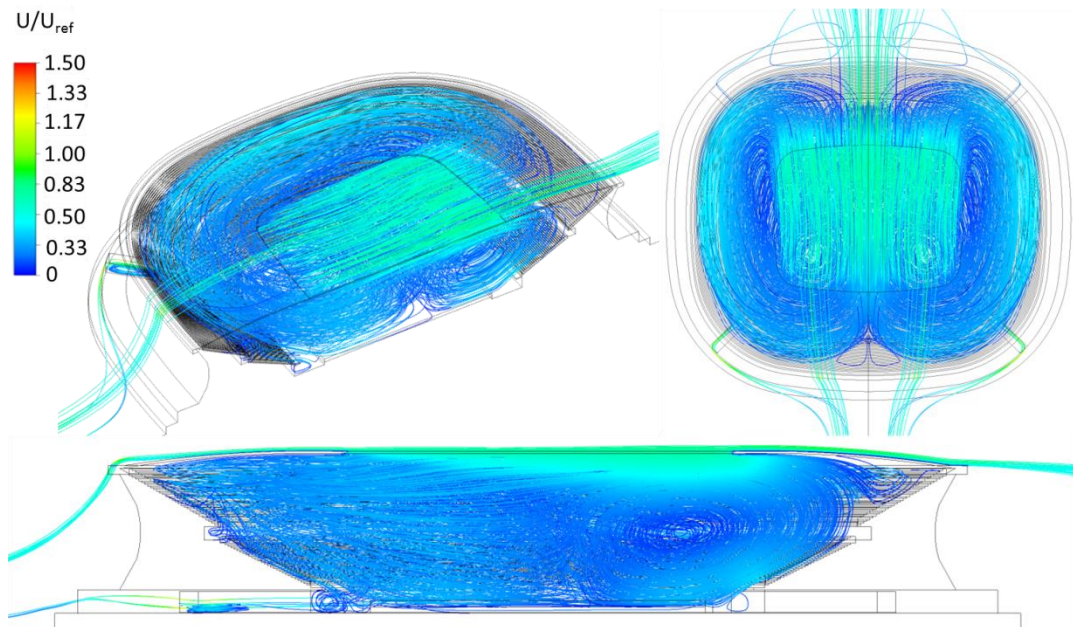


Figure Error! No text of specified style in document.-22 Dimensionless velocity streamlines for the DP 11; $U_{ref} = 5.23$ m/s.

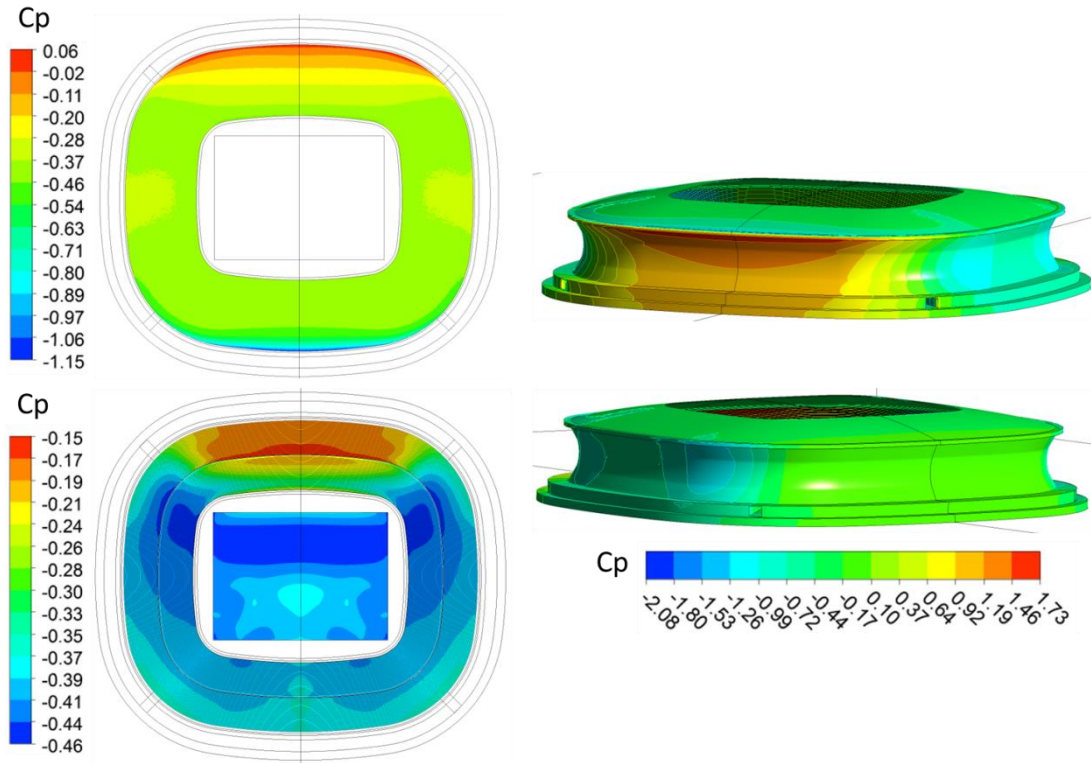


Figure Error! No text of specified style in document.-23 Local C_p values on the exterior and interior stadium surfaces for the DP 12.

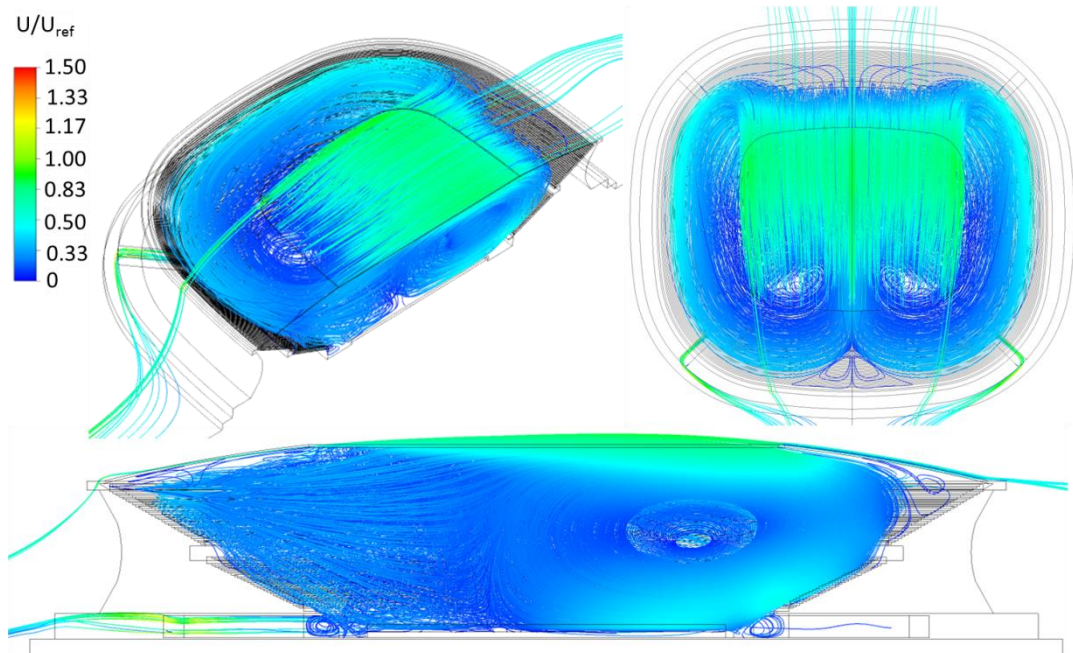


Figure Error! No text of specified style in document.-24 Dimensionless velocity streamlines for the DP 12; $U_{ref} = 5.23$ m/s.

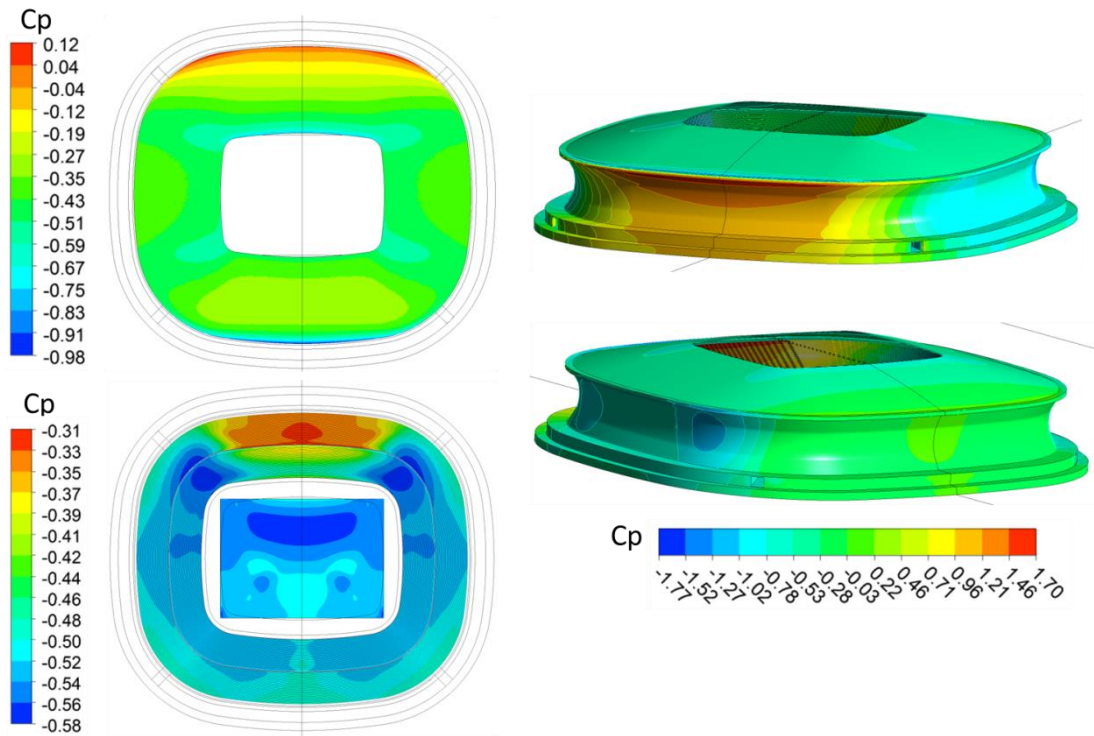


Figure Error! No text of specified style in document.-25 Local C_p values on the exterior and interior stadium surfaces for the DP 13.

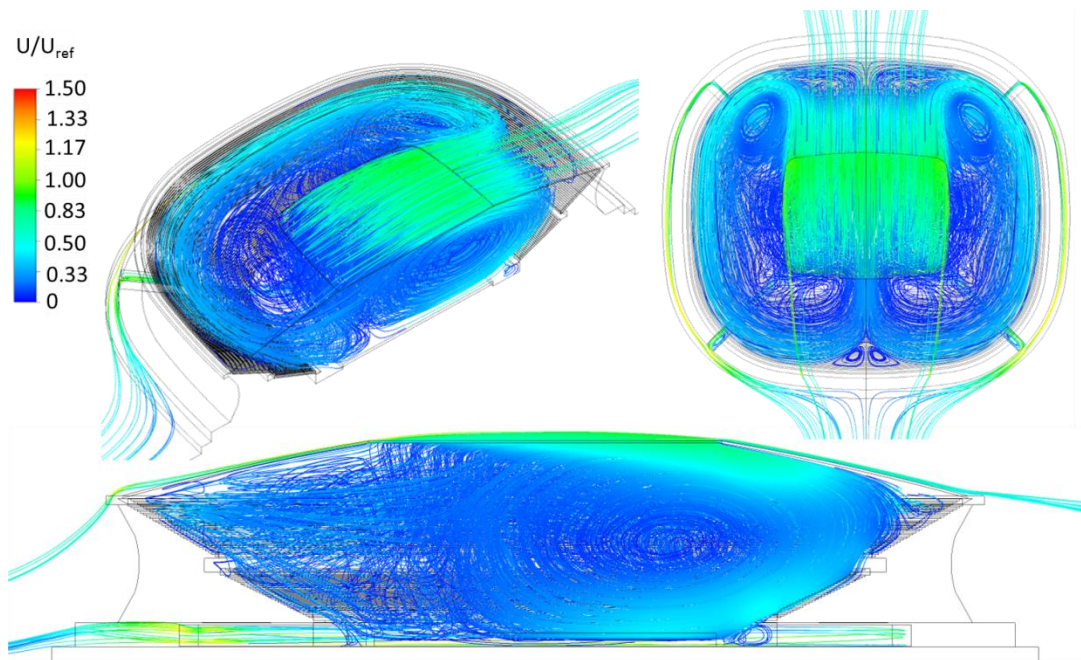


Figure Error! No text of specified style in document.-26 Dimensionless velocity streamlines for the DP 13; $U_{ref} = 5.23$ m/s.

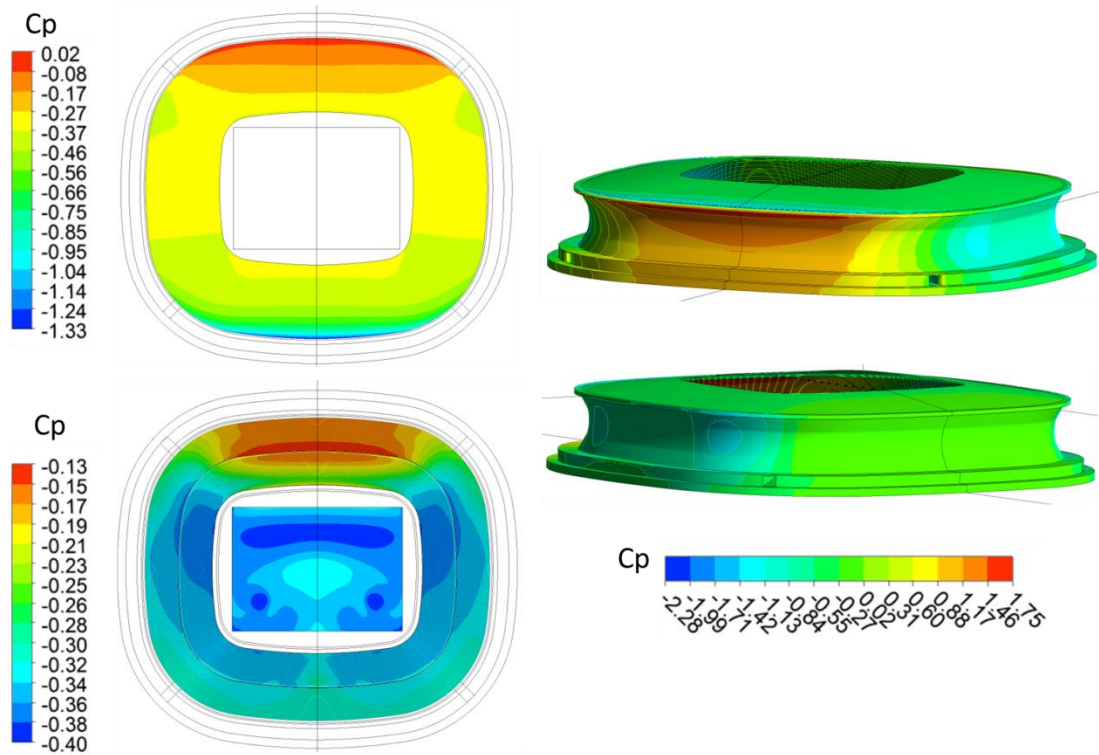


Figure Error! No text of specified style in document.-27 Local C_p values on the exterior and interior stadium surfaces for the DP 14.

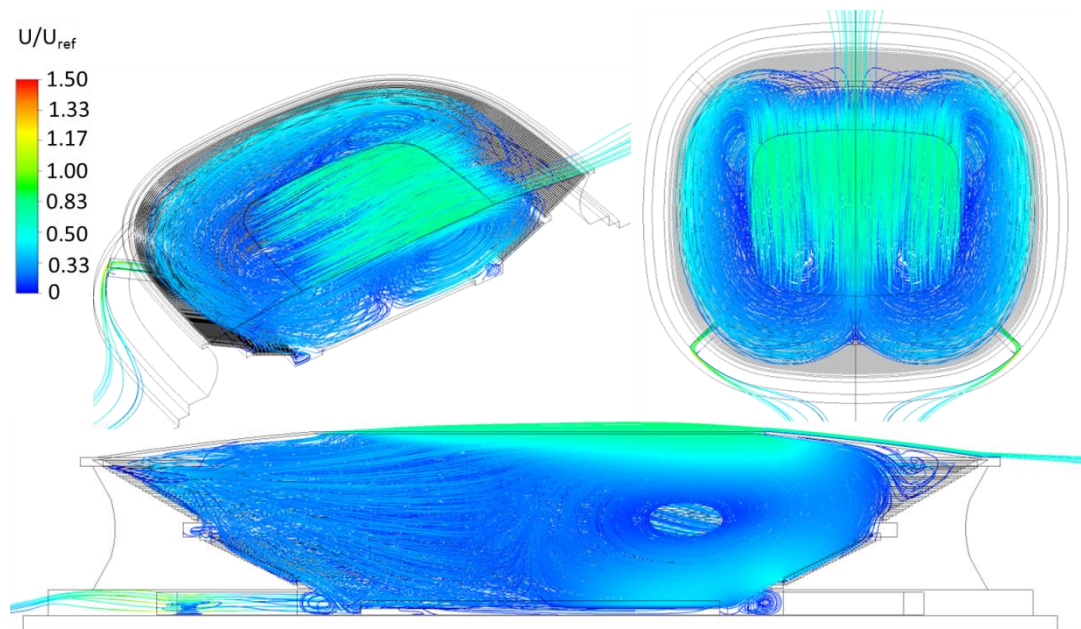


Figure Error! No text of specified style in document.-28 Dimensionless velocity streamlines for the DP 14; $U_{ref} = 5.23$ m/s.